MEASUREMENTS OF MINOR CONSTITUENTS WHICH AFFECT OZONE CONCENTRATIONS IN THE STRATOSPHERE.

by J.R. Eyre, B.A.

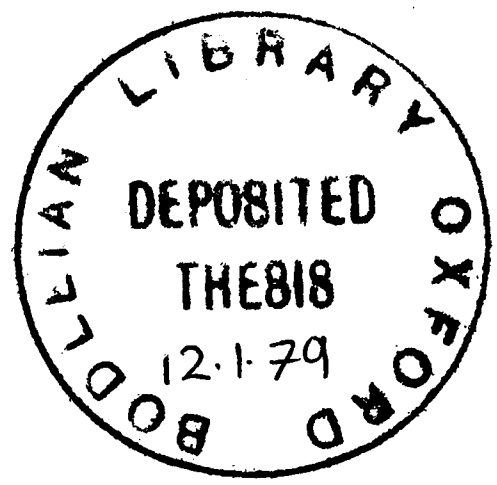

A thesis submitted to the Faculty of Physical Sciences for the degree of Doctor of Philosophy in the University of Oxford.

Wadham College. July 1978.

Frontispiece. Balloon launch.

ABSTRACT

The chemistry of stratospheric ozone is discussed and particular consideration is given to the role of chlorine compounds and to the impact of human activity on the ozone layer. An account is given of the methods used by other researchers to measure hydrogen chloride (HCl) in the stratosphere and their results are summarized.

The pressure modulator radiometer (PMR) is an instrument which can be used to make remote measurements of atmospheric temperature and composition by sensing the radiation transmitted by or emitted from an atmospheric path containing gases with absorption bands in the infra-red. A balloon-borne PMR has been used to detect the absorption of solar radiation by the fundamental vibration-rotation band of HCl at 3.5 micrometres. Using a limb scanning technique, the mixing ratio profile of HCl has been measured over the height range, 16 to 39 km.

It is shown that the amount of HCl in an atmospheric path can be related to the PMR signals using a line-by-line method. The theory is developed in sufficiently general terms for it to be applicable to line-by-line calculations for many other gases with absorption bands in the infra-red. Consideration is given to the modelling of PMR measurements of transmission and emission both in the atmosphere and in the laboratory.

The instrument used to measure HCl is described in detail. The problems associated with the interpretation of the signals are discussed and an account of the

instrument's laboratory testing is given. The reduction of the balloon flight data is described and the method used to retrieve the mixing ratio profile from the FMR signals is presented.

ACKNOWLEDGEMENTS

The pressure modulator radiometer (PMR) has been developed at Oxford over a number of years as an instrument for remote sensing of atmospheric temperature and composition. Consequently I am indebted to all those members of the Department of Atmospheric Physics who have been involved in developing the instrument and interpreting its data, as I have drawn on their experience many times during my work.

I am particularly grateful to my supervisor, Professor J.T. Houghton, for his valuable advice at many stages during the course of the research and for reading this thesis and suggesting improvements. I am indebted to Dr. H.K. Roscoe for the work he did on the feasibility and basic design of the HCl PMR experiment and for his encouragement and practical advice throughout the project. I received considerable help from Dr. R.F. Jarnot and Dr. J. Delderfield in the design and building of the hardware, and I should also like to thank them both for useful discussions on various subjects, both practical and theoretical.

I am grateful to two members of the staff of the Meteorological Office — to Dr. D.R. Pick for his help and co-operation with the integration and testing of the instrument in the U.S.A., and to Dr. B. Barwell for solving the problems associated with the original data tape. While in the U.S.A. I was greatly assisted by the co-operation of many people: Professor D.G. Murcray and his colleagues at

Denver University, the balloon launch team at Holloman USAF base, and Dr. L.L. Stowe and his colleagues, particularly Mr. R. Griffin and Mr. L. Johnson, at NOAA, Washington D.C. I am also grateful to Dr. Stowe for much helpful correspondence which assisted me in analysing the data.

Much of the instrument hardware was made in the Department of Atmospheric Physics workshop by Mr. G.B. Marshall, and most of the optical components were coated by Dr. J. Seeley and his colleagues at Reading University. Mr. K.H. Davies advised me on the design of certain pieces of hardware, organized their construction and obtained the support of the Rutherford Laboratory in analysing the contents of the pressure modulator. I should also like to thank Dr. J.A. Pyle for several useful discussions on stratospheric chemistry.

I was supported throughout my research by a grant from the Natural Environment Research Council, and the HCl PMR project was funded by a grant from the Meteorological Office.

I am indebted to Mrs. L.M. Watson for the care she took in typing this thesis.

Finally, I should like to thank my wife, Deborah, who not only provided constructive comments on my literary style but was also a constant source of support and encouragement throughout my work.

CONTENTS

Chapter 4 (continued)

Appendices

CHAPTER 1. INTRODUCTION.

This thesis contains an account of research undertaken into some aspects of minor constituent measurements in the stratosphere. The structure of the thesis, however, does not reflect closely the order in which the work was done, and it is hoped that some explanation at this stage of the nature of the particular research projects involved may prove enlightening.

The first project undertaken was an attempt to make measurements from a balloon-borne platform of one particular stratospheric minor constituent - gaseous hydrogen chloride - using a pressure modulator radiometer (PMR). The primary objective of this experiment was to determine the total amount and distribution with height of stratospheric hydrogen chloride and thus help to improve our understanding of the role of chlorine compounds in stratospheric chemistry. A full account of this work comprises a major part of the thesis, descriptions of the instrument, its testing and the experimental results being presented in chapters 5, 6 and 7.

The retrieval of results from the data obtained by this instrument required theoretical calculations specific to the infra-red absorption of hydrogen chloride and its detection using a PMR. When this work was concluded, the theoretical studies

were extended to include aspects of the measurement by PMR of several other minor constituents in the upper atmosphere. These were mainly prompted by the Stratospheric and Mesospheric Sounder Experiment (SAMS), which is to form part of the Nimbus G satellite and is designed to make remote measurements of a number of gaseous compounds with absorption bands in the infra-red. Consequently, the theory developed in chapter 4 is sufficiently general for it to be applicable to the measurement of many gases, although the particular case of hydrogen chloride is discussed specifically.

Chapter 2 contains a summary of the chemistry of stratospheric ozone followed by a more detailed discussion of those species and reactions relevant to the measurement of hydrogen chloride. Similarly, chapter 3 summarizes the measurements of chlorine compounds in the stratosphere with particular emphasis on hydrogen chloride. Research into stratospheric chlorine chemistry and the measurement of minor constituents have recently been progressing very quickly, and it is therefore probable that the conclusions of any summary will rapidly be superseded in the light of new results. Consequently it should be noted that these two chapters represent an attempt to summarize developments in these fields reported in the literature up to the end of 1977.

The m.k.s. system of units has been used throughout except in those cases where other units are in such common use that adherence to m.k.s. would

have proved unhelpful. Notable exceptions are the atmosphere as a unit of pressure and atm.cm as a unit of absorber amount. Infra-red frequencies are expressed in wavenumbers (cm^{-1}).

CHAPTER 2. STRATOSPHERIC CHEMISTRY.

2.1. Atmospheric Ozone.

The last few years have seen a considerable growth in the study of the minor constituents of the atmosphere. Efforts have been made to measure their total amounts, their variations with altitude and latitude, and their seasonal and diurnal fluctuations. Also the atmospheric chemistry of these species has been studied in detail in order to explain the complex equilibrium which exists between them and to predict changes in the equilibrium induced by human activity. In particular, interest has centred on the chemistry of ozone. The major chemical reactions involved in the creation and destruction of ozone are now fairly well understood, and computer models of the atmosphere have been developed to study ozone distribution and total amount.

Ozone is a minor constituent comprising less than 10^{-6} of the atmospheric mass. It is found almost entirely in the stratosphere - in the layer 18 to 50 km at lower latitudes and 10 to 50 km near the poles - where it absorbs ultra-violet radiation in the spectral region 240 to 300 nm. The absorption of this radiation is the dominant energy source in the stratosphere and is responsible for the temperature of the stratopause ($\sim$260K), which is high compared to that which would prevail in the absence of ozone (see figure 2.1). It is the only atmospheric species which absorbs significantly in this wavelength region, and it shields the earth's surface from all but a small fraction of this radiation.

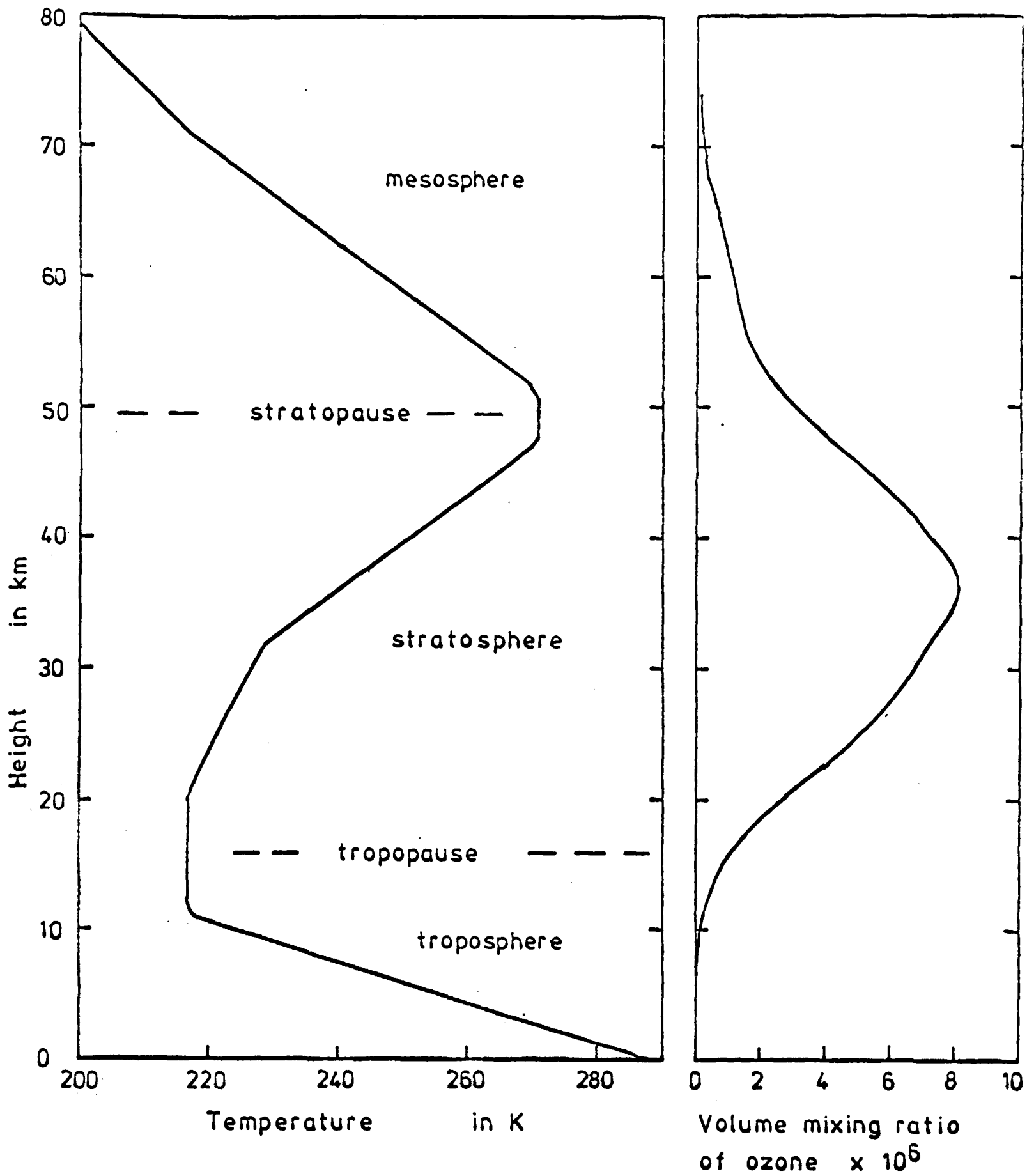

From U.S. Standard Atmosphere, 1976.

Mid-latitude ozone model. Krueger and Minzner (1973).

Figure 2.1 Atmospheric temperature and ozone concentration.

Any reduction in the amount of ozone would permit increased penetration in the biologically important region between 290 and 300 nm. The consequences of such a reduction would include an increase in the incidence of skin cancer and various other changes which cannot at present be calculated or dismissed as negligible, such as the effects on plants, insects, plankton, and important organic molecules including proteins and DNA. Other results of a substantial decrease in ozone (or even a change in its distribution with height) could include changes in stratospheric heating rates, wind system and even temperatures at ground level. It is therefore evident that any human activity which substantially reduces the total amount of atmospheric ozone could seriously affect the circulation and energy flows of the atmosphere, human health and ecological balances in general.

2.2 Modelling atmospheric chemistry.

The equilibrium amount of ozone is determined by the numerous and complex reactions involved in its creation and destruction - their rates of reaction and the abundancies of the species which participate in them. A rigorous treatment of stratospheric chemistry requires that all significant chemical reactions are considered, and that the atmospheric motion is represented by a three-dimensional model. In practice numerical models are unable to include all these aspects due to limitations of computer size and speed. Most models used at present to study stratospheric chemistry are

one-dimensional; variables are averaged over latitude and longitude, and vertical mixing is expressed in terms of eddy diffusion coefficients usually calculated to give agreement with measurement for the vertical profile of a constituent with a lifetime which is long compared to the typical time scales for vertical mixing. However, progress is now being made with multi-dimensional models in which the effects of real atmospheric dynamics on minor constituent distributions can be included and from which latitudinal variations can be predicted. The reliability of all models suffers from our lack of knowledge of many of the important reaction rates and of the abundances and distributions of the species involved, though modellers often find justification for omitting some known species, as their atmospheric lifetimes are calculated to be very short and hence their effects on other reactions are negligible. Also, as the amount of atmospheric data increases, so does the degree to which we can believe the results of models and their ability to predict the effects of man's activities on future atmospheric composition. Indeed, we may have to rely on the results of models when taking action against human activities which threaten the ozone layer, since the large spatial and seasonal fluctuations of ozone amount preclude the measurement with any certainty of small changes in total ozone which represent long term trends. It may prove necessary to take action long before large changes occur for reasons explained in section 2.6.

2.3 The Ozone Cycle.

Stratospheric ozone is produced mainly by the photodissociation of oxygen as follows:

$$O_2 + h\nu \longrightarrow O + O \quad (\lambda < 240 \text{ nm})$$

and then $O_2 + O + M \longrightarrow O_3 + M$.

It is destroyed by the reverse reaction:

$$O_3 + h\nu \longrightarrow O + O_2 \quad (\lambda < 114 \text{ nm}),$$

but the rate of this reaction is too slow to account for the low ozone abundance found. The reactions responsible for most ozone destruction are of the form,

$$X + O_3 \longrightarrow XO + O_2$$

followed by

$$XO + O \longrightarrow X + O_2 .$$

These have a net effect of

$$O + O_3 \longrightarrow 2O_2 .$$

It is a cyclic process and will continue until X or XO is removed from the cycle by some other reaction.

Various naturally occurring species can be represented by X, the most important in the lower stratosphere being NO by the reaction cycle,

$$NO + O_3 \longrightarrow NO_2 + O_2$$

and $$NO_2 + O \longrightarrow NO + O_2 .$$

NO_x is removed from the cycle mainly by the reaction,

$$NO_2 + OH \longrightarrow HONO_2 .$$

Most of the nitric acid so created eventually undergoes photolysis or reacts with some other species restoring the NO_x. NO is produced in the stratosphere mainly by the oxidation of N_2O (Crutzen, Ambio, 1974):

$$N_2O + O(^1D) \longrightarrow 2NO .$$

Another source of NO is the action of galactic cosmic rays in the stratosphere. This source is probably minor under present conditions but in the event (albeit infrequent) of a supernova within about 50 light years of the earth it is estimated that atmospheric ozone would be drastically reduced in this way.

Other species which influence the ozone cycle strongly above 40 km are H, OH and HO_2 by the reactions,

$$H + O_3 \longrightarrow OH + O_2 ,$$

$$OH + O_3 \longrightarrow HO_2 + O_2$$

and $$HO_2 + O_3 \longrightarrow OH + 2O_2 .$$

2.4 Stratospheric chlorine.

Another species which may be represented by X in the equations of section 2.3 is free radical chlorine, Cl.

Some of the chlorine present in the stratosphere is naturally occurring. However, probably more important, is chlorine liberated from man-made compounds.

The impact on the ozone cycle of naturally occurring chlorine species is thought to be small but is not known accurately for the following reasons. Firstly, the input to the stratosphere of natural chlorine is thought to be very low. It is probable that the major source is volcanic injection, but the importance to the ozone cycle of this source depends on the rate of injection into the stratosphere - a value over which there is still much dispute. However, using measured values of HCl in the lower stratosphere, it has been calculated (Crutzen and Isaksen, 1976) that the effects are unimportant. Also there is no evidence for a reduction in ozone following the volcanic eruption of Mt. Agung on Bali in 1963 (Crutzen, Ambio, 1974).

In the troposphere sea-water is a source of HCl but it is so soluble that it is "washed out" in rain-water and is not able to diffuse into the stratosphere in significant amounts. It has been predicted (Stedman et al., 1975) that tropospheric HCl exhibits a steep negative gradient with altitude roughly proportional to the gradient of water vapour. For the same reason we cannot expect any soluble chlorine species, natural or man-made, with a source at ground level to contribute significantly to stratospheric chlorine levels.

Since man-made chlorine compounds may already dominate the chlorine content of the stratosphere, the natural equilibrium of chlorine is probably obscured.

Indeed, because the effects of man-made chlorine species on the ozone layer are predicted to be significant and because such substances influence the amounts of other chlorine species including HCl (see section 2.5), the chemistry of stratospheric chlorine will now be considered in detail.

Free radical chlorine destroys ozone in the following cycle:

$$Cl + O_3 \longrightarrow ClO + O_2 ,$$

$$\text{and then } ClO + O \longrightarrow Cl + O_2$$

$$\text{or } ClO + NO \longrightarrow Cl + NO_2 .$$

The first of these reactions is so rapid that the expected ratio of ClO : Cl is of the order of 10 : 1 (Molina and Rowland, Nature, 1974). It should also be noted that the chlorine and NO_x cycles are interconnected through the third reaction. The above cycle is more efficient in ozone destruction than the equivalent NO_x cycle (Crutzen, Geophys. Res. Lett., 1974), and it continues to destroy ozone until the chlorine is removed from the cycle by one of a number of reactions to give HCl:

$$Cl + CH_4 \longrightarrow HCl + CH_3 ,$$

$$Cl + H_2 \longrightarrow HCl + H$$

$$\text{and } Cl + HO_2 \longrightarrow HCl + O_2 .$$

The reaction,

$$Cl + H_2O_2 \longrightarrow HCl + HO_2 ,$$

is usually omitted from models due to its low rate constant (Ackerman et al., 1977).

In contrast to the troposphere where it is quickly removed in rain water, HCl is comparatively stable in the stratosphere. Consequently most models predict that stratospheric chlorine will be mainly in the form of HCl. However, it is eventually destroyed liberating Cl back into the ozone destruction cycle by the reactions,

$$HCl + OH \longrightarrow H_2O + Cl \ ,$$

$$HCl + h\nu \longrightarrow H + Cl \quad (\lambda < 240 \text{ nm})$$

and $$HCl + O \longrightarrow OH + Cl \ .$$

The main reactions involved in ozone destruction by chlorine compounds are illustrated in figure 2.2 .

Chlorine species do take part in other reactions in the stratosphere, such as

$$Cl + NO \longrightarrow NOCl \ ,$$

but most compounds so formed are quickly photodissociated by the intense solar fluxes at short wavelengths present in the stratosphere (Molina and Rowland, Nature, 1974). However, recent work in stratospheric chemistry has suggested several other reactions of possible importance, and some of these are discussed in section 2.7 . The only way in which chlorine compounds can be removed from the stratosphere is by the slow process of downward diffusion to the troposphere where they are "washed out".

Other halogens are present in the stratosphere but are thought to be less important. Fluorine is present in amounts slightly lower than those of chlorine, but the catalytic efficiency of its equivalent ozone destruction cycle

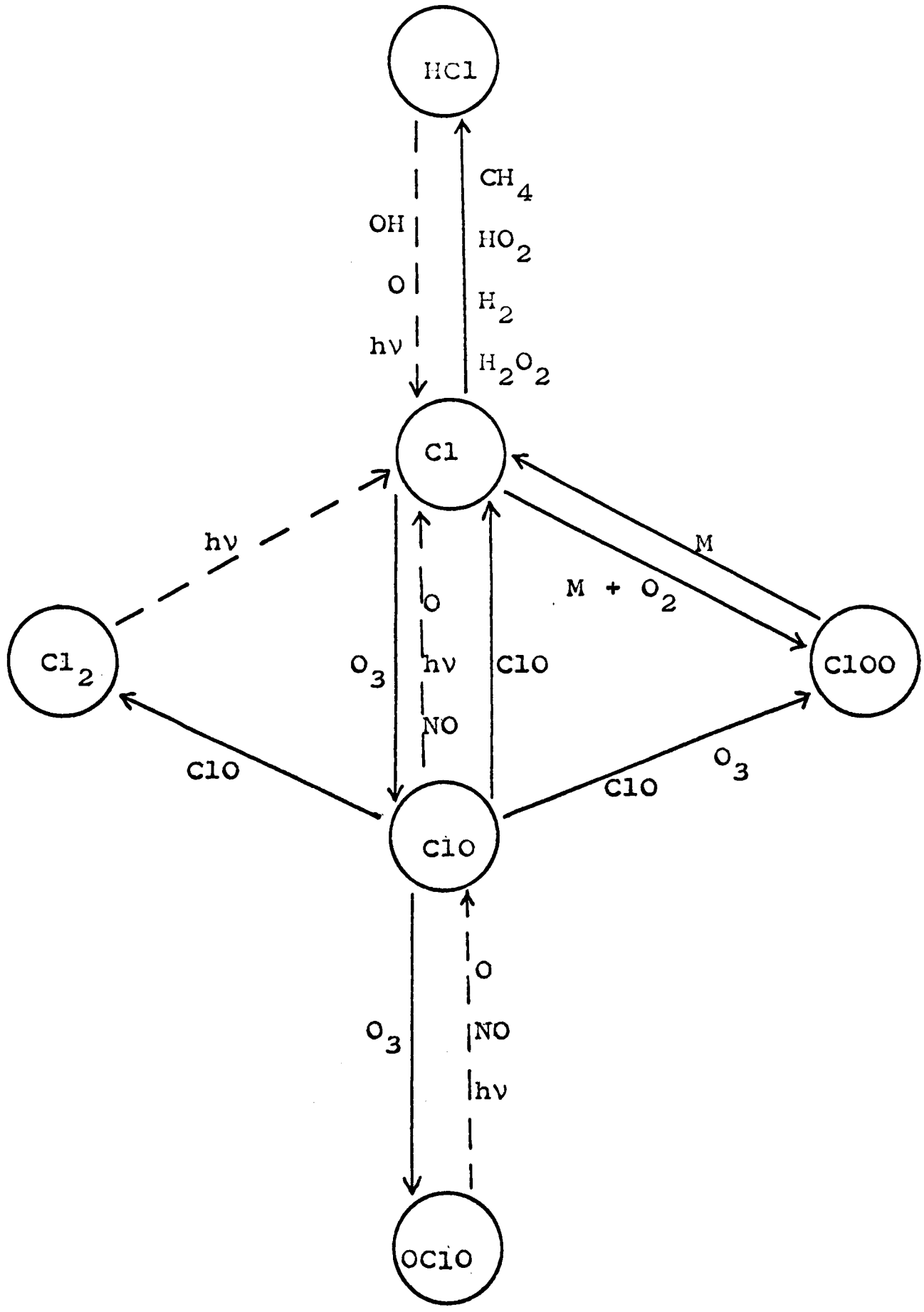

⟶ Reactions occurring day and night.

⟶ (dashed) Reactions which do not occur at night or which occur much more slowly at night than during the day.

Figure 2.2 Schematic of chlorine reactions in the stratosphere.

is a factor of about 10^4 less than that of chlorine (Stolarski and Rundel, 1975). On the other hand bromine has a higher catalytic efficiency but will probably not be present in the stratosphere in significant amounts unless there is a vast increase in the input at ground level of man-made CH_3Br (Wofsy et al., Geophys. Res. Lett., 1975).

2.5 Man's impact on the ozone layer.

Recent concern over the ozone layer has been caused by the realization that certain human activities cause an increase in ozone-destroying species in the stratosphere. Consequently reaearch has been undertaken to estimate the effects of present and projected levels of these activities on the ozone layer.

Several human activities threaten ozone by increasing levels of stratospheric NO. One of these is the growth of supersonic transport. The localized high temperatures created by such aircraft lead to injection of NO directly into the lower stratosphere. Similarly, the use and testing of nuclear weapons causes localised NO production accompanied by strong vertical mixing, and thus the NO concentrations in the stratosphere are affected. The major source of natural stratospheric NO is thought to be N_2O , which is formed by the decomposition of nitrates and organic matter in the soil. It has been suggested that the recent vast increase in the use of artificial nitrate fertilizers will greatly increase the amount of N_2O liberated and so be a source

of species which will change ozone concentrations. The impact of these particular activities has been discussed in detail by many authors (for example, see Crutzen, Ambio, 1974).

Another activity which has caused concern is the rapid growth of the Freons industry, and because it is relevant to measurement of stratospheric HCl it will now be discussed in more detail. Freons are trade-names for certain fluorochlorocarbons, the most important being Freon - 11 ($CFCl_3$) and Freon - 12 (CF_2Cl_2) - substances which do not occur naturally. Both of these are now widely used as propellants in aerosol cans and Freon - 12 is also used as a refrigerant.

These compounds are particularly stable in the troposphere. They are almost insoluble in water and so, unlike HCl and most other chlorine compounds produced by industry, they are sufficiently long-lived in the troposphere to diffuse in considerable amounts into the stratosphere. Even other chlorocarbons tend to have much shorter tropospheric lifetimes than do Freons, which diffuse throughout the troposphere and so have a flux into the stratosphere proportional to their tropospheric mixing ratio. $CFCl_3$ was first measured near the ground in 1971 (Lovelock, 1971) and was soon shown to be present at all latitudes (Lovelock et al., 1973) even though its liberation is confined almost entirely to mid-latitudes in the northern hemisphere. In 1974 its tropospheric mixing ratio was of the order of 10^{-10} (Crutzen, Ambio, 1974). This is in good agreement with what would be expected from the production up to that time and is further evidence for the fact that Freons are particularly long-lived in the troposphere.

$CFCl_3$ and CF_2Cl_2 are broken down by ultra-violet radiation in the wavelength region 190 to 230 nm with the release of free radical chlorine :

$$CFCl_3 + h\nu \longrightarrow CFCl_2 + Cl \quad (\lambda < 230 \text{ nm})$$

$$\text{and} \quad CF_2Cl_2 + h\nu \longrightarrow CF_2Cl + Cl \quad (\lambda < 230 \text{ nm})$$

These reactions are not significant in the troposphere as solar radiation in this region is absorbed by the ozone above. However, there is a partial stratospheric "window" allowing the 190 to 250 nm region to penetrate to the middle of the stratosphere. When the Freons have diffused to sufficiently high altitudes, the rate of photodissociation becomes significant liberating chlorine atoms in a region of the atmosphere where they can effect ozone destruction. The fates of the products of these reactions, $CFCl_2$ and CF_2Cl, have not been studied in detail, but it is thought that they undergo further reactions, probably mainly with O_2, to give more Cl or ClO. Most photodissociation of Freons occurs in the region between 20 and 30 km and recent stratospheric measurements show a decrease in Freon concentrations above about 20 km (see chapter 3). Other destruction mechanisms are thought to be relatively unimportant (Rowland and Molina, 1975). A possible sink is capture of electrons formed in the high atmosphere, for example

$$e^- + CFCl_3 \longrightarrow Cl^- + CFCl_2 ,$$

though more experimental data are needed on this type of

reaction. The reaction of $CFCl_3$ with $O(^1D)$ is very slow and that with OH is endothermic. Indeed, a recent report (NASA Assessment Report, 1977) concludes that no other sinks for Freon - 11 and Freon - 12 have yet been found to alter radically the initial predictions about their role in ozone destruction.

Most other chlorocarbons are probably less important than Freons because they have much shorter tropospheric lifetimes. CCl_4 has a sufficiently long lifetime to reach the stratosphere in significant quantities. It affects ozone via reactions similar to those of Freons and so should be taken into account in models. However there is not yet sufficient evidence to indicate whether tropospheric CCl_4 is mainly natural or man-made (Molina and Rowland, Geophys. Res. Lett., 1974). Crutzen and Isaksen (1976) have studied the possible roles of other chlorocarbons and have concluded that, compared to CF_2Cl_2, $CFCl_2$ and CCl_4, all others are relatively unimportant, except perhaps CH_3CCl_3.

2.6 The effects of Freons.

The effect of Freons on total ozone amount is as yet uncertain. Computer models have been developed to study the effects of various projected levels of Freons production over the next century, but because of a lack of data on diffusion rates, reaction rates and basic stratospheric chemistry, the estimates of the absolute level of ozone depletion must be treated with caution. Also, most models are only one-dimensional which limits their ability to simulate reality. However the models

do indicate some basic features of the problem. Figure 2.3 shows the history of Freons production from 1950 to 1973. If the trend shown were to continue over the next few years the tropospheric mixing ratio (of the order of 10^{-10} in 1974) would be expected to increase by about 10^{-10} every three years, with an attendant increase in diffusion to the stratosphere . Thus, although the present reduction of ozone due to Freons may be negligible, the situation could become appreciably worse within a decade. Measurable effects are to be expected when the ozone destruction due to free chlorine from Freons becomes comparable with natural ozone destruction. Indeed, assuming that atmospheric Freons do cause net ozone depletion and that production continues to increase, it is inevitable that sooner or later the ozone cycle will be dominated by Cl from Freons.

Another feature of the problem is the long time scale. Upward diffusion of Freons is slow and there may be a time constant of 40 to 150 years for Freon photolysis (Rowland, 1974). It is therefore evident that there will be a delay, probably of decades, before the full effects of any release to the atmosphere are shown, and that any changes in ozone amount so produced will be observable for about a century. According to Cicerone et al. (1974), if Freons production stops in the 1970s, ozone depletion will not maximize until about 1990. These features seem to be common to all models and suggest that if action to limit Freons production is required it must occur many years before the effects become fully evident.

The computed magnitude of the effect of Freons on ozone varies from model to model and has changed as the models have become more complex. In 1974, there existed

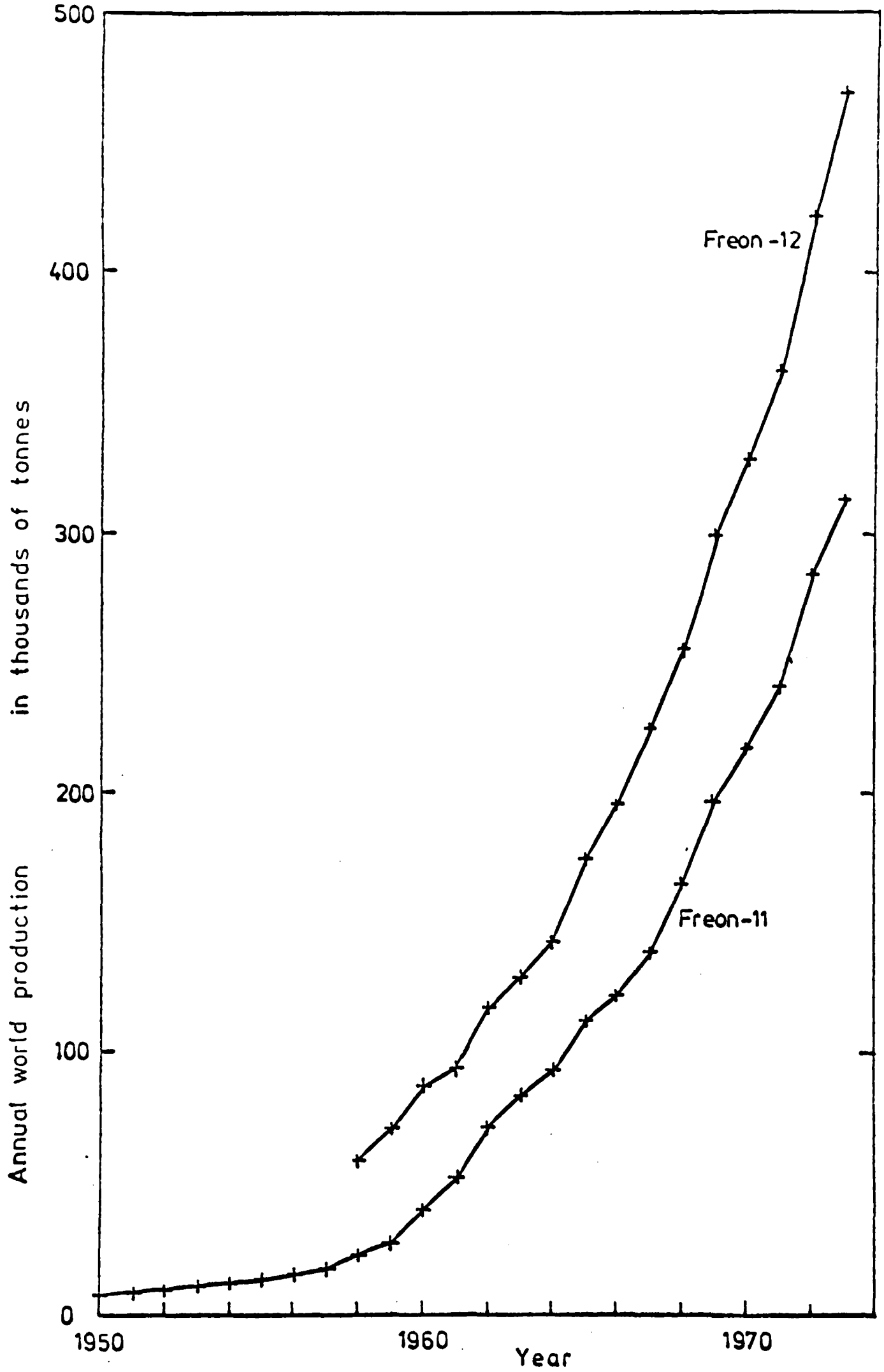

Figure 2.3 Annual world production of Freon-11 and Freon-12.
(Reference: Rowland and Molina, 1975)

four models which included Freons. Their predictions for ozone depletion at equilibrium, if Freon production were to continue at 1972 rates, ranged from 7 to 18%. They agreed that after the cessation of production stratospheric chlorine would increase for 10 years and then decrease with a half-life of 70 to 100 years. Typical of these models is Wofsy's at Harvard (see Wofsy et al., Science, 1975), the results of which are given in figure 2.4 for various scenarios of Freons production.

It must be stressed that the trends shown can be expected to be more reliable than the absolute values for depletion, although as our knowledge of the relevant data improves we may expect these predictions to become more accurate. Also, agreement between models does not indicate a conclusive result since for some important chemical reactions all modellers use the same reaction rates. An illustration of this problem is given in the recent NASA Assessment Report (1977). Before January 1977 the consensus of 9 groups of one-dimensional modellers was that, for steady state conditions with Freons production at its 1975 level, total ozone depletion would be 5 to 9%. It was then suggested that the reaction,

$$NO + HO_2 \longrightarrow NO_2 + OH,$$

occurs 60 times faster at stratospheric temperatures than previously thought. The new reaction rate gives ozone depletion for the same conditions of 11 to 16%. The report gives this as the present best estimate for ozone depletion (and from it calculates a corresponding increase in skin

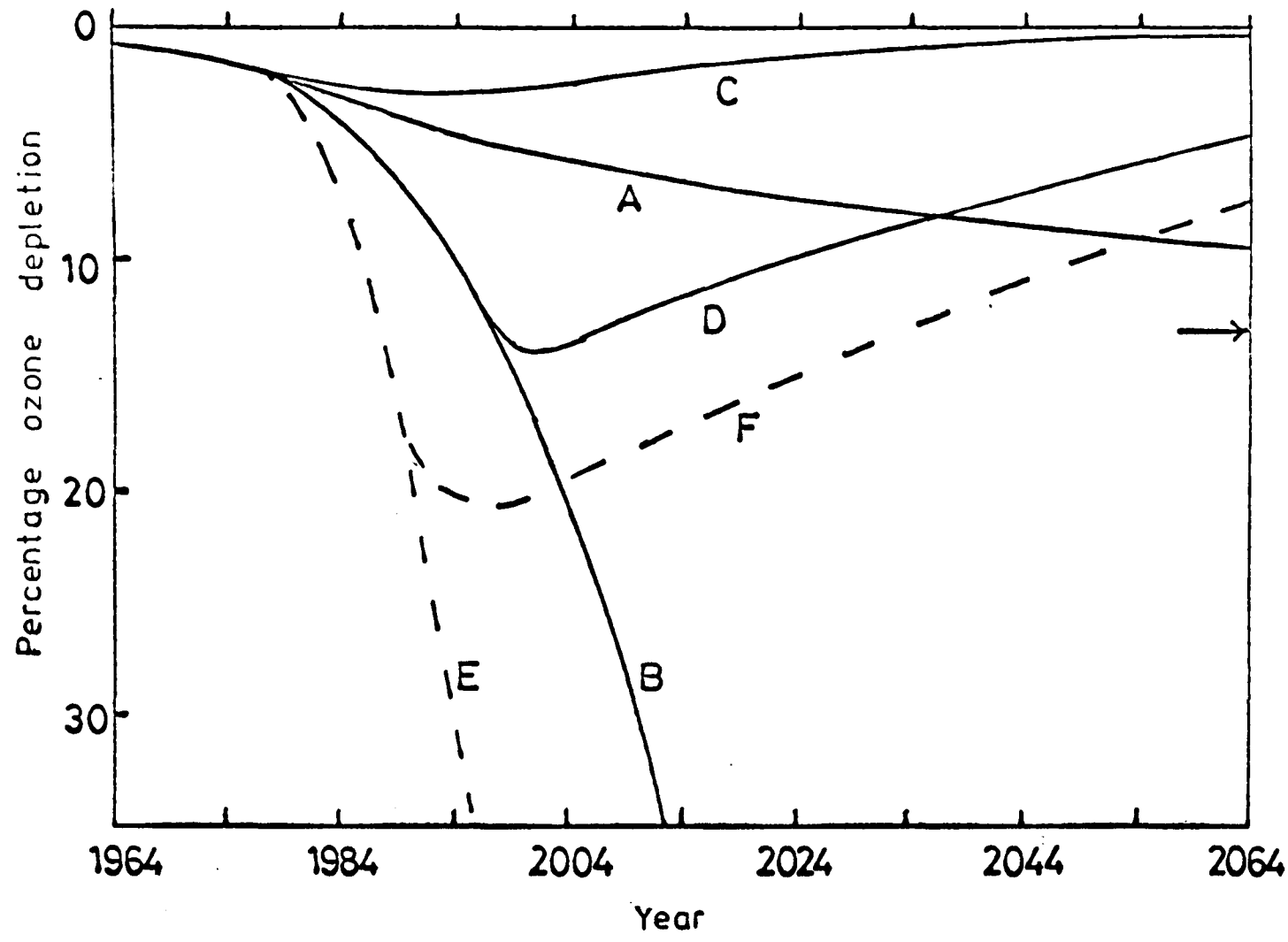

A Production of Freons held constant at 1972 levels. Arrow indicates long-term steady-state conditions.

B Growth rate of 10% per year (7 year doubling).

C As B, with production ceasing in 1978.

D As B, with production ceasing in 1995.

E Growth rate of 22% per year (3·5 year doubling).

F As E, with production ceasing in 1987.

Figure 2.4 Scenarios for ozone depletion calculated by Wofsy et al. (Science, 1975)

cancer of 40 to 100%).

Interesting results have recently been obtained from a two-dimensional model at Oxford (J.A. Pyle, private communication). Although the globally averaged value for ozone depletion due to Freons is calculated to be of the same order as that obtained by one-dimensional models, considerable latitudinal variation is predicted. The model indicates that the expected depletion at high latitudes (where ozone concentrations are highest) is ~ 5 times greater than at the equator. Thus the increase in penetration of ultra-violet will be greatest in those latitudes where the initial penetration is lowest.

2.7 Recent developments.

Since our knowledge of atmospheric chemistry is still limited, the results of models are continually open to review. The validity of any model depends on the inclusion of all the major chemical reactions and the use of fairly accurate reaction rates. Recently it has become apparent that the chlorine-ozone cycle is far more complicated than previously thought, and research into the details of stratospheric chlorine chemistry has increased. A summary of some recent work is given below.

The existence has been predicted (Rowland et al., 1976a) of a species not yet detected in the stratosphere - chlorine nitrate, $ClONO_2$. It is formed by the reaction,

$$ClO + NO_2 + M \longrightarrow ClONO_2 + M ,$$

and thus may act as a temporary sink for free chlorine.

It does not react rapidly with most stable stratospheric species but is decomposed giving ClO by photodissociation and by reactions with O, NO and perhaps other radicals. Initial calculations (such as those of Eggleton et al., 1976) using estimated reaction rates suggested that the formation of $ClONO_2$ might effectively lower ozone depletion by Freons very considerably. Reaction rates have since been measured and at present its importance is not thought to be so great, but the chemistry of this species is far from fully understood.

Another possible temporary sink for chlorine is via the postulated reactions,

$$Cl + O_3 + O_2 \longrightarrow ClO_3 + O_2$$

and $$ClO_3 + OH \longrightarrow HClO_4 ,$$

(Simonaitis and Heicklen, 1975; Prasad, 1976). However this is still speculative since the reaction rates are unknown and the species undetected in the atmosphere. Rundel and Stolarski (1976) suggest that other reactions may affect the chlorine-ozone cycle even though their rates are slow, since the lifetime associated with diffusion to the troposphere of HCl is of the order of 8 years. As an example they give

$$ClO + O_3 \longrightarrow ClOO + O_2$$

and $$ClOO + M \longrightarrow Cl + O_2 + M .$$

The significance of these reactions is that they allow

the ozone destruction cycle to continue in the absence of atomic oxygen, leading to increased ozone depletion at lower altitudes.

Yet another species of possible importance, HOCl, has been suggested by Sze (1977). This may also act as a temporary sink for reactive species by means of a number of postulated reactions:

$$ClO + H_2O_2 \longrightarrow HOCl + HO_2 ,$$

$$ClO + HO_2 \longrightarrow HOCl + O_2 ,$$

$$OH + ClONO_2 \longrightarrow HOCl + NO_3$$

$$\text{or} \quad H_2O + ClONO_2 \longrightarrow HOCl + HNO_3 ,$$

$$\text{and then} \quad HOCl + h\nu \longrightarrow OH + Cl ,$$

$$HOCl + OH \longrightarrow H_2O + ClO ,$$

$$HOCl + O \longrightarrow ClO + OH$$

$$\text{or} \quad HOCl + O \longrightarrow Cl + HO_2 .$$

Sze's calculations show that HOCl may be a very important stratospheric sink, but they suffer from a lack of fundamental data not only for the above reactions but for the chemistry of oxides of hydrogen in general.

It must be stressed that, although all the above reactions almost certainly occur, their rates and hence their importance are still in doubt, and more work into the theory of the chemistry involved and measurements of the relevant species are required.

CHAPTER 3. MEASUREMENTS OF CHLORINE COMPOUNDS IN THE STRATOSPHERE.

3.1 Methods of measuring stratospheric HCl

Since the first measurements in late 1974, five research groups have reported profiles of stratospheric HCl. Most of these (including our own, which will be described in detail in later chapters) have been obtained through measurements from balloon platforms of the infra-red absorption by the fundamental vibration-rotation band of HCl at 3.5 micrometres, with the sun as a source. Using this method, vertical profiles can be obtained by tracking the setting sun at zenith angles greater than 90^{o}. The advantages of this geometry are discussed in chapter 4.

Farmer's group at Jet Propulsion Laboratory, California, have used a solar tracking system and a high speed, stepped, Michelson interferometer with a spectral resolution of 0.13 cm^{-1} and an ability to measure in the spectral range 1750 to 3050 cm^{-1} (Farmer et al., 1976). They have made measurements from high altitude aircraft and balloon platforms, and they have studied the spectra obtained to identify the features corresponding to HCl absorption lines. Compared to other species with absorption lines in the same spectral region (e.g. methane), HCl is present in the stratosphere in very small amounts. For this reason many HCl lines are found to be overlapped and difficult to identify - a problem common to all infra-red methods and accentuated for conventional

spectroscopic techniques by limited instrumental resolution. In fact, Farmer suggests a reanalysis of the 3 to 4 micrometre spectra of atmospheric gases to render such features unambiguous. However, they have found the lines R1, P5 and P6 of the fundamental vibration-rotation band of $H^{35}Cl$ to be the most distinct and they have also used the R2 and R3 lines of $H^{35}Cl$ and the R1, R2 and R3 lines of $H^{37}Cl$. Their retrievals have been made by comparing the measured spectra with synthetic spectra calculated for simulated atmospheric paths containing different amounts of HCl. Correct identification of HCl features is supported by the fact that the relative strengths of the absorptions due to different lines for the same observation are in agreement with theory.

Ackerman's group at Institut d'Aéronomie Spaciale de Belgique in Brussels use another infra-red technique; they have flown a grille spectrometer on board a balloon gondola equipped with a sun-tracking system (Ackerman et al., 1976). The instrument has a resolution of 0.22 cm^{-1} and a scanning time of 6.5 minutes across the spectral region 2916 to 2970 cm^{-1}. Six pairs of HCl lines occur in this interval and they use the lines R1 and R2 of both $H^{35}Cl$ and $H^{37}Cl$. From their data, they make plots of integrated absorptions for the HCl lines against the tangent heights of the solar rays, and from these they retrieve a vertical profile for HCl.

Murcray's group at Denver University use a similar instrument - an infra-red grating spectrometer and sun-seeker (Williams et al., 1976 b). To measure HCl they adapted their spectrometer to scan in the region

containing the R1 line of $H^{35}Cl$ at 2925.9 cm^{-1}, and they have derived their profile from the measured absorption of this line only. Their scan time of 110 seconds allows a number of spectra to be obtained during the period of about 30 minutes for which the sun is visible above the horizon at zenith angles greater than 90^{o}.

The only other reported measurements of stratospheric HCl have been made by Lazrus' group at NCAR, Boulder, Colorado (Lazrus et al., 1976; Lazrus et al., 1977). These measurements differ fundamentally from all the others in that they use in situ chemical techniques rather than remote infra-red spectroscopic methods. The instrument, mounted on an aircraft, has been used to take samples in the lower stratosphere, while measurements above 20 km have been made from a balloon platform. Hydrogen halides are captured by drawing air through base-impregnated filters. Other areas of filter are masked during sampling to give a contamination control. After the flight, the chlorine is extracted from the filters and analysed chemically. Comparison is made between the impregnated filters (measured to be almost 100% efficient in trapping HCl) and other unimpregnated filters. Since gaseous HCl is only trapped by the base-impregnated filters, this method gives discrimination between gaseous and particulate chlorine species. However, some other gaseous chlorides are also trapped by the base, and laboratory measurements are performed to find the trapping efficiency for each species. It has been found that the base is quite efficient in trapping acidic gases such as chlorine nitrate ($\sim$ 80% efficiency). Therefore this method will tend to

give a result related to the total amount of gaseous acidic chlorine species rather than HCl alone.

3.2 Results.

The first positive identification of HCl in the stratosphere was made by Lazrus' group using the data from aircraft and balloon flights made in autumn 1974 (Lazrus et al., 1975; Lazrus et al., 1976). The balloon flight was made from Holloman USAF base, New Mexico (33^{o}N) and the aircraft flights at various latitudes in the northern hemisphere, measurements generally being made in the early morning. From the data of these flights they were able to deduce that the mixing ratio of HCl decreased sharply below 21 km - a profile consistent with a high altitude source of HCl. Another interesting result of these measurements was that the ratio of particulate to gaseous chlorine was found to be very small. This suggests that stratospheric aerosols do not provide a significant sink for chlorine species. Further measurements were made throughout 1975 ranging in altitude from 12 to 33 km (see Volz et al., 1977). Another series of balloon flights from Holloman was undertaken in 1976 (Lazrus et al., 1977). They were made between 6 a.m. and 10 a.m. local time at different seasons of the year. Together with lower altitude measurements made from aircraft, they yielded results over the altitude range 12 to 36 km and gave evidence of very little seasonal variation. The mean profile derived

from the 1976 measurements is given in figure 3.1 and is very similar to that obtained from the 1975 results.

Farmer's group have reported two sets of measurements of HCl in the stratosphere. The first was made in the winter of 1974-5 from an aircraft flight at 21 km over continental U.S.A. (Farmer et al., 1976). From the data a profile was obtained for the lower stratosphere up to the platform height, and the peak of the HCl mixing ratio was shown to be above 21 km. The second reported profile (Raper et al., 1977) was the result of two balloon-based measurements made from Palestine, Texas (32^{o}N) on 26th September, 1975, and 18th May, 1976, from altitudes of 40 km and 37 km respectively. The results from the two flights were very similar and gave no evidence of seasonal variability. They yielded a profile over the range 21 to 37 km to an accuracy of the order of 30%.

The results of Ackerman's group were obtained from a balloon flight on the 2nd October, 1975, from Aire sur l'Adour in France (44^{o}N). Measurements were made at sunset from a float altitude of 35 km and a profile retrieved for the range 18 to 33 km (Ackerman et al., 1976).

Murcray's group flew their balloon-borne instrument to an altitude of 30 km from Holloman on 16th December, 1975, and deduced a profile up to the balloon height from the data taken at sunset (Williams et al., 1976 b). However because of a low signal-to-noise ratio, the profile above 26 km is reported to be uncertain.

The results of the infra-red measurements, including our own, are also shown in figure 3.1. It can be seen that they are all similar in amount, but no firm conclusion can be drawn from them concerning the shape of

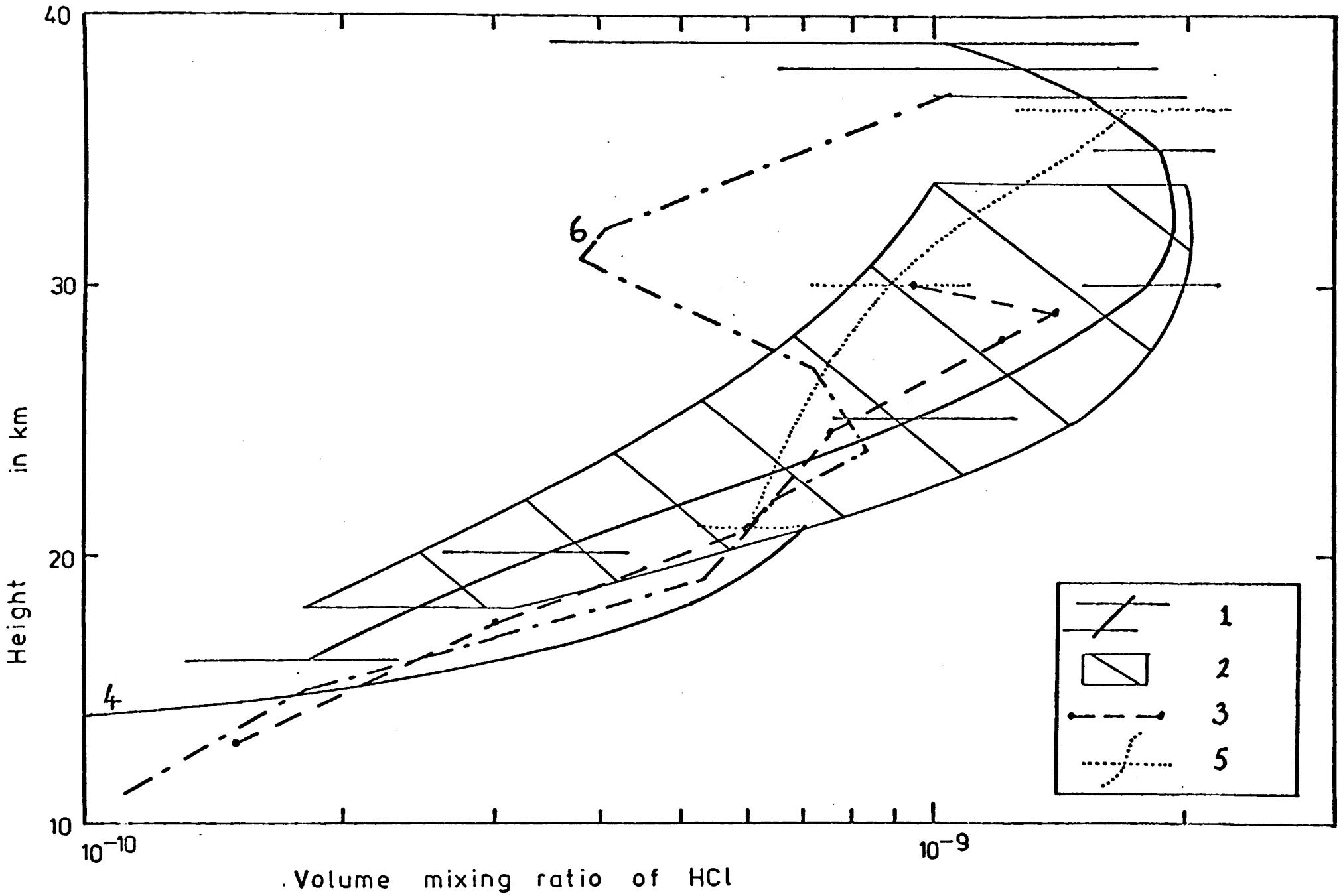

References

1. This work
2. Ackerman et al. (1976)
3. Williams et al. (1976 b)
4. Farmer et al. (1976)
5. Raper et al. (1977)
6. Lazrus et al. (1977)

Figure 3.1 Measurements of stratospheric HCl.

the profile above about 25 km. They are also similar to the results of the direct sampling measurements in the lower stratosphere, but Lazrus' results tend to fall below those obtained by infra-red methods at higher altitudes. On average there is a fairly good agreement between HCl measurements, particularly by infra-red techniques, and the results of models (see, for example, Volz et al., 1977, and Sze, 1977). However, model results have not been included in figure 3.1 since the profile shapes which they predict vary noticeably from each other and are dependent on details of chlorine chemistry, such as those outlined in chapter 2.7, which are not well understood. Present models do not show a fall in the mixing ratio profile above 30 km as suggested by some measurements, but this is not surprising since at these altitudes the sensitivity of the infra-red techniques is at its lowest and large uncertainties are to be expected.

3.3 Variations in stratospheric HCl

When comparing the results of different researchers, agreement need not necessarily be expected since the measurements are made in various places at different times of day and year. However, for the HCl measurements reported above, it seems reasonable to expect similar results for the reasons now outlined.

Compared to other chlorine compounds in the stratosphere, HCl has a long lifetime and is a major sink for the more reactive species. Therefore, although there will obviously be large diurnal variations in the

rates of creation and destruction of HCl, the total amount of this species is expected to show little diurnal variation. This has been confirmed by the results of two one-dimensional models which include the effects on chemistry of the day-night cycle (Kurzeja, 1977; Rowland et al., 1976 b). Both show a negligible diurnal change in HCl amount at all stratospheric altitudes. In contrast, Kurzeja shows that, as expected from simple arguments, the amount of Cl varies diurnally by several orders of magnitude, and that ClO varies by a factor ~3 at 40 km and by more at lower altitudes. Kurzeja also suggests that, since temporary sinks such as $ClONO_2$ exhibit a considerable diurnal variation, one-dimensional models which neglect night-time chemistry cannot be expected to calculate accurately ozone depletion due to chlorine species.

To study seasonal and latitudinal variations a two-dimensional model is required. Preliminary results from the Oxford model show that for mid-latitudes very little seasonal variation in HCl is expected (J.A. Pyle, private communication). The expected latitudinal variation varies with altitude; at 40 km the model shows very little variation with latitude, but at 25 km the HCl amount is calculated to vary by a factor ~4 between equator and pole. Since all the measurements listed in section 3.2 were made in mid-latitudes, little variation is to be expected between them.

On top of the spatial and short term variations, however, a long term increase in total stratospheric HCl is expected as the total chlorine amount is increased by input from the troposphere. At present, reported results only cover the period 1974 to 1976 - too short a time for long term effects to be noticeable - but if

man-made chlorine compounds are the dominant source of stratospheric chlorine then we may expect future measurements of HCl to show an upward trend.

3.4 Measurements of other halogen compounds

Since the prediction of the interaction between ozone and Freons was first made in 1974, many measurements have been reported of $CFCl_3$ and CF_2Cl_2 in both the troposphere and stratosphere. These are compared in figures 3.2 and 3.3. Despite a substantial scatter in the measurements, it can be seen that their average value is in fairly good agreement with the theoretical prediction of Crutzen and Isaksen (1976). Two other species which may play a significant role in stratospheric chemistry, $CHCl_3$ and CCl_4 , are shown in figure 3.4. At present they have only been measured in the lower stratosphere.

The important short-lived species , Cl and ClO, have only been measured by one group (Anderson et al., 1977). The results are shown in figure 3.5 along with the theoretical calculations of Chang (see Volz et al., 1977). Agreement between measurement and calculation is only good for the winter measurements, but for reactive species such as these greater spatial and temporal variations are to be expected. Also it has recently been suggested (Ackerman et al., 1977) that models have tended to under-estimate the amount of ClO above 25 km because of an over-estimate of the methane amount. Ackerman's group show, using their remeasured methane profile and a simple calculation,

Key to figures 3.2 and 3.3

Measurements of CF_2Cl_2 and $CFCl_3$

	Researchers	Year of measurement	Reference
□	Schmeltekopf et al.	1975	Schmeltekopf et al. (1975)
○	Heidt et al.	1973, 1974, 1975	Heidt et al. (1975)
+	Lovelock et al.	1971	Lovelock et al. (1973)
		1973,1974	Lovelock (1974)
——	Rasmussen	1975	See Volz et al. (1977)
▽	Hester et al.	1974	See Heidt et al. (1975)
▲	Volz et al.	1976	Volz et al. (1977)
×	Goldan et al.	1975	See Sundararaman (1976)
⊗	Williams et al.	1968, 1975	Williams et al. (1976 a)
◇	Zafonte et al.	1973	See Sundararaman (1976)
●	Krey et al.	1975	Krey et al. (1977)
		1974	See Sundararaman (1976)
△	Ehhalt et al.	1976	See Volz et al. (1977)
⊠	Tyson et al.	1976	See Sundararaman (1976)

Theoretical predictions for late 1975:
Crutzen and Isaksen (1976)

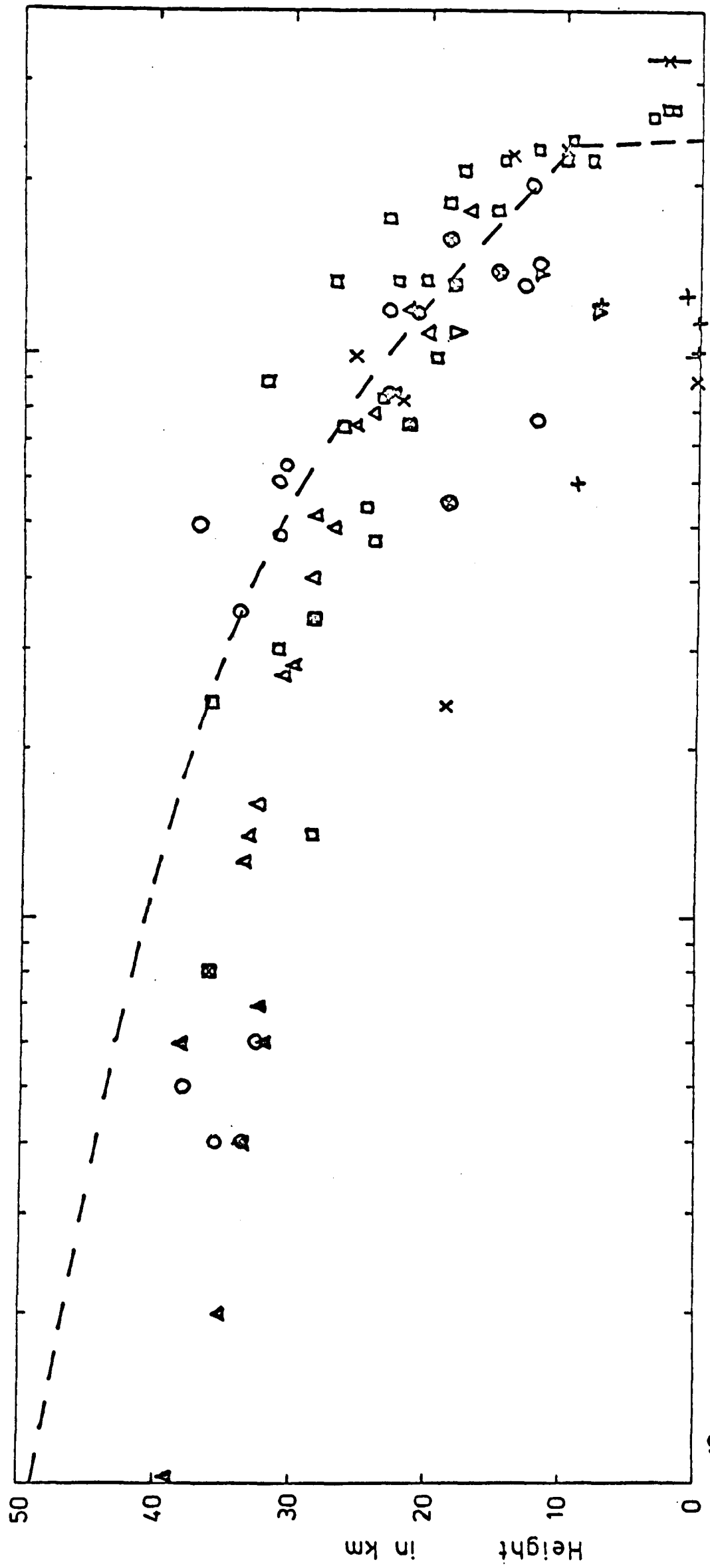

Figure 3.2 Measurements of atmospheric $CF_2\underline{Cl}_2$.

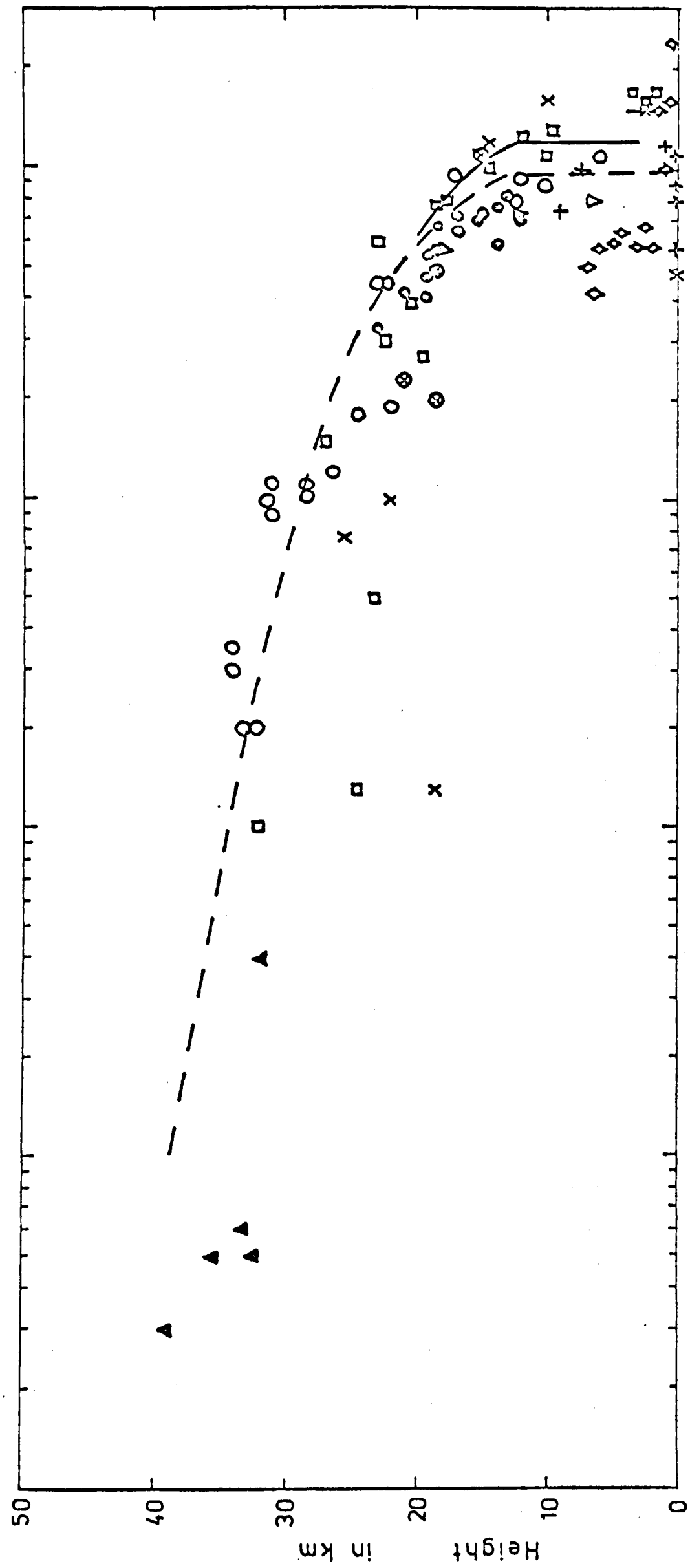

Figure 3.3 Measurements of atmospheric $CFCl_3$.

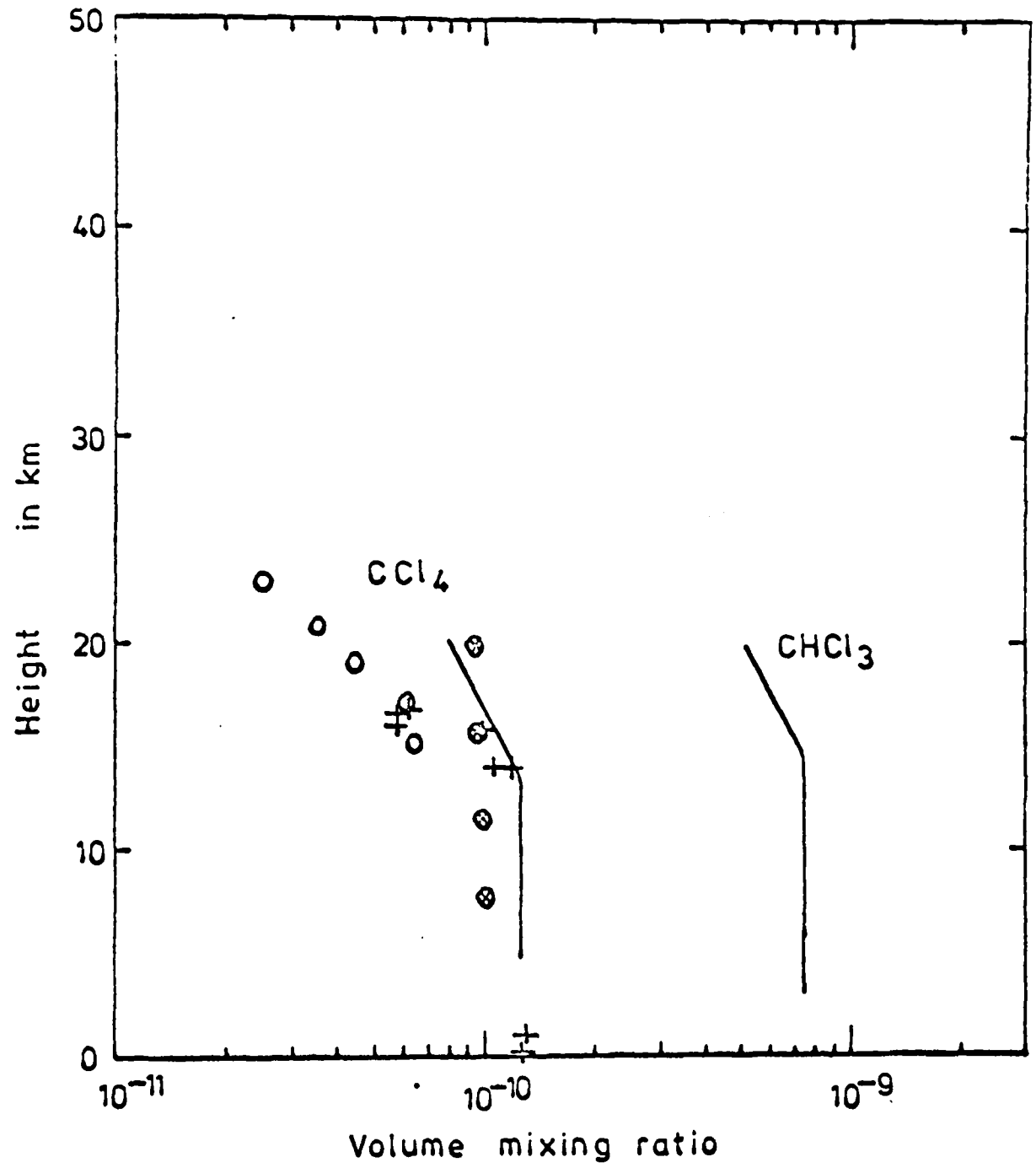

	Researchers	Year of measurement	Reference
+	Lovelock	1974	Lovelock (1974)
o	Krey et al.	1975	Krey et al. (1975)
——	Rasmussen	1975	see Volz et al. (1977)
⊗	Williams et al.	1975	Williams et al. (1976 a)

Figure 3.4 Measurements of atmospheric CCl_4 and $CHCl_3$.

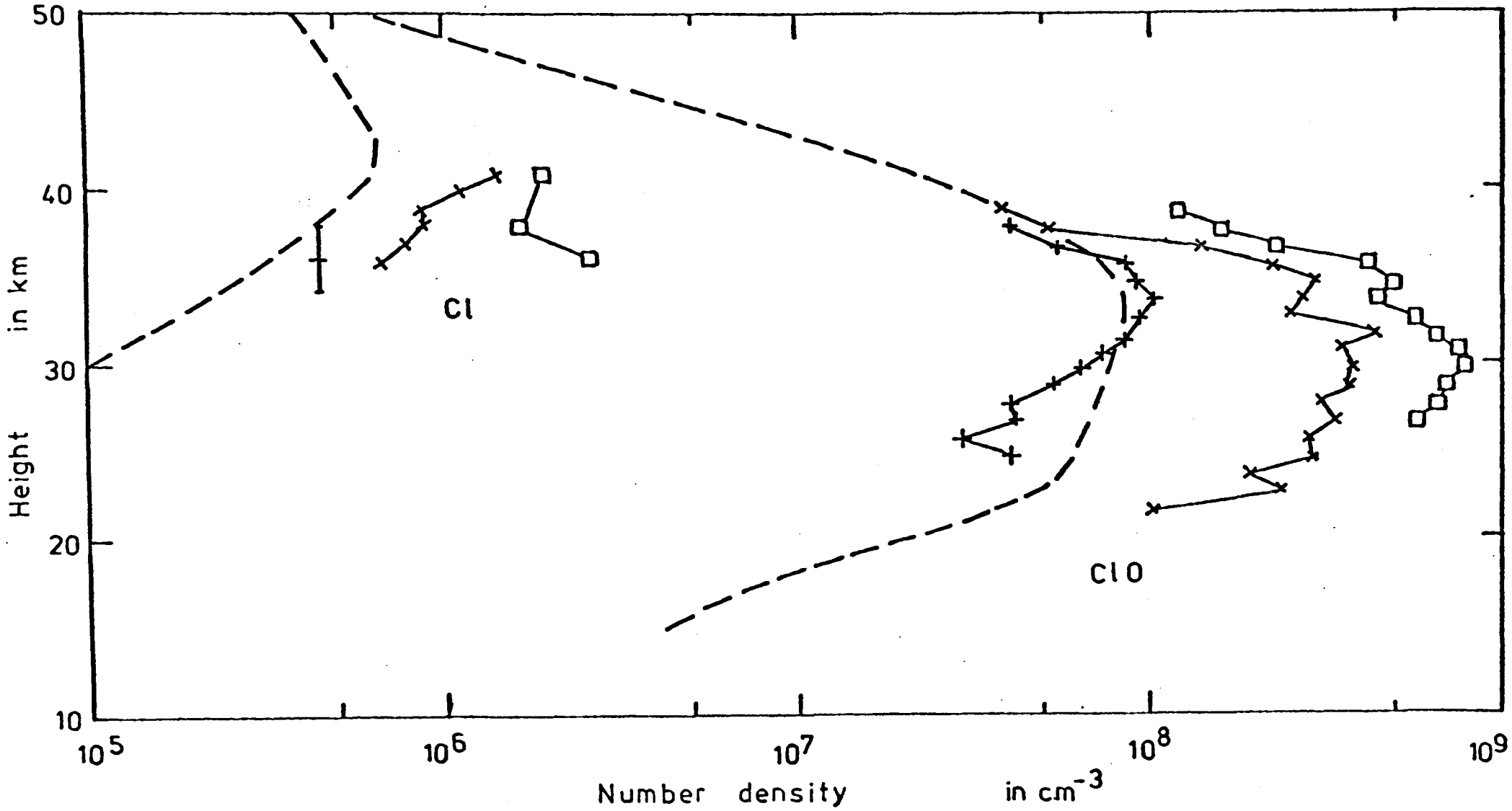

Measurements by
Anderson et al.

28 July 1976
2 Oct. 1976
8 Dec. 1976

Reference:
Anderson et al. (1977)

— — — — :
theoretical curves calculated by Chang for noon with 1.6×10^{-6} volume mixing ratio of total chlorine.

Reference:
Volz et al. (1977)

Figure 3.5 Measurements of stratospheric Cl and ClO.

that the expected ratio of HCl : ClO above 30 km decreases from about 4 (the value found by modellers with the old methane profile) to a value close to the measured ratio of $\sim$ 0.8.

Species of other halogens have not been studied as intensively as chlorides, but recently three measurements of HF in the stratosphere have been reported (see figure 3.6). Zander et al.(1977) have measured an average volume mixing ratio of 3.6×10^{-10} above 27.9 km obtaining their results from spectroscopic data. The result of Lazrus' group given here is an average profile for total fluoride obtained from the data of 4 balloon flights in 1976 (Mroz et al., 1977). This group has also measured stratospheric bromides (Lazrus et al., 1976). In the lower stratosphere they report HBr to be present in mass mixing ratios between 10^{-12} and 10^{-11}. Another interesting measurement of stratospheric halogens has been reported by Farmer and Raper (1977). Using their high resolution Michelson interferometer on a balloon flight from Broken Hill, Australia, (30.5^{o}S) they have made a simultaneous observation of the absorption due to spectral lines of HCl and HF. Without retrieving profiles for each species individually, they have been able to estimate the ratio of HF : HCl between 14 and 38 km to be constant at about 0.1 to within their estimated errors ($\pm$ 50%). This is not in agreement with the higher ratios presently predicted by models (see Sze, 1977).

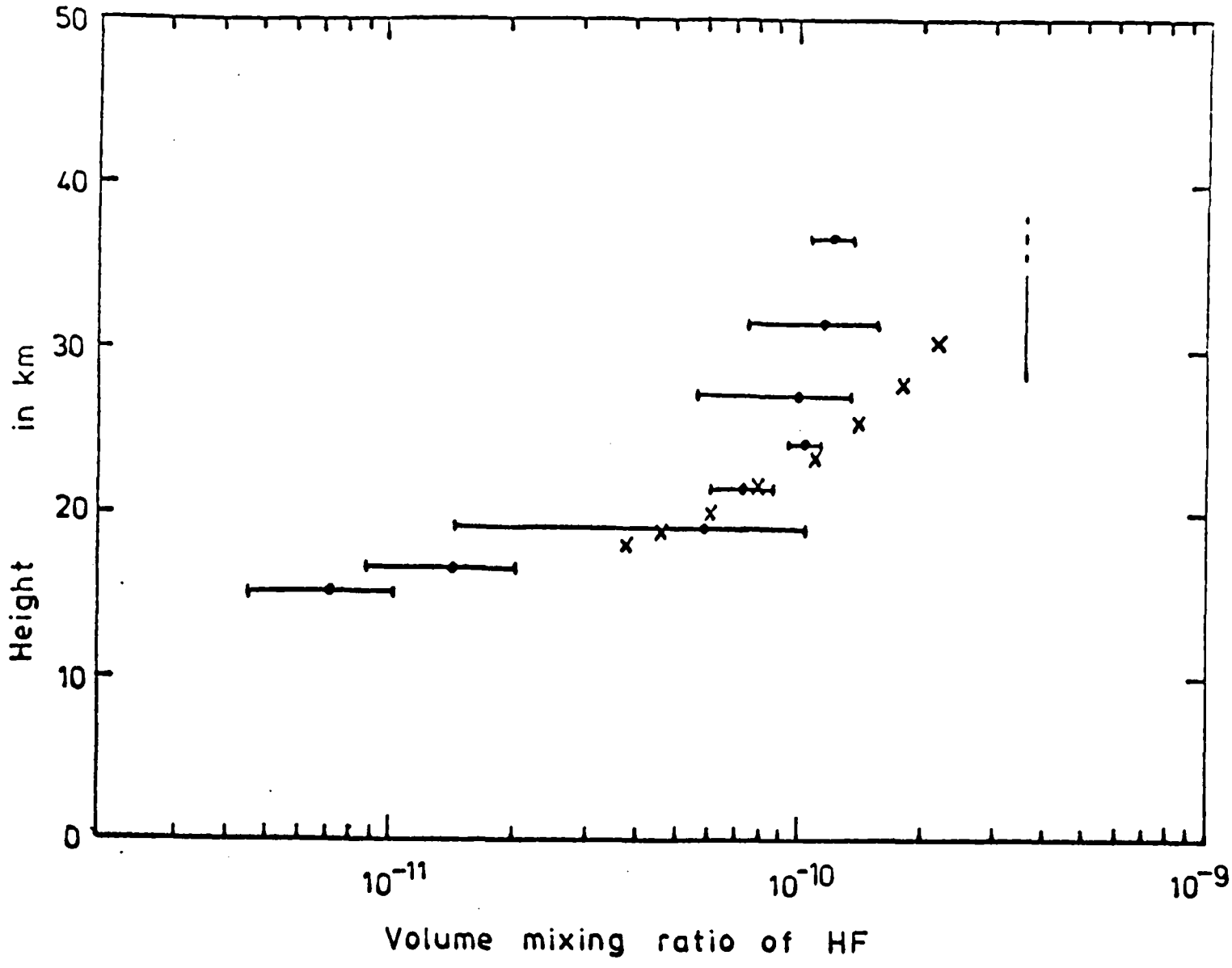

	Researchers	Year of measurement	References
⊢●⊣	Mroz et al.	Average for 1976	Mroz et al. (1977)
|	Zander et al.	1976	Zander et al. (1977)
×	Buijs et al.	1977	see Sze (1977)

Figure 3.6 Measurements of stratospheric HF.

CHAPTER 4. REMOTE SOUNDING OF THE ATMOSPHERE WITH A PRESSURE MODULATOR RADIOMETER.

This chapter contains the theory required in order to develop a computer model to calculate the signals expected from a pressure modulator radiometer (PMR), particularly when measuring the transmission of solar radiation by an atmospheric limb path or the emission of thermal radiation from such a path. The theory is discussed in sufficiently general terms for it to apply to measurements of many atmospheric gases with absorption bands in the infra-red region. The particular case of a PMR designed to measure stratospheric HCl is considered in more detail.

4.1 Transmission of radiation by an absorbing gas.

Consider a flux of radiation, I_ν, at wavenumber, ν, incident on an element of absorbing gas of length, dx, density, $\rho(x)$, and absorption coefficient, $k_\nu(x)$. The change in the flux due to absorption by the path is given by

$$dI_\nu = - I_\nu \, k_\nu(x) \, \rho(x) \, dx \; . \qquad (4.1)$$

If radiation is transmitted along a path from $x = x_1$ to $x = x_2$, integration of equation 4.1 gives

$$I_\nu(x_2) = I_\nu(x_1) \exp\left\{ - \int_{x_1}^{x_2} k_\nu(x) \, \rho(x) \, dx \right\} . \qquad (4.2)$$

Therefore the transmission, τ_ν, of this path at wavenumber, ν, is given by

$$\tau_\nu = \frac{I_\nu(x_2)}{I_\nu(x_1)} = \exp\left\{-\int_{x_1}^{x_2} k_\nu(x)\rho(x)\,dx\right\}. \qquad (4.3)$$

For a homogeneous path, equation 4.3 simplifies to

$$\tau_\nu = \exp\left\{-k_\nu \rho x\right\} = \exp\left\{-k_\nu u\right\}, \qquad (4.4)$$

where $x = x_2 - x_1$ = the path length,

and $u = \rho x$ = the absorber amount in the path.

For a structured path, such as an atmospheric path along which pressure, temperature and composition are variables, the integral in equation 4.3 cannot in general be evaluated exactly and must be approximated numerically. This problem is discussed further in section 4.4.

4.2 The shape and strength of spectral lines.

The absorption coefficient, k_ν, in the region of a spectral line is a function of the line strength and the line shape. The line shape depends on the physical nature of the mechanisms causing the line to be broadened, and in the infra-red two such mechanisms dominate the broadening under most atmospheric or laboratory conditions:

i) Doppler broadening

This is caused by the fact that the absorbing

molecules have a range of velocities relative to the observer. The components of the velocities along any direction have a Maxwell distribution, and hence the variation of the absorption coefficient with wavenumber has a corresponding shape:

$$k_\nu \quad \alpha \quad \exp\left\{-\frac{(\nu-\nu_o)^2}{\alpha_p^{\,2}}\right\} , \qquad (4.5)$$

where ν_o is the wavenumber of the line centre,

and $$\alpha_p = \frac{\nu_o}{c}\left(\frac{2RT}{M}\right)^{1/2} , \qquad (4.6)$$

in which T is the temperature, M is the molecular weight, c is the speed of light and R is the gas constant.

α_p, which will be referred to as the "Doppler half-width", is the half-width at the point where $k_\nu = k_{\nu_o}/e$. Equation 4.5 is normalized using the definition of line strength,

$$S = \int_o^\infty k_\nu \, d\nu . \qquad (4.7)$$

Using equations 4.5 and 4.7, we obtain

$$k_\nu = \frac{S}{\alpha_p \sqrt{\pi}} \exp\left\{-\frac{(\nu-\nu_o)^2}{\alpha_p^{\,2}}\right\} . \qquad (4.8)$$

ii) <u>Lorentz or pressure broadening</u>

This effect is caused by the perturbation of molecular energy states during collisions with other molecules. It has been discussed in detail by many authors including Goody (1964), who derives an approximate relation,

$$k_\nu \propto \frac{\alpha_L}{(\nu-\nu_0)^2+\alpha_L^2} , \qquad (4.9)$$

where α_L is called the Lorentz half-width and is the half-width at the point where $k_\nu = \frac{1}{2} k_{\nu_0}$

α_L can be shown, using simple kinetic theory, to be proportional to pressure - a relation verified by experiment over the range of pressures found in the atmosphere. Although equation 4.9 is a simplified formula, it is sufficiently accurate for the purposes of most calculations of atmospheric radiation in the infra-red. More general formulae are discussed by Goody but will not be considered here.

Combining equations 4.7 and 4.9, we obtain the normalized absorption coefficient for a Lorentz profile,

$$k_\nu = \frac{S}{\pi} \frac{\alpha_L}{(\nu-\nu_0)^2+\alpha_L^2} \qquad (4.10)$$

For many atmospheric and laboratory situations of interest, the Doppler and Lorentz half-widths are of comparable magnitude. In such cases a convolution of the two shapes must be considered - this is the Voigt profile:

$$k_\nu = \frac{S}{\alpha_D \pi^{3/2}} y \int_{-\infty}^{\infty} \frac{\exp(-t^2)\, dt}{y^2 + (x-t)^2} , \qquad (4.11)$$

where $y = \alpha_L / \alpha_D$ and $x = (\nu - \nu_0) / \alpha_D$.

The above integral does not have an analytic solution and must be evaluated by numerical approximation. Since the Voigt function appears in so many calculations

of transmission, it is important to be able to calculate it sufficiently quickly to allow the computer programs involved to run in an acceptably short period of time. The efficient evaluation of the Voigt integral using computers is considered in detail in appendix A.

4.3 Temperature variations of line width and line strength.

It can be seen from equation 4.11 that k_ν is a function of $(\nu - \nu_0)$, α_D, α_L and S. α_D has a simple temperature dependence given by equation 4.6. α_L, besides being proportional to pressure, is also a function of temperature. Simple kinetic theory arguments based on the frequency of molecular collisions which lead to the correct dependence on pressure can also be used to derive a temperature dependence in which α_L is proportional to $T^{-\frac{1}{2}}$. However, to understand the process of pressure broadening fully, more complex theory must be employed which yields a dependence on pressure and temperature given by

$$\alpha_L(p, T) = \alpha_L(p_0, T_0) \frac{p}{p_0} \left(\frac{T_0}{T}\right)^{\gamma} , \qquad (4.12)$$

where $\gamma \sim \frac{1}{2}$ but varies from line to line and from gas to gas. Also, since the origin of pressure broadening lies in the interaction between the electric dipole or quadrupole of one molecule and those of its neighbours, the magnitude of the half-width depends on the gas causing the broadening. For atmospheric

calculations the dominant broadening gas is nitrogen, and so it is necessary to know the nitrogen-broadened half-width of the absorber, $(\alpha_L)_N$. For gas mixtures in which the mixing ratio of the absorber is not $\ll 1$, the self-broadened half-width, $(\alpha_L)_S$ must also be known. The resulting half-width for a mixture of absorber and nitrogen is given by

$$\alpha_L(p,T) = (\alpha_L)_N(p_N,T) + (\alpha_L)_S(p_S,T), \qquad (4.13)$$

where p_N and p_S are the partial pressures of nitrogen and absorbing gas respectively, and p is the total pressure.

Line strength is also a function of temperature, its dependence being given by the general equation,

$$S(T) = S(T_o)\frac{Q(T_o)}{Q(T)}\,\frac{\exp(-E_L/kT)}{\exp(-E_L/kT_o)}\,\frac{\{1-\exp(-hc\nu/kT)\}}{\{1-\exp(-hc\nu/kT_o)\}}, \qquad (4.14)$$

where Q(T) is the total partition function of the molecular energy states,

E_L is the energy of the lower level in the transition,

ν is the wavenumber of the transition,

and h, c and k are fundamental constants symbolized in the standard way.

The derivation of this equation is discussed in appendix B along with approximate forms which may be used in certain cases.

4.4 Theory of limb scanning.

This term is used to describe situations in which an instrument views the atmosphere along a path which passes below the instrument to a point at which the path is tangential to the curvature of the atmosphere and extends out to space on the other side. It is illustrated in figure 4.1. With instruments mounted on satellites or balloon platforms, this technique can be used to measure the emission of radiation by the atmospheric limb. It can also be employed to measure the radiation from an external source (usually the sun) transmitted by the limb. Both emission and transmission experiments have been performed to measure various atmospheric constituents.

For a balloon instrument at a typical float altitude of 35 km, the measurement is performed from within the atmosphere and limb paths can be observed for a range of zenith angles from 90^{o} to $\sim 96^{o}$, at which angle the path intersects the earth's surface. For a satellite instrument at a typical orbital height of 1000 km (outside the atmosphere), limb paths with tangent heights between 0 and 100 km are observed over only a small range of view angles - a range ~ 1.8 degrees at zenith angles around 120^{o}.

This geometry has the following advantages:

i) The amount of absorber in the path is very large compared to that in a vertical path. For a constant volume mixing ratio, ϵ, the amount of absorbing gas, u, in a complete limb path is approximately given by

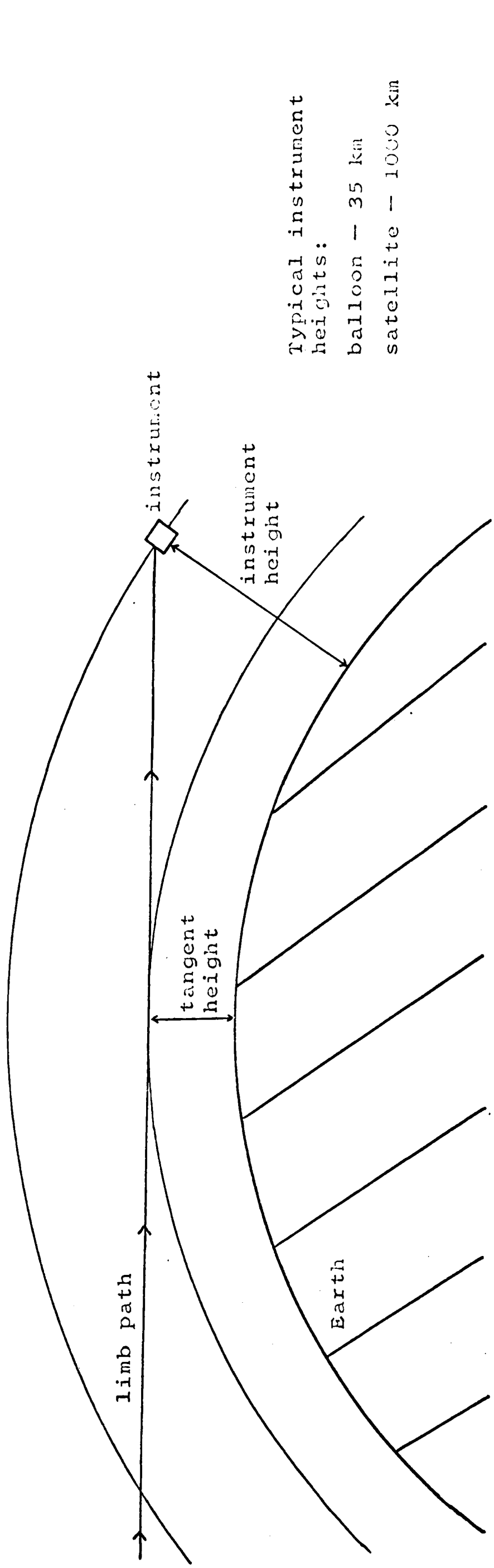

Typical instrument heights:

balloon – 35 km

satellite – 1000 km

not to scale

Figure 4.1 The geometry of limb scanning.

$$u \simeq \epsilon p_T \sqrt{2\pi H R_o} \quad , \qquad (4.15)$$

where p_T is the pressure at the tangent height,

H is the atmospheric scale height ,

R_o is the radius of the earth,

and u is defined here in units of pressure x length (and not density x length as in section 4.1).

The above formula is derived in appendix C along with several other useful approximations for limb paths. At typical stratospheric temperatures equation 4.15 gives

$$u \simeq 70 \epsilon p_T H \quad , \qquad (4.16)$$

which should be compared to the expression for the absorber amount in a vertical path above the pressure level, p_T , for the same atmosphere:

$$u \simeq \epsilon p_T H \qquad (4.17)$$

ii) This geometry also tends to give good height resolution in retrieved mixing ratio or temperature profiles, since, for a constant mixing ratio or one which varies slowly with height, the majority of the absorber lies in the section of path just above the tangent height. In fact, for a limb path about 42% of the mass of the path lies in the 1 km thick layer just above the tangent height, and about 80% in the

lowest 5 km.

iii) Another feature, which may be advantageous, is the fact that the long atmospheric path lengths involved lead to retrieved values which are averages over a horizontal range $\sim$ 400 km, thus smoothing out short spatial variations in the atmospheric state.

Equation 4.15 is only an approximation and cannot be used for accurate calculations of absorber amount; nor can it be used when the mixing ratio varies with height. In general absorber amount must be calculated using a ray tracing technique. This involves splitting each limb path into many parts such that the vertical range of each part is small. If the ith part of the path has length, x_i , the absorber amount in it is given by

$$u_i = \epsilon_i \, p_i \, x_i \qquad (4.18)$$

where the path is divided such that ϵ_i and p_i can be treated as constant over the length, x_i . A vertical interval of 0.1 km has been found empirically to give negligible error for typical atmospheric profiles.

The total absorber amount in the path is then given by

$$u = \sum u_i \quad , \qquad (4.19)$$

where the summation is over all the parts of the path

from the balloon or satellite through the atmospheric limb to space.

To find the transmission of the path we must also calculate a pressure and temperature which are characteristic of the path so that we may then treat it as homogeneous. It seems reasonable to use absorber amount weighted mean values:

$$\bar{p} = \frac{\int p \, du}{u} \tag{4.20}$$

and

$$\bar{T} = \frac{\int T \, du}{u} \tag{4.21}$$

These values will not yield exactly the correct result for the transmission of the path at any wavelength, since the absorption coefficient is a complicated function of pressure and temperature. The accuracy of this approximation varies with the shape of the mixing ratio profile, the wavelength of operation of the instrument, the spectral data involved and other variables. However, it can be improved by treating each path as comprising several sections of path; u, $\bar{p}$ and $\bar{T}$ are calculated for each section, and the whole path is simulated by several homogeneous sections in series.

The justification for the representation of a structured path by one or more homogeneous paths characterized by their own $\bar{p}$ and $\bar{T}$ is purely empirical - the approximation has been found to be satisfactory for all the atmospheric calculations for which it has

been tested. However, since the computer time needed for such calculations increases with the number of subdivisions of the path, it is desirable to use the lowest number of subdivisions to give the required accuracy.

4.5 Limb scanning in transmission and emission.

i) Transmission

An instrument on a balloon platform or satellite can be used to measure the radiation coming from a bright source and passing through the atmospheric limb. The usual source is the sun although the moon and stars may also be used. This technique is also known as occultation. Since the limb absorbs radiation, the drop in radiation reaching the instrument gives a measure of the transmission of the atmospheric path.

If the limb path is represented by a series of n homogeneous paths as described in section 4.4 , the combined monochromatic transmission of the path, τ_a, is given by

$$\tau_a = \prod_{i=1}^{n} \tau_i \quad , \qquad (4.22)$$

where τ_i is the transmission of the ith section of the path. The flux of incident solar energy at most infra-red wavelengths is sufficiently high for the emission from the path to be negligible in comparison.

Since the theory given above refers to general calculations of transmission, it is also applicable to

laboratory transmission measurements in which the instrument views a source through an absorbing path. In the laboratory case, the path is homogeneous and difficulties caused by the temperature and pressure structure of the path do not arise.

ii) Emission

Alternatively, an instrument may be used to measure the radiation emitted by the limb itself. It can be shown (see, for example, Houghton, 1977) that the monochromatic radiation emitted in the x direction by a path of gas between the points x_1 and x_2 is given by

$$I_\nu = \int_{\tau(x_1, x_2)}^{1} B_\nu(x)\, d\tau_\nu(x, x_2), \qquad (4.23)$$

where $\tau_\nu(x,x_2)$ is the transmission of the path between x and x_2, and $B_\nu(x)$ is the black body function of the gas at wavenumber, ν. For a homogeneous path of temperature, T, and transmission, τ_ν, this simplifies to

$$I_\nu = B_\nu(T)\left[\tau_\nu(x, x_2)\right]_{\tau_\nu}^{1} = B_\nu(T)\left\{1 - \tau_\nu\right\}. \qquad (4.24)$$

If a limb path is represented by a single homogeneous path as described in section 4.4, then the energy incident at the instrument in the elemental spectral interval, ν to $\nu + \delta\nu$, is given by

$$E_\nu \, \delta\nu = B(\nu, \bar{T}) \{1 - \tau_\nu(\bar{T}, \bar{p}, u)\} \delta\nu, \qquad (4.25)$$

where $\bar{T}$, $\bar{p}$ and u are as defined in section 4.4.

If the path is represented by n paths in series, the equivalent equation is

$$E_\nu \, \delta\nu = \{[\ldots(B_1(1-\tau_1)\tau_2 + B_2(1-\tau_2))\tau_3 \ldots]\tau_n + B_n(1-\tau_n)\} \delta\nu , \qquad (4.26)$$

where the paths are numbered 1 to n, the nth being nearest the instrument,

and B_i , τ_i stand for $B(\nu, \bar{T}_i)$, $\tau_\nu(\bar{T}_i, \bar{p}_i, u_i)$ respectively.

4.6 The pressure modulator radiometer (PMR).

The theory derived in section 4.5 has considered only monochromatic energies and transmissions. In general, the radiation incident on an instrument detector is a complicated function of wavenumber with structure in the spectral regions of absorption bands.

A pressure modulator radiometer (PMR) is a type of gas correlation spectrometer which "looks" selectively at radiation in the spectral regions near the absorption line centres of a specific gas. In this way it can be used to measure the emission or absorption due to a particular atmospheric gas, and hence the atmospheric mixing ratio of the gas may be deduced.

Alternatively, if the mixing ratio is known as in the case of carbon dioxide, a PMR can be used to deduce the temperature structure of the atmosphere. Such an instrument has been used on the Nimbus 6 satellite to measure temperatures in the stratosphere and mesosphere (see Curtis et al., 1974).

The structure of a PMR is shown schematically in figure 4.2. The pressure of the gas in the pressure modulator cell (PMC) is cycled at constant frequency by the piston. This causes a modulation of the transmission of the gas in the cell and hence leads to a modulation of the energy reaching the detector, but only in those spectral regions where the gas in the cell has absorption lines.

The operation of a PMR can be understood by considering the transmission of the PMC with the piston in its extreme positions - a high pressure (high absorption) state and a low pressure (low absorption) state. The component of energy reaching the detector at the frequency of the pressure modulation is related to the difference in transmissions between the high and low pressure states. This is illustrated for the case of a single absorption line in figure 4.3, which shows how a PMR may be used to measure the emission of radiation from a single atmospheric species or the absorption of radiation from an external source by that species.

The shape of the PMC transmission function is obviously dependent on the line shape and strength and on the absorber amount in the PMC, but it will always lead to modulation only in the regions of spectral lines. When sounding for minor constituents

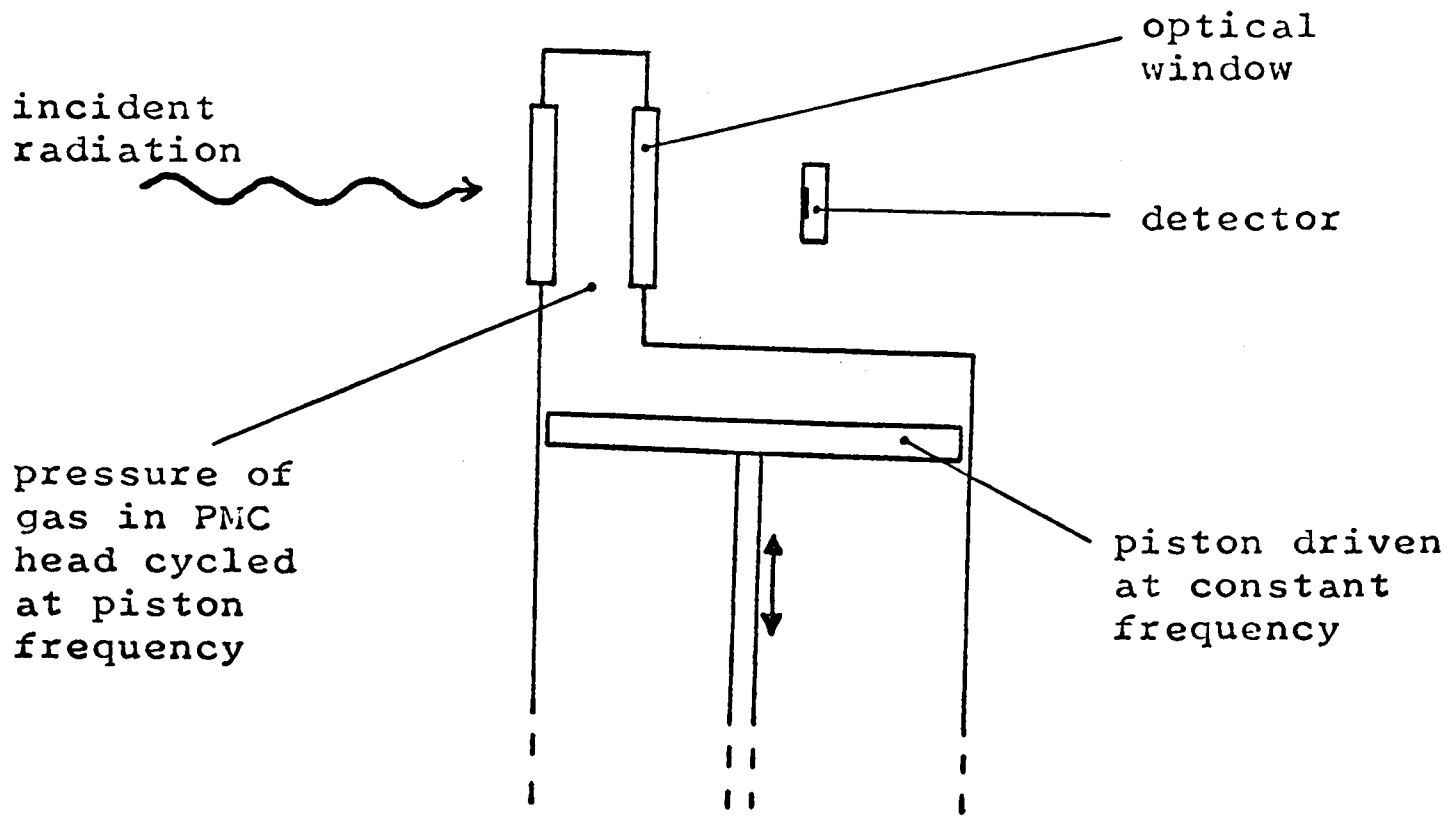

Figure 4.2 Schematic representation of a PMR.

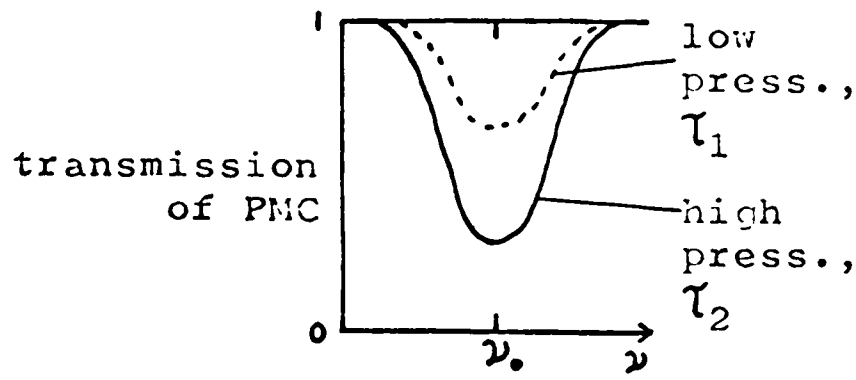

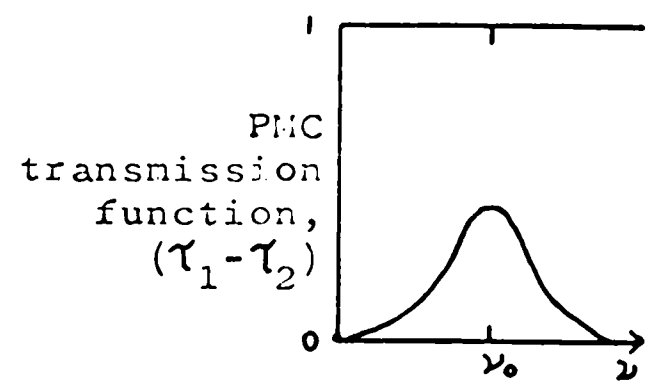

Transmission

No absorber in path

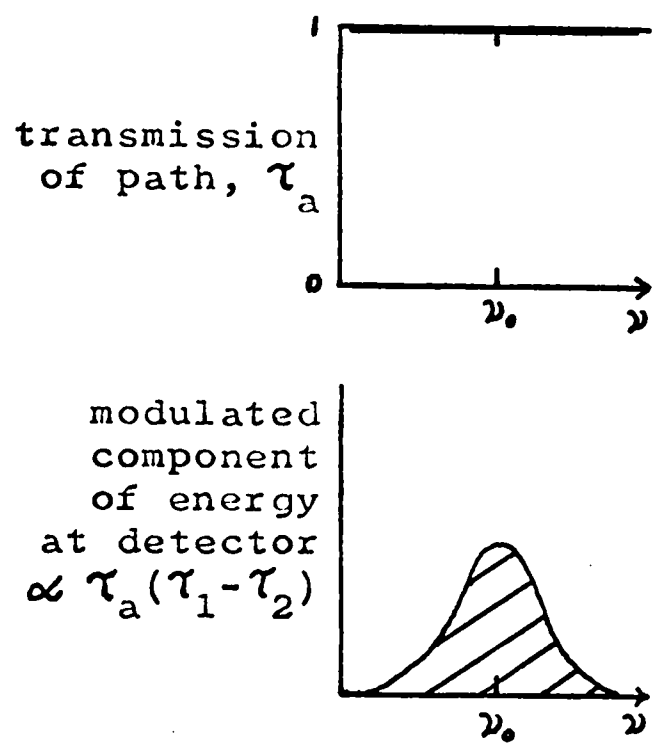

Small amount of absorber in path

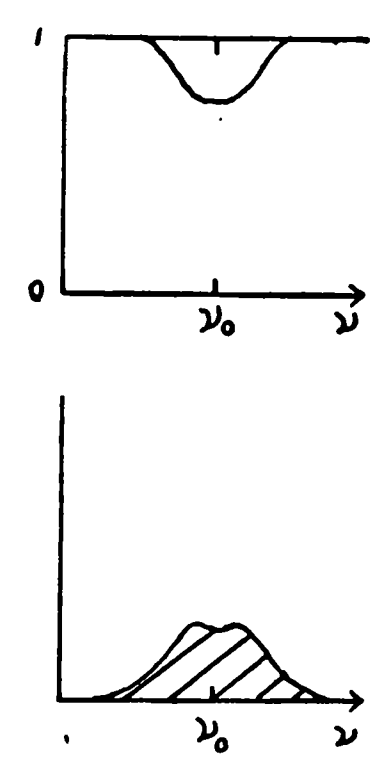

Emission

Small amount of emitting gas in path

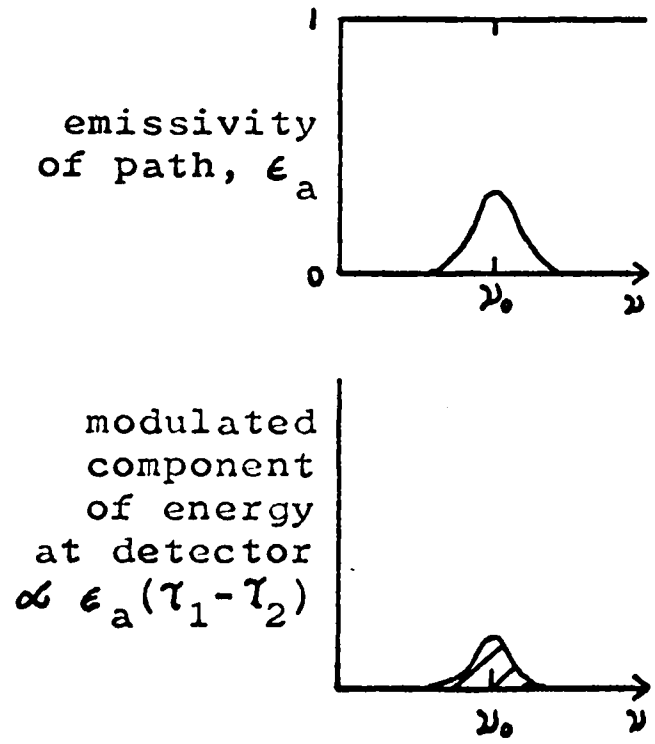

Large amount of emitting gas in path

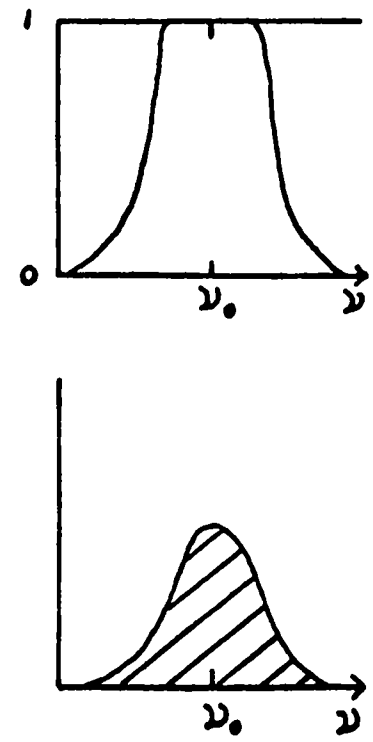

Figure 4.3 Illustrating the operation of a PMR in transmission and emission by considering one spectral line.

with very low atmospheric mixing ratios, it is often advisable to select the pressure in the PMC such that there is a large transmission modulation at line centres, thus making the instrument sensitive to small amounts of absorber in the atmospheric path. It can be seen that this gives the instrument an effective spectral resolution of the order of the line width of the gas ($\sim 10^{-2}$ cm^{-1} or less for typical PMC pressures). This resolution is 1 to 2 orders of magnitude better than most conventional spectrometers.

The component of energy incident on the detector at the frequency of the PMC modulation, E_{PMR}, is calculated using the equation,

$$E_{PMR} \propto \int_0^\infty (E_a)_\nu \left\{(\tau_1)_\nu - (\tau_2)_\nu\right\} (\tau_o)_\nu \, d\nu + A_1 \quad , \qquad (4.27)$$

where $(E_a)_\nu$ is the energy per unit wavenumber incident on the instrument along its direction of view - from the atmosphere, calibration black body, laboratory path, etc.,

$(\tau_1)_\nu$ and $(\tau_2)_\nu$ are the transmissions of the low pressure and high pressure PMC states respectively,

$(\tau_o)_\nu$ is the combined transmission of the PMR optics,

and A_1 is a term to account for the component of energy at PMC frequency due to the changing emission of the gas in the PMC.

As long as the PMC is stable in temperature, pressure and amplitude of modulation, A_1 is a constant which

can be calibrated out and so can be ignored when modelling PMR signals.

Equation 4.27 is only exact when the transmission modulation of the incident energy by the PMC is sinusoidal. In practice this is never the case, since the pressure modulation is not exactly sinusoidal and the relationship between PMC transmission and pressure is not, in general, linear. In theory this problem can be partly solved by using in the calculation pressures which represent the fundamental component of the energy modulation rather than the physical pressure extremes themselves. The way in which the pressures used in a two-pressure model are calculated varies from one PMR to another, as does the accuracy of the approximation involved in a two-pressure representation. This problem has been discussed by other authors (see Drummond, 1977; Delderfield, 1977) and is considered further in Chapter 6 in terms of the retrieval of results from the signals for a particular PMR.

If a rotating chopper is also included in the optical system, a component of energy is incident on the detector at the frequency of chopping. This component is called the wideband energy and is given by an equation which includes the mean transmission of the PMC:

$$E_{WB} \propto \int_0^{\infty} (E_a)_\nu \tfrac{1}{2} \{(\tau_1)_\nu + (\tau_2)_\nu\} (\tau_o)_\nu \, d\nu + B_1 , \qquad (4.28)$$

where B_1 is a term to account for the fact that the chopper modulates the incident energy between $(Ea)_\nu$ and the

emission of the chopper. For a stable instrument B_1 will be constant and so may also be calibrated out and ignored when modelling signals.

Using equations 4.27 and 4.28, it is possible to make calculations of the signals, S_{PMR} and S_{WB}, expected from a PMR:

$$S_{PMR} = c_{PMR} \int_0^\infty (E_a)_\nu \{(\tau_1)_\nu - (\tau_2)_\nu\} (\tau_o)_\nu r_\nu \, d\nu \qquad (4.29)$$

and $$S_{WB} = c_{WB} \int_0^\infty (E_a)_\nu \tfrac{1}{2}\{(\tau_1)_\nu + (\tau_2)_\nu\} (\tau_o)_\nu r_\nu \, d\nu \,, \qquad (4.30)$$

where c_{PMR} and c_{WB} are factors introduced by the gains of the electronics and the shapes of the modulating waveforms,

r_ν is the responsivity of the detector,

and other symbols are as defined above.

Since terms involving A_1 and B_1 appear only as offsets on the signals, they have been omitted. $(\tau_o)_\nu$ and r_ν are usually slowly varying functions of ν and for the sake of calculations may be combined into one variable.

A concept which is found to be useful when using PMRs for either laboratory or atmospheric transmission measurements is that of "PMR transmission". It is defined for a path containing absorber as follows:

PMR transmission of path =

$$\frac{\text{Signal viewing source through absorbing path}}{\text{Signal viewing same source through no path}} \qquad (4.31)$$

The term "PMR transmission" is used in this work to mean that derived from PMR signals (those caused by the PMC modulation); the equivalent term for wideband signals is called "wideband transmission".

4.7 A general line-by-line model.

Using the equations derived in this chapter it is possible to make calculations to predict the signals expected from the channels of a PMR when used in a given atmospheric or laboratory situation. The signal is calculated by performing a numerical integration over the spectral region for which the instrument's optics have a sufficiently high transmission to give an appreciable contribution to the signal. All the spectral lines in the region are considered.

The information required for such calculations is given below:

i) The spectral data for each line:
   a) the line position,
   b) the line strength at a given temperature, the ground state energy and other parameters required for the evaluation of the change of line strength with temperature,
   c) the Lorentz half-widths for nitrogen broadening and self-broadening, along with coefficients for the evaluation of the changes of half-width with temperature.

ii) The optics transmission profile (weighted by

detector responsivity).

iii) For a laboratory path, the length, temperature, pressure and mixing ratio of the absorber in the path between the source and the instrument.

iv) For an atmospheric path:

a) the temperature and pressure profile against height,

b) the mixing ratio profile against height,

c) parameters defining the geometry of the path.

v) PMC parameters:

a) the length,

b) the pressures and temperatures defining its high and low pressure states (or a mean pressure and compression ratio from which they can be calculated).

vi) The black body temperature of any radiation source or internal black body used.

The advent of fast computers has made possible this type of numerical integration, even for spectral bands containing thousands of lines. A program called GENLIN has been developed on the PDP 11/70 computer at Oxford which performs calculations of expected PMR signals using a line-by-line numerical integration routine for any absorbing gas for which sufficient spectral line data is available. The program computes PMR signals or wideband signals (or signals from a radiometer which does not include a PMC) and can be used to simulate atmospheric or laboratory conditions.

The numerical integration is performed by a routine called SIMRULE which approximately evaluates an integral to a specifiable accuracy using Simpson's rule. Care is taken in dividing up the spectral region into convenient intervals so that the integration is fast while maintaining its accuracy.

Each monochromatic energy is calculated by considering the laboratory or atmospheric path and the PMC as a series of homogeneous paths. The contribution due to all the spectral lines is calculated for each path. In practice only those lines with line centres within $\sim 1\ cm^{-1}$ of the monochromatic energy being considered need be included individually - the contributions from the far wings of all other lines can adequately be expressed in terms of precomputed coefficients.

4.8 A line-by-line model for an HCl PMR.

A balloon-borne PMR has been used in the solar occultation mode to measure HCl in the stratosphere. The instrument, its testing and the retrieval of results from the data are discussed in later chapters.

HCl is a simple diatomic molecule with a fundamental vibration-rotation band in the infra-red region centred around 3.5 micrometres ($2880\ cm^{-1}$). Its spectrum is shown in figure 4.4 along with the combined optics profile of the instrument used. The doublet

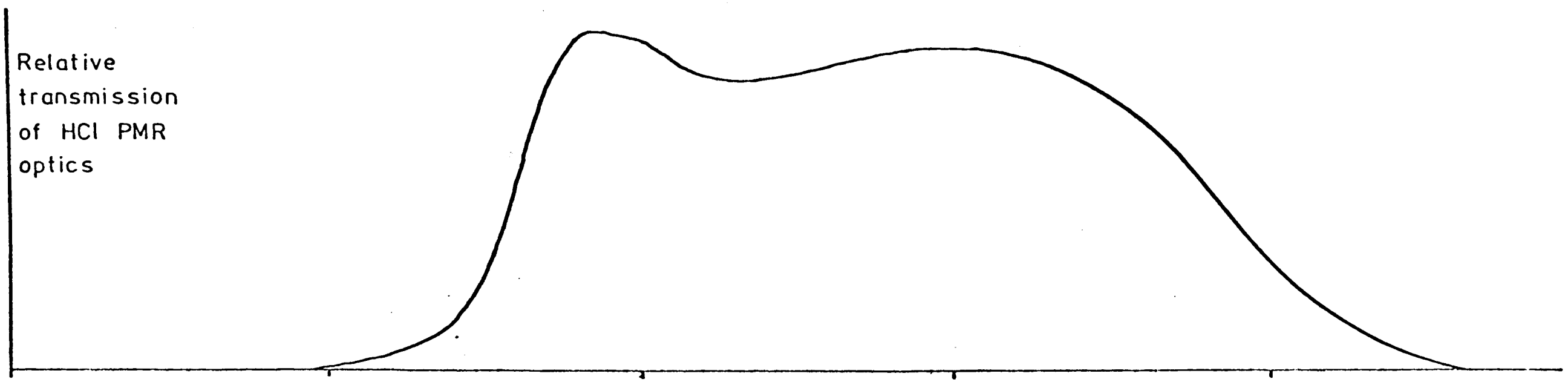

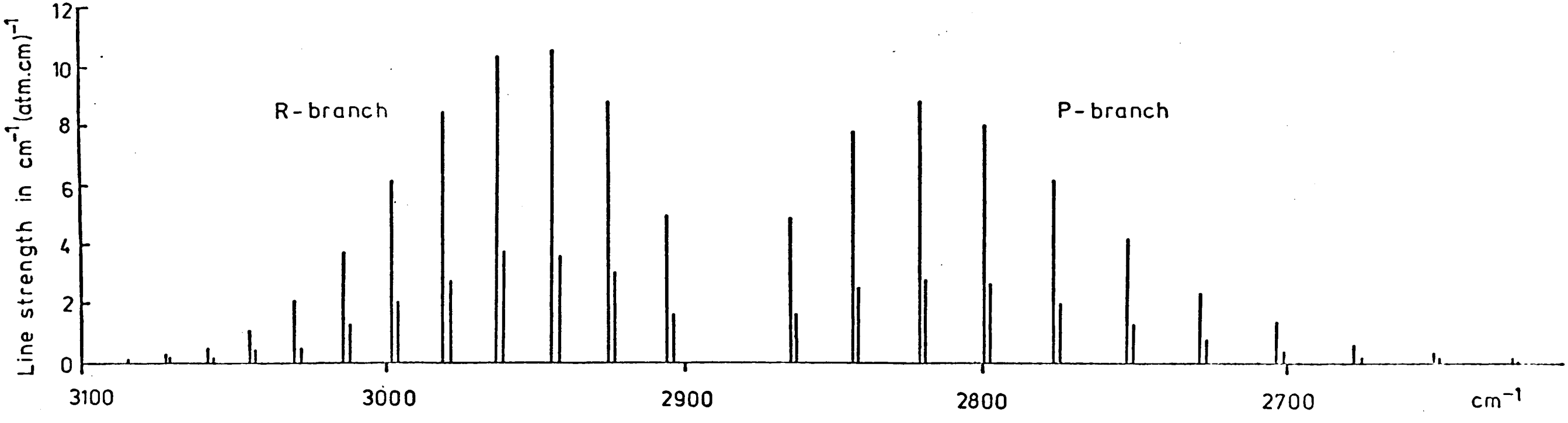

Figure 4.4 HCl line strengths and HCl PMR optics transmission profile.

structure is caused by the fact that chlorine occurs predominantly in two isotopic forms, the natural ratio between them being $^{35}Cl : {}^{37}Cl \simeq 3 : 1$ (hence the ratio of the line strengths). Each doublet has a separation $\simeq 2\ cm^{-1}$. This is very much greater than the half-widths typical of either PMC or stratospheric pressures, which are less than $10^{-2}\ cm^{-1}$ For a gas with few, widely spaced lines, such as HCl, gas correlation spectroscopy in general and PMRs in particular have advantages over instruments which use wideband techniques, since they are able to measure a large change in the transmission in the regions of spectral lines rather than a very small change in the mean transmission of the whole spectral interval.

The fact that HCl has only a few, widely spaced, non-overlapping lines also simplifies the calculation technique described in section 4.7. Since the wings of a line contribute no appreciable absorption near the line centre of any other line (for the absorber amounts typical of either the atmosphere or the PMC), the numerical integration can be performed for each line in isolation. Thus, for this instrument, an appropriate expression equivalent to equation 4.29 is

$$S_{PMR} = c_{PMR} \sum \int_{\nu_0 - \Delta\nu}^{\nu_0 + \Delta\nu} B(T_s)\,(\tau_a)_\nu \left\{(\tau_1)_\nu - (\tau_2)_\nu\right\} (\tau_0)_\nu\, r_\nu\, d\nu\,, \qquad (4.32)$$

where τ_a, τ_1, τ_2 are the transmissions (for one spectral line centred at ν_0) of the atmosphere and the cell in its low and high pressure states respectively, the summation is over all the lines in the band,

T_S is the effective black body temperature of the sun,

$\Delta\nu$ is an interval chosen such that the signal due to the modulation of the line wings is calculated sufficiently accurately ($\Delta\nu = 1\ cm^{-1}$ has been found to be satisfactory),

and all other variables are as defined in section 4.6.

The small number of HCl lines in the band - only 32 occur in the region of significant optics transmission - enables the computer calculations to be performed very quickly compared to those for gases such as CO_2 or H_2O in which thousands of lines must be considered. Also calculations are simplified by the fact that the HCl band occurs in a "window" region of the spectrum, where absorption due to other atmospheric constituents has only a minor effect on the signals. However, even in this region the effects of other stratospheric constituents including CH_4 , O_3 , N_2O and H_2O are measurable when limb scanning at tangent heights in the lower stratosphere, and these effects are considered in detail in chapter 7.

The wideband signal, S_{WB} , can be calculated using an expression similar to equation 4.32. However, since the equivalent width of HCl in a stratospheric limb path is always less than 0.2 cm^{-1} and the optics pass band is $\sim$ 250 cm^{-1} wide, the change in wideband signal due to HCl absorption is negligible. The wideband

signal does change due to absorption by other atmospheric constituents and a variation in the reflectivity of the optical components with changing solar zenith angle. Since these two effects also cause changes in the PMR signals, the wideband signal must be used as a calibration. This is discussed in detail in chapter 7.

4.9 The spectroscopy of HCl.

Since HCl is a simple molecule, it was chosen for many of the experiments which were performed in order to study the basic physics of molecular energy states. Consequently its spectral line data are comparatively well known and agreement between measurement and theory is good. The data for the fundamental vibration-rotation band of HCl used in the calculations of transmission are given in table 4.1. The whole band is not tabulated; only those lines which lie in the spectral region where the optics has a significant transmission are required, and so part of the R-branch which contributes about 10% of the total band strength at 300K has been omitted.

Although measurements of the variation of Lorentz half-width with temperature have been made for this band (see, for example, Houdeau et al., 1977; Goldring et al., 1962; Petrov et al., 1975; Petrov, 1975), no conclusive agreement between experiment and theory

Key to table 4.1

HCl spectral line data.

1st column — line identification: branch label followed by rotational quantum number of lower energy level.

ν_0 — line centre in cm^{-1}, Plyler and Tidwell (1960).

S — line strength in $cm^{-1}(atm.cm)^{-1}$ at 300 K, Toth et al. (1970).

E_L — lower energy level for the transition in cm^{-1}, calculated from the pure rotation spectrum wavenumbers given by Plyler and Tidwell (1960).

$(\alpha_L)_N$ — nitrogen-broadened Lorentz half-width in $cm^{-1}atm^{-1}$ at 296 K, Toth and Darnton (1974).

$(\alpha_L)_S$ — self-broadened Lorentz half-width in $cm^{-1}atm^{-1}$ at 300 K, Benedict et al. (1956). Values given for lines of the same m have been averaged. [If J is the rotational quantum number of the lower energy level, $m = J$ for the P-branch and $m = J + 1$ for the R-branch.]

M.W. — molecular weight of the isotopic species: 36 for $H^{35}Cl$ and 38 for $H^{37}Cl$.

Table 4.1 HCl spectral line data.

	ν_0	S	E_L	$(\alpha_L)_N$	$(\alpha_L)_S$	M.N.
P10	2650.233	0.1	1140.35	0.021	0.09	38
P10	2651.980	0.3	1142.05	0.021	0.09	36
P9	2675.960	0.2	933.95	0.025	0.10	38
P9	2677.741	0.6	935.35	0.025	0.10	36
P8	2701.198	0.4	747.84	0.033	0.13	38
P8	2703.019	1.3	748.96	0.033	0.13	36
P7	2725.930	0.8	582.12	0.042	0.15	38
P7	2727.790	2.4	583.00	0.042	0.15	36
P6	2750.142	1.3	436.90	0.056	0.19	38
P6	2752.047	4.2	437.56	0.056	0.19	36
P5	2773.833	2.0	312.26	0.065	0.23	38
P5	2775.768	6.2	312.73	0.065	0.23	36
P4	2796.976	2.7	208.28	0.081	0.25	38
P4	2798.952	8.0	208.59	0.081	0.25	36
P3	2819.566	2.8	125.02	0.091	0.25	38
P3	2821.575	8.8	125.20	0.091	0.25	36
P2	2841.587	2.5	62.53	0.096	0.22	38
P2	2843.628	7.8	62.62	0.096	0.22	36
P1	2863.024	1.6	20.85	0.098	0.22	38
P1	2865.101	4.8	20.88	0.098	0.22	36
R0	2904.118	1.6	0.00	0.098	0.22	38
R0	2906.252	4.9	0.00	0.098	0.22	36
R1	2923.743	3.0	20.85	0.096	0.22	38
R1	2925.910	8.8	20.88	0.096	0.22	36
R2	2942.739	3.4	62.53	0.091	0.25	38
R2	2944.924	10.6	62.62	0.091	0.25	36
R3	2961.081	3.3	125.02	0.081	0.25	38
R3	2963.300	10.3	125.20	0.081	0.25	36
R4	2978.774	2.7	208.28	0.065	0.23	38
R4	2981.021	8.5	208.59	0.065	0.23	36
R5	2995.790	2.0	312.26	0.056	0.19	38
R5	2998.070	6.1	312.73	0.056	0.19	36

has been found. Houdeau et al. have reported measurements at 298K and 163K of several lines and have shown the temperature dependence of Lorentz half-width to vary from line to line. Using their measurements, it is estimated that the $T^{-\frac{1}{2}}$ relation derived from kinetic theory using simple arguments leads to errors in half-width at stratospheric temperatures only $\sim 10\%$ for a worst case. Since for the PMC conditions and most atmospheric cases considered in this work Doppler broadening is the dominant effect, it has been considered adequate to represent the temperature and pressure dependence of Lorentz half-width for all lines by the approximate expression,

$$\alpha_L(p, T) = \alpha_L(p_o, T_o)\left(\frac{p}{p_o}\right)\left(\frac{T_o}{T}\right)^{1/2} \qquad (4.33)$$

The line strength variation with temperature for this band is discussed in appendix B. Briefly, the stimulated emission factor and the vibrational partition function vary insignificantly for all temperatures of interest, and so equation 4.14 simplifies to

$$S(T) = S(T_o)\,\frac{T_o}{T}\,\exp\left\{-\frac{E_L}{k}\left(\frac{1}{T}-\frac{1}{T_o}\right)\right\} \cdot \qquad (4.34)$$

4.10 Pressure shifting.

A phenomenon which could affect the interpretation of PMR signals is pressure shifting.

When the energy states of an absorbing molecule are perturbed by collisions with other molecules, not only does this cause the spectral lines to be broadened, but it also shifts the line centre in wavenumber by an amount proportional to the pressure of the broadening gas (see Kimel et al., 1959). Since the pressure of the gas in the PMC and the atmosphere are different, pressure shifting causes the line centres of the atmospheric gas to be displaced relative to those of the PMC gas and adds a complication to calculations of expected signals. However, it has been shown that for all cases of interest pressure shifting has a negligible effect for an HCl PMR.

The HCl line-by-line model was adapted to allow for a shift of the spectral lines of the atmospheric gas relative to those in the PMC (which are shifted relatively little, since the PMC pressure used is typically only ~ 2 mb). Research into the pressure shifts of HCl broadened by nitrogen has been very limited; most experiments have used noble gases as broadening agents. Also the pressure shifting is of a different magnitude for each line in the band. However, for the 2-0 band of HCl the shifts caused by nitrogen are similar to those due to argon (Rank et al., 1960), and for the 1-0 (fundamental) band of HCl shifts caused by argon are of the order of 0.01 cm^{-1} atm^{-1} (Ben-Reuven et al., 1961). Using this value for all lines and a constant atmospheric

volume mixing ratio for HCl of 5×10^{-10}, comparison has been made between the calculated PMR transmissions with and without pressure shifting. To study the effect of pressure shifting on the retrieved value of HCl concentration, a useful quantity to calculate is the change due to shifts in the PMR transmission (as defined in section 4.6) compared to the difference between the PMR transmissions with and without HCl in the path, i.e.

$\frac{\Delta \bar{\tau}}{1 - \bar{\tau}}$, where $\bar{\tau}$ is the PMR transmission.

As expected the worst case was found for the lowest tangent height pressures - at a tangent height of 15 km the above quantity is only 0.24%. Doubling the pressure shifting to 0.02 cm^{-1} atm^{-1} changes this value to 0.9%. Also, for a realistic HCl stratospheric mixing ratio profile (with concentrations less than 5×10^{-10} in the lower stratosphere), the effect will be even less.

It is therefore concluded that the effects of pressure shifting are negligible for this PMR, and a qualitative explanation of this fact is illustrated in figure 4.5. When the pressure shift of a line in the atmosphere has become comparable to the half-width of the line in the PMC, the atmospheric line is so broad that its transmission near line centre only changes slowly with wavenumber. Thus the product of the atmospheric transmission and the PMC transmission function is changed very little by the shifting. For these reasons we may expect pressure shifting to have little effect for most PMRs, so long as the shifts of

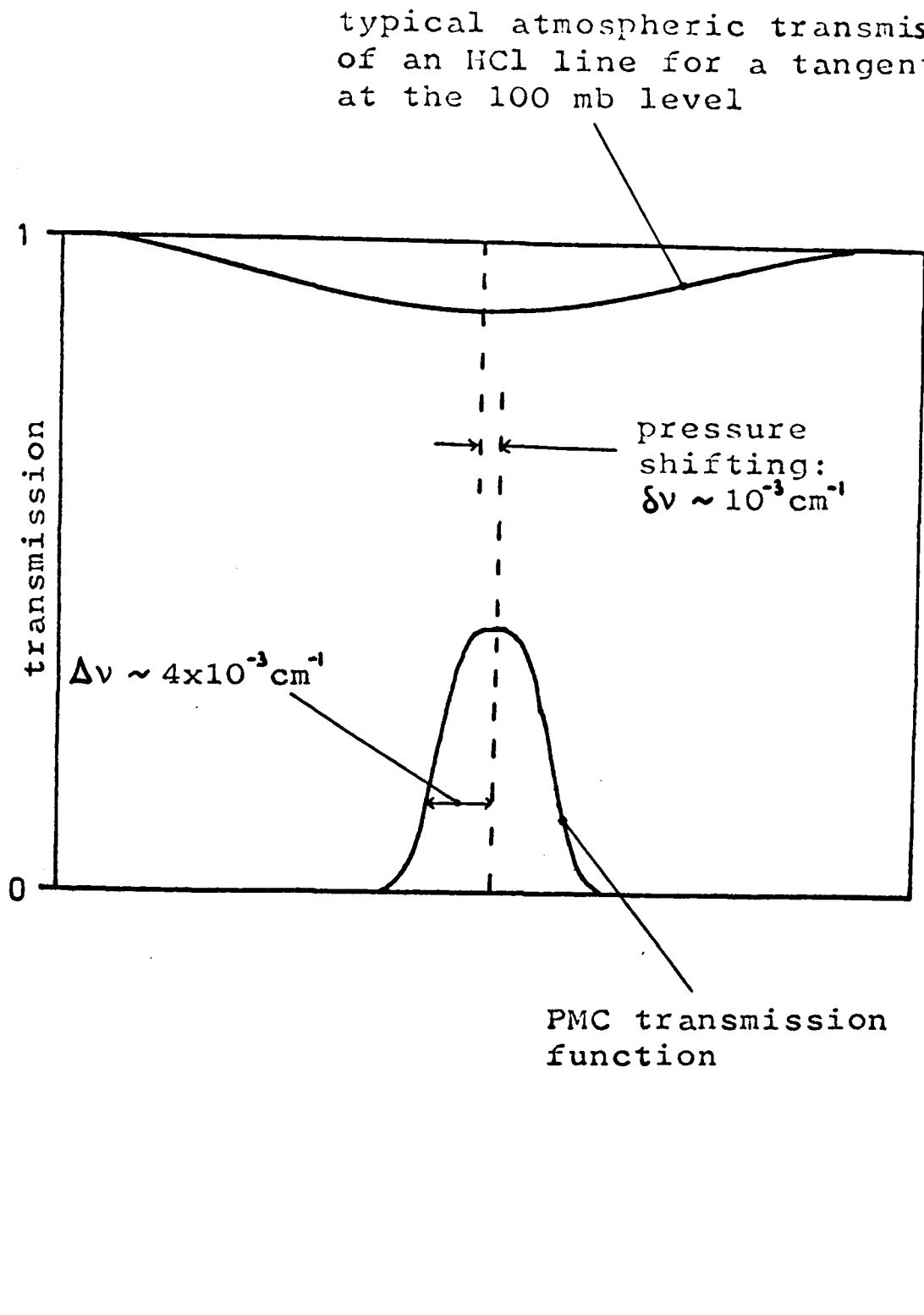

Figure 4.5 Illustrating the effect of pressure shifting on PMR transmission measurements.

the lines are much less than the Lorentz half-widths.

4.11 Atmospheric refraction.

The theory of limb scanning given in section 4.4 assumes that the paths followed by atmospheric radiation are straight. In general, however, whenever there exists a density gradient perpendicular to the direction of the radiation flux, the rays will be refracted. Thus for a vertical path there will be no refraction (assuming atmospheric parameters to vary only with height), but for a limb path refraction does occur and its magnitude increases with density (i.e. with decreasing tangent height). This effect has been studied in detail and is discussed in appendix D, which includes a description of the way in which refraction is represented in a limb path ray tracing routine and calculations of the effects on calculated tangent heights and absorber amounts caused by neglecting refraction. The conclusions reached from these calculations can be summarized as follows:

i) For experiments involving limb sounding of stratospheric emission from either balloon platforms or satellites, refractive effects are small. For a given angle of view the change in tangent height due to refraction is only $\sim$ -0.25 km for a tangent

height pressure of 110 mb (which represents the worst stratospheric case). The consequent change in the mass of the path is ~ 5%.

ii) For solar occultation experiments the known angle is the solar zenith angle and not the view angle of the instrument. Consequently, when viewing from a balloon platform at a typical altitude of 35 km, neglecting refraction causes the tangent height to be calculated ~ 1.2 km too low for a tangent height pressure of 110 mb and a given solar zenith angle. It also causes the mass in the path to be overestimated by ~ 20%. When viewing from a satellite at 1000 km, this effect is even more pronounced - refraction can cause miscalculations of tangent height ~ 10 km.

These calculations have been performed using a constant refractive index typical of infra-red wavelengths. A rigorous calculation should include the effects of the change of refractive index across a spectral line. However, Chaloner (1976) has shown that this effect can be neglected, as it is lower than the effects due to bulk refraction by several orders of magnitude.

CHAPTER 5. THE BALLOON-BORNE HCl PMR.

The HCl PMR was a late addition to an already existing instrument. In a joint project between Oxford University, the Meteorological Office, NOAA (Washington D.C.) and Denver University, an instrument had been developed as part of the test programme for the ITOS operational satellite. It consisted of a carbon dioxide PMR measuring in the 15 micrometre region and a 12 micrometre window channel. The front optics was a sun-tracking system, the beam from which was shared between this instrument and a scanning infra-red spectrometer built by Denver University. The package was flown mounted on a balloon gondola on 2nd December, 1974 and was later modified to include the HCl PMR for a second flight in 1976. Consequently most of the development work for the instrument as a whole preceded the design of the HCl PMR. The modifications required and the HCl PMR itself are discussed here in detail. Other aspects are described briefly and reference should be made to Delderfield (1977) for further details.

5.1 The sun-seeker

The front optics of the radiometer is a servocontrolled sun-tracking system built by Denver

University (see Murcray et al., 1967, and Delderfield, 1977). It is housed in a tower above the rest of the instruments and has an unobstructed view for all zenith angles between 16° and 100°. It is illustrated in figure 5.1. The scatter plate, which accepts the solar radiation, is an aluminized, ground glass plate. The roughness of its surface is determined by the size of the particles used in its grinding, and its effect is to remove unwanted short-wave radiation. It achieves this by reflecting coherently radiation of wavelength much greater than the r.m.s. roughness of its surface, while shorter wavelengths are reflected incoherently and thus scattered (see Bennett, 1963). The plate used for the first flight had a low specular reflectivity at 3.5 micrometres and so was exchanged for a smoother plate with a reflectivity $\sim$ 50% in this wavelength region. The effect on the signals of the variation of reflectivity with wavelength and angle of incidence is discussed in chapter 7.

The scatter plate reflects radiation on to the concave mirror at the top of the tower and from there into the instruments. As the position of the sun relative to the gondola changes, the scatter plate is able to maintain an image of the sun at the same point inside the instrument by means of a photosensitive "eye" which tracks the sun, and a mechanical system which allows rotation of the whole tower about a vertical axis and movement of the plate about its own horizontal axis. The plate can also be made to "look" away from the

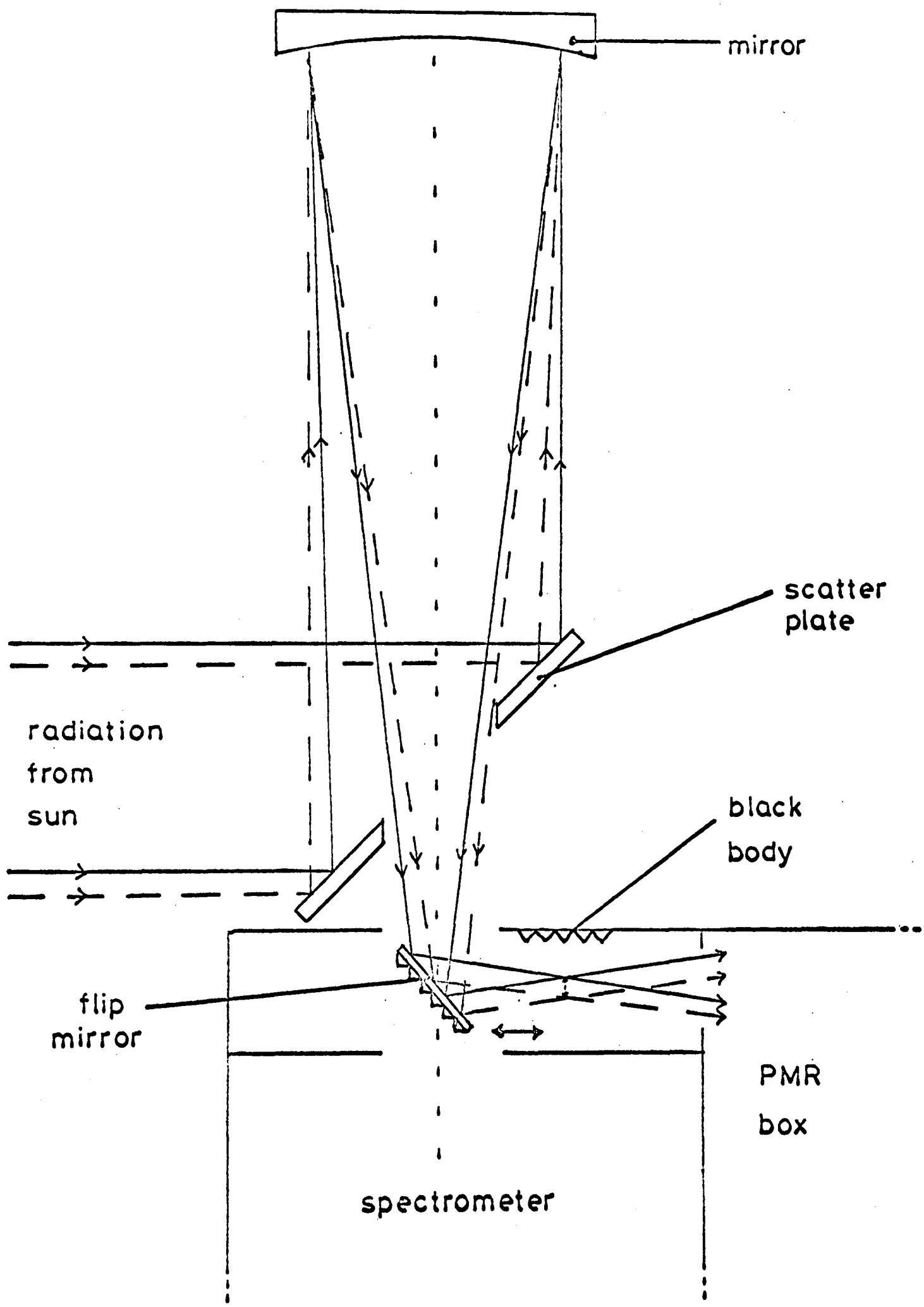

Figure 5.1 The sun-seeker system.

sun to space by inserting a refractive wedge in front of the tracking sensor to shift the apparent position of the sun. This mode is used in flight to give a space view calibration.

The "flip mirror" shown in the diagram is the mechanism which enables the beam to be shared between the Denver spectrometer and the PMRs. The mirror has two positions and is driven from one to the other every two minutes. In the first position it reflects the beam into the PMR box while the spectrometer views a black body on the back of the mirror as shown in figure 5.1. In the second position it allows the beam directly into the spectrometer while the PMRs view a black body, the temperature of which is monitored.

5.2 PMR housing and optical system

The PMRs and their optical system are housed in a partitioned dural box, measuring approximately 100 cm x 60 cm x 20 cm. The optical system was designed by J. Delderfield and built by the Satellite Experiment Laboratory (SEL) at NOAA. It is shown schematically in figure 5.2.

The long light pipe serves to scramble the sun's image so that the PMRs' field of view is more uniformly illuminated. In this way the problems caused by the sun's disc moving around within the instrument's field of view are minimized. The optical beam is shared

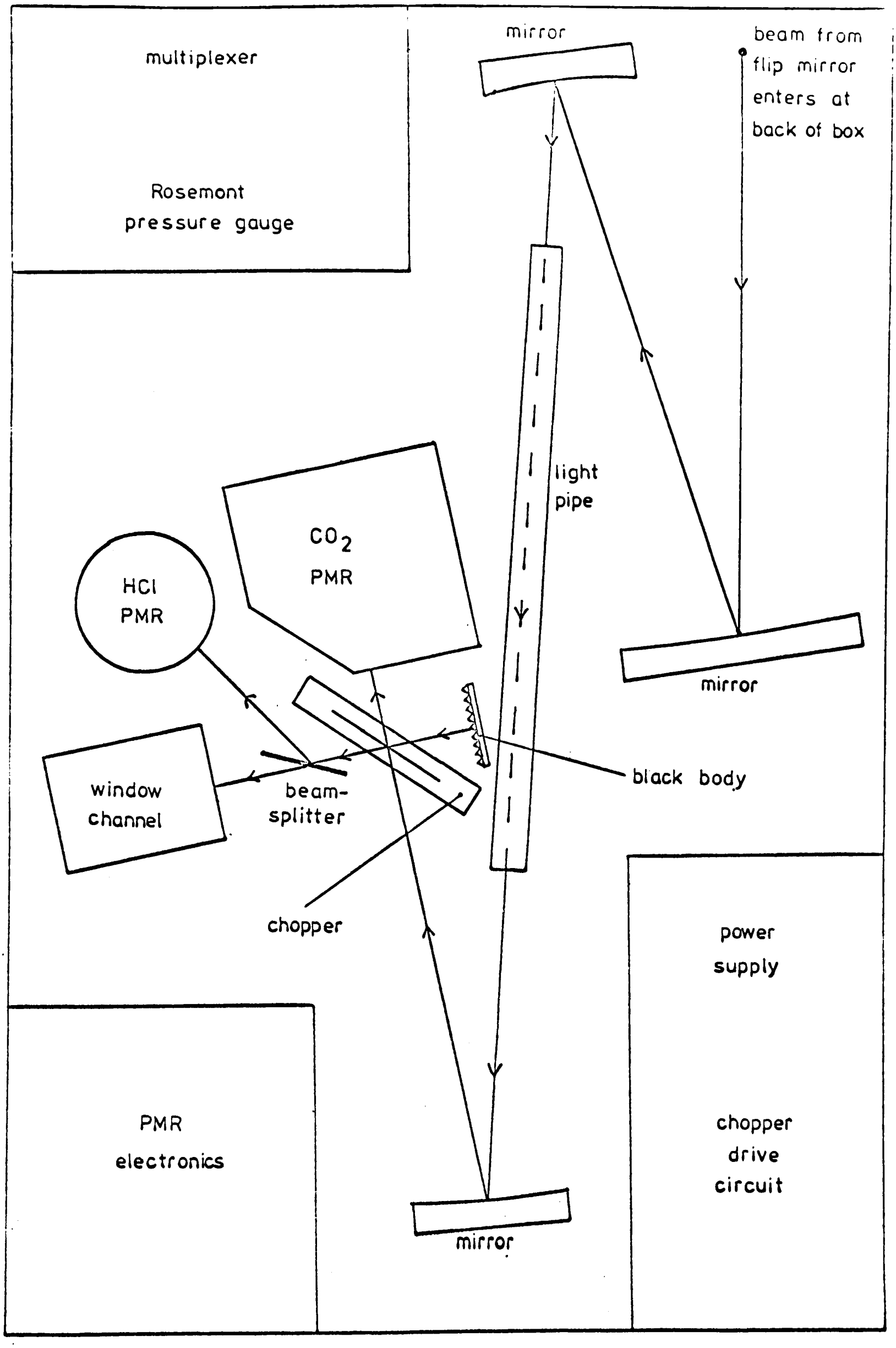

Figure 5.2 The PMR box layout and optical system.

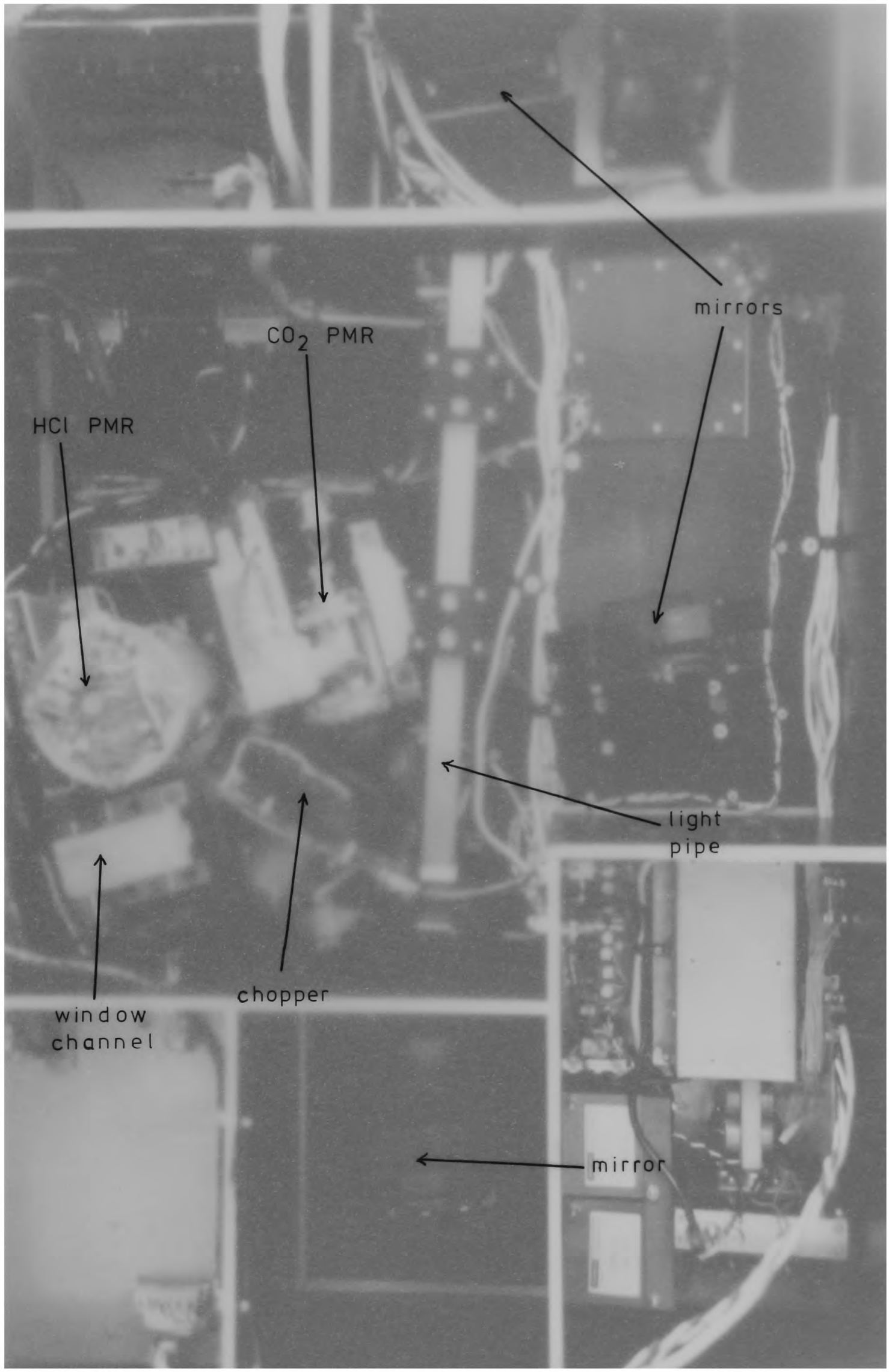

Plate 1. The PMR box.

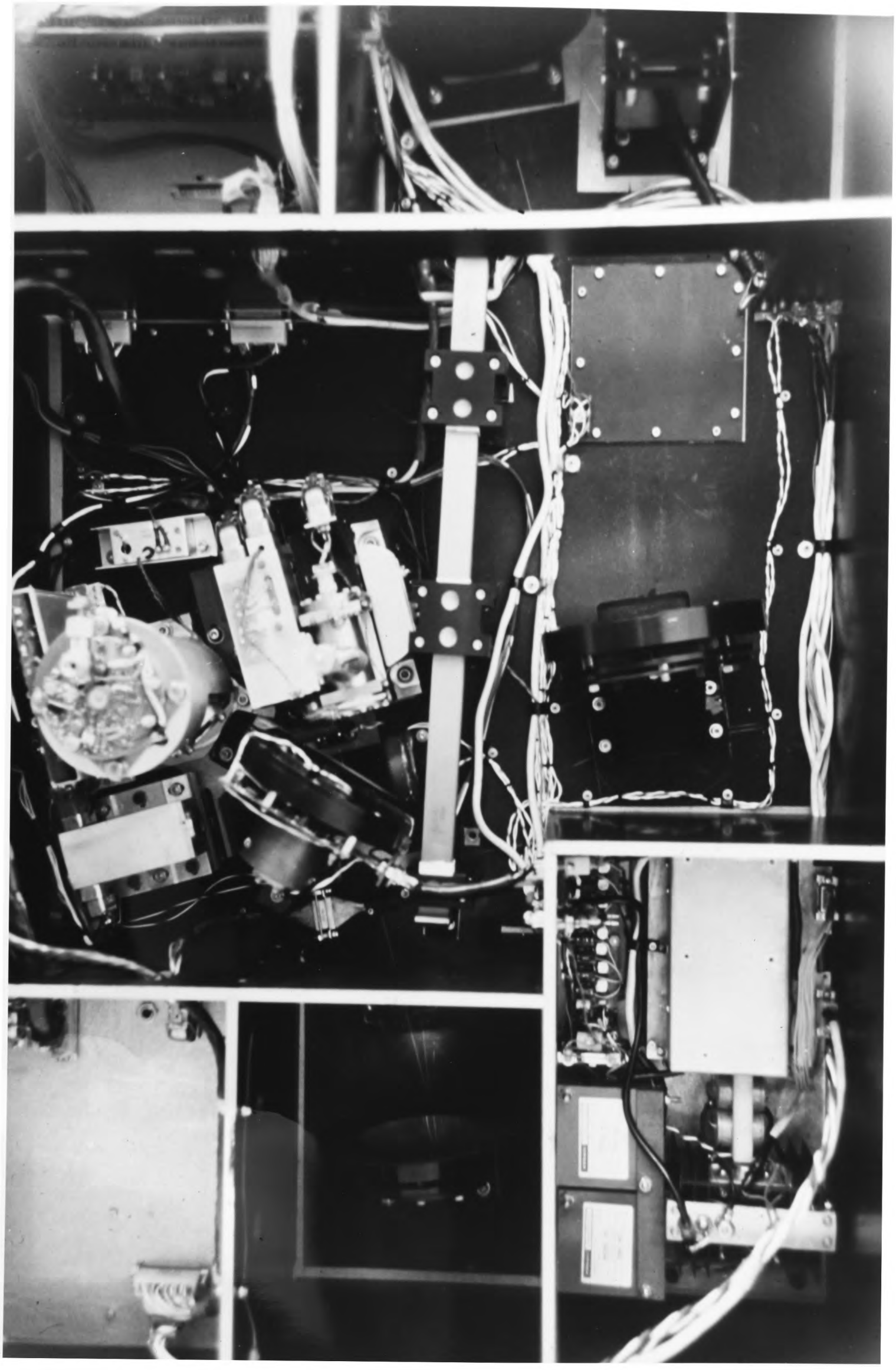

between the CO_2 PMR on one path and the window channel and HCl PMR on the other by means of a rotating reflective chopper. Thus the CO_2 PMR "sees" the image of the end of the light pipe directly and the black body in reflection; the other channels "see" the image of the light pipe in reflection and the black body directly. Besides allowing the optical beam to be utilized in this way, the chopper creates a wideband signal at 400 Hz , since it modulates the incident beam, the sun and the internal black body being viewed alternately as the chopper rotates.

The PMR electronics are also housed in the PMR box, as is a Rosemont pressure gauge to sense the atmospheric pressure at the instrument height.

The optical system was modified to allow for the inclusion of the HCl PMR by means of a beamsplitter in the optical path of the window channel. The beamsplitter transmits around 12 micrometres, but it reflects radiation in the 3.5 micrometre region through about 60 degrees as shown. It has a reflectivity measured to be greater than 97% for all wavelengths in the pass band of the HCl PMR filters. The only effect of the modifications on other channels, apart from a small decrease in the energy reaching the window channel in the 12 micrometre region, was the displacement of the window channel's optical beam due to refraction at the beamsplitter faces. A repositioning of the window channel involving a movement ~ 2 mm was required.

5.3 HCl PMR : Optical system.

Figure 5.3 illustrates the structural design and the optical system of the HCl PMR. An image of the end of the light pipe lies in a plane between the beamsplitter and the chopper. This is focused on the detector by means of two plano-convex lenses and a meniscus lens, all of which are anti-reflection coated at 3.5 micrometres. The first lens produces a slightly convergent beam which passes through the filter combination and the PMC head before being focused on the detector by the back optics. The first lens and the beamsplitter are held in the same mounting assembly along with a window channel lens. Neither this lens nor the beamsplitter is shown in figure 5.3 as their optical axes are not aligned with those of the other components (see figure 5.2). The dural mount is painted black to reduce stray radiation. The back optics is held in the detector mounting block as shown. Both of these mountings and the brass tube holding the pressure modulator are bolted to a dural plate supporting the HCl PMR components only. This enables them to be assembled and aligned independently from the rest of the optics. The HCl PMR base-plate is then aligned on appropriate markings on the base-plate of the main instrument housing.

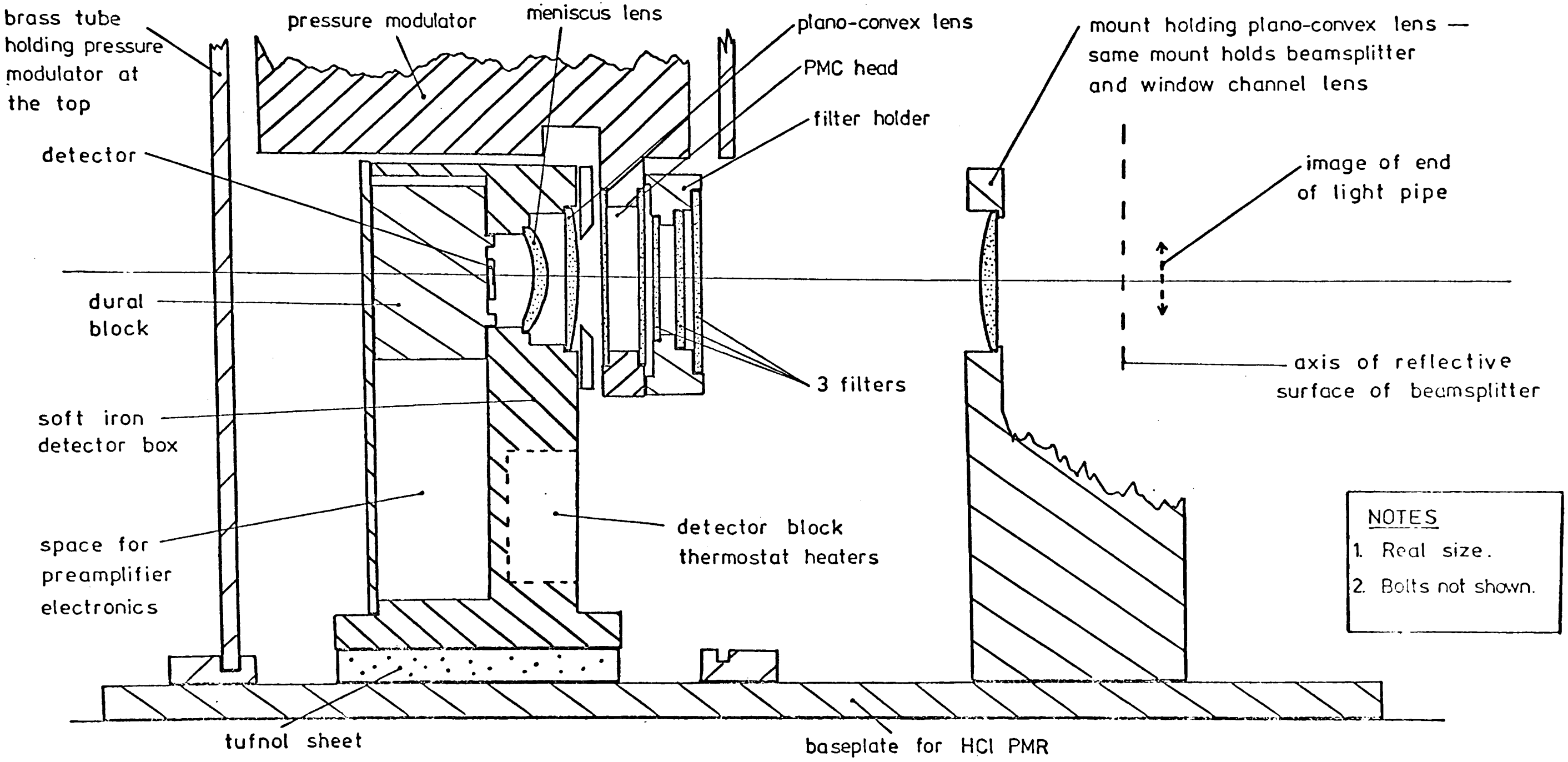

Figure 5.3 Mechanical and optical layout of HCl PMR.

Section through optical axis and perpendicular to baseplate.

5.4 The filters

The filter combination, which defines the spectral pass band of the instrument, is held in a dural mounting bolted on to the front of the PMC head. Each filter consists of a substrate on which multiple coatings of suitable material have been deposited to calculated thicknesses. A high-pass filter with a transmission rising from less than 5% at 2600 cm^{-1} to about 85% above 2800 cm^{-1} was obtained from Rofin Ltd. The two other filters were coated by the Filter and Coatings Group at Reading University, who were also responsible for the beamsplitter coatings and the anti-reflection coatings of the lenses.

One filter was designed to be a low-pass filter with a sharp cut off around 2950 cm^{-1}. This feature was included to avoid unwanted effects from the Q-branch of atmospheric methane around 3010 cm^{-1} while maintaining a high optics transmission over as great a part of the HCl band as possible. The transmission of this filter falls to less than 1% at 3000 cm^{-1} but increases again above 3500 cm^{-1} . It was therefore necessary to include a short-wave blocking filter as well. The combined transmission of the filter assembly, calculated from the manufacturers' spectra for the individual components, is shown in figure 4.4.

The shape of the profile was checked for the assembled

combination using a spectrometer (albeit one of low resolution). Since the retrieval of results requires no calculations involving absolute energies, only the relative filter profile is shown, but the maximum transmission of the combination is about 50%.

5.5 The pressure modulator cell (PMC)

The structure of the pressure modulator is shown in figure 5.4. The particular modulator used had previously been employed filled with NO to make a measurement of this species in the stratosphere (Jarnot, 1976). For a detailed description of its design and testing see Drummond (1977).

The gas - HCl, for this instrument - is contained in a titanium cylinder. The gas pressure in the PMC head is modulated at constant amplitude by means of piston with only a small clearance between the piston and the cylinder wall. In this way a physical compression ratio ~ 3 is possible for the gas in the PMC head. The optical windows are made of Irtran 1 and have an almost constant transmission over the pass band of the filters. The materials exposed to the gas inside the PMC are chosen to minimize chemical reactions and the resulting contamination of the gas. However, HCl is a particularly reactive species and was found slowly to attack some part of the structure - possibly the glue holding the windows. This problem is discussed

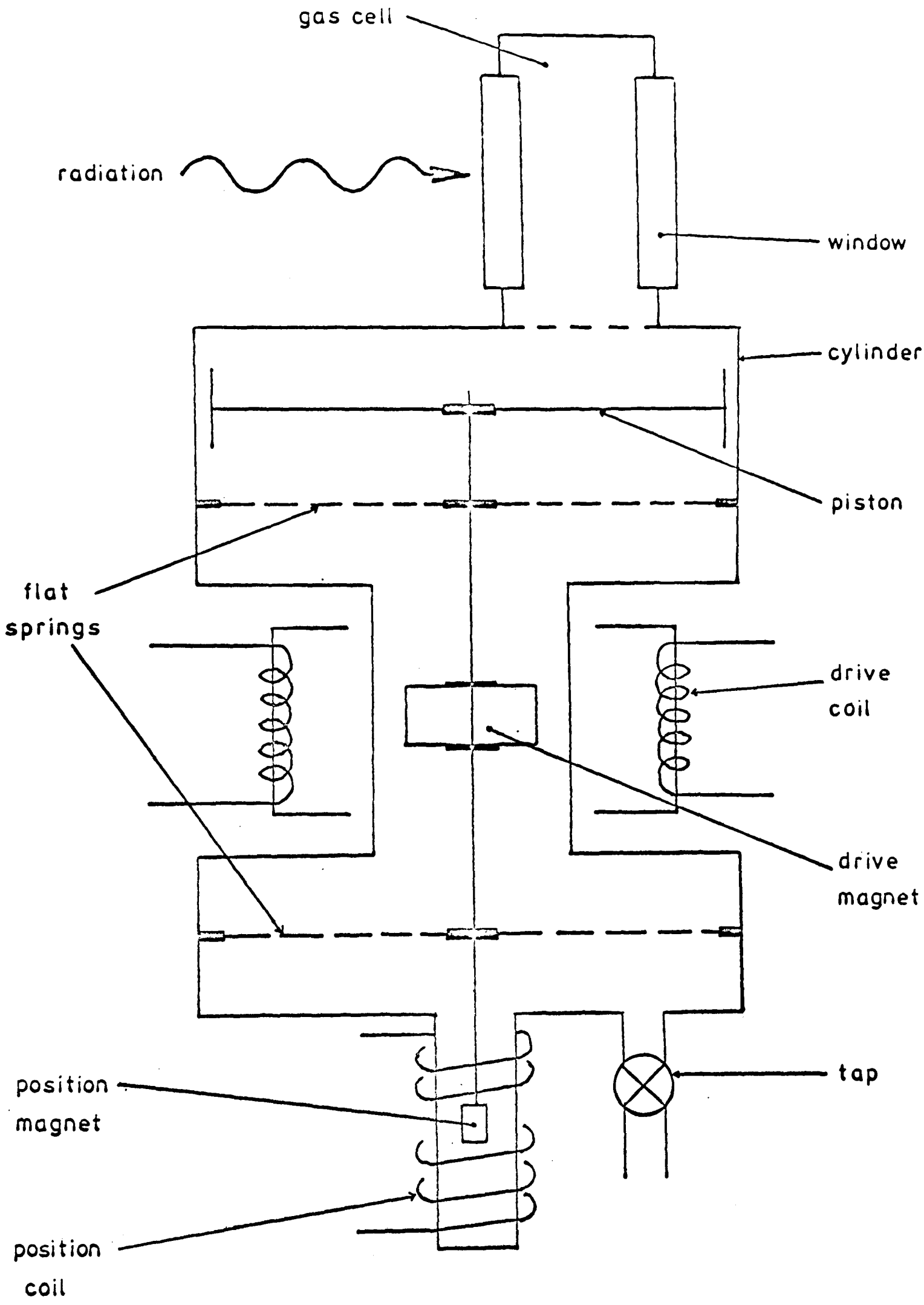

Figure 5.4 Pressure modulator cell.

further in chapter 6.

The piston is driven by the effect of the alternating magnetic field produced by the drive coils on the permanent magnet attached to the drive shaft. The amplitude and frequency of the modulation are held constant by means of an amplitude sensor at the tail of the PMC. A signal derived from the sensor is introduced as feedback into the drive circuit which provides the current to the magnets. The drive circuit was designed and built by J. Delderfield.

A feature of the PMC behaviour is the variation of the frequency of modulation with the mean pressure in the cylinder. Thus, if the frequency is monitored, the mean pressure can be deduced from a calibration curve of pressure against frequency. At a typical PMC pressure of 2.5 mb, the frequency of modulation is about 19 Hz. The temperature of the gas in the PMC is also monitored by means of a thermistor in good thermal contact with the PMC head.

The PMC was designed with the axis of the cylinder vertical. However, when modifying the already existing instrument to include the HCl PMR, limitations of available space necessitated the PMC being mounted with its axis horizontal. This introduces a small shift in the equilibrium position of the piston, but it still runs with satisfactory stability.

The PMC is supported in position with its head in the optical beam by a cylindrical brass tube inside which it is slotted. It is secured on a flange at the

end of the tube. The brass tube has appropriate holes in it to allow through the optical beam and necessary electronics leads.

5.6 The detector and preamplifier

The detector is made of lead selenide mounted on a substrate, and its active area has dimensions of 2 mm x 2 mm. It is photoconductive and at room temperature the HCl band lies close in wavelength to the maximum responsivity point (~ 2700 cm^{-1}). The responsivity does vary slightly across the filter pass band and this is taken into account in calculations in the form of a weighting to the optics profile.

The detector is mounted on a dural block which locates precisely inside the soft-iron detector mounting block as shown in figure 5.3. The insulated detector leads pass along grooves in the dural block into the preamplifier chamber. In this way the detector leads are kept as short as possible, and the detector and preamplifier are almost completely surrounded by the soft-iron box, which reduces magnetic interference.

The detector block temperature is thermostatically controlled by means of a series of heaters and a thermistor glued into slots in the front of the block. The thermistor resistance is sensed by an external thermostat circuit which controls the current to the heaters such that the whole detector assembly is maintained at about 38°C during flight. This is ~ 2 degrees higher than the temperature at which the PMR housing is maintained. The temperature

differential between the detector block and the rest of the instrument is maintained by an insulating sheet of Tufnol as shown in figure 5.3. The block is fastened to the base-plate through the Tufnol by three stainless steel (low conductivity) bolts. The thermal isolation so provided ensures that the detector temperature fluctuates as little as possible and does not tend to follow variations in PMR box temperature. The detector temperature is monitored by a thermistor just behind the detector in the dural block. The degradation of the responsivity caused by the high operating temperature is unimportant for this instrument as the energy incident from the sun is so large.

The preamplifier circuit was designed and built by R.F. Jarnot, and it is shown in figure 5.5. It was constructed on a board which fits inside the chamber at the back of the detector block. Its primary function is not to amplify voltage, as the high level of solar radiation incident on the detector leads to suitably large signals, but to provide a constant bias voltage across the detector so that the change in detector current and preamplifier output voltage are proportional to the change in detector conductivity and therefore proportional to the power of the incident radiation. The preamplifier also serves to lower the effective output impedance of the detector.

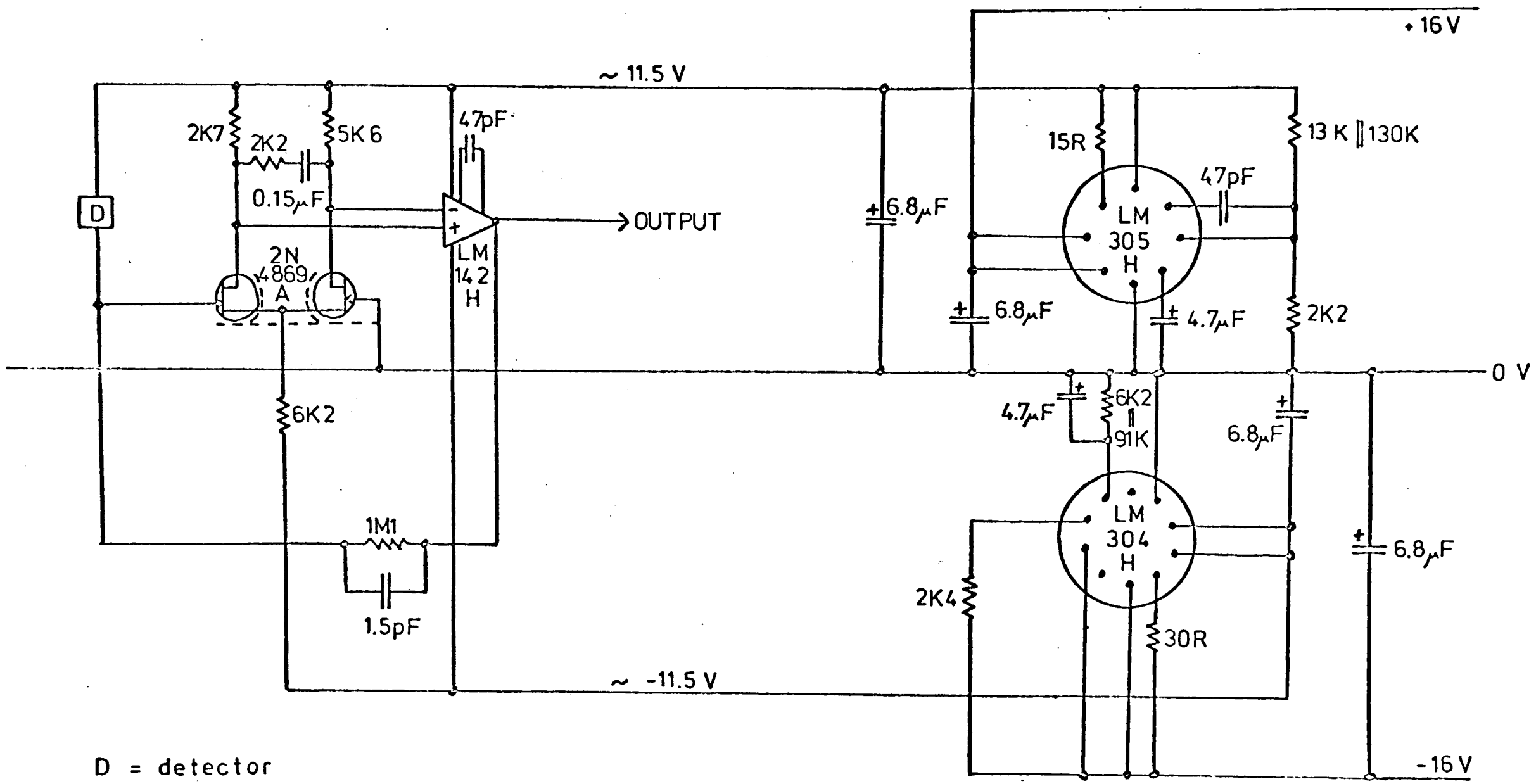

D = detector

Figure 5.5 Preamplifier.

5.7 Electronics

The basic units in the PMR electronics are shown in figure 5.6. The signal from the preamplifier is fed to the signal channel, which was built by J. Delderfield. It is held on a printed circuit board, screened by surrounding aluminium covers and fastened to the side of the brass tube holding the PMC. The development of a signal channel for a minor constituent PMR is discussed in detail by Jarnot (1976), on whose design this one is based. The major feature of the signal channel is its use of sideband signals rather than the signal at PMC frequency. The sideband frequencies are those at (wideband ± PMC) frequency - in this case, 400 ± ~ 19 Hz. Certain aspects of sideband signals are discussed in chapter 6, but the subject is treated more fully by Jarnot. Briefly, the sideband signals contain the same information as the direct PMR signal, but, by raising the frequency used from ~ 20 Hz to ~ 400 Hz, 1/f noise is reduced. Also the sideband signals contain no contribution from emission from optics on the detector side of the chopper, though this feature is unimportant for this particular PMR since optics emission is negligible compared to incoming solar radiation (see chapter 6). The function of the signal channel is to isolate the signals at wideband and sideband frequencies and to output voltage ramps proportional to their amplitudes. The functional blocks

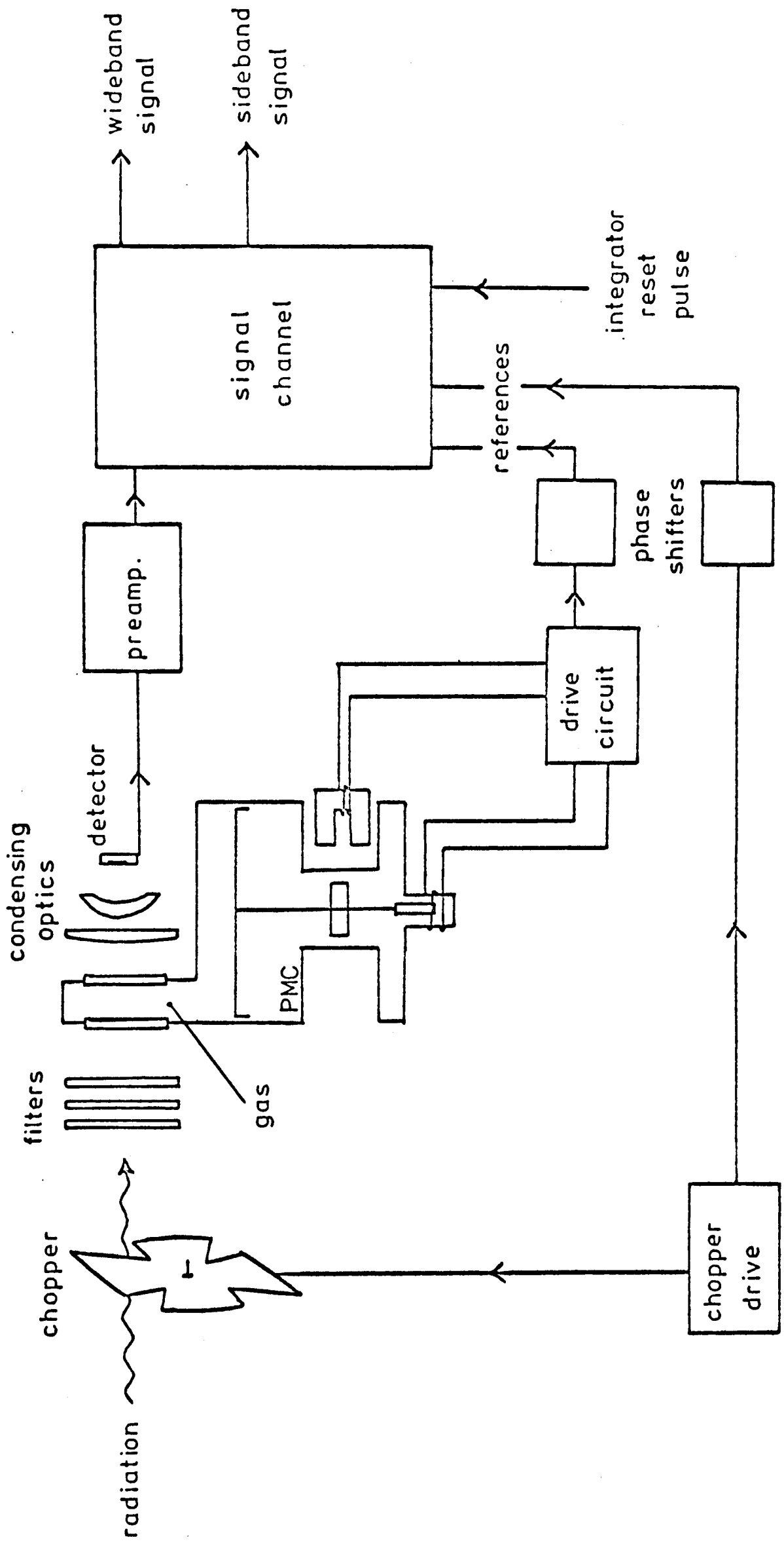

Figure 5.6 Block diagram of PMR electronics.

in the signal channel are illustrated in figure 5.7; details of the circuit are given by Delderfield (1977).

The chopper and PMC drive circuits maintain the constant frequencies of their respective components and also provide reference waveforms for the phase-sensitive detectors and the synchronous filter in the signal channel, to which they are fed via phase shifter circuits which ensure correct phasing of the references with respect to the signals. Also, every 1 s, the signal channel is sent an integrator reset pulse derived from the fundamental clock of the data system.

The wideband and sideband output ramps, the equivalent signals for the CO_2 PMR and the window channel, and the housekeeping data are sampled by a multiplexer, converted into a digital stream and recorded on magnetic tape. The multiplexer was built by SEL and is housed in a compartment of the PMR box. The data recording system was built by Denver University and records the data from all the instruments on the gondola.

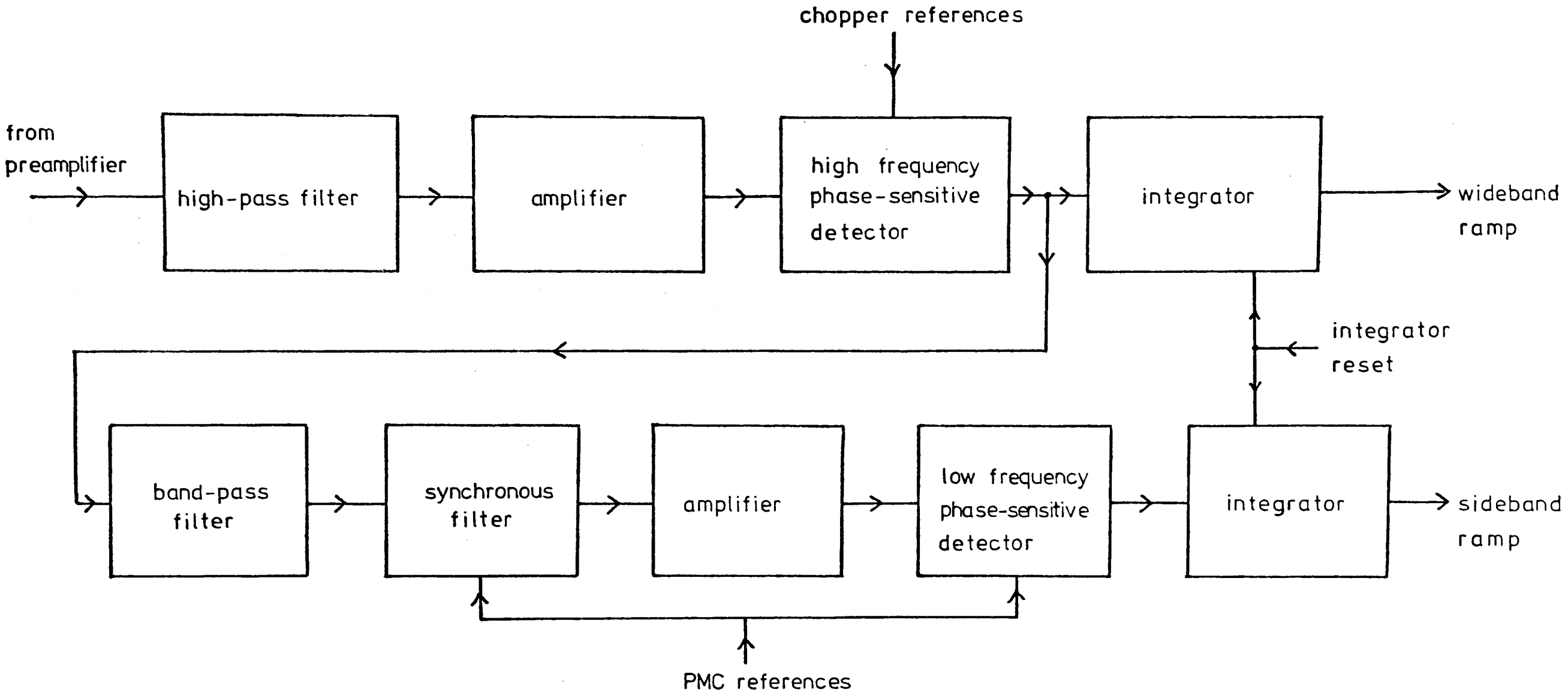

Figure 5.7 Block diagram of signal channel.

CHAPTER 6. INSTRUMENT TESTING AND LABORATORY MEASUREMENTS.

In order to interpret the signals output by the PMR, it is necessary to understand what information is contained in them. This involves an analysis of the information in the energy received at the detector and the way in which it is processed by the electronics. The analysis is also aided by an understanding of the approximations which may be made when describing the response of the instrument. These aspects are now discussed in detail and an account of the instrument's laboratory testing is given.

6.1 Emission

The radiometer is designed to measure incident solar radiation and to detect the amount of that radiation which is absorbed in the atmosphere, particularly by HCl. However, the detector also receives thermal radiation from the instrument and the atmosphere, and the relative magnitudes of these components will affect the interpretation of signals.

The power incident on the detector at wavelengths in the filter pass band with the sun in the field of view was calculated. This entailed estimations of the solid angle subtended by the sun

at the instrument, the area of the input optics and the transmission of the whole optical system. It was shown that the solar power incident on the detector is $\sim$ 8 mW. This is very much greater than the total energy incident on the detector over the spectral region of appreciable detector responsivity when surrounded by a black body at instrument temperature (310 K), which is estimated to be $\sim$ 8 μW. This figure represents the constant component of thermal radiation incident on the detector. However, the electronics detects only chopped signals. For the wideband channel the incident energy waveform represents chopping between solar radiation and energy from the internal black body. The latter will be less than the constant component by a factor $\sim$ 10, due to optics absorption and the limited acceptance angle of the optics. Therefore the chopper modulates energy between a high level and one lower by a factor $\sim 10^4$, which approximates very well to chopping between solar radiation and zero. A similar calculation shows that atmospheric emission contributes energy less than solar radiation by a factor $\sim 10^7$.

It follows, therefore, that all radiation other than that from the sun may be neglected in calculations. This is confirmed by the fact that the difference between signals from the internal black body and space views recorded during flight was less than the resolution of the instrument (see chapter 7).

Also the difference between the signals and the integrator offset voltage could not be resolved. Emission from other sources can also be neglected when viewing a bright laboratory source which gives output voltages comparable in magnitude with those produced by the sun.

6.2 Information in the signals.

The energy incident from the sun is first modulated by the chopper at 400 Hz with an approximately square waveform. It is further modulated at low frequency (~ 19 Hz) by the PMC. However, this chopping is very shallow since only energy in the region of HCl spectral lines is modulated, and so it imposes a shallow, low frequency envelope on the chopper-modulated waveform, as shown in figure 6.1. The signal channel isolates the signals at wideband and sideband frequencies and outputs voltage ramps proportional to their amplitudes. The details of signal processing are discussed in appendix E. Equations are derived which relate the levels of the output voltages to the amplitudes of the wideband and PMR waveforms, x_W and x_S respectively, as defined by figure 6.1.

Consider the PMR viewing a source through a path containing a fixed amount of HCl. If the power of the source is increased (while maintaining the relative distribution of power with wavenumber),

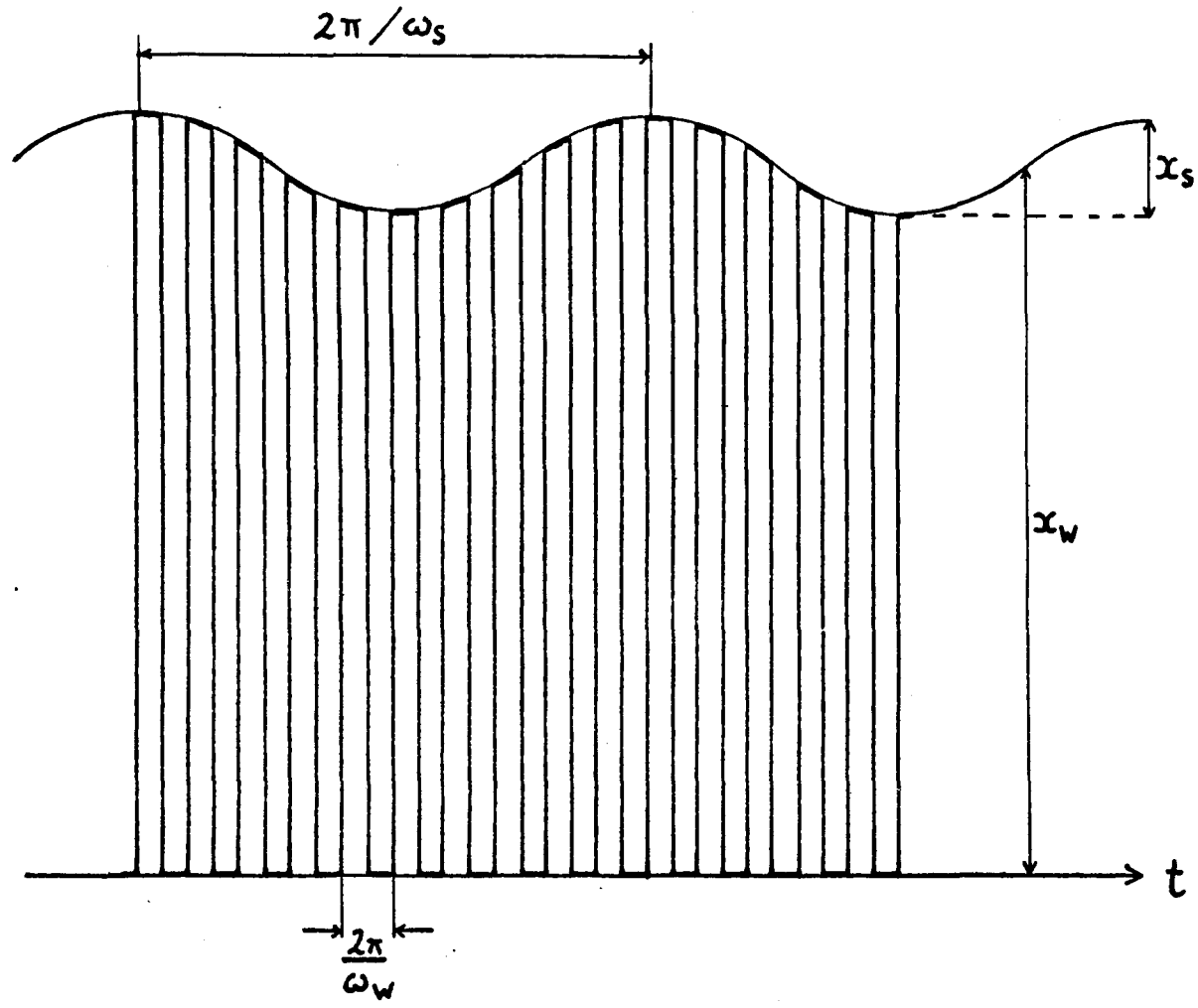

Figure 6.1 Illustrating the variation with time of the energy incident on the detector.

then the wideband signal will rise and the sideband signal will increase proportionally. Therefore, for a variable power source, the amount of HCl in the path is related to the ratio of the sideband and wideband signals but not to either in isolation. In flight the wideband signal changes due to the variation of scatter plate reflectivity with zenith angle and due to absorption by other atmospheric constituents. These effects are discussed in detail in chapter 7, but they have the same effect as a varying power source. Therefore it is necessary to calibrate out the variation of wideband energy by using the ratio of signals from the two channels when analysing the data.

6.3 An electronics fault

The signal channel of the PMR contained a fault which affected the data obtained on the balloon flight. This is discussed in detail in appendix F. It is shown that, although the fault causes both the wideband and sideband channels to be non-linear, the ratio between the two is expected to be unaffected. For reasons explained above, only the ratio of signals is used in the retrieval and so the fault does not affect the results.

Experimental confirmation of this can be obtained from the data received before sunset.

In this period the instrument views the sun through a comparatively thin layer of atmosphere, and calculations show that the corresponding atmospheric absorption has a negligible effect on the signals. Therefore the ratio of sideband to wideband signals is expected to be constant. Also the changing scatter plate angle leads to a wideband signal which varies with time and thus provides data from which any effect of non-linearity on the ratio of signals should be detectable. However, the ratio of signals for the pre-sunset data was seen to be constant to within the level of the noise (see chapter 7).

6.4 Laboratory measurements

In order to test the performance of the instrument and to make transmission measurements, the PMC and detector block were mounted on a rigid plate in the same relative positions as used in the flight instrument. The mounting system was designed such that the PMC axis was horizontal, as in flight, and the optical axis was aligned with a source, a chopper and a 10 cm cell as shown in figure 6.2. All the components were bolted to a large, rigid base-plate. To achieve the signal levels required a 500 W "Photoflood" light bulb was used. Both the 10 cm cell and the PMC were attached to a filling system and vacuum pump. The system allowed the cell and the PMC to be filled independently and included a digital manometer to monitor

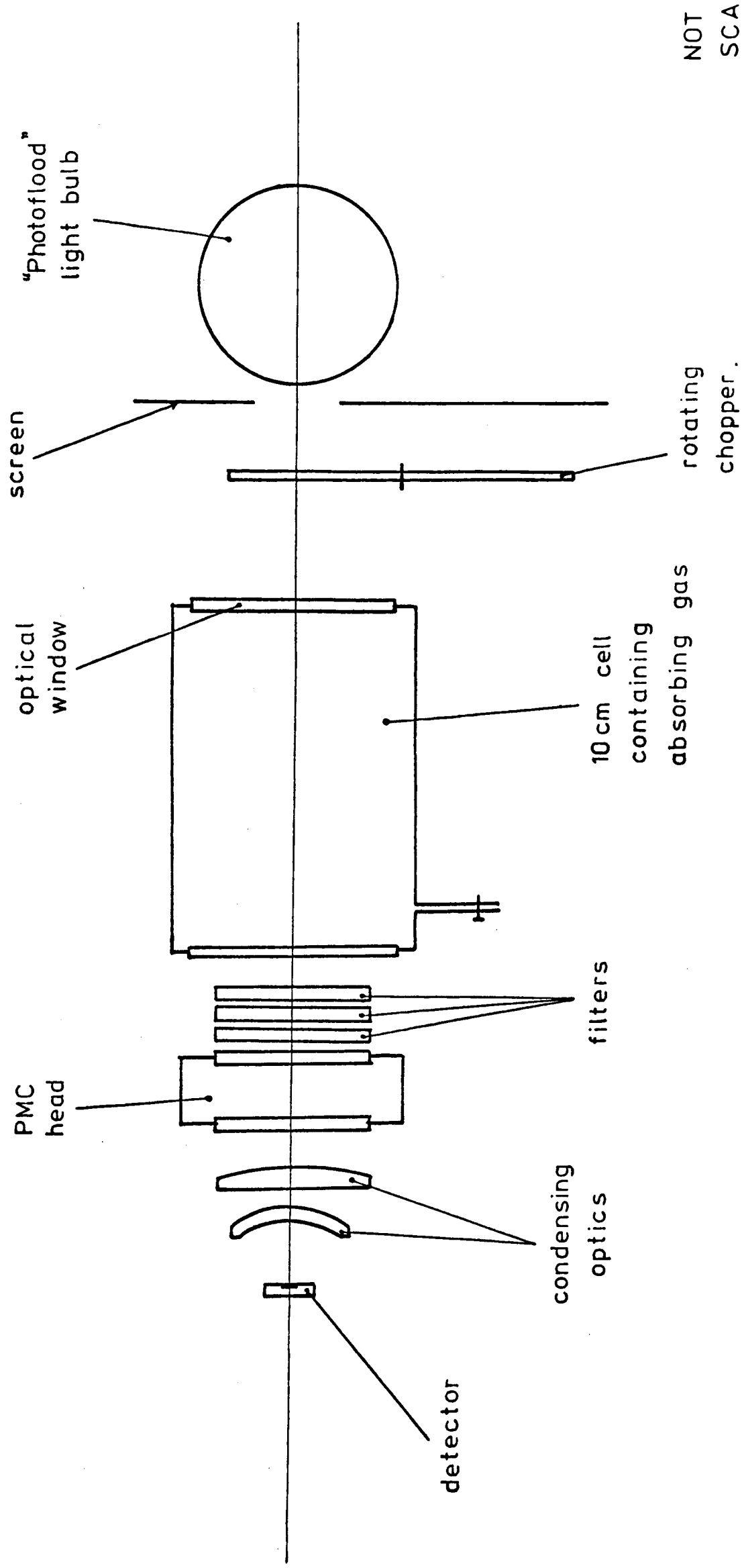

Figure 6.2 Schematic representation of laboratory testing system.

the pressure in the apparatus. The filling system is described in more detail by Drummond (1977). As in flight, the detector block was thermostatically maintained at constant temperature.

A different signal channel was used for these measurements, but its design was almost identical to that of the flight signal channel. The output signals were fed to a sample and hold circuit and displayed on a chart recorder.

Since the pressure of gas in the modulator during flight was monitored indirectly through measurement of the PMC frequency, a laboratory calibration of frequency against pressure was performed using the digital manometer to measure pressure. The resulting calibration curve is shown in figure 6.3. The frequency to voltage convertor used during flight to monitor the PMC frequency was also calibrated. The two curves were used in conjunction to infer the PMC pressure in flight from the output level of the frequency to voltage convertor. For laboratory measurements the PMC frequency was obtained directly using a frequency meter.

6.5 Transmission measurements

Using the system described above, a series of measurements was made of sideband and wideband signals with different amounts of HCl in the 10 cm cell. Measurements were also made of the full scale

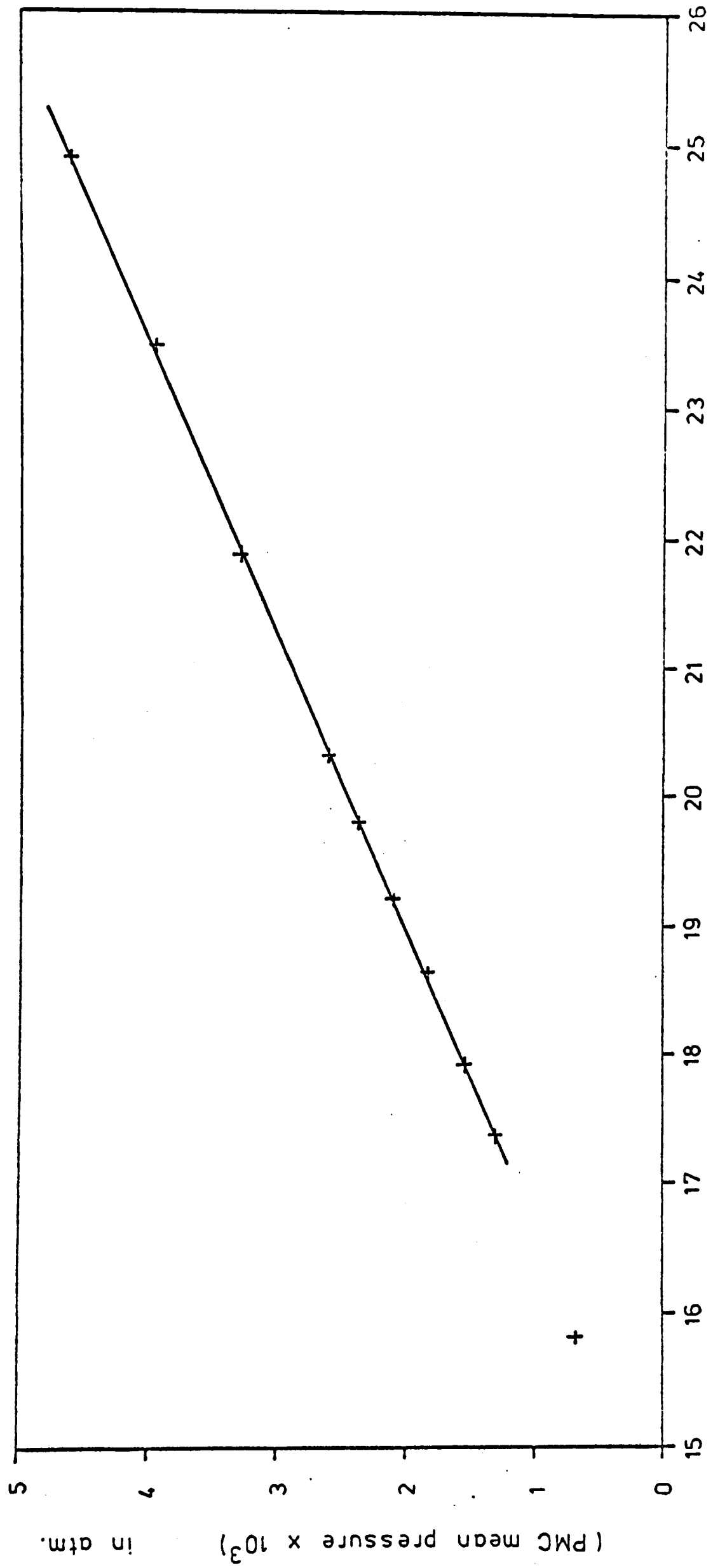

Figure 6.3 PMC calibration: mean pressure v. frequency.

signals, by flushing the 10 cm cell with dry nitrogen and then evacuating it, and of the zero signals, by blocking the optical beam. For a constant source no detectable change is expected in the wideband signal for small amounts of HCl in the path (see chapter 4.8) and so this signal can be used to check the constancy of the source. From the measurements of signal, PMR transmissions as defined by equation 4.31 can be calculated. These are plotted in figure 6.4 against the measured pressure of pure HCl in the 10 cm cell.

Also plotted in figure 6.4 is a curve of PMR transmission calculated theoretically from the spectral line data using a line-by-line model as described in chapter 4. The instrumental parameters used in the calculation are given in the diagram. The mean pressure in the PMC was obtained from a measurement of PMC frequency and the PMC and cell temperatures from the measured resistances of thermistors in good thermal contact with the bodies of the appropriate components. The determination of PMC compression ratio and the way in which it is combined with the PMC mean pressure to give the high and low pressures used in the line-by-line model are discussed in section 6.6.

The source temperature used is an estimate of the effective black body temperature of the light bulb. It is probable that the glass of the envelope transmits an appreciable fraction of the radiation from the filament at wavelengths around 3.5 micrometres, and so the energy emitted by the bulb will be

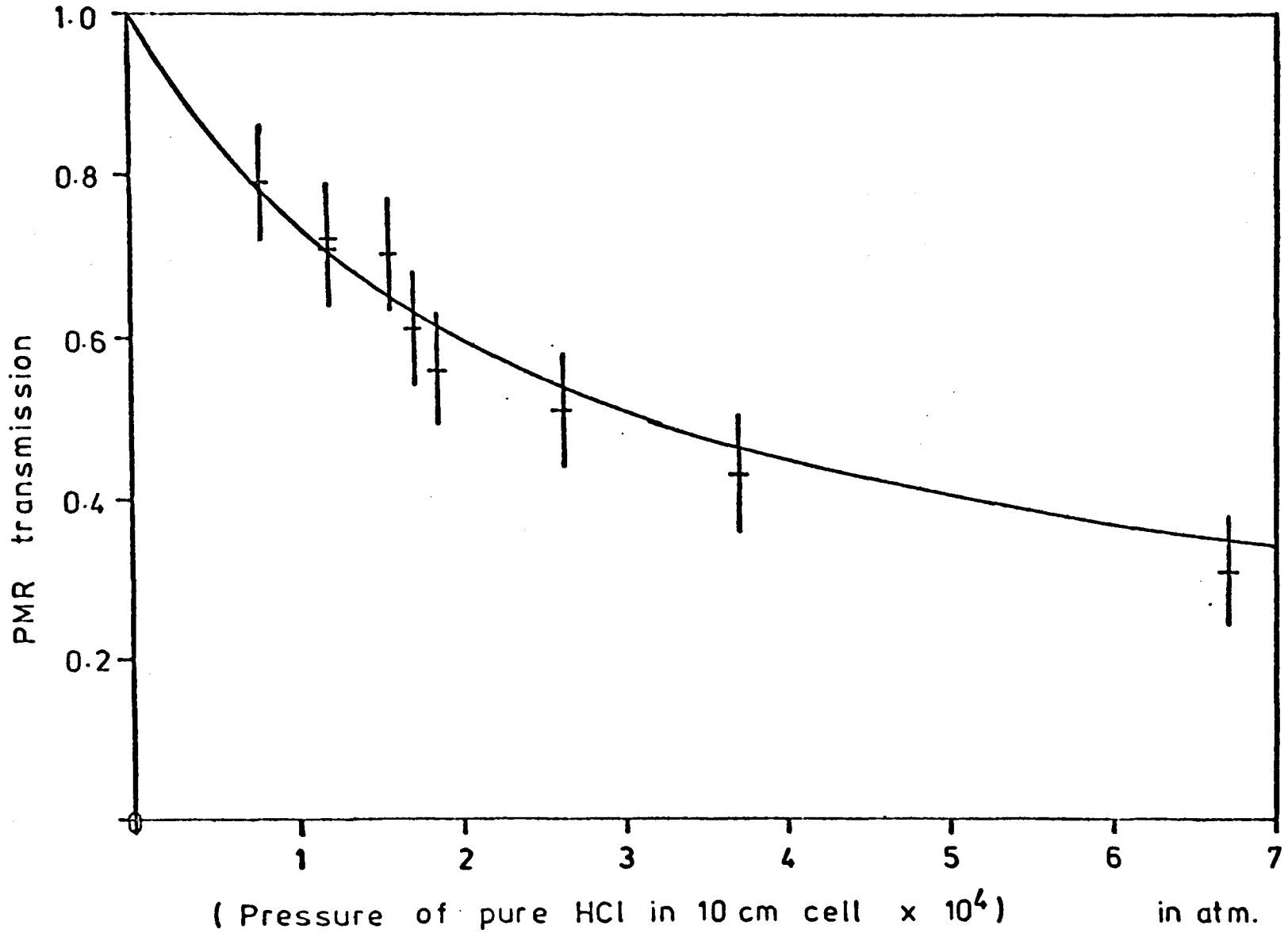

Calculation parameters:

PMC length = 0.51 cm
PMC mean pressure = 1.6 τ = 0.00211 atm.
PMC compression ratio = 1.96
PMC temperature = 304 K
Cell temperature = 304 K
Source temperature = 500 K

Figure 6.4 PMR transmissions for HCl: measured transmissions and theoretical calculations.

characteristic of a combination of source functions corresponding to the temperatures and emissivities of the filament and the envelope. Since the variation of source function with wavenumber might affect the calculation of PMR transmissions, a series of calculations was performed for a range of black body functions between 400 K and 2500 K. The calculated values of transmissions varied by less than 0.5% over the range of source temperatures and HCl absorber amounts used. Therefore, although the effective source temperature is not known, PMR transmissions are insensitive to its value.

For these calculations the combined optics transmission profile shown in figure 4.4 was weighted by a function to account for the variation of detector responsivity with wavenumber. Since the manufacturer's specifications for the detector show that the responsivity changes only by $\sim$ 6% over the pass band of the optical filter, this variation is small compared to that of the filter itself. It was therefore considered adequate to represent the relative responsivity at wavenumber, ν, using the formula,

$$\tau(\nu) = \tau(2880)\left\{1 + 0.00017\,(2880 - \nu)\right\}. \qquad (6.1)$$

The coefficient was estimated from the manufacturer's responsivity curve for the appropriate temperature. Calculations which neglect $\tau(\nu)$ give an almost negligible change in PMR transmission and so a more exact knowledge of $\tau(\nu)$ is not required.

Figure 6.4 shows that the measured PMR transmissions are compatible with theoretical calculations. However, deductions from these measurements are limited by the large error bars on the measured PMR transmissions caused by the low signal-to-noise ratio achieved by the transmission measurements. The HCl PMR is particularly prone to this problem since the amplitude of the energy modulation at PMC frequency is so low - only $\sim$ 0.015% of the wideband energy. In principle it is possible to overcome this problem by integrating the signals for a long time. In practice under laboratory conditions the instrument was not sufficiently stable for this to be practicable. It is probable that the laboratory system could be improved, but not to the point at which it could be used to test precisely the spectral line data and instrumental parameters used. Also, since HCl is a simple molecule which has been widely studied, we may have greater confidence in the line data than those of most other molecules. The discrepancies between the measured and theoretical line strengths are generally only $\sim$ 2% (Toth et al., 1970), and, although the Lorentz half-widths are known less accurately ($\sim$ 10%), for most PMC and laboratory paths of interest the dominant broadening mechanism is Doppler, for which the appropriate half-widths and their temperature dependence can be accurately computed. Consequently further transmission measurements have not been attempted.

In flight the problems outlined above are present, but they are much reduced for a number of

reasons. Firstly the sun provides higher energy levels at the required wavelengths than are conveniently achieved with this laboratory system. Also, the balloon-borne instrument is very stable in temperature, particularly at float altitude, and the stability of the electronics is found to be considerably better than in the laboratory.

6.6 Behaviour of the PMC

The PMR model described in chapter 4 assumes that the PMC behaviour can be adequately represented by considering two pressures corresponding to high and low pressure PMC states. This is equivalent to assuming the PMC pressure modulation to be square wave, whereas the volume modulation is approximately sinusoidal about a mean volume and the pressure modulation is more complicated. Consequently, a rigorous treatment involves consideration of more than two pressures. Other researchers have shown, by considering the Fourier components of the pressure modulation and those of the modulation of energy at the detector so produced, that a two pressure model introduces a negligible error for two particular PMRs - one containing NO_2 (Drummond, 1977) and another containing CO_2 (Delderfield, 1977). It will therefore be assumed here that a two pressure model is adequate for the HCl PMR.

Since the PMC modulation is approximately sinusoidal in volume about a state at mean pressure, p_m , the high and low pressures, p_1 and p_2 , can easily be shown to be given by

$$p_1 = p_m \frac{r+1}{2} \quad \text{and} \quad p_2 = p_m \frac{r+1}{2r} , \qquad (6.2)$$

where r = compression ratio = p_1/p_2 . The pressures used by the line-by-line model were calculated in this way both in the comparison with laboratory measurements and in the retrieval of the atmospheric HCl profile.

An investigation of the effect on calculated PMR transmissions of a variable compression ratio is shown in figure 6.5. Although the magnitude of the signal is roughly proportional to compression ratio, it can be seen that PMR transmission, as defined by equation 4.31, is affected only slightly by a variation of compression ratio over a large range (1.5 to 3.0). The effect of changing a parameter, such as compression ratio, on the sensitivity of the PMR to HCl in the atmosphere is best quantified by calculating the change in PMR transmission as a fraction of the "PMR absorption":

$$D = \frac{\Delta \bar{\tau}}{1 - \bar{\tau}} , \qquad (6.3)$$

where $\bar{\tau}$ is the PMR transmission. For a 100% change in compression ratio, it can be seen from figure 6.5 that, for small amounts of HCl in the path, D is $\sim$ 13%.

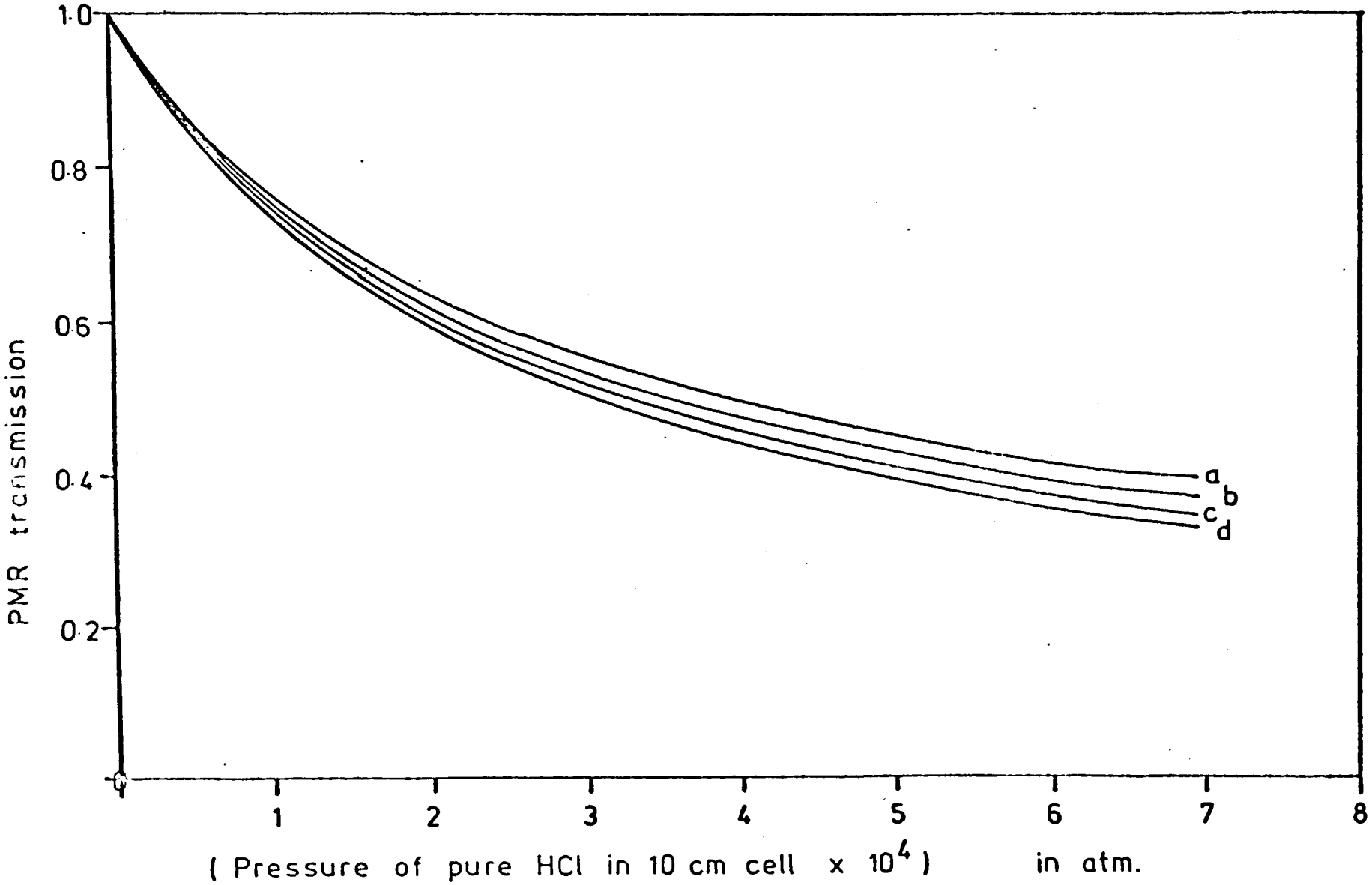

PMC compression ratio:

a) 3.00
b) 2.50
c) 1.96
d) 1.50

PMC length = 0.51 cm
PMC mean pressure = 1.6 τ
= 0.00211 atm.
PMC temperature = 304 K
Cell temperature = 304 K
Source temperature = 500 K

Figure 6.5 Calculated PMR transmissions for HCl: variation of transmission with PMC compression ratio.

Therefore errors in the assumed value of compression ratio only give rise to small errors in measured HCl amount.

In spite of the argument presented above, an attempt was made to calculate an appropriate compression ratio as accurately as possible. Since the PMR model effectively represents square wave modulation, it is not obvious what compression ratio should be used. The physical peak-to-peak compression is inappropriate since the physical pressure waveform is not square, the relationship between the modulation of pressure and that of the energy at the detector is not linear, and the signal channel isolates only the fundamental component of the modulated waveform. It was therefore decided to use a compression ratio which gave agreement between the measured and theoretical ratios of the magnitudes of sideband and wideband signals, taking into account the gains of the relevant signal channel stages. The theoretical ratio of the sideband and wideband signals, S_{SB}/S_{WB} , in terms of the amplitudes of the energy modulations, x_S and x_W , is derived in appendix E:

$$\frac{S_{SB}}{S_{WB}} = \frac{1}{\pi} G \frac{x_{SB}}{x_{WB}} , \qquad (6.4)$$

where G is the gain of the electronics between the wideband PSD output and the low frequency PSD input. An analysis of the gains of the stages involved yielded a value, $G \simeq 6850$, which was confirmed by measuring

the gain of these stages for a signal at PMC frequency fed directly to the sideband input. The value of S_{SB}/S_{WB} can be obtained most accurately from the pre-sunset data taken during flight (see chapter 7). Using the line-by-line model with the mean PMC pressure during flight and different values of compression ratio, a series of theoretical values for x_S/x_W was calculated. Interpolating between these values it was found that a compression ratio of 1.96 gave the best fit to equation 6.4. Since the physical peak-to-peak compression ratio is $\sim$ 3 for the particular PMC used, a value of 1.96 for the compression ratio of the equivalent square wave modulation is reasonable. This value was used in the retrieval and in calculations for comparison with laboratory measurements. It should be noted that this approach also takes effective account of any phasing error between the sideband signal and its PSD references.

Equation 6.2 uses a mean PMC pressure to calculate the pressures to be applied in the model. It has been assumed that the appropriate mean pressure is that derived from the PMC frequency measurement. This will not be exactly true since the signal channel isolates the fundamental component of the modulation of energy at the detector - modulation about a mean level which does not necessarily correspond to the physical mean pressure level. Figure 6.6 gives the variation of PMR transmission with PMC mean pressure. It shows that for small amounts of absorber in the path a 10% change in mean pressure causes a change

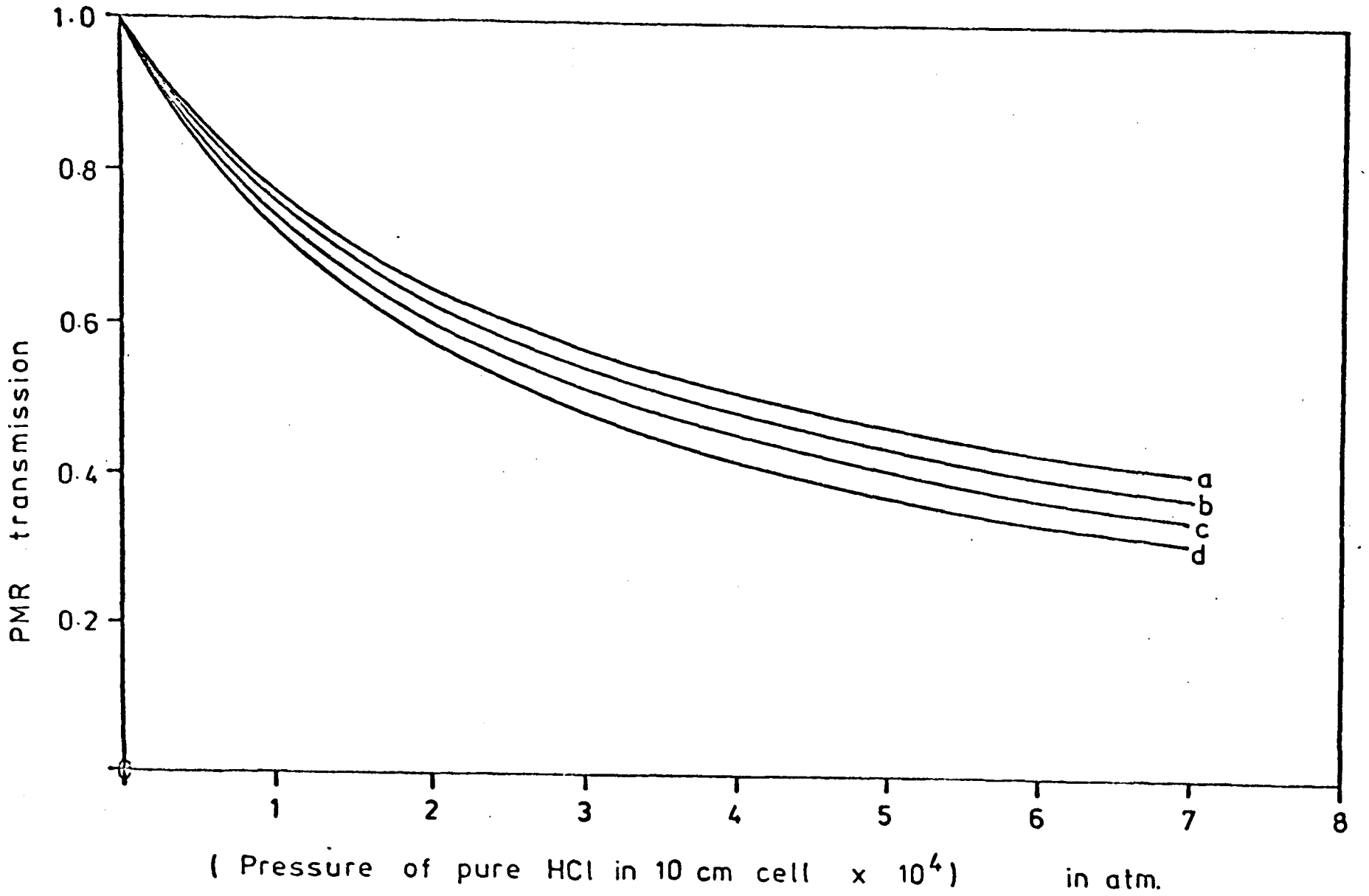

Mean PMC pressure:

a) 2.0 τ = 0.00263 atm.
b) 1.8 τ = 0.00237 atm.
c) 1.6 τ = 0.00211 atm.
d) 1.4 τ = 0.00184 atm.

PMC length = 0.51 cm
PMC compression ratio = 1.96
PMC temperature = 304 K
Cell temperature = 304 K
Source temperature = 500 K

Figure 6.6 Calculated PMR transmissions for HCl: variation of transmission with PMC mean pressure.

$\sim$ 7% for the quantity, D, indicating a much larger sensitivity of D to mean pressure than to compression ratio. For this reason the mean pressure must be known accurately. The physical mean pressure is deduced precisely from the PMC frequency measurement, but since this does not necessarily represent accurately the effective mean pressure "seen by the electronics" an uncertainty is introduced which contributes to the absolute error in the retrieved mixing ratio profile.

A further complication to calculations is temperature variation in the PMC caused by the pressure cycling. This problem is considered in detail elsewhere (see Schofield J.T.). It can be shown that the temperature cycling will be considerably less than that produced by an adiabatic compression if the time constant of thermal relaxation between the gas and the PMC is much less than the period of oscillation. For the HCl PMR, order of magnitude calculations give a thermal relaxation time constant $\sim$ 0.2 ms compared to an oscillation period $\sim$ 50 ms. Using these values and a compression ratio of 1.96, it can be shown that the expected temperature cycling is less than 3 deg. K in amplitude. The line-by-line model was used to calculate the effect on the PMR transmission of this size of temperature variation (in phase with the pressure cycling), and a value of D $\sim$ 1% was found. The effect will in practice be lower than this since the temperature variation is

almost 90° out of phase with the pressure variation As the effect is small and difficult to calculate precisely, it has been omitted from the retrieval calculations.

6.7 Motional chopping

Any mechanical vibration of an optical component at PMC frequency which leads to a modulation of energy at the detector will produce a sideband signal. It will be spurious in the sense that it is not related to absorption in the PMC and will not be decreased by an atmospheric path which absorbs strongly in the regions of spectral lines. Also, since the energy modulation at PMC frequency for an HCl PMR is such a small fraction of the total wideband energy, a spurious signal of magnitude comparable with the real sideband signal can originate from motional chopping of very low amplitude. It is therefore necessary to perform tests on the PMR to check for motional chopping. If it is present, efforts must be made to minimize it, since it affects the interpretation of signals.

During the transmission measurements the level of motional chopping was checked by filling the 10 cm cell with pure HCl to pressures ~ 100 mb. This absorbs almost all radiation in the regions of HCl spectral lines and in the absence of motional chopping will cut the sideband signal to the level obtained with no incident energy. This procedure

confirmed that the level of motional chopping during the transmission measurements was less than the noise level. A similar technique was used to test the flight instrument; it is discussed further in section 6.9.

6.8 PMC contamination

HCl is a reactive species and tends to attack its container, thus decreasing the amount of HCl present and producing other gaseous species. Although the materials in the PMC are chosen to minimize these effects, a slow change in the composition of the PMC contents does take place. An analysis of the gases present in the PMC 6 months after flight was performed at the Rutherford Laboratory. It showed the contents to be approximately 44.5% acetone or similar molecules, 3.6% CO_2, 2.5% O_2, 19.5% N_2 and CO, 0.4% Ar and 29.4% H_2. No Cl_2, HCl or gaseous chlorides were found. This indicates that during the long period in question the HCl attacked some part of the structure, probably organic compounds in the glue holding the PMC windows, and also that the PMC leaked slightly.

In general such contamination causes a decrease in signal from HCl pressure modulation and a possible increase in spurious signal due to other

molecules with absorption bands in the same spectral region. Like signal due to motional chopping, spurious signal caused by contamination is not removed by inserting a strongly absorbing path of HCl in the optical beam. The problem was minimized by evacuating the PMC and refilling it with pure HCl several times in the weeks preceding the flight and for the last time within 48 hours of flight. The tests performed before and after flight, which are described below, also provide evidence that the destruction of HCl in the PMC is sufficiently slow for it not to affect significantly the instrument's performance during flight.

6.9 Pre- and post-flight testing

In February, 1976, the HCl PMR was transported to NOAA, Washington D.C., where it was assembled and aligned inside the PMR housing. Several performance checks were made using a quartz-iodine lamp as an energy source and NOAA's bench testing system to record the data.

In order to measure spurious signal, a cell 3 cm long containing ~ 400 mb of pure HCl was inserted in the optical beam. The measured ratio of sideband to wideband signal expressed as a fraction of the ratio with no absorbing cell present

gives a measure of the spurious signal. In the pre-flight test this was found to be 5 ± 3% of the full signal, and it is concluded that this is the level of the spurious signal from both motional chopping and contamination soon after refilling the modulator. Spurious signal acts as an offset on the zero level of the real signal. However, since the amount of HCl in the atmospheric path is related to absorption - the difference between the signal and its full scale value - this level of spurious signal causes only a small error in the absolute value of the retrieved HCl amount.

8 days after flight further tests were performed without refilling the PMC. It was found that the ratio of the sideband to wideband signal had not measurably decreased. This confirms that the rate of destruction in the PMC is sufficiently slow for the effect of this process on the flight data to be neglected. Also the level of spurious signal was found to be 9 ± 3%. If the increase in spurious signal is real and is due to absorption by another constituent, then the rate of production of that species is sufficiently slow for its effect on the flight data to be neglected. Alternatively the difference between the pre- and post-flight tests may simply be due to the large errors in the measurements caused by the low signal-to-noise ratio obtainable in the sideband channel.

These tests show that spurious signals, whatever their sources, are sufficiently small for them to be neglected in the retrieval. Their presence will lead to a small error in the absolute value of the retrieved HCl mixing ratio but will not affect the shape of the profile.

A peculiarity in the PMC behaviour was noted when the temperature of the instrument was varied during testing. An increase in temperature caused a rise in pressure much greater than the change calculated from the gas laws. This indicates that HCl is adsorbed on to a material inside the PMC and that a temperature increase causes out-gassing.

The PMRs, spectrometer and sun-seeker tower were assembled and aligned at Denver University. The whole assembly was then tested viewing the sun at noon. Making corrections for the change of scatter plate reflectivity with angle and the estimated attenuation of radiation due to the atmosphere between ground level and the sun, the expected levels of signals during flight were calculated. The gain resistors in the signal channel were then selected accordingly so that the output voltage ramps obtained during flight utilized the dynamic range of the data system.

CHAPTER 7. RESULTS.

7.1 The flight

The instruments were assembled on the gondola at Denver University and transported to the launch site - Holloman USAF base, New Mexico ($32^{o}52'N$, $106^{o}07'W$). The final checks on the instruments and the data system were then performed. The scientific pay-load consisted of the following instruments:

i) the HCl PMR,

ii) a 15 micrometre CO_2 PMR and a 12 micrometre window channel measuring atmospheric absorption of solar radiation (see chapter 5),

iii) a scanning infra-red spectrometer, built by Denver University, also measuring atmospheric absorption of solar radiation,

iv) A downward scanning polarimeter with visible and infra-red channels, built by NOAA,

v) an ozone-sonde.

The package was launched on 17th March, 1976, at 1030 local time (Mountain Standard Time) and was raised over a period of about 3 hours to a float altitude of around 36 km by a helium-filled balloon of volume 11.6 million cubic feet. The ascent was timed to span local noon so as to achieve optimum results for the CO_2 PMR. Having reached its float altitude, the balloon maintained its height until after sunset in order to

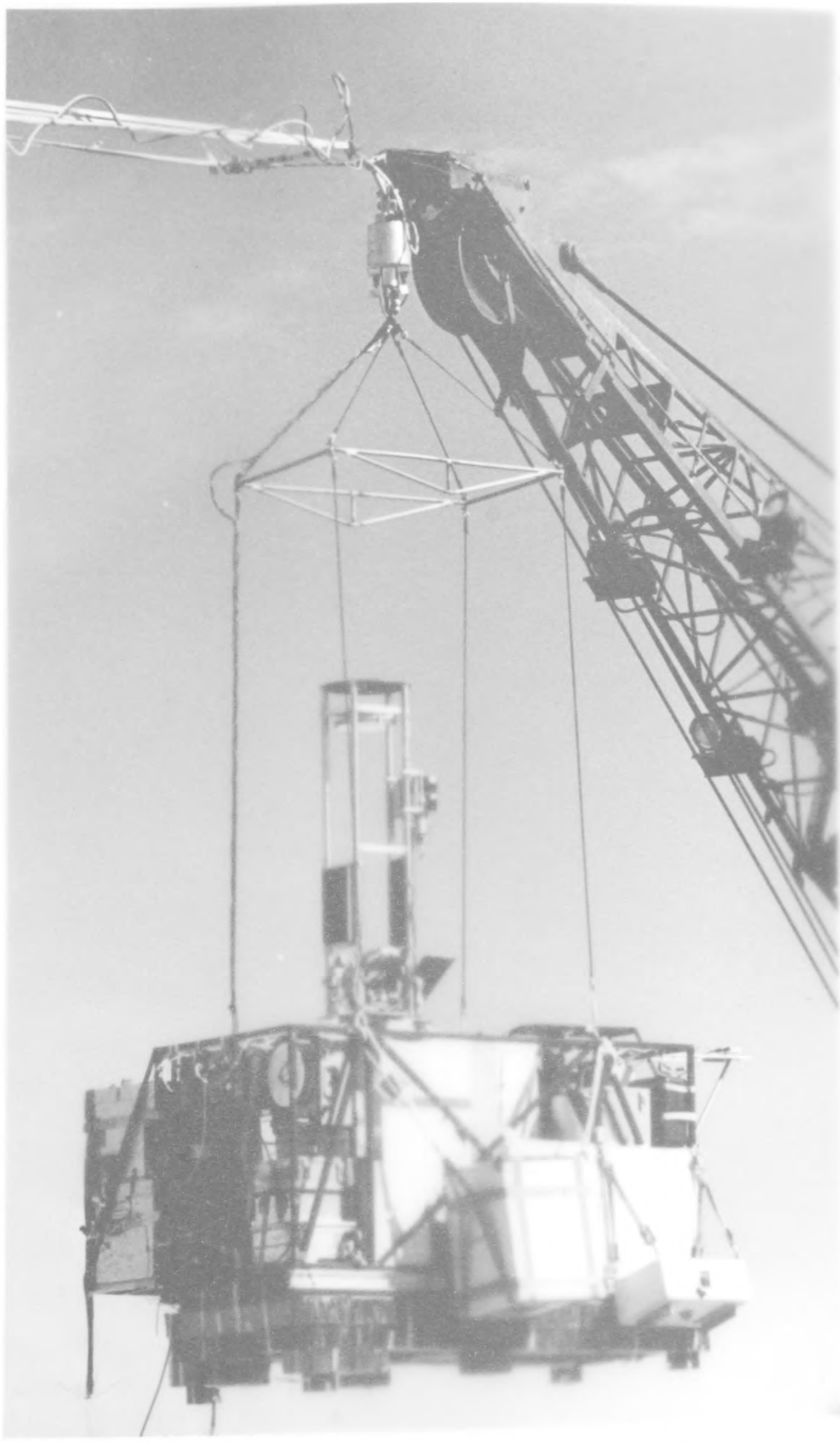

Plate 2. The instruments assembled on the gondola.

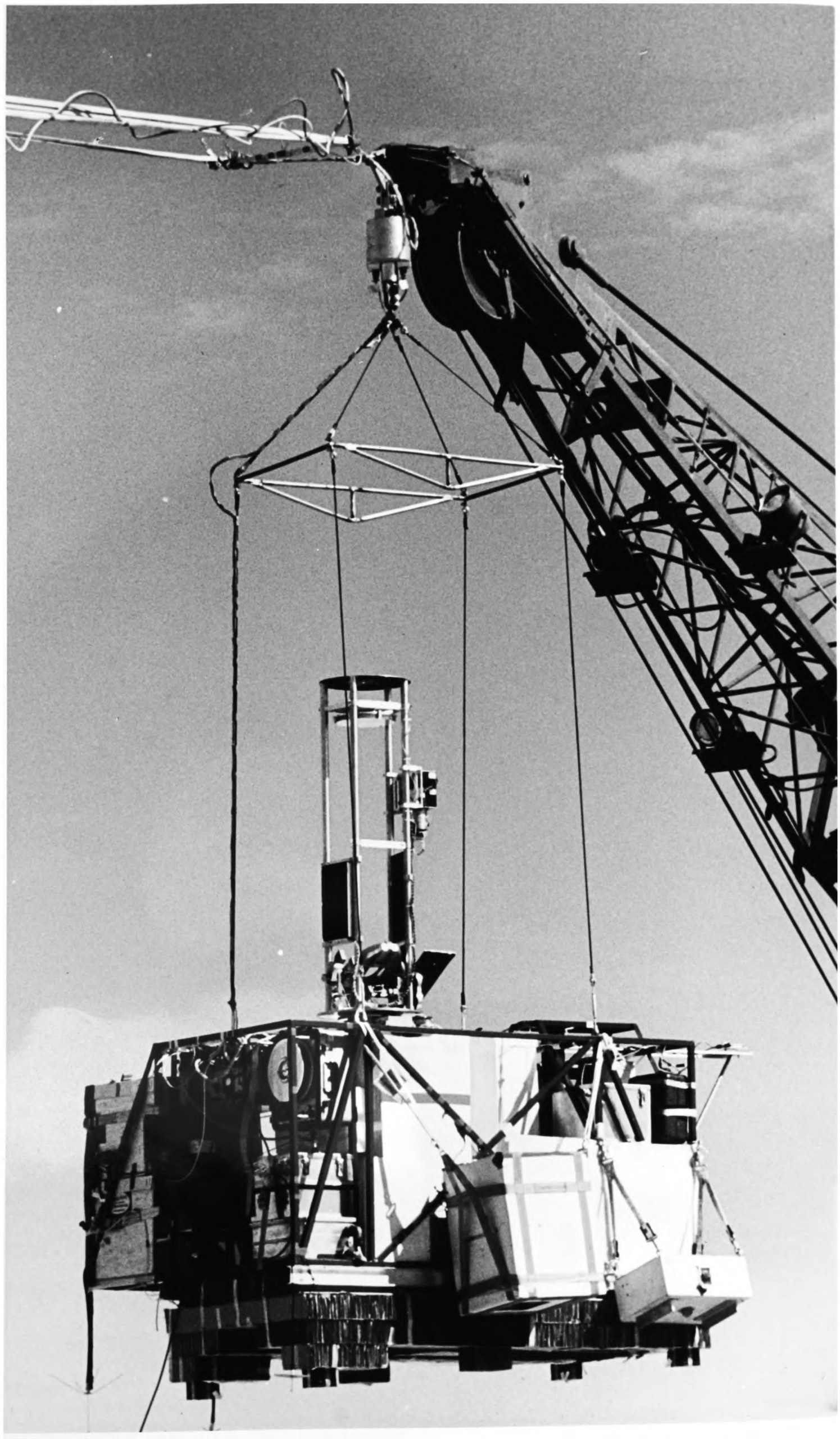

obtain useful data for the HCl PMR. The payload was then detached from the balloon. It returned to the ground by parachute and was recovered undamaged about 200 km from the launch site. The balloon was tracked by radar from the launch site and a map of the flight path produced. This is shown on figure 7.1.

7.2 The raw data

The data system contained 8 channels of which 3 were used to record PMR data. Each channel produced a data frame containing 50 slots repeated every 2 seconds. Most of the PMR housekeeping data, including temperature information, instrument status and clock data, were recorded in channel 4. The HCl PMR sideband ramp was sampled 6 times during each 1 second integration period at intervals of 160 ms along the ramp. This information was stored in channel 6. The wideband ramp was sampled in a similar way but only 4 times per ramp, and its value stored in channel 8.

The incoming solar radiation was shared between the PMRs and the spectrometer by means of the "flip mirror" which switched the beam from one instrument to the other approximately every two minutes. Each two minute sequence, referred to as a "scan", was divided into 4 blocks, the beginning of each coinciding with the switching in or out of the wedge which caused the instrument to "look" away from the sun. Thus the viewing sequence for the PMRs was as follows:

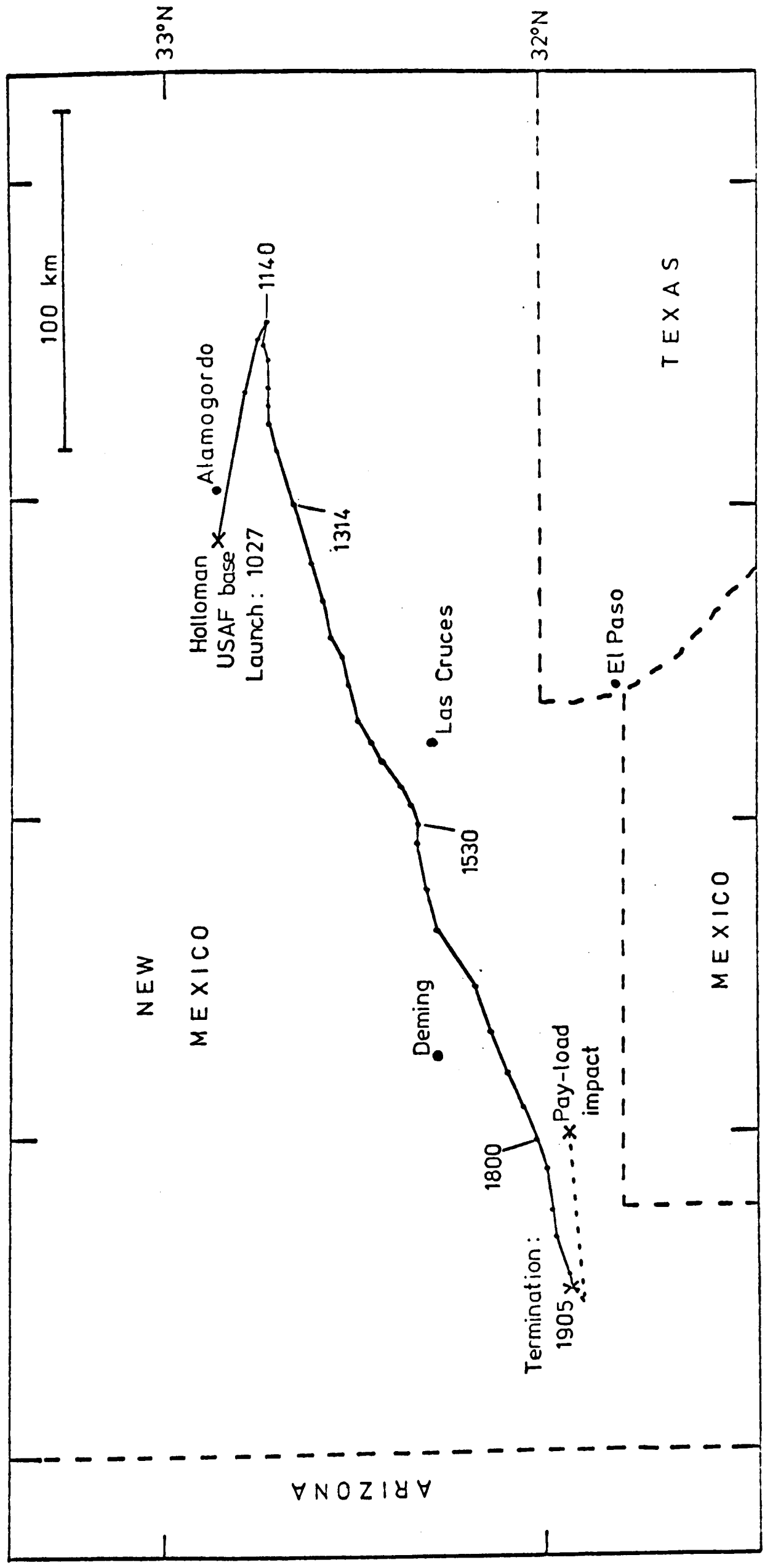

Times are given in Mountain Standard Time on 17th March, 1976.

Figure 7.1 The balloon flight path.

Block	View	Length(s)	No. of complete data frames
1	Sun	32	16
2	Away from sun	32	16
3	Sun	32	16
4	Away from sun	~ 24	~ 12
5		32	16
6	Instrument black body	32	16
7		32	16
8		~ 24	~ 12

It was intended that this sequence should be repeated continuously throughout flight. On analysing the data, however, it was found that the "flip mirror" had often failed to move at the end of a scan, and this had led to an irregular sharing of the sun views between the Oxford and Denver instruments. Instead of alternate scans of sun view and instrument black body view, sequences of up to 3 successive views in one state were found. The cause of the fault was not isolated, but it proved unimportant since the sun view blocks were easily recognizable and overall they were shared equally between Oxford and Denver.

Initially the analysis was hampered by the state of the data tape. A tape deck fault had caused false characters to be written to the tape, and these had to be recognized and removed before the analysis could proceed. This task was performed by Dr. B. Barwell at the Meteorological Office. He included in the routine

to "clean up" the data some initial quality checks and also calculated the block mean values of those housekeeping data slots for which slow variations with time were expected. Thus the raw data was not only cleaned but compressed into 400 word blocks, each of which corresponded to a block of the original data. It was recorded on a magnetic tape suitable for reading on the 1906A computer at Oxford. The tape contains the data for about the last 6 hours of the flight - 1330 to 1930 local time - and the format of each block is given in table 7.1. The analyses of the signals and certain elements of the housekeeping data are discussed in other sections of this chapter.

7.3 Housekeeping data

The temperatures of many components in the instrument were monitored, as were the frequencies and amplitudes of the PMC piston oscillations and certain reference voltages. They were stored in words 194-359 and 376-391 of the formatted data block. It is shown in chapter 6.1 that thermal emission from the optics can be ignored when interpreting the signals, and so a detailed analysis of the variation of instrument temperatures was not required.

The block averages of those elements of the housekeeping data for which analysis was needed were plotted against time for the last six hours of the flight. The constancy of the gain of the data system was investigated by studying the difference between the Denver 5V reference slot and the ground slots. It was found to be constant

Table 7.1 Format of compressed data tape

Word number	
0	Length of block = 400
1	Scan number
2	Running block count
3	Block number in scan (0, 1, 2 or 3)
4	Error flags
5	Number of 6-bit bytes in original scan
6	Number of 6-bit bytes in cleaned scan
7	Number of complete 2 second frames in scan
8-21	Counter increments for ramps
22-49	PMR signal output ramps: CO_2 direct PMR signal
50-77	PMR signal output ramps: CO_2 wideband
78-105	PMR signal output ramps: CO_2 sideband
106-133	PMR signal output ramps: HCl wideband
134-161	PMR signal output ramps: HCl sideband
162-189	PMR signal output ramps: Window channel
190	Counter increments from last frame in previous scan to first frame in this scan
191	Counter increments since clock reset
192	Mean of channel 4, slot 1
193	Time flag monitor
194-263	Housekeeping data: means x 16 and variances x 256
264-279	AFCRL pressure, channel 4
280-311	AFCRL pressure, channel 6
312-343	AFRCL pressure, channel 8
344-359	NOAA pressure
360-375	Ozone-sonde reading
376-391	Instrument black body temperature
392-399	Status word analysis

over this period to ~ 2 counts in 4000.

The PMC drive circuit design is such that the amplitude of the piston oscillation should be constant. The amplitude was monitored and its constancy confirmed to within 10 counts in 3000 over the 6 hour period. The PMC head temperature increased from 34.6°C to 36.9°C over this period. However, since the useful HCl data was confined to sunset, only the period from 1800 to 1900 need be considered when deriving the parameters to be used in the retrieval. Over this period the PMC temperature varied by only about 0.4 degrees, and a mean value of 36.7°C was used for the retrieval. The PMC pressure was deduced from the output of the frequency to voltage convertor. Over the sunset period the mean value was 2.42 V, and the calibration curves for the PMC showed that this represented a pressure of 2.01 torr (0.00264 atmospheres).

Several slots in channel 4 were affected by a fault in the NOAA multiplexer which caused them to float with respect to the data system ground level for a large part of the flight. Since this affected the ground slot in channel 4, which floated down outside the range of the data system, these slots could not be interpreted with certainty. The affected slots included the HCl PMR detector temperature, the thermistor reference voltage, the AFCRL pressure gauge in channel 4 and the NOAA pressure gauge. However, there were some short periods of the flight during which these slots were correctly grounded with respect to the rest of the data system, and two such intervals occurred during the sunset period. Using this

data the detector temperature was deduced to have been constant at 38.2°C to within 0.1°C, thus confirming that the detector responsivity was constant throughout flight. Also the thermistor reference voltage was shown to have been constant at the expected value, which enabled the voltage to temperature conversion for the thermistor circuit outputs to be performed with certainty. The way in which the pressure gauge output voltages were analysed to find the instrument altitude is discussed in section 7.6.

7.4 Variation of solar zenith angle with time

In order to determine the angle of view corresponding to each PMR signal, the relationship between the solar zenith angle at the instrument and the time measured by the data system clock must be known. Figure 7.2 shows how the solar zenith angle is calculated. Using this geometry it can easily be shown that the solar zenith angle, θ_z, is given by

$$\cos\theta_z = \sin\theta \sin\theta_s + \cos\theta \cos\theta_s \cos(\phi - \phi_s), \qquad (7.1)$$

where the symbols used are as defined in the diagram.

The latitude and longitude of the instrument, θ and ϕ respectively, were obtained as a function of time from the flight path data. Linear interpolation was used between the points for which the time was recorded.

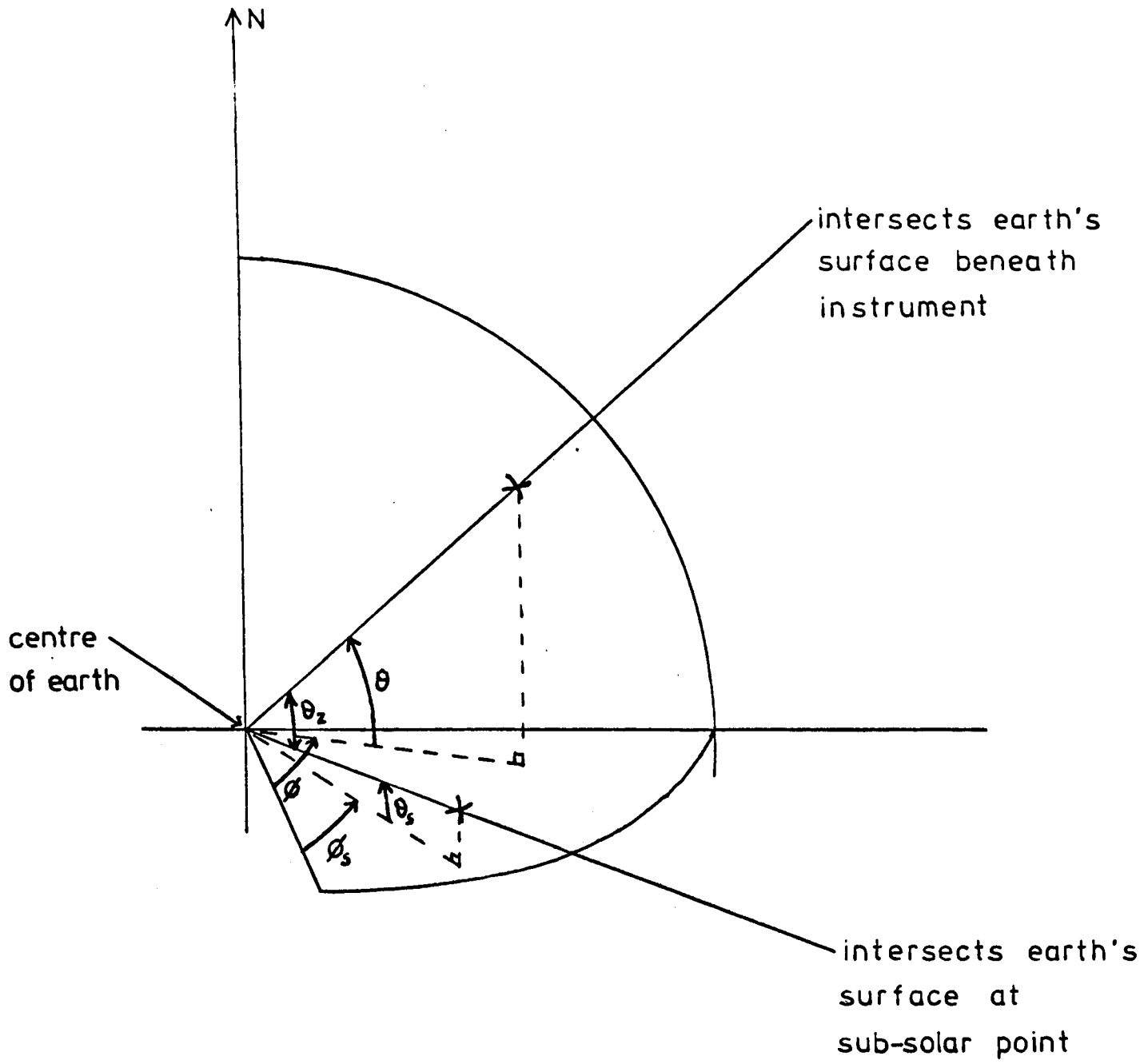

θ_s, ϕ_s are latitude and longitude of sub-solar point.

θ, ϕ are latitude and longitude of instrument.

θ_z is the solar zenith angle at the instrument.

Figure 7.2 Illustrating the calculation of solar zenith angle.

The latitude of the sub-solar point is called the solar declination, and it is obtained by linear interpolation between the solar declinations for the days in question which are tabulated in the Astronomical Ephemeris. The longitude of the sub-solar point is obtained by interpolation from the equation,

$$\phi_s = \frac{360\ (t - t_1)}{(24 + t_2 - t_1)}\ , \qquad (7.2)$$

where t_1 and t_2 are the ephemeris transits in hours (Ephemeris Time) preceding and following the observation,

t is the time of the observation in hours (Ephemeris Time),

and ϕ_s is in degrees west of the Greenwich meridian.

The ephemeris transits are also tabulated in the Astronomical Ephemeris. The flight took place on March 17th, 1976, and so the data used from the Astonomical Ephemeris (1976) was as follows:

Date (1976)	Declination in degrees (at time 0000 ET)	Ephemeris transit (in hours ET)
March 17th	-1.38061	12.13880
March 18th	-0.98542	12.13393

The difference of 7 hours between Universal Time and Mountain Standard Time (MST) was taken into account, as was the small difference of -0.01304 hours between Universal Time and Ephemeris Time.

The equations and corrections given above were incorporated in a computer program which calculated the solar zenith angle at the instrument from the flight data of time against latitude and longitude. The results are given in table 7.2. It can be seen that the HCl PMR signals of most interest, for which the sun was visible at zenith angle greater than 90^{o}, were recorded between 1815 and 1900 MST. The program was also used to calculate the solar zenith angle at intervals of 0.01 hours around sunset, the results of which are shown in figure 7.3. Interpolation between points calculated at these intervals gives a satisfactory accuracy. In fact for a given time the major contribution to the error in the zenith angle is the accuracy to which the longitude is known ($\sim \pm$ 0.01 degrees).

The calculation described above neglects the correction to the zenith angle to account for the small angle subtended by the earth's radius at the sun. However this introduces an error of less than 0.003 degrees in the calculated zenith angle.

From the data available the solar zenith angle can be calculated to an accuracy of about $\pm$ 0.01 degrees for a given time. This represents an error of up to 0.1 km in stratospheric tangent height and is equivalent to a miscalculation of the time of the corresponding observation of about 30 seconds. Consequently an effort was made to find the time of each observation to a comparable or higher accuracy. Each 2 second frame of data contained the number of counter

Table 7.2 Variation of solar zenith angle during flight

Time in MST	Latitude in ^{o}N	Longitude in ^{o}W	Solar zenith angle in degrees
1027	32.862	106.12	42.127
1110	32.795	105.66	36.796
1123	32.755	105.49	35.622
1140	32.730	105.43	34.535
1150	32.742	105.51	34.151
1206	32.725	105.55	33.807
1222	32.730	105.64	33.895
1231	32.733	105.70	34.120
1240	32.728	105.76	34.459
1252	32.710	105.84	35.086
1314	32.660	106.01	36.721
1336	32.610	106.20	38.938
1346	32.585	106.31	40.100
1400	32.570	106.43	41.905
1406	32.536	106.49	42.704
1415	32.517	106.58	43.977
1425	32.490	106.69	45.449
1435	32.455	106.76	46.994
1445	32.425	106.82	48.617
1500	32.375	106.90	51.147
1515	32.340	106.96	53.802
1530	32.332	107.01	56.561
1540	32.340	107.07	58.430
1600	32.305	107.22	62.192
1615	32.275	107.35	65.062
1700	32.180	107.53	74.075
1715	32.140	107.67	77.070
1730	32.090	107.80	80.094
1745	32.050	107.91	83.152
1800	32.010	108.01	86.232
1815	31.990	108.11	89.322
1830	31.974	108.24	92.391
1845	31.965	108.33	95.493
1900	31.927	108.44	98.577

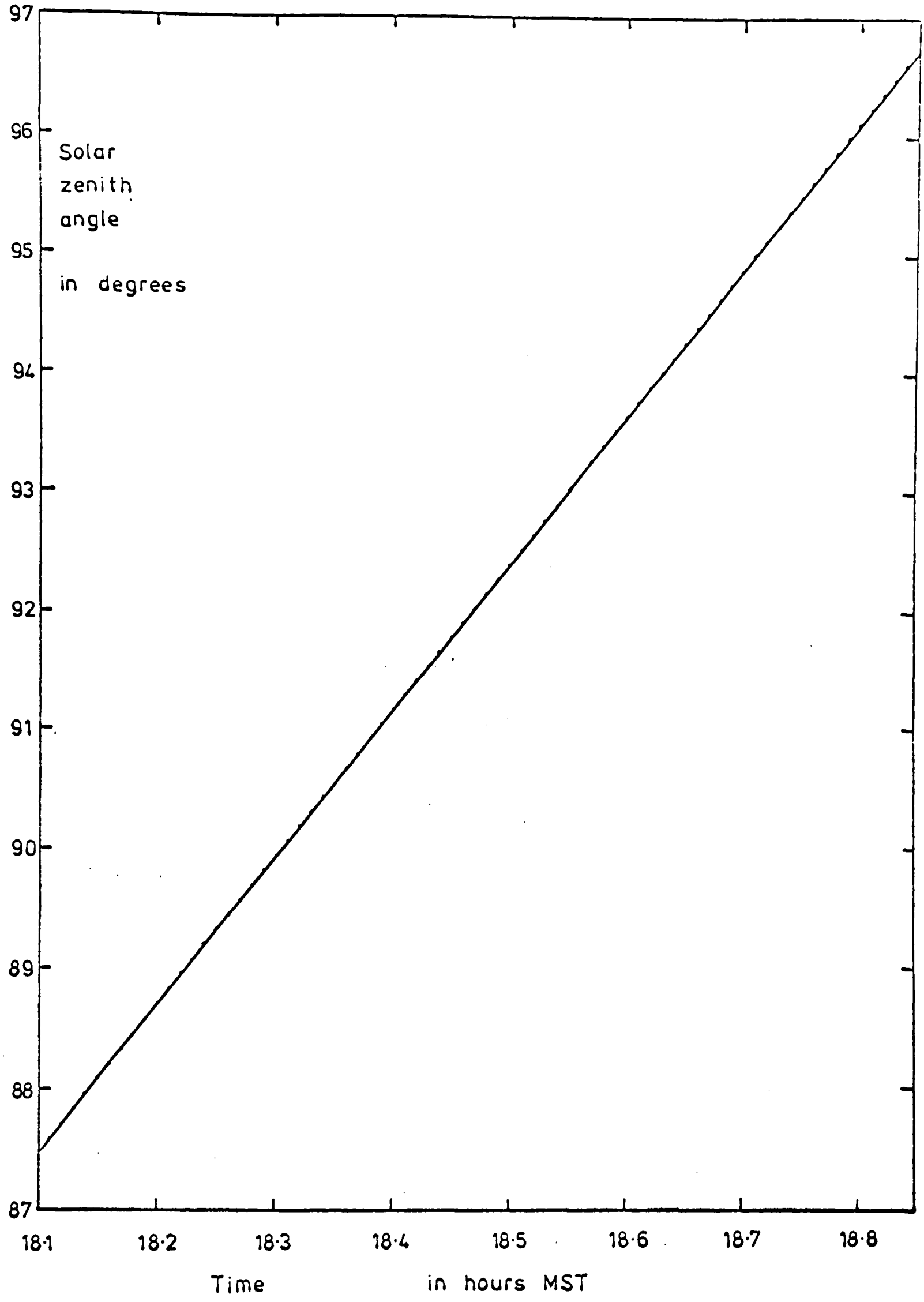

Figure 7.3 Zenith angle v. time around sunset.

increments since the clock was reset. The numbers of counts between successive frames and successive blocks were checked and found to be consistent with the expected behaviour of the timing systems. The instrument clock was reset at precisely 0930 MST and a time flag command sent at 1830 MST. The accuracy of the clock was checked by comparing the time between these events with the number of counts on the clock corresponding to this interval. The two periods were in agreement to better than one second. This indicates that the retrieved value of time for each observation is sufficiently accurate for it to contribute a negligible error to the retrieval of mixing ratio. Indeed, the accuracy is such that it would have been adequate even if the signal-to-noise ratio of the PMR signals had been much higher.

It should be noted that the apparent solar zenith angle at the instrument differs from the true zenith angle due to atmospheric refraction. This is accounted for directly in the retrieval by the program which calculates the absorber amount in a path of given tangent height. The program includes the effects of refraction and also evaluates the true solar zenith angle for that tangent height. It is outlined in appendix D.

7.5 Atmospheric temperature profile.

In order to calculate the balloon altitude from the atmospheric pressure measured at the instrument and

to evaluate accurately atmospheric transmissions, it is necessary to know the variation of atmospheric temperature with height in the troposphere and the stratosphere. The information required was obtained from the 1300 MST Holloman radio-sonde which reached an altitude of about 35 km. The profile obtained was compared with those retrieved from the 0700 MST and 1030 MST radio-sondes, which did not reach such high altitudes and were further from the sunset data in time. The differences in temperature measured by the three radio-sondes were negligible, which indicates that the atmospheric state above New Mexico on that day was changing very slowly and hence suggests that the 1300 MST radio-sonde data will reflect closely the temperature profile appropriate for the retrieval of balloon altitude and the calculation of atmospheric transmissions.

The temperature and pressure variations with height were calculated as follows:

i) Above the 100 mb level, the measured radio-sonde temperatures were corrected for radiation effects at both visible and infra-red wavelengths using the manufacturer's suggested correction formulae.

ii) The measured relative humidities were used to calculate the virtual temperature, T^*, from the real temperature, T, at each pressure level:

$$T^* = T\left(1 - m\epsilon\right)^{-1}, \qquad (7.3)$$

where m = $\frac{\text{molecular weight of water vapour}}{\text{molecular weight of dry air}}$

and ϵ = volume mixing ratio of water vapour.

iii) Assuming the atmosphere to be in hydrostatic equilibrium, the height difference between adjacent pressure levels was calculated using the hydrostatic equation and allowing for the variation of gravitational acceleration with height:

$$\Delta z = \ln\left(\frac{p_1}{p_2}\right) \frac{R\,\overline{T^*}}{m_d\, g_o} \left(\frac{r + \bar{z}}{r}\right)^2 , \qquad (7.4)$$

where p_1 and p_2 are the measured pressures,

$\overline{T^*}$ is the mean virtual temperature of the interval,

m_d is the molecular weight of dry air,

g_o is the gravitational acceleration at sea level for 32°N (taken as 9.8011 ms^{-2}),

r is the mean radius of the earth (taken as 6370 km),

and $\bar{z}$ is the mean altitude of the interval.

Thus the height of each pressure level above Holloman (altitude 1.258 km) was calculated.

iv) Above the range of the radio-sonde, the temperature profile was taken to be that measured by the 1700 MST White Sands rocket-sonde.

These data were smoothed to give a temperature profile of reasonable shape and the corresponding pressures calculated using the hydrostatic equation

and the highest pressure of the radio-sonde data. Between 25 and 35 km the radio- and rocket-sonde data overlapped and agreement between the two was good (within 2 degrees K).

The resulting variations of pressure and temperature with height are given in table 7.3, and the temperature profile is plotted in figure 7.4. This profile was used in the calculation of balloon altitude and atmospheric path parameters with appropriate interpolation between the given data points - linear for temperature and exponential for pressure.

7.6 Altitude

The atmospheric pressure at the instrument was measured by four gauges - a 0-2 p.s.i. Rosemont gauge owned and calibrated by NOAA and three Computer Instruments Corporation potentiometer-type sensors (0-0.3 p.s.i., 0-2 p.s.i. and 0-15 p.s.i.) owned and calibrated by the USAF Geophysics Laboratory (AFCRL). The AFCRL gauges were switched during ascent so that the appropriate gauge reading was recorded in channels 4, 6 and 8. An intercomparison of the gauges' outputs was performed at NOAA. It was concluded that the most accurate gauge for the float altitude was the AFCRL 0-0.3 p.s.i. gauge. The relevant slot in channel 4 was affected by the multiplexer fault, and

Table 7.3 Temperature-pressure profile

Altitude in km	Temperature in K	Pressure in atmos.
1.258	294.7	0.8657
2.281	282.9	0.7671
7.466	250.4	0.3948
10.736	222.7	0.2469
12.157	210.2	0.1975
13.089	202.6	0.1694
13.892	203.4	0.1484
14.250	203.6	0.1395
14.885	210.0	0.1256
15.235	211.0	0.1187
16.237	205.2	0.0987
18.540	208.7	0.0691
20.632	213.5	0.0494
23.871	216.7	0.0296
26.486	220.5	0.0197
31.091	227.0	0.0099
33.516	232.8	0.0069
35.590	238.6	0.0051
36.0	239.0	0.00481
37.0	241.0	0.00418
38.0	243.0	0.00364
39.0	246.0	0.00317
40.0	248.0	0.00276
45.0	260.0	0.00142
50.0	264.0	0.00075
55.0	257.0	0.00039
60.0	246.0	0.00020
65.0	235.0	0.00010

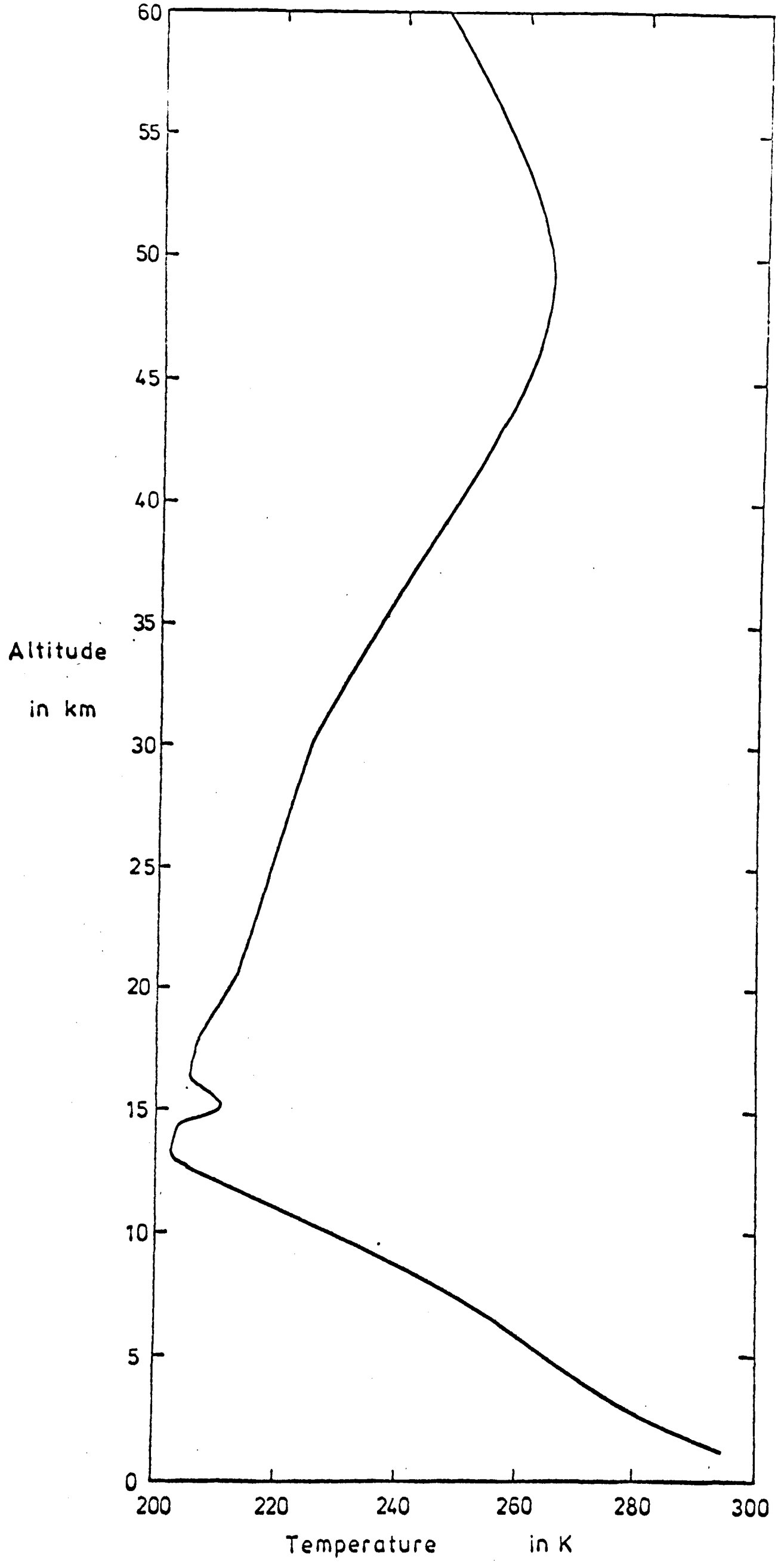

Figure 7.4 Atmospheric temperature profile.

so the values recorded in channels 6 and 8 were used for the altitude calculation.

The output voltage of the gauge during the sunset period (1818 to 1845 MST) was 1.25 V. Using the calibration data for this gauge provided by NOAA, an atmospheric pressure at the instrument of 5.21 mb was calculated. The pressure versus height profile given in table 7.3 was used to derive the corresponding balloon height of 35.54 km. The total error in this value was calculated to be ± 0.45 km. It includes contributions from the variation of pressure gauge output over the sunset period, the calibration accuracy of the gauge and the limited resolution of the recorded radio-sonde pressures at high altitude.

7.7 PMR signals

The sideband and wideband signals were first investigated by plotting out their values against time for the period 1700 to 1900 MST. This included the sunset period - those times during which the sun was visible at the instrument at zenith angles greater than 90^{o} - which lasted from 1818 until about 1845. The signals obtained during this period are plotted in figure 7.5, which clearly shows the signals decreasing as the mass of all the absorbing gases in the path increases with time. It can also be seen that the signal zero levels are constant and that views away from the sun

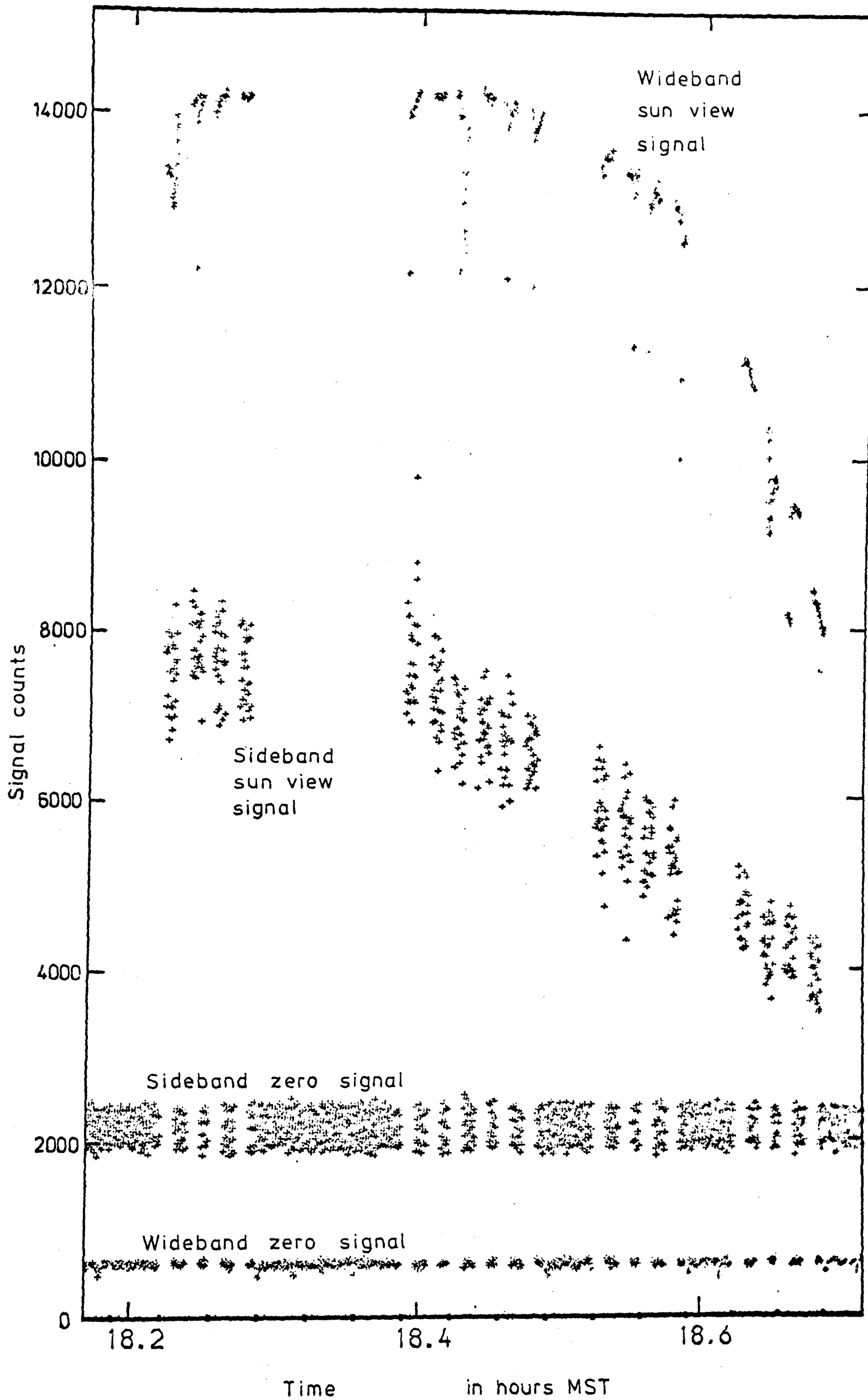

Figure 7.5 Signals during sunset period.

cannot be distinguished from internal black body views, thus confirming that signals from radiation sources other than the sun can be ignored. The sun view signals occur in groups, each of which represents a 32 s block of data. The irregular block pattern was caused by the fault in the "flip mirror" discussed in section 7.2. The signals plotted in figure 7.5 are expressed in terms of counts per 160 ms ramp interval x 16; this is the form in which they were written to the formatted tape. The sun view signals for the pre-sunset period (1700 to 1818 MST) showed, as expected, a slow increase with time corresponding to an increase in scatter plate reflectivity with changing solar zenith angle.

The signals for the first 4 seconds of each block were discounted as they suffered from transient effects associated with the change in field of view. They were not included on the formatted tape and so have been omitted from figure 7.5. However, an inspection of the wideband signals showed other periods of rapidly changing signal, probably corresponding to occasions on which the sun-seeker was not tracking the sun correctly. This output also contains the effects of transient signals and is unreliable. Therefore the relevant periods of data were identified and the wideband and sideband signals discounted during each period of rapidly changing wideband signal and for 4 seconds following it. Using the remaining data the mean values of wideband

and sideband signals for each block were calculated. These are plotted against the mean time for the block in figure 7.6. The mean values for the zero signals were found to be constant over the whole period to within ± 20 counts. Their levels are shown in the diagram.

7.8 Calibration of signals

Since the wideband signal is not a constant, the sideband signal cannot be used directly in the retrieval of HCl amounts, but the ratio of sideband to wideband must be used (see chapter 6.2). The required quantity was calculated from the block mean values of the signals less the corresponding zero signals, which represent the integrator offsets:

$$\frac{\text{Sideband signal}}{\text{Wideband signal}} = \frac{SB}{WB} = \frac{\text{Sideband counts} - 2150}{\text{Wideband counts} - 582}. \quad (7.5)$$

The block mean values of (SB/WB) x 25000 thus calculated are shown in figure 7.7.

In order to express these signals as PMR transmissions (as defined by equation 4.31), it is necessary to know the full scale signal level - that value of (SB/WB) which corresponds to no HCl in the path between the instrument and the sun. This level was calculated using the data from 17.0 to 18.1

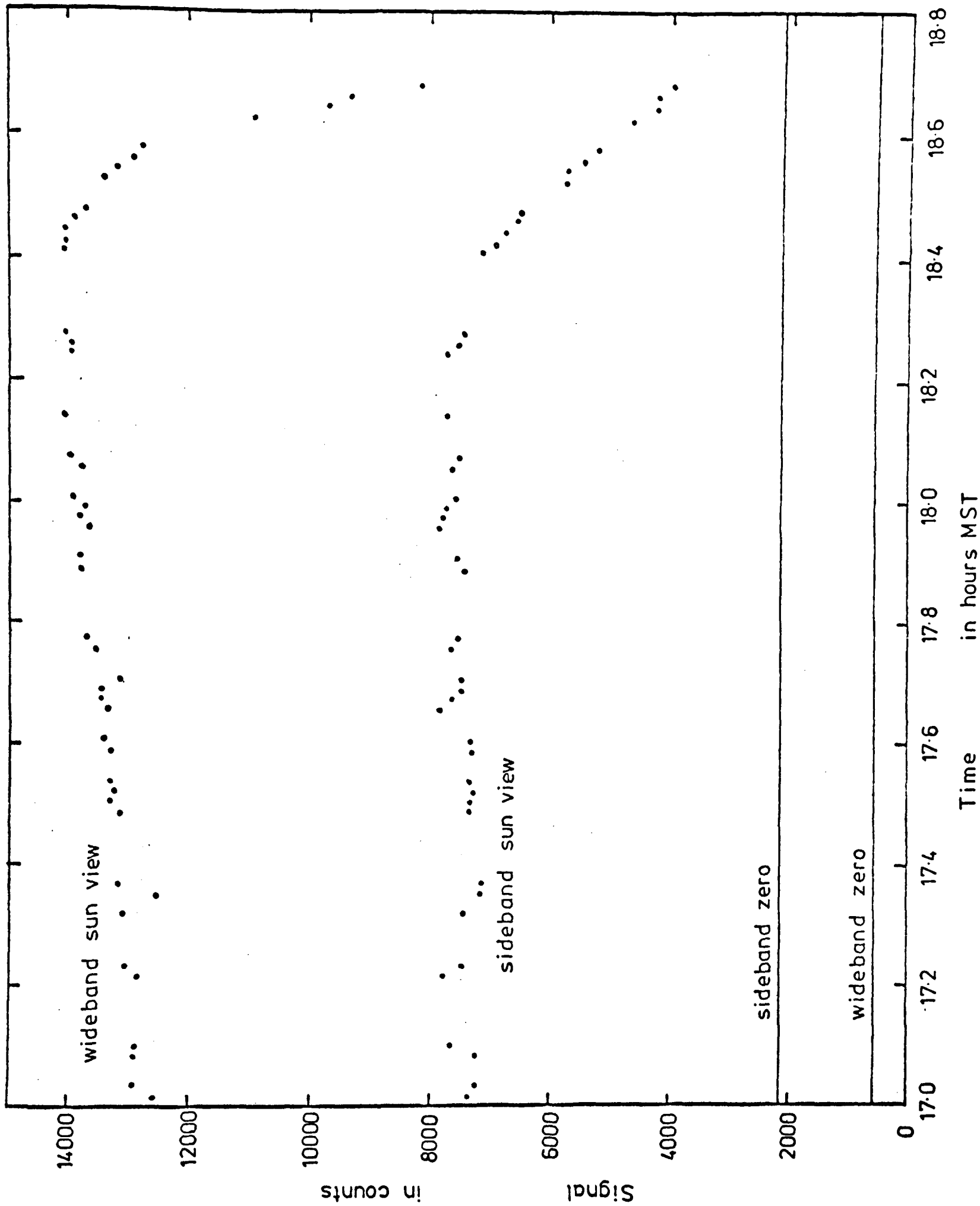

Figure 7.6

Wideband and sideband signals: block means.

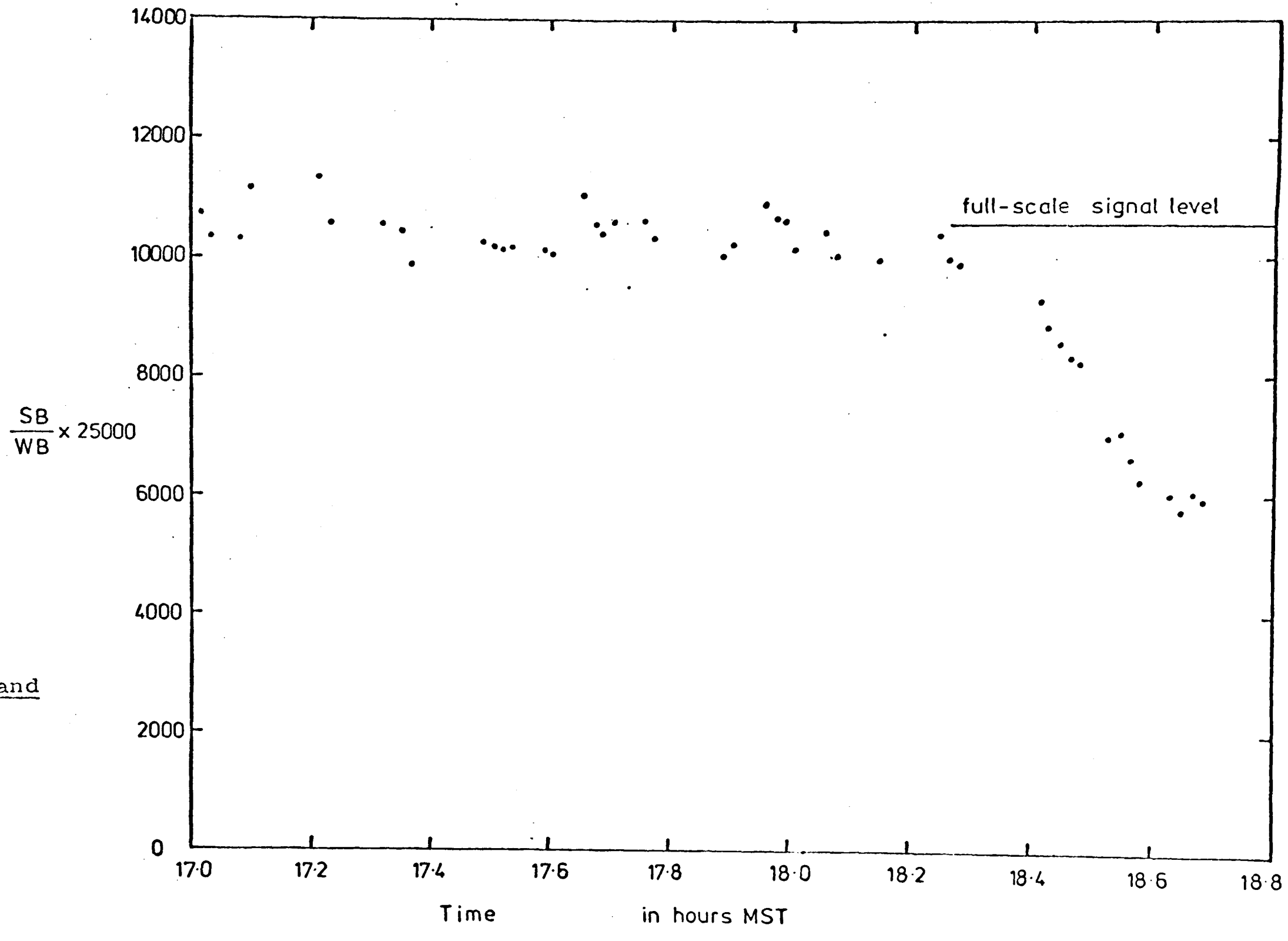

Figure 7.7

Block mean values of the ratio of sideband to wideband signals.

hours MST, corresponding to zenith angles between 74.1 and 87.5 degrees. At these angles the absorber amount in the path is sufficiently low for the signal to be very close to full scale. The mean value of the sun view signals for this period was 10452 counts with a standard error of 64 counts.

To allow for the small amount of HCl in the path for these sun views, a correction was made to the value given above. Using the line-by-line model and an estimated HCl volume mixing ratio above the balloon of 1.5×10^{-9}, calculations were made of the corresponding PMR transmissions for the period 17.0 to 18.1 hours, and from the results a correction of 139 counts was deduced. If the retrieved mixing ratio had shown that the value used here was inappropriate, an iterative retrieval procedure would have been applied, using a more accurate value for the correction in each successive retrieval. However, since the correction was small and the retrieval showed that the absorber amount used to calculate the correction was approximately equal to that retrieved, no further correction was necessary. Applying the computed correction, therefore, gave a full scale signal of 10590 $\pm$ 70 counts, and this level is also shown in figure 7.7. PMR transmissions were now calculated by expressing the (SB/WB) signals as fractions of the full scale value.

Another product of this analysis was the effective PMC compression ratio, calculated by the method outlined in chapter 6.6. Using the full scale

value of (SB/WB) and the gains of the appropriate stages of the electronics, the ratio of the amplitudes of the sideband and wideband signals at the detector was calculated to be 1.97×10^{-4}. The line-by-line model was used to show that the PMC compression ratio corresponding to this signal ratio was 1.96, and this value was used in the retrieval.

7.9 Effects of other atmospheric constituents

The retrieval method discussed so far has not considered the effects of other atmospheric constituents. It might be expected that to a first approximation the absorption lines of other species would be distributed randomly among the HCl lines, and so the wideband and sideband signals would be attenuated proportionately. Since only the ratio of sideband to wideband is used in the retrieval, it is therefore possible that the effects of other constituents may cancel out. This argument is expected to hold best when the absorption lines of one gas are truly randomly distributed amongst those of another and both absorption bands contain enough lines for statistics to be used with confidence. However, for the HCl band, only 32 lines lie in the region of significant optics transmission and of these the strongest 10 contribute more than half the band strength at PMC temperatures. It is therefore evident that statistical methods may be inappropriate

when applied to such a small number of lines.

In order to investigate this problem, two computer programs were written to calculate the effects on the wideband and sideband signals of an atmosphere containing other constituents but not HCl. It is shown in appendix G that the measured PMR transmission can be corrected approximately for the effects of other constituents using the equation,

$$\bar{\tau}_c = \bar{\tau}_m \times \frac{\bar{\tau}_{WB}}{\bar{\tau}_{SB}} , \qquad (7.6)$$

where $\bar{\tau}_m$ is the measured PMR transmission,

$\bar{\tau}_{WB}$ and $\bar{\tau}_{SB}$ are respectively the estimated wideband and PMR transmissions due to other constituents,

and $\bar{\tau}_c$ is the corrected PMR transmission, which will be comparable with values calculated by a line-by-line model which considers HCl as the only absorber.

The two programs calculate the values of $\bar{\tau}_{WB}$ and $\bar{\tau}_{SB}$ corresponding to different atmospheric paths. They use the spectral line data tabulated by McClatchey et al. (1973) for those gases which have absorption lines in the region of the HCl band. These gases are water vapour, carbon dioxide, ozone, dinitrogen oxide and methane, and of these methane is expected to have the greatest effect since some of the HCl lines lie in the wings of strongly absorbing methane lines.

The assumed mixing ratio profiles of the other

constituents are given in figure 7.8. Each atmospheric path considered is treated as a single homogeneous path defined by an absorber amount and an absorber-weighted mean pressure and temperature, using the approximate expressions for limb paths derived in appendix C.

The wideband model calculates the equivalent width of each line under the filter profile using the approximate formula for the equivalent width of a Voigt line given by Rodgers and Williams (1974). The equivalent width of all the lines in each 10 cm^{-1} interval is calculated and weighted by the optics profile and the black body function of the source. Thus the total wideband absorption due to other constituents is estimated and the value of $\overline{\tau}_{WB}$ obtained.

The sideband model considers all the lines of other species within 10 cm^{-1} of each HCl line centre, ν_o. It calculates the absorption of solar radiation at ν_o due to these lines. Since almost all the sideband energy modulation occurs very close to HCl line centres, the mean transmission of other absorbers across each HCl line can be estimated using these monochromatic values. The mean sideband transmission due to other absorbers, $\overline{\tau}_{SB}$, is then calculated by weighting the transmission at each line with the contribution to the signal by that line with no absorber in the path using the PMC parameters appropriate to flight conditions. Each line's

Key to figure 7.8

The volume mixing ratio profiles were taken from the following sources:

O_3 : Krueger and Minzner (1973).
U.S. standard atmosphere ozone model for mid-latitudes.

CH_4 : Ehhalt et al. (1974).

N_2O : Harries et al. (1974); Harries (1975); Ehhalt et al. (1974).
An average value is plotted.

H_2O : Harries (1976).

For CO_2 a constant volume mixing ratio of 3.3×10^{-4} was used.

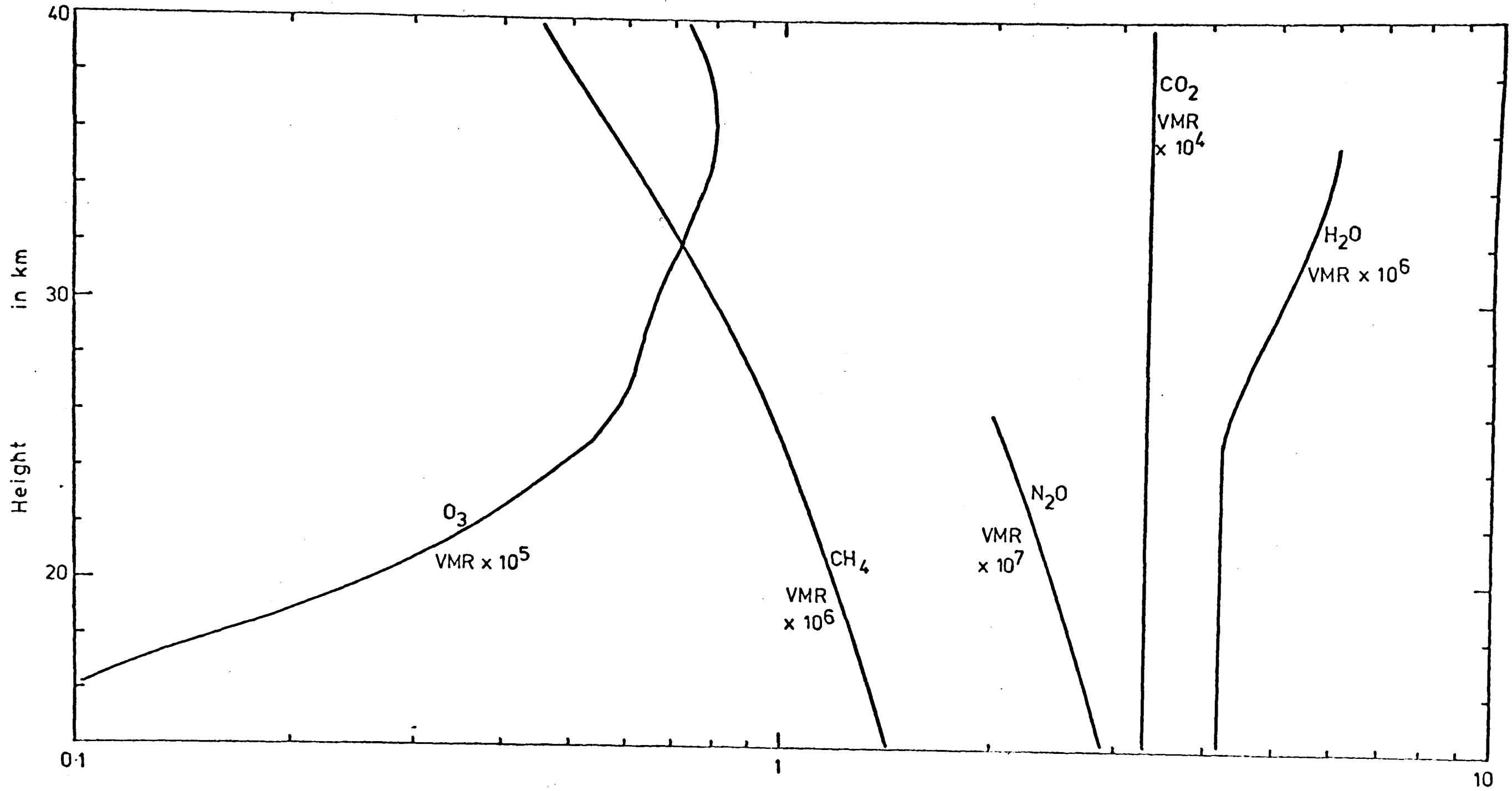

Figure 7.8 Assumed volume mixing ratio profiles of other atmospheric constituents.

contribution is also weighted with the optics transmission and source black body function.

These calculations were performed for a range of tangent heights from 15 km to the balloon altitude. The parameters used for these paths and the resulting values of $\overline{\tau}_{SB}$ and $\overline{\tau}_{WB}$ are given in table 7.4. Equation 7.6 shows that the correction factor to be applied to the measured PMR transmissions is the ratio, $(\overline{\tau}_{WB}/\overline{\tau}_{SB})$. This is plotted against time in figure 7.9. The time appropriate to each tangent height was calculated using the limb path model described in appendix D. This calculates at each tangent height the solar zenith angle, which can then be related to time using the method given in section 7.4.

The correction curve of $(\overline{\tau}_{WB}/\overline{\tau}_{SB})$ was used to adjust the measured data for the effects of all the other constituents. It can be seen from table 7.4 that the correction only has a significant effect for paths with tangent heights below about 26 km. The accuracy of this correction was investigated in several ways. Firstly, the contribution to the correction from each gas was calculated. It was found that CH_4 not only had the greatest effect on $\overline{\tau}_{WB}$ and $\overline{\tau}_{SB}$ but also was mainly responsible for their ratio deviating from unity. By comparison, H_2O and CO_2 were found to have a negligible effect on both sideband and wideband, and they could well have been omitted from the calculations.

The major source of error in this method of correction is probably that in $\overline{\tau}_{SB}$ caused by errors

Time in hours MST	Tangent height in km	Mean pressure in atm.	Mean temperature in K	Absorber amounts in path (atm.cm)					$\bar{\tau}_{WB}$	$\bar{\tau}_{SB}$	$\frac{\bar{\tau}_{WB}}{\bar{\tau}_{SB}}$
				H_2O	CO_2	O_3	N_2O	CH_4			
18.691	15	0.0872	210.3	26.1	2050	11.0	1.61	7.8	0.845	0.794	1.064
18.669	17	0.0620	210.9	18.8	1475	12.1	1.10	5.0	0.880	0.818	1.076
18.647	19	0.0454	214.3	13.6	1071	12.0	0.74	3.4	0.904	0.846	1.072
18.623	21	0.0330	217.0	9.9	776	11.3	0.51	2.3	0.925	0.878	1.054
18.600	23	0.0240	220.4	7.7	564	9.34	0.35	1.5	0.943	0.913	1.033
18.575	25	0.0176	223.0	6.0	410	7.62	0.25	1.0	0.956	0.941	1.016
18.547	27	0.0129	226.3	4.7	298	6.14	0.18	0.71	0.965	0.961	1.004
18.517	29	0.0096	228.0	3.7	215	4.69	0.13	0.45	0.974	0.976	0.998
18.482	31	0.0071	234.8	2.8	153	3.53	0.09	0.28	0.981	0.986	0.995
18.305	35.54	0.0036	242.3	0.8	46	1.03	0.03	0.067	0.993	0.997	0.996

Table 7.4 Effects of other constituents: calculations of $\bar{\tau}_{SB}$ and $\bar{\tau}_{WB}$ for a range of tangent heights.

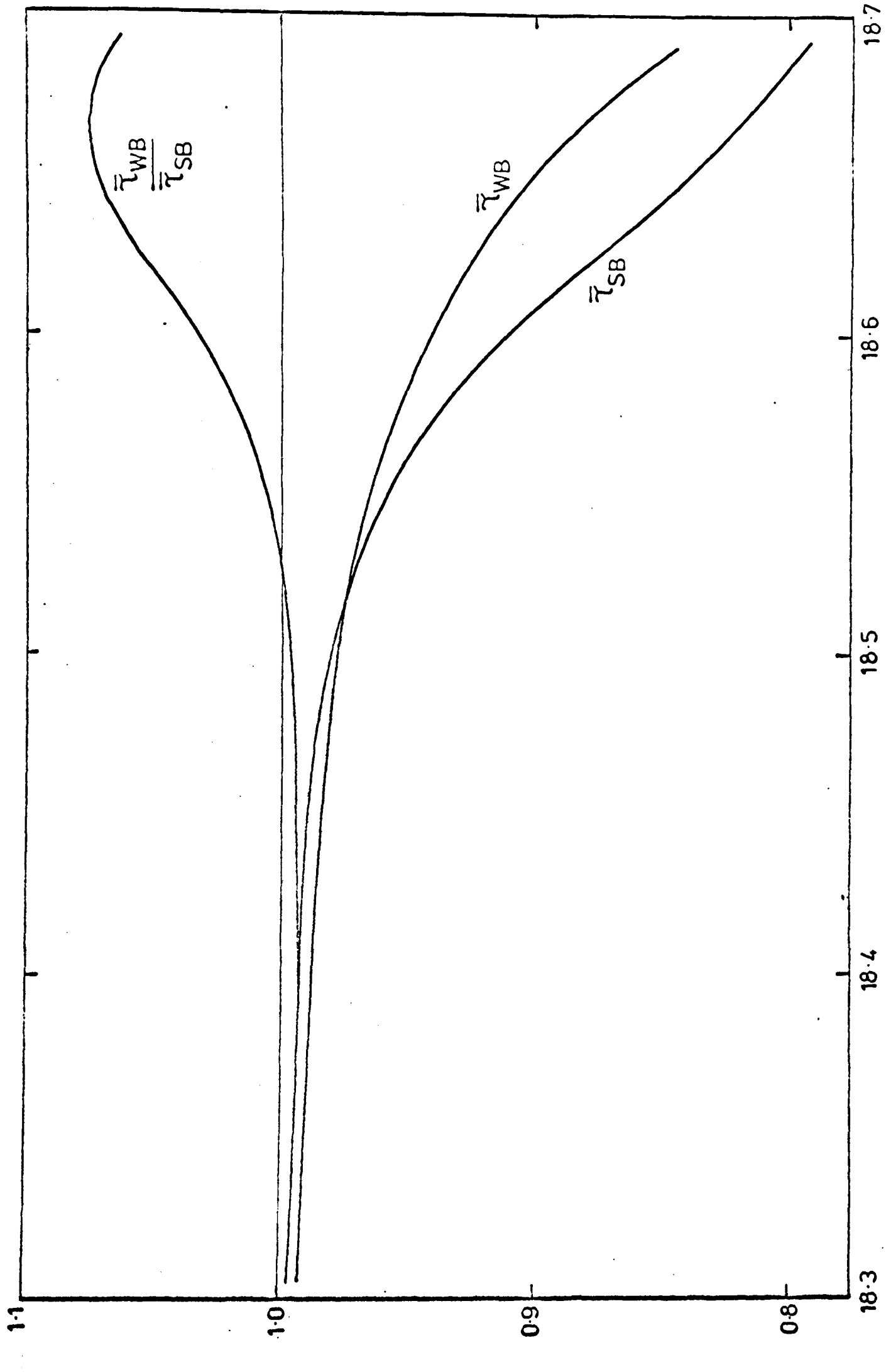

Figure 7.9 Correction curve for the effects of other atmospheric constituents.

in the wavenumbers of the tabulated line data relative to those of the HCl lines. The magnitude of this error was tested by shifting all the HCl lines relative to the other lines by values between $-0.02\ cm^{-1}$ and $+\ 0.02\ cm^{-1}$ - shifts considered to be comparable to the accuracy of the tabulated line positions. Thus the change in the signal from each HCl line due to an error in its relative position was calculated and the errors for all the lines combined statistically to find the standard error in the quantity, $\bar{\tau}_{SB}$. This calculation was performed for a worst case - a tangent height of 17 km for which the absorber amounts are large. The result of this analysis was that the error in ($\bar{\tau}_{WB} / \bar{\tau}_{SB}$) was estimated to be $\pm$ 0.051 for a tangent height of 17 km. The size of this error, however, is expected to fall with increasing tangent height as the absorber amount decreases.

Other possible sources of error lie in the assumed mixing ratio profiles, and so calculations were performed, again for 17 km tangent height, for estimated extremes of mixing ratios. Firstly, since the calculations are affected most by CH_4 , the mixing ratio of the species was doubled. Also, calculations were performed using estimated maximum and minimum values for all constituents applying the following changes to the profiles shown in figure 7.8 :

	H_2O	CO_2	O_3	N_2O	CH_4
Maximum	+ 50%	+ 2%	+ 20%	+ 50%	+ 100%
Minimum	- 50%	- 2%	- 20%	- 50%	- 50%

The results of these calculations showed that the errors produced by uncertainties in the mixing ratio profiles were small compared to those caused by inaccuracies in the relative line positions.

7.10 Reflectivity of the scatter plate

It has already been shown that the PMR signals vary due to the changing reflectivity of the scatter plate. The specular reflectance of the aluminized, ground glass surface is a function of wavenumber and angle of incidence, and so the optics profile given in figure 4.4 for the combination of all other optical components must be weighted by the variation with wavenumber of the scatter plate reflectivity at the appropriate angle of incidence.

The theory of specular reflection by aluminized, ground glass surfaces has been considered in detail by Bennett (1963), who reports that to a first approximation the relative specular reflectance at wavenumber, ν, and angle of incidence, ψ, is given by

$$R = R_0 \exp\left(-A \nu^2 \cos^2\psi\right), \qquad (7.7)$$

where A is a constant for a plate of given roughness. From this relation we obtain

$$\ln R = - A \nu^2 \cos^2 \psi + \ln R_o . \qquad (7.8)$$

A sample of the scatter plate material was tested at NOAA using the flight detector assembly to measure relative reflectivity as a function of angle of incidence. From the gradient of a graph of $\ln R$ v. $\cos^2 \psi$ and equation 7.8, the value of $A\nu^2$ was found to be 1.14. Differentiating equation 7.7, we obtain

$$\frac{dR}{R} = - 2 A \cos^2 \psi \, \nu \, d\nu$$

$$= - 2 A \nu^2 \cos^2 \psi \, \frac{d\nu}{\nu} \qquad (7.9)$$

Assuming the variation of reflectivity across the pass band of the optics to be small, equation 7.9 can be applied to give

$$\frac{R(\nu, \psi)}{R(2880, \psi)} = 1 + \frac{\delta R}{R(2880, \psi)}$$

$$\simeq 1 - 2{\cdot}28 \cos^2 \psi \left(\frac{\nu - 2880}{2880} \right) . \qquad (7.10)$$

The optics profile shown in figure 4.4 may therefore be weighted by this function to obtain the combined transmission of the system.

Equation 7.10 describes only the change in reflectivity

relative to the value at 2880 cm^{-1} for a constant angle of incidence. However, since taking the ratio of sideband to wideband signals effectively accounts for the variation of the absolute value of reflectivity, only the relative response is required. Calculations using equation 7.10 and the line-by-line model showed that the small variation of angle of incidence over the range of the useful flight data caused a negligible change in the full scale value of the sideband to wideband ratio. It was therefore considered adequate to use the value, $\psi = 45^{o}$, corresponding to a solar zenith angle of 90^{o}, in the retrieval, and hence to use equation 7.10 to represent the variation of scatter plate reflectivity with wavenumber. This is only an approximate form, but it is not required more accurately for the same reasons as apply to the parameterization of the variation of detector responsivity with wavenumber (see chapter 6.5).

7.11 Retrieval of the mixing ratio profile

Using the values presented in figure 7.7 . a curve was drawn manually through the data points. It was divided by the full scale signal to obtain a plot of PMR transmission and corrected for the effects of other minor constituents using the correction curve given in figure 7.9. The resulting corrected PMR transmissions, which can be compared with the results of the HCl PMR transmission model, are shown in figure 7.10.

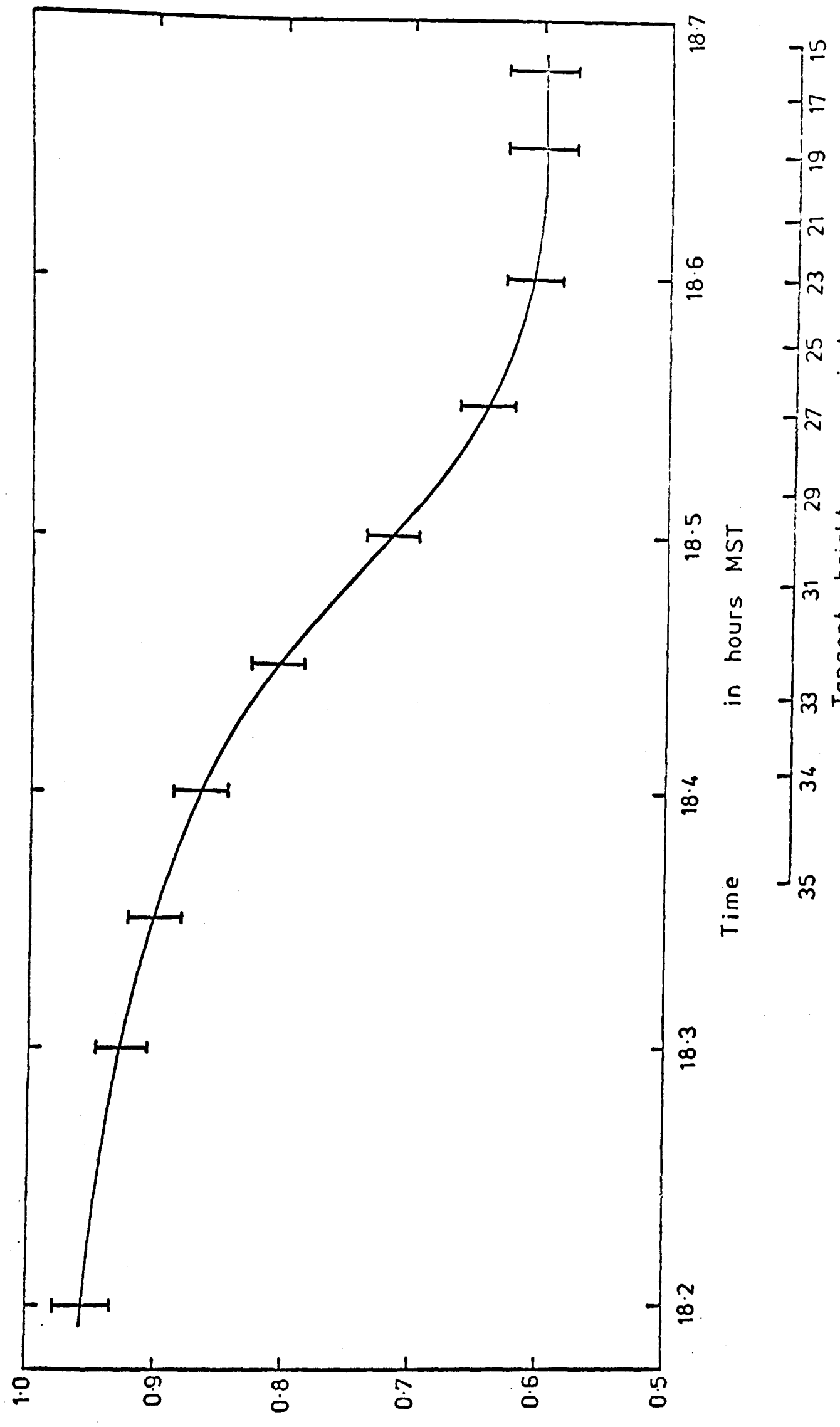

Figure 7.10 Variation of corrected PMR transmission with time at sunset.

The retrieval was performed using the HCl PMR line-by-line model described in chapter 4.8 and the parameters already discussed, which are summarized in table 7.5. The appropriate effective solar black body function was calculated from the data given by Thekaekara (1973). A retrieval method was used which involved postulating a mixing ratio profile and calculating the PMR transmissions corresponding to this profile for a range of tangent heights. The resulting PMR transmission curve was then compared with the measured curve (figure 7.10) and thus a better mixing ratio profile was estimated. The procedure was repeated until the postulated profile gave good agreement between measured and calculated PMR transmissions. For these calculations the atmospheric path was represented by a series of homogeneous paths, each 3 km or less in vertical extent (for those sections below the balloon) and each characterized by an absorber amount and absorber-weighted pressure and temperature using the ray tracing routine described in appendix D. In this way the effects of refraction were included directly.

The tolerances on the shape of the mixing ratio profile were estimated by varying that shape which fitted the data best and investigating by how much it could be changed before the calculated transmission curve no longer lay within the error bars on the measured profile. The final retrieved profile and the tolerances on its shape are shown in figure 7.11. Also shown, for comparison, is the profile retrieved from the measured PMR transmissions

Table 7.5 Summary of parameters used in the retrieval.

PMC length :	0.51 cm
PMC mean pressure :	2.01 torr = 0.00264 atm.
PMC effective compression ratio :	1.96
PMC temperature :	309.8 K
Spectral line data :	see table 4.1
Effective solar black body temperature :	5800 K
Combined optics transmission profile :	Profile in figure 4.4 weighted by scatter plate reflectivity and relative detector responsivity
Instrument altitude :	35.54 km
Atmospheric temperature-pressure profile :	see table 7.3

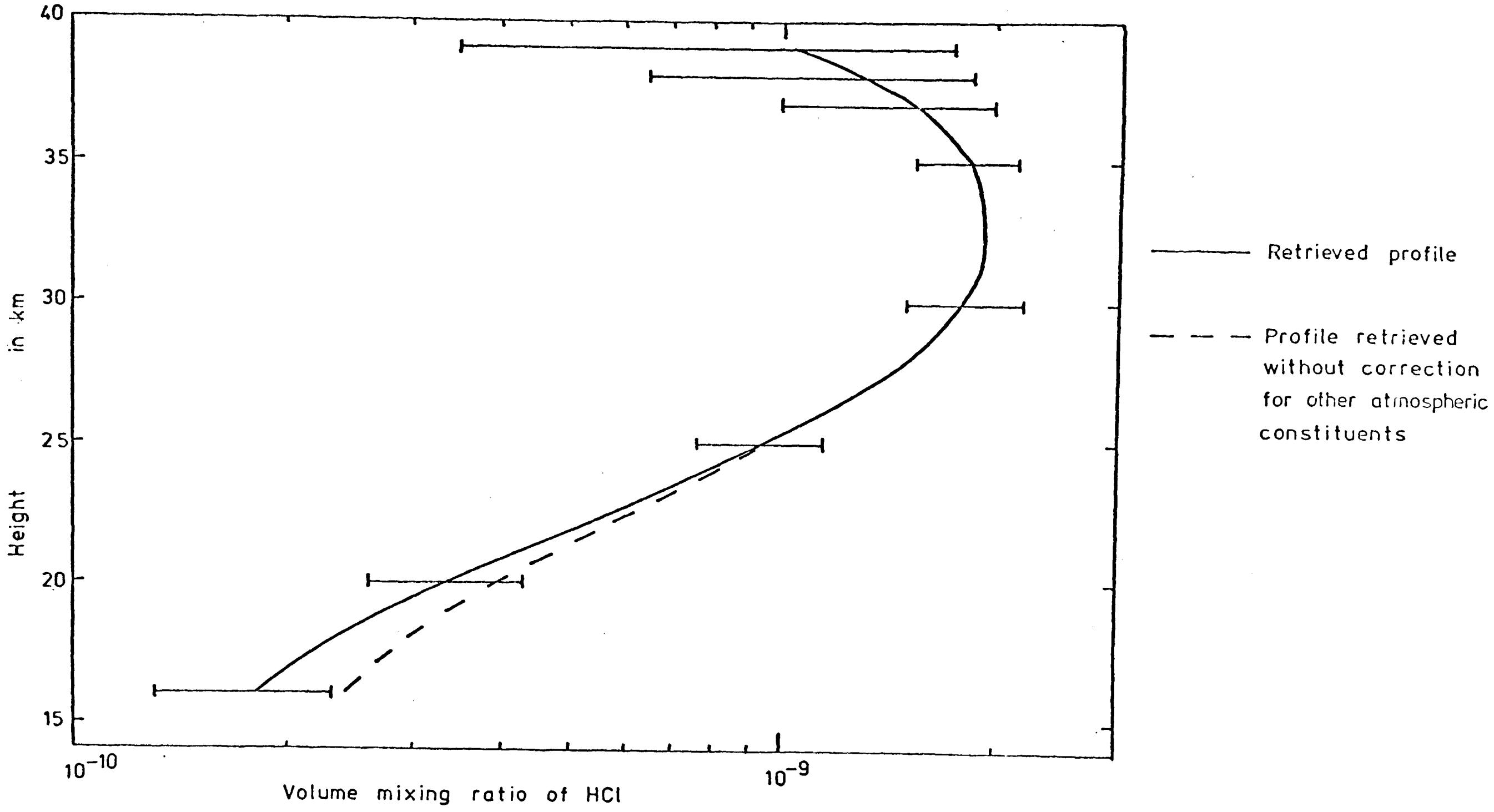

Figure 7.11 Retrieved mixing ratio profile.

uncorrected for the effects of other atmospheric constituents .

Figure 7.11 shows that a mixing ratio profile can be retrieved for stratospheric heights below the instrument with reasonable accuracy. However, above the balloon there are large uncertainties caused by the greatly decreased optical path length and the lack of height resolution inherent in the viewing geometry at zenith angles less than 90°.

7.12 Field of view

It has been assumed throughout that the sun can be considered as a point energy source with a position defined by the zenith angle of the centre of the sun's disc. In fact the diameter of the sun subtends an angle of about 0.27 degrees at the earth, and this corresponds to a range of tangent heights of about 2 km when limb scanning to tangent points in the lower stratosphere.

The error caused by considering the solar energy to be emanating from the centre of its disc rather than distributed over it was calculated for a worst case - a tangent height 20 km below the instrument height. It was found that the point source approximation caused the mean atmospheric mass between the sun and the instrument to be under-estimated by only about 1.4%. At greater tangent heights the error is lower since the

range of tangent heights subtended by the sun's disc is decreased at smaller zenith angles. In practice the important variable is not the mass of the atmospheric path but the absorber amount in it. For a mixing ratio profile such as that found, which increases with height, the error in the mean absorber amount caused by the point source approximation will be much less than 1.4%. Consequently errors caused by the effects of the real field of view have been considered negligible.

7.13 Error analysis

The sources of error in the retrieved mixing ratios may be divided into two categories - those which affect the shape of the profile and those which change the absolute values of the mixing ratios while maintaining the same profile shape. The former are shown in figure 7.11. They are caused mainly by the limited signal-to-noise ratio of the measured PMR signals which leads to uncertainties in the measured PMR transmissions. The mixing ratio inaccuracies so produced are largest above the balloon since the PMR transmission for zenith angles less than 90^{o} is close to unity. The uncertainties in the correction curve for the effects of other constituents also contribute to the error on the profile shape but only at the lower altitudes.

Sources of significant error in the absolute value of the mixing ratio are several. Firstly, any miscalculation of the balloon altitude leads to the profile being shifted up or down in height and to an error in the retrieved mixing ratio. The uncertainty in the balloon altitude pressure is estimated to be $\simeq$ 6%. Therefore an inaccuracy of this amount is present in the mixing ratio, and the position of the profile in height is uncertain to $\sim$ 0.5 km.

The other major source of absolute error is the accuracy of the appropriate PMC mean pressure. Although the physical mean pressure of the gas in the PMC is known to better than 1%, this is not necessarily the appropriate pressure to use in the retrieval calculations for reasons given in chapter 6.6. Also, any contamination of the PMC will cause the amount of HCl present to be less than that derived from the PMC frequency measurement. The result of these effects is to introduce an uncertainty $\sim$ 10% into the retrieved mixing ratio.

The field of view approximations discussed in section 7.12 also introduce an uncertainty, though less than 1% in the lower stratosphere and even less at higher altitudes. Some error will also be introduced by the small uncertainties in the atmospheric temperature profile (which affect calculations of transmission) and in the spectroscopic data. Similarly uncertainty in the effective compression ratio of the PMC and omission of the effects of its gas temperature cycling each lead to errors $\sim$ 1%.

It is therefore concluded that the total error in the absolute magnitude of the mixing ratio is ~ 20%. This is not included in the error bars shown in figure 7.11 but acts as a displacement on the profile given without affecting the shape. It should be taken into account when making comparison with other measurements.

CHAPTER 8. CONCLUSIONS AND SUGGESTIONS FOR FURTHER WORK.

8.1 Measurement of stratospheric HCl

A PMR detecting absorption of radiation by stratospheric HCl has been used to measure the mixing ratio of this species over the altitude range 16 to 39 km, and the results illustrate the feasibility of using this technique to obtain accurate measurements of stratospheric HCl. The accuracy obtained from the PMR data reported in this work is equal or superior to that claimed for any currently reported measurement and, with minor alterations to the instrument, could probably be improved considerably. Also, the altitude range of the PMR measurement is larger than that achieved by any other remote sounding technique and is comparable with that of the in situ measurements made by Lazrus' group (Lazrus et al., 1977).

The techniques used by other groups and the results which they have reported are given in chapter 3. The mixing ratio profiles obtained are compared in figure 3.1 and indicate that, while there is considerable similarity between the results, there are also some areas of disagreement. The arguments presented in chapter 3.3 suggest that there is little diurnal or seasonal variation in stratospheric HCl, and so we should expect all the reported measurements (which have been made at about the same

latitude) to be similar. In the lower stratosphere, below 25 km, this is the case; most of the reported profiles are similar in both absolute amount and shape. However, between 25 and 35 km the profiles are markedly different. It can be seen from figure 3.1 that our results are most similar to those of Ackerman et al. (1976). Williams et al. (1976 b) also show a similar profile but their signal-to-noise ratio limits their accuracy at higher altitudes and their retrieval technique is less sophisticated than our own or those of Ackerman's group and Farmer's group. Of the 4 remote sounding groups, all but our own produce absorption spectra and so direct comparison between their results and retrieval techniques should be relatively easy. Of the 3 groups, Farmer and his group (see Raper et al., 1977) claim that their latest measurements yield the best quality spectra, but their profile shape is at greatest variance with those of other remote measurements, showing an inflection in the profile around 30 km. The results of Lazrus' group using in situ techniques (Lazrus et al., 1977) show an altogether different profile above 25 km with a minimum mixing ratio around 32 km.

It has been shown in chapter 2 that the chemistry of stratospheric chlorine and its interaction with the ozone cycle are very complicated. Also the shape of the HCl mixing ratio profile is sensitive to the details of the chemical reactions involved in this complex system. Therefore the measurement of HCl provides

useful data with which the results of chemical models may be compared. Reported measurements have so far produced results which can be used to test the validity of models up to about 35 km, although more advantage would have been obtained had the reported profiles been in better agreement with each other. A better understanding of stratospheric chemistry would also be expected if accurate measurements of the HCl profile could be extended to above 40 km.

8.2 Further measurements

Having demonstrated the suitability of the PMR for measuring HCl, it is apparent for several reasons that further flights using the same instrument could yield useful data. Firstly, there are a number of minor improvements which could be made to the instrument in order to obtain better results. These are discussed later in this chapter. Also, it is possible for balloon-borne assemblies, such as that used, to reach float altitudes of 45 km. Since the limb scanning technique used is unable to provide good height resolution in the retrieved profile above the balloon height, it is only by ascending to greater altitudes that the range of the measurement can be extended. By reaching higher float altitudes, accurate results could be achieved for the range 35 to 45 km

over which they have yet to be made.

It has been shown in chapter 4 that the PMR has a much better effective spectral resolution than do conventional spectrometers, and so it should be capable of more precise measurements of HCl than can be obtained by other remote sounding techniques. This advantage is not clearly illustrated by the PMR measurements reported here, but it is probable that their quality could be improved considerably. Implementation of the minor improvements detailed below would enhance the data, and even better quality would be expected if greater constancy in the incoming radiation could be achieved through a more stable solar tracking system. In these ways it is estimated that the accuracy of the HCl measurement might be improved by an order of magnitude, producing an instrument considerably superior to the conventional spectrometers currently in use.

More generally, the number of HCl measurements is still sufficiently low for any other observation, whatever the technique, to be a useful addition to the available data, as there are marked differences between the shapes of the profiles reported so far. Further measurements around $30^{o}N$ would be useful as they would be most directly comparable with currently reported observations. Although Lazrus' group have made a series of measurements over 2 years allowing seasonal variability to be investigated, it would be useful if such a programme could be undertaken using a remote

sensing technique, in view of the present disparity between the results of remote and in situ techniques. Interesting results would also be obtained if two or more instruments using different techniques could be flown together on the same gondola to obtain a more direct comparison of the results of different methods.

The latitudinal variations in HCl amount predicted by models have yet to be confirmed by experiment, and so a series of measurements over a range of latitudes could usefully be undertaken. Since the main objective of HCl measurement is the achievement of a better appreciation of the interaction between chlorine species and ozone to improve our ability to predict ozone depletion caused by chlorine compounds, it is just as important that efforts be made to monitor other chlorine species and to determine their diurnal, latitudinal and seasonal variations. Particularly important are the reactive species, Cl and ClO, for which measurements are at present very limited and agreement between measurement and model prediction is poor. It would also be useful to detect and measure those species, such as $ClONO_2$, which may act as temporary sinks for free chlorine, in order to understand their importance in the chlorine-ozone cycle.

Besides undertaking measurement programmes in the near future, it seems reasonable that plans should be made for continued monitoring of stratospheric chlorine species on a long term basis. Only by making

measurements at intervals of 5 years or longer can we hope to identify long term trends and thus predict the likely consequences of increasing chlorine levels. In conjunction with such measurements it will also be useful to study average ozone amounts in an effort to observe any signs of a long term depletion of ozone underlying the large, short term variations which are present in the natural equilibrium.

8.3 Instrumental improvements

The electronics fault which caused a non-linearity in the signal channel has been discussed in chapter 6.3. No problems of signal interpretation were created by the fault, but the signal-to-noise ratio of the output signal was reduced by a factor ~ 2. Rectification of this problem would therefore lead directly to improved data. On analysing the flight data, several minor faults were also found to have been present in the data system. None of these seriously affected the data analysis but their elimination would lead to a more reliable instrument.

A further improvement could be achieved by altering the system of ground commands to the instrument to allow the sun view sequences to be changed during flight so that the HCl PMR could receive a greatly increased proportion of the sun view around sunset. Also, as far as HCl measurements are concerned, views away from the sun are of very little value and could be

reduced in number, since they give a zero signal which need only be recorded occasionally. With these two changes the time allotted to PMR sun views could be raised from 25% of the total to 75% or more, thus increasing considerably the amount of useful data around the sunset period.

By choosing more carefully the substances exposed to HCl inside the PMC, the instrument could be used for very much longer periods without refilling and, more importantly, the decrease in contamination would reduce a source of inaccuracy in the retrieval. However, this might involve a major alteration requiring a re-designed PMC.

8.4 Theoretical work

Several sources of error in the retrieved mixing ratio profile are caused by lack of knowledge of the precise behaviour of the PMC. More work is required in order to quantify a number of variables. Firstly, a model of the PMC pressure cycling is needed in order to discover the waveform of the pressure modulation for a PMC of given dimensions. Such a model could also be used to investigate the nature of the associated temperature cycling of the gas in the PMC head. Secondly, from the pressure modulation the form of the modulation of energy transmitted through the PMC head could be investigated.

From such a study it would become apparent whether a two pressure model of a PMC (as used in the HCl retrieval) is always sufficiently accurate, and if so which two pressures should be used for a given PMC.

The theoretical investigation of the effects of other minor constituents on HCl PMR signals could profitably be extended. More conclusive results would be expected from a rigorous line-by-line model of the type described in chapter 4 which included the effects of overlapping between spectral lines of different species. In the case of the HCl PMR such calculations would be aided by the results of a recent analysis of the spectrum of methane around 2900 cm^{-1} (Toth et al., 1977). In general, all PMRs measuring radiation emitted from or transmitted by the atmosphere are affected to a greater or lesser degree by the problems of overlapping between lines of different species. It would therefore be useful if the general line-by-line model could be extended to compute transmissions through paths of gases containing more than one absorber or the signals produced by a PMR filled with one gas when viewing along a path containing another.

The development of a fast computer routine to evaluate the Voigt integral has been discussed in appendix A. There is still scope for improving this routine by replacing some of it with parts of the routine due to Drayson (1976) in those regions where

the latter is more efficient. Also a faster but less accurate routine reported by Pierluissi et al. (1977) could usefully be investigated. -

The technique used for retrieving the HCl mixing ratio profile from the PMR signals is described in chapter 7.11. It is an iterative method involving successive manual correction to the postulated profile until it gives agreement with the measured signals. It would be interesting to develop a computer routine to automate the process completely and to perform a statistical evaluation of the errors on the retrieved profile. The small amount of data used in the HCl retrieval did not necessitate such a routine, but for instruments from which the output of data was much higher, processes involving manual correction would not be practicable.

8.5 Laboratory measurements

In chapter 6.5 it is concluded that, although the laboratory transmission measurements performed with the HCl PMR were compatible with theoretical calculation, the quality of the measurements would have to be increased considerably before such parameters as the spectral line data could be tested accurately. This would require a re-designed experimental system including a brighter source or a properly focused optical system. Also the stability of the system would

need to be increased in several ways: an improved structural design would be required to minimize all sources of vibration, and thermal stability and electrical shielding comparable with flight conditions would also be needed. With such a system transmission measurements could be performed to verify the parameters used in the retrieval. Also, the problem of overlapping lines of other constituents could be investigated by viewing a source with an HCl PMR through a path containing methane.

8.6 The Stratospheric and Mesospheric Sounder (SAMS)

This experiment is to be launched in 1978 on board the Nimbus G satellite. It will include several channels in which PMRs are used to monitor a number of minor constituents in the stratosphere and mesosphere. SAMS has many similarities to the instrument used to measure HCl, but it also contains some fundamental differences. It employs a limb scanning technique from its satellite platform in orbit about 1000 km above the earth's surface. However, the instrument does not measure solar energy transmitted through the atmosphere but senses the thermal radiation emitted from the limb path. The satellite is to follow a sun-synchronous orbit and in this way will achieve global coverage. The objectives, design, development and testing of SAMS are described in detail elsewhere (see, for example,

Houghton et al., 1976; Proposal for the Nimbus G satellite, 1973; Ballard J.; Wale M.J.). The following discussion is confined solely to a brief description of the various channels and an explanation of the relevance of aspects of this thesis to some of the scientific problems associated with SAMS.

A primary objective of SAMS is the measurement of 5 minor constituents of the upper atmosphere - H_2O, NO, N_2O, CH_4 and CO. The instrument employs 7 pressure modulators, one for each of the gases listed above and the other two containing CO_2. The latter are used to provide the attitude and atmospheric temperature information vital to the retrieval of the minor constituent mixing ratio profiles. The incoming radiation can pass along a number of optical paths illustrated schematically in figure 8.1, and the signal from each of the six detectors is processed to provide a wideband and PMR output signal.

Since a PMC containing a specific gas causes modulation of the incoming radiation which originates mainly from that gas in the atmosphere, the PMR signal associated with each detector is related principally to the gas in the PMC which is operating in the corresponding branch of the instrument. In order to retrieve mixing ratios from the PMR signals it is necessary to model the response of each channel. Although the spectral bands utilized by SAMS PMRs cover a wide range of wavelengths and differ markedly in band strength,

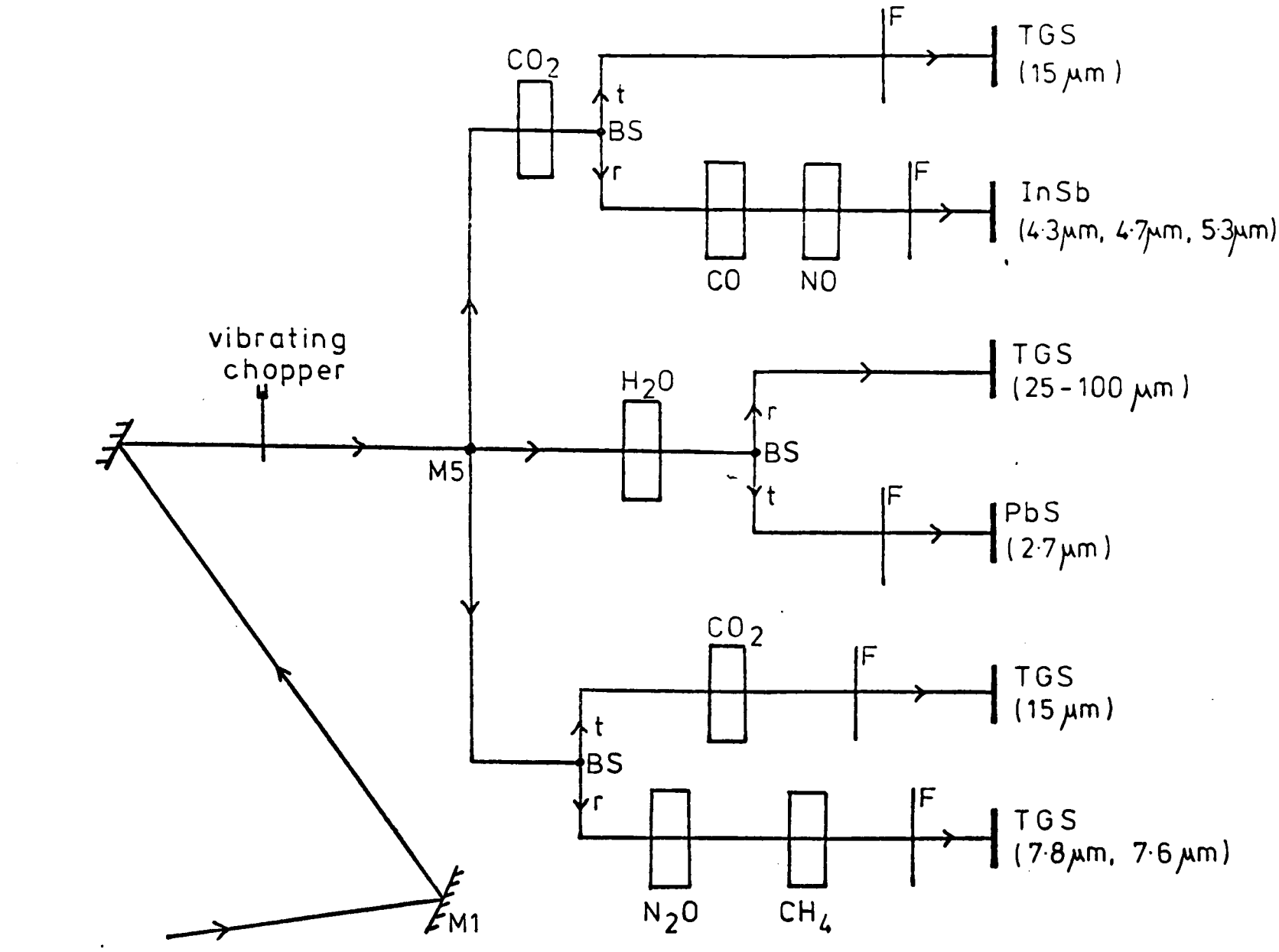

KEY

M1	Scan mirror
M5	Multi-facet mirror
BS	Beamsplitter
t	Transmitted beam
r	Reflected beam
▭	Pressure modulator cell (labelled with filling gas)
F	Optical filter
▮	Detector (labelled with detector type and the wavelengths of the spectral bands of the PMC gases)

Figure 8.1 Schematic representation of SAMS.

line width, line separation, etc., the PMRs' responses can all be simulated by computing monochromatic transmissions and integrating over the wavelength region of the appropriate optical filter. It is primarily for this reason that the general line-by-line program described in chapter 4 has been developed. It enables the transmission of radiation from an atmospheric limb path by a SAMS PMC containing any of the gases to be modelled. Calculations can also be performed for comparison with laboratory transmission measurements. It will not be possible to use a line-by-line method as part of the routine retrieval program; fast empirical models must be developed in order to perform the retrieval from each radiance or set of radiances in the short time available. However, the line-by-line model provides a method of performing accurate spectral calculations and so can be used to check the validity of the empirical models or as a tool in their development.

8.7 Other applications of a line-by-line model

The program, GENLIN, described in chapter 4 has already been used in a re-analysis of the data obtained by a balloon-borne PMR measuring thermal emission by stratospheric water vapour. The flight took place in July 1974, and the instrument is described in detail by Chaloner (1976). The initial retrieval

was made using a strong pressure-broadened line approximation for both the PMC and the atmosphere and a single homogeneous path model to represent each atmospheric limb view. The line-by-line approach enables more accurate spectral calculations to be performed and also allows the atmospheric path to be represented by more than one homogeneous section to obtain a closer approximation to the true radiative transfer along a structured path. The results of the reappraisal are given in appendix H, but for all details of the instrument and the initial retrieval reference should be made to Chaloner (1976).

GENLIN is sufficiently general for it to be applied to many different types of radiation calculations. It can be used to model PMRs measuring either emission or transmission of radiation by structured atmospheric paths or homogeneous paths in the laboratory. It also performs calculations for simple filter radiometers with no PMC and in all cases allows for the effects of overlapping spectral lines. The program might usefully be extended in future to perform accurate calculations of transmission for overlapping bands of different gases and thus attain a more general applicability.

Appendix A. Evaluation of the Voigt integral.

It is shown in chapter 4 that an important expression in the calculation of absorption coefficients is the Voigt function,

$$V(x,y) = \frac{y}{\pi^{3/2}} \int_{-\infty}^{\infty} \frac{e^{-t^2}\,dt}{(x-t)^2 + y^2} \qquad (A.1)$$

The integral does not have an analytic form and must be approximated by some other expression which is amenable to numerical evaluation.

A study of the calculations in which the Voigt function is required has shown that it is necessary to develop a computer routine to evaluate the Voigt function for all values of x and all positive values of y. It should be accurate to about 1 part in 10^4 or better and must run as quickly as possible, since many thousand such evaluations are needed in one calculation.

A routine called VOIGTF has been developed which meets the accuracy criterion and, on average, runs as fast or faster than the other available routines which have been examined. The routine divides the positive quadrant of the xy plane into three regions and employs a different approximation in each. The regions used are shown in figure A.1. Since the Voigt function is even in x, only positive values of x need be considered.

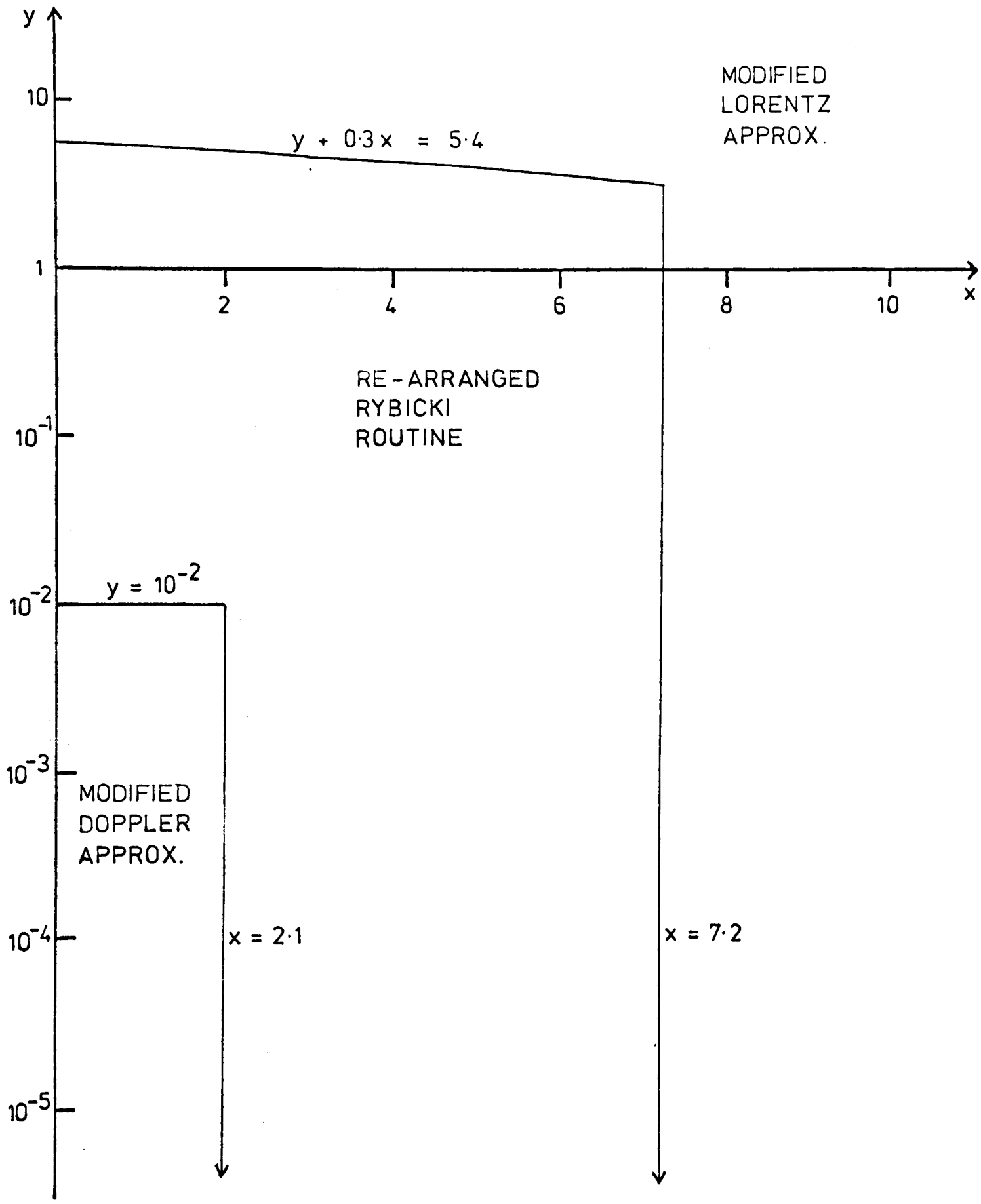

Figure A.1 Regions used by VOIGTF in evaluation of Voigt integral.

A.1 Region 1. Modified Lorentz approximation.

Barnett has derived an expansion of the Voigt integral which converges to a good approximation using only the first few terms of the expansion in the regions $x \gg 1$ or $y \gg 1$. In the routine VOIGTF, the first three terms are used:

$$V(x,y) \simeq \frac{y}{\pi(x^2+y^2)}\left\{1 + \frac{\frac{2x^2}{x^2+y^2} - \frac{1}{2}}{x^2+y^2} + \frac{\frac{3}{4} - \frac{9x^2}{x^2+y^2} + 12\left(\frac{x^2}{x^2+y^2}\right)^2}{(x^2+y^2)^2}\right\}. \quad (A.2)$$

Barnett's own routine uses only the first two terms, but it has been found empirically that inclusion of the third term enables an approximation differing from the Voigt integral by less than 1 part in 10^4 for a considerably increased region. Boundaries which meet this accuracy criterion were found empirically to be $x > 7.2$ or $(y + 0.3x) > 5.4$. The area of this region could be increased, but this would involve a more lengthy calculation for the boundary conditions and so would not improve the speed of the routine.

A.2 Region 2. Modified Doppler approximation.

By examining the percentage difference between the pure Doppler expression (i.e. $V(x,y) = \pi^{-\frac{1}{2}} e^{-x^2}$) and the Voigt function over the xy plane, an empirical expression was found which meets the accuracy criterion for the region $x < 2.1$, $y < 10^{-2}$:

$$V(x,y) \simeq \frac{1}{\sqrt{\pi}} \exp(-x^2)\left\{1 - (y - \tfrac{1}{2}y^2)\sum_{n=0}^{5} A_n x^{2n}\right\}. \quad (A.3)$$

The values of the coefficients, A_n, were calculated by fitting a polynomial in x^2 to the difference between the pure Doppler expression and the Voigt function calculated accurately using Rybicki's routine (see section A.3). A least squares fit was used to the values at the points, $x = 0, 0.1, 0.2, \ldots, 2.0, 2.1$ and $y = 4.8828 \times 10^{-3}$. The coefficients thus calculated are as follows:

n	A_n
0	+1.1289
1	-1.1623
2	-0.080812
3	-0.13854
4	+0.033605
5	-0.0073972

A.3 Region 3. Re-arranged Rybicki routine.

Rybicki has shown (see Armstrong and Nicholls, 1973) that an approximation to the Voigt integral which may be used over the whole of the positive quadrant of the xy plane is the summation,

$$V(x,y) \simeq \frac{h}{\pi^{3/2}} \sum_{n=+\infty}^{-\infty} \exp(-n^2h^2) \frac{(x-nh)(-1)^n Im(q) + y\{1-(-1)^n Re(q)\}}{(x-nh)^2 + y^2}, \qquad (A.4)$$

where $q = \exp(i\pi z/h)$,

$z = x + iy$,

and Re(q) and Im(q) are the real and imaginary parts of q, respectively.

h is an arbitrary constant which has the following effect. The smaller the value of h, the more accurate is the approximation, but the greater is the number of terms in the summation which is needed to ensure that the summation converges to the required accuracy. Consequently a compromise value of h must be used in order to obtain the accuracy required with the smallest number of terms. Rybicki's own routine uses h = $\frac{1}{3}$ and a summation from n = -15 to n = +15, and he claims an accuracy of 1 part in 10^8 for any point in the positive quadrant. For the region, y < 0.1, Rybicki's routine uses a re-arrangement of equation A.4,

$$V(x,y) \simeq \frac{1}{\sqrt{\pi}} \exp(y^2-x^2)\cos(2xy) + \frac{h}{\pi^{3/2}} \sum \exp(-n^2h^2) \frac{(x-nh)(-1)^n \mathrm{Im}(q') + y\{1-(-1)^n \mathrm{Re}(q')\}}{(x-nh)^2 + y^2}, \qquad (A.5)$$

where $q' = \cos(\pi z/h)$.

It has been found that the computation time of this routine can be cut by folding over the summation in equations A.4 and A.5 to give fewer terms:

$$V(x,y) \simeq A + \frac{1}{\pi^{3/2}} \left\{ \frac{Hx\,\mathrm{Im}(q) + Hy\{1-\mathrm{Re}(q)\}}{H^2x^2 + H^2y^2} + \sum_{n=1}^{N} \exp\left(-\frac{n^2}{H^2}\right) \frac{(-1)^n Hx\,\mathrm{Im}(q)\{(Hx-n)(Hx+n)+H^2y^2\} + Hy\{1-(-1)^n \mathrm{Re}(q)(H^2x^2+H^2y^2+n^2)\}}{\frac{1}{2}\{(Hx-n)(Hx+n)\}^2 + H^2y^2(H^2x^2+\frac{1}{2}H^2y^2+n^2)} \right\}, \qquad (A.6)$$

where H = 1/h,

A = 0 and $q = \exp(i\pi zH)$ for $y \geqslant 0.1$,

and $A = \pi^{-\frac{1}{2}} \exp(y^2 - x^2) \cos(2xy)$ and $q = \cos(\pi z H)$

for $y < 0.1$.

The routine was found empirically to give an accuracy of better than 1 part in 10^4 (and usually better than 1 part in 10^5) using the values $H = 2.5$ and $N = 10$. The Rybicki routine re-arranged by this method runs ~ 2.5 times faster than Rybicki's original routine. However, it is still considerably slower than the modified Lorentz and modified Doppler routines given in sections A.1 and A.2, and so the re-arranged Rybicki routine is only used in the region shown, where the other approximations do not give the required accuracy.

A.4 Other Voigt routines.

Much research has been done on approximations to the Voigt function, and recently it has been directed towards fast computation of the Voigt integral using computers. Some of this work is discussed by Armstrong and Nicholls (1973).

A recent routine due to Drayson (1976) has been studied in terms of its speed relative to VOIGTF. Drayson's routine splits the positive quadrant of the xy plane into 4 regions. A study of the comparative run times on the PDP 11/70 computer at Oxford shows that in some regions Drayson's routine is faster than the equivalent section in VOIGTF while in other regions it is slower. The relative efficiency of the two routines will therefore depend on the particular calculation involved and the frequency with which it uses

the Voigt profile in different regions of the xy plane.

Appendix B. Variation of line strength with temperature.

B.1 Derivation

Penner (1959) derives from first principles an equation for the line strength of a transition between the vibration-rotation states L and U:

$$S_{Lu} = \frac{8\pi^3 \nu_{Lu}}{3hcp} |R_{Lu}|^2 \frac{N}{Q} \exp\left\{\frac{-E_L}{kT}\right\}\left\{1 - \exp\left(\frac{-hc\nu_{Lu}}{kT}\right)\right\}, \quad (B.1)$$

where ν_{LU} is the wavenumber of the transition,

N is the number of molecules per unit volume at pressure, p, and temperature, T,

Q is the total partition function,

E_L is the energy of the lower state relative to the ground state,

R_{LU} is the matrix element of the electric dipole moment for the transition,

and h, c and k are fundamental constants symbolized conventionally.

Allowing for differences in units, this equation agrees with equivalent expressions derived by other authors (see Houghton and Smith, 1966, and Goody, 1964). The factor, $\{1 - \exp(-hc\nu_{LU}/kT)\}$ arises because of stimulated emission transitions from the upper to the lower state which have the same effect as would a negative absorption.

From equation B.1 it follows that

$$\frac{S(T)}{S(T_o)} = \frac{Q(T_o)}{Q(T)} \frac{\exp(-E_L/kT)}{\exp(-E_L/kT_o)} \frac{\{1 - \exp(-hc\nu/kT)\}}{\{1 - \exp(-hc\nu/kT_o)\}} , \qquad (B.2)$$

where ν has replaced ν_{LU}. This general form can usually be approximated by an equation which assumes the vibrational and rotational parts of the partition function, $Q_v(T)$ and $Q_r(T)$ respectively, to be independent:

$$\frac{S(T)}{S(T_o)} = \frac{Q_v(T_o)Q_r(T_o)}{Q_v(T)Q_r(T)} \frac{\exp(-E_L/kT)}{\exp(-E_L/kT_o)} \frac{\{1 - \exp(-hc\nu/kT)\}}{\{1 - \exp(-hc\nu/kT_o)\}} . \qquad (B.3)$$

The rotational partition function can easily be shown to vary as (T/T_0) for diatomic and linear molecules (see Houghton and Smith, 1966); it varies as $(T/T_0)^m$ for non-linear molecules. The vibrational partition function is calculated from the expression,

$$Q_v(T) = \sum \exp(-E_n/kT) , \qquad (B.4)$$

where E_n is the energy above the ground state of the nth vibrational level, and the summation is performed over all vibrational levels. A further approximation — the assumption that the vibration is like that of a simple harmonic oscillator — leads to vibrational levels equally spaced in energy. This gives

$$Q_v(T) = \{1 - \exp(-E_o/kT)\}^{-1} , \qquad (B.5)$$

where E_0 is the spacing between the levels.

From these expressions for the vibrational and

rotational parts of the partition function we obtain the approximation,

$$\frac{S(T)}{S(T_0)} = \left(\frac{T_0}{T}\right)^m \frac{\{1-\exp(-hc\nu_0/kT)\}}{\{1-\exp(-hc\nu_0/kT_0)\}} \frac{\exp(-E_L/kT)}{\exp(-E_L/kT_0)} \frac{\{1-\exp(-hc\nu/kT)\}}{\{1-\exp(-hc\nu/kT_0)\}}, \tag{B.6}$$

where $E_0 = hc\nu_0$.

B.2 Further approximations

For many absorption bands in the infra-red region, the equations given above may be approximated further. The possible simplifications may be illustrated by consideration of two particular infra-red bands:

i) The fundamental vibration-rotation band of HCl at 3.5 micrometres

For this band, $\nu \sim 2880\ cm^{-1}$, and so at 300 K, $\exp(-hc\nu/kT) \sim 10^{-6}$. Therefore, at all temperatures of interest, the stimulated emission factor varies insignificantly from 1 and can be omitted. Also, because this band represents the lowest energy vibrational transition, $\nu \simeq \nu_0$. It can now be seen from equation B.6 that in this case the stimulated emission factor is of the same form as the vibrational partition function, and so the latter also shows negligible temperature dependence. Equation B.6 therefore simplifies to

$$\frac{S(T)}{S(T_0)} = \frac{T_0}{T} \exp\left\{-\frac{E_L}{k}\left(\frac{1}{T}-\frac{1}{T_0}\right)\right\}. \tag{B.7}$$

In general, the stimulated emission factor can be omitted at wavelengths sufficiently short for $\{1 - \exp(-hc\nu/kT)\}$ to change negligibly for all laboratory and atmospheric temperatures of interest. The vibrational partition function can be neglected when it varies insignificantly with temperature — for those molecules in which the first vibrational level is of sufficiently high energy.

ii) <u>The bands of CO_2 around 15 micrometres</u>

For these bands, $\nu \sim \nu_0 \simeq 670\ cm^{-1}$, and so at 300 K the quantity, $\exp(-hc\nu_0/kT)$, ~ 0.04. Therefore the variation with temperature of the stimulated emission and vibrational partition function factors cannot be neglected. Also, considerable work has been done on the energy levels of CO_2 (see Gray and Selvidge, 1965). This work shows that errors are introduced into the calculations of partition functions if the molecule is treated as a rigid-rotator, harmonic oscillator, or if vibration and rotation are assumed to be independent. For the isotope, $^{12}C^{16}O_2$, Gray and Selvidge tabulate the total partition function against temperature allowing for the interaction between vibration and rotation. Using their tabulation a quadratic function was fitted to the values of the function, $Q(T)/T$, for the temperature range, 170 to 330 K. The following function was found to be a very good fit to the data:

$$\frac{Q(T)}{T} = 0.94417 - 0.73873 \times 10^{-3}\, T + 0.27477 \times 10^{-5}\, T^2, \qquad (B.8)$$

$$\therefore \quad Q(T) = 0.94417\, T - 0.73873 \times 10^{-3}\, T^2 + 0.27477 \times 10^{-5}\, T^3 . \qquad (B.9)$$

Consequently, a suitably accurate expression for the variation of line strength with temperature for these bands is equation B.2, where $Q(T)$ is given by equation B.9.

B.3 Units

The equations derived in this appendix are appropriate for calculations involving line strengths expressed in $cm^{-1}(mol.cm^{-2})^{-1}$ or $cm^{-1}(g.cm^{-2})^{-1}$ – two forms in which infra-red line strengths are often tabulated. However, for the form, $cm^{-1}(atm.cm)^{-1}$, another factor of (T_0/T) must be included in the equations given above to allow for the fact that, for a path at a given pressure, the number of molecules per cm^2 (or $g.cm^{-2}$) falls as the temperature rises.

Appendix C. Useful formulae for limb path calculations.

C.1 Constant mixing ratio

An element of absorbing atmospheric path of length, dx, at pressure, p, with an absorber volume mixing ratio, ϵ_0, contains an absorber amount given by

$$du = \epsilon_0 \, p \, dx \quad . \tag{C.1}$$

Consider a spherically symmetric atmosphere with a constant mixing ratio of absorber. A limb path through such an atmosphere is illustrated in figure C.1. It can be seen that the total absorber amount in the path may be calculated by integrating along it from $x = -\infty$ to $x = +\infty$:

$$u = \int du = \int_{-\infty}^{+\infty} \epsilon_0 \, p(x) dx = 2\epsilon_0 \int_0^{\infty} p(x) \, dx \quad . \tag{C.2}$$

Now, $p(z) = p_T \exp\{-(z-z_T)/H\}$,

where p_T is the pressure at the tangent height, z_T,

and H is the scale height of the atmosphere.

Also, $x^2 = (z - z_T)(2R_0 + z + z_T)$,

using the intersecting chords theorem.

Since z and $z_T \ll R_0$,

$$x \simeq \sqrt{2R_0}\sqrt{z - z_T}$$

and $x \, dx \simeq R_0 \, dz$.

Substituting these expressions into equation C.2, we obtain

$$u \simeq 2\epsilon_0 \int_{z_T}^{\infty} p_T \exp\left\{\frac{-(z-z_T)}{H}\right\} \frac{\sqrt{R_0}\, dz}{\sqrt{2}\sqrt{z-z_T}} \quad , \tag{C.3}$$

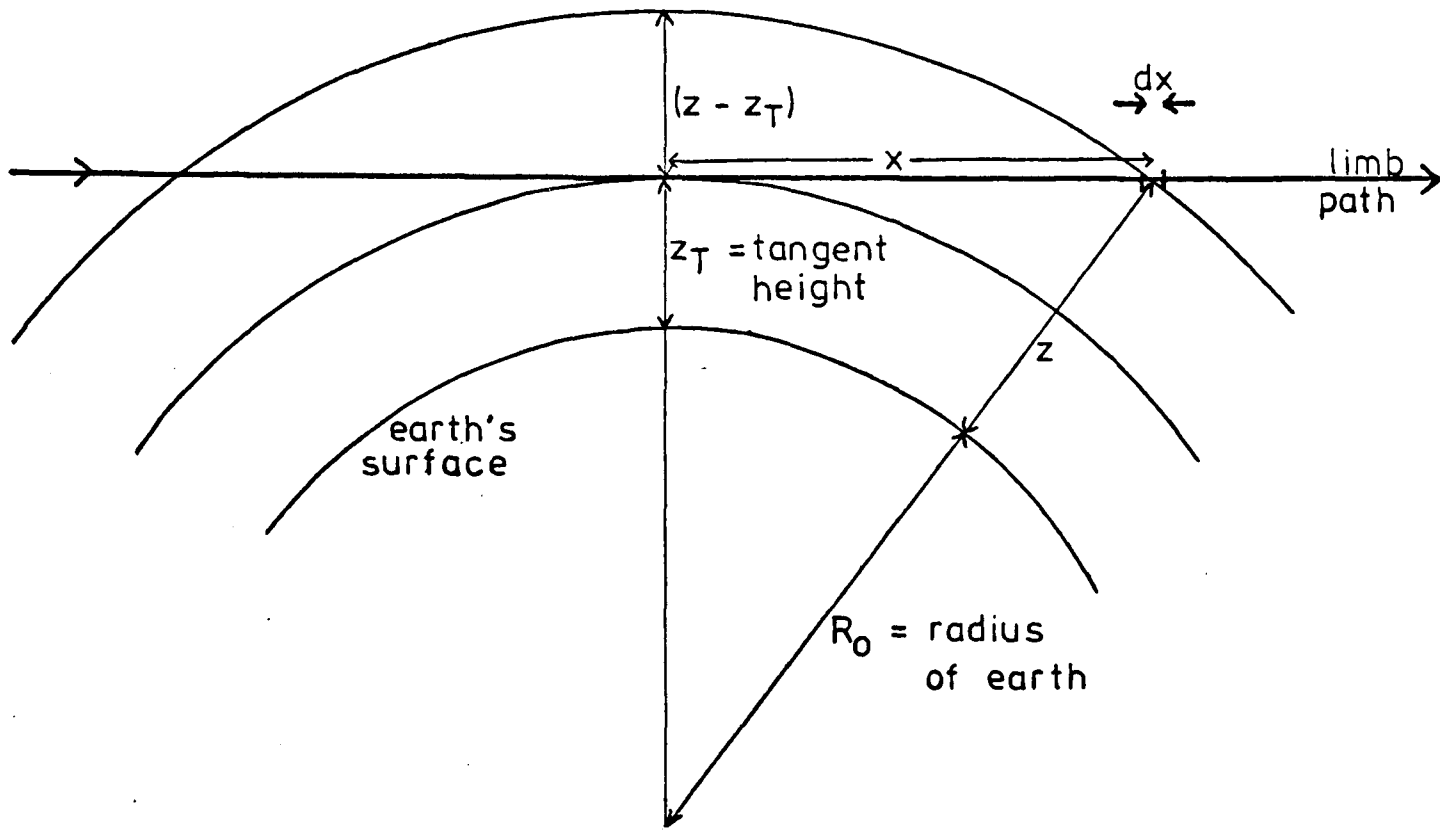

Figure C.1 Calculation of absorber amount in a limb path.

$$\therefore \quad u \propto \epsilon_0 p_T \sqrt{2\pi H R_0} \quad . \qquad (C.4)$$

It has been assumed that H is independent of height. Since H is a function of temperature, this will not be true, but as the vast majority of the absorber lies within a few kilometres of the tangent height, the error introduced by this approximation is small.

C.2 Variable mixing ratio

Equation C.4 is a good approximation for mixing ratio profiles which are constant or slowly varying with height. When considerable mixing ratio gradients are present, a better approximation can be obtained by fitting a polynomial to the mixing ratio profile above the tangent height. If it can be expressed in the form,

$$\epsilon = \sum_{n=0}^{N} \epsilon_n (z - z_T)^n \quad , \qquad (C.5)$$

then the expression equivalent to equation C.3 is

$$u \simeq \frac{\sqrt{2}\, p_T}{\sqrt{R_0}} \sum_{n=0}^{N} \int_{z_T}^{\infty} \epsilon_n \frac{(z-z_T)^n}{\sqrt{z-z_T}} \exp\left\{\frac{-(z-z_T)}{H}\right\} dz \quad . \qquad (C.6)$$

On integration, this expression gives

$$u \simeq p_T \sqrt{2\pi H R_0} \sum_{n=0}^{N} \frac{\epsilon_n H^n (2n)!}{n!\, 2^{2n}} \quad . \qquad (C.7)$$

For example, if we approximate the profile by

$$\epsilon = \epsilon_0 + \epsilon_1 (z - z_T),$$

where ϵ_1 is the gradient at the tangent height, then

$$u \simeq p_T \sqrt{2\pi H R_e} \left(\epsilon_e + \tfrac{1}{2} H \epsilon_1 \right) . \qquad (C.8)$$

C.3 Other parameters for a limb path

In a similar way, approximate expressions can be derived for two other useful quantities — the mass-weighted pressure and temperature of a limb path.

$$\bar{p} = \frac{\int p \, dm}{\int dm} = \frac{\int p^2 dx}{\int p \, dx} . \qquad (C.9)$$

Using equation C.3,

$$\bar{p} \simeq \frac{\int_{z_T}^{\infty} p_T^2 \exp\left\{\frac{-2(z-z_T)}{H}\right\} \frac{dz}{\sqrt{z-z_T}}}{\int_{z_T}^{\infty} p_T \exp\left\{\frac{-(z-z_T)}{H}\right\} \frac{dz}{\sqrt{z-z_T}}} , \qquad (C.10)$$

which simplifies to

$$\bar{p} \simeq p_T / \sqrt{2} \qquad (C.11)$$

If the temperature profile above the tangent height is approximated by

$$T = \sum_{n=0}^{N} T_n (z - z_T)^n ,$$

then by analogy with the derivation in section C.2,

$$\bar{T} = \frac{\int T\,dm}{\int dm} \simeq \frac{p_T \sqrt{2\pi H R_0} \sum_{n=0}^{N} H^n T_n (2n)!/n!\,2^{2n}}{p_T \sqrt{2\pi H R_0}}$$

$$\therefore \bar{T} \simeq \sum_{n=0}^{N} \frac{(2n)!\,T_n H^n}{n!\,2^{2n}} \quad . \tag{C.12}$$

If the original value of H was calculated using $T = T_0$, then a value of H more characteristic of the whole path can now be calculated from $\bar{T}$. Using the new value of H, u can be recalculated. This iterative method can therefore be used to find better approximations to all the limb path parameters.

C.4 Equivalent expressions for a vertical path

Similar calculations can be performed to find the equivalent parameters for a vertical path above the height, z_T, at which the pressure is p_T. The results only are given below.

	Limb path	Vertical path
u, for constant mixing ratio, ϵ_0	$\epsilon_0 p_T \sqrt{2\pi H R_0}$	$\epsilon_0 p_T H$
u, for $\epsilon = \sum_{n=0}^{N} \epsilon_n (z-z_T)^n$	$\epsilon_0 p_T \sqrt{2\pi H R_0} \sum_{n=0}^{N} \frac{(2n)!\,H^n}{n!\,2^{2n}}$	$\epsilon_0 p_T H \sum_{n=0}^{N} n!\,H^n$
$\bar{p}$ (mass-weighted)	$p_T/\sqrt{2}$	$\frac{1}{2}\,p_T$
$\bar{T}$ (mass-weighted) for $T = \sum_{n=0}^{N} T_n (z-z_T)^n$	$\sum_{n=0}^{N} \frac{T_n H^n (2n)!}{n!\,2^{2n}}$	$\sum_{n=0}^{N} n!\,H^n\,T_n$

Appendix D. Refraction of radiation by an atmospheric limb path.

D.1 Refraction in a ray tracing routine

In chapter 4.4 a method of calculating the absorber amounts in a limb path is discussed. A ray tracing technique is used whereby a ray is followed through the atmosphere in small steps and the absorber amount in each step calculated. The routines used to find absorber amount have been developed with refraction as an intrinsic part; starting at the tangent point, the ray is followed in such a way that the refracted angle and the absorber amount are calculated at each step. The method is illustrated in figure D.1. The atmosphere is treated as a series of thin, spherically symmetric, homogeneous shells of thickness, Δz, and state characterized by the pressure, temperature and mixing ratio at a point midway through the shell. Assuming that the angle, θ_1, of the ray incident on the lower boundary of the shell is known, the angle, θ_2, can be calculated from the refractive indices (found using the variables of state) of this shell and the adjacent lower shell. The angle, θ_3, at the upper boundary can then be calculated geometrically using the radii of the shell boundaries as shown in the diagram. The length of the path inside the shell, x, is calculated similarly, and hence the absorber amount can be found. The process is then repeated for the shell above. The effect of the homogeneous shells approximation has been tested by changing the thickness, Δz. It has been found that

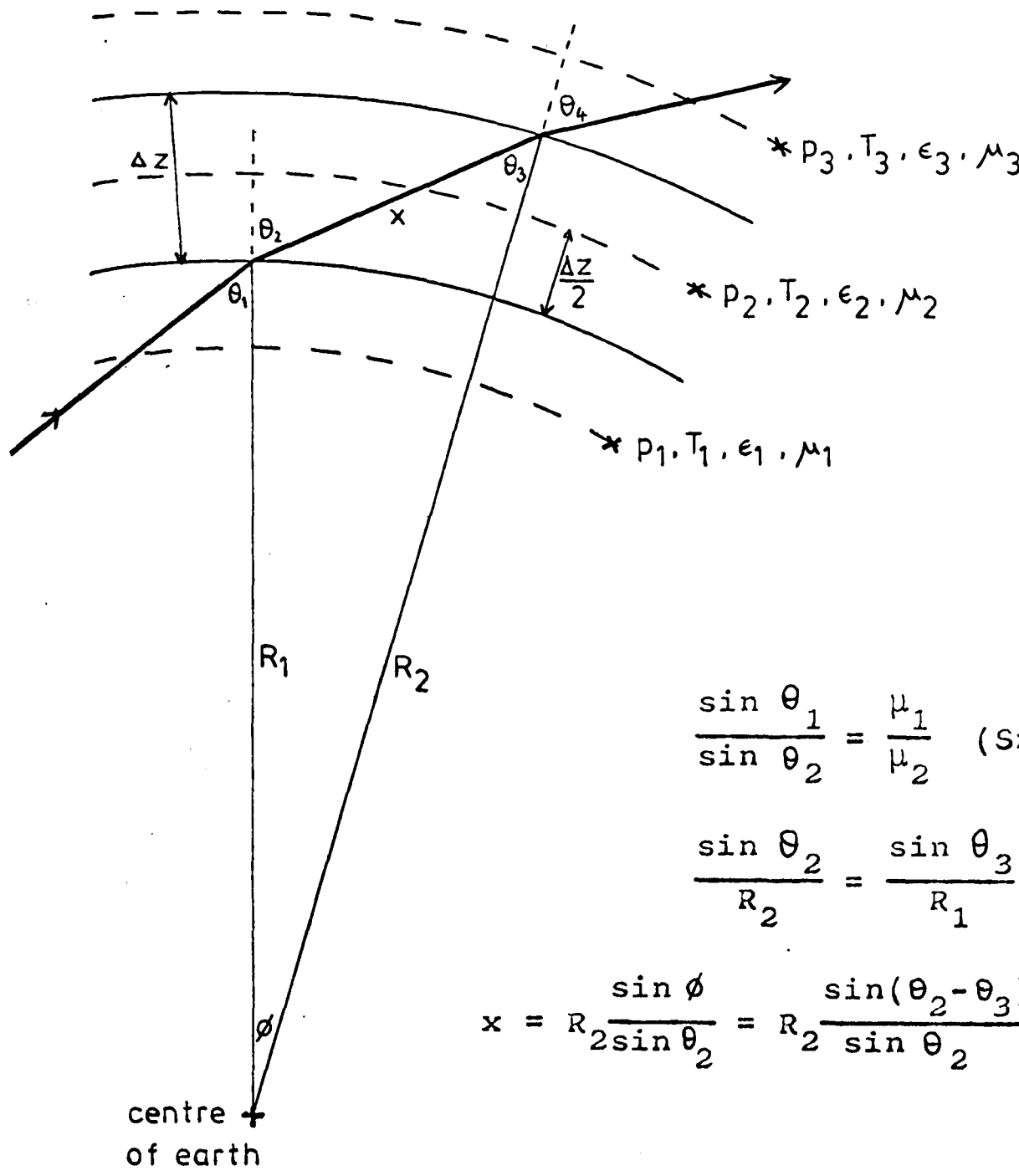

$$\frac{\sin \theta_1}{\sin \theta_2} = \frac{\mu_1}{\mu_2} \quad \text{(Snell's law)}$$

$$\frac{\sin \theta_2}{R_2} = \frac{\sin \theta_3}{R_1} \quad \text{(Sine law)}$$

$$x = R_2 \frac{\sin \phi}{\sin \theta_2} = R_2 \frac{\sin(\theta_2 - \theta_3)}{\sin \theta_2} \quad \text{(Sine law)}$$

p = pressure

T = temperature

ϵ = volume mixing ratio of absorber

μ = refractive index

absorber amount, $u = x\, p_2\, \epsilon_2$

Δz = thickness of shell

Figure D.1 Treatment of refraction using a ray tracing routine.

the error in the refracted angle introduced through using shells of 0.1 km thickness is negligible compared to other errors, such as that caused by small uncertainties in the temperature profile. 0.1 km thick shells have therefore been used in the ray tracing routines developed.

D.2 The refractive index of air

Snider (1975) gives an expression for the refractive index of dry air at 1013.25 mb and 288.16 K:

$$\mu = 1 + \gamma \times 10^{-6}, \qquad (D.1)$$

where $$\gamma = 64.238 + 29498.1\left(146 - \frac{1}{\lambda^2}\right)^{-1} + 255.4\left(41 - \frac{1}{\lambda^2}\right)^{-1}, \qquad (D.2)$$

λ being in micrometres. At stratospheric humidities, the correction to this formula caused by water vapour is negligible.

The calculations reported in section D.3 have been made for λ = 3.5 micrometres and assuming that the atmosphere behaves as an ideal gas. Using equations D.1 and D.2, this gives

$$\mu = 1 + 2.878 \times 10^{-4} \frac{p}{p_o} \frac{T_o}{T}, \qquad (D.3)$$

where T_0 = 273 K and p = 1 atmosphere = 1013.246 mb. The results will be applicable to most infra-red wavelengths since the value of γ in equation D.2 varies by less than 0.2% for all wavelengths greater than 2 micrometres.

D.3 The effects of refraction

Since the model described in section D.1 includes refraction directly, no correction need be made to the absorber amounts calculated. However, it is interesting to look at the magnitudes of the errors produced when refraction is neglected.

In order to study the effects of refraction on limb scanning experiments, a series of calculations of absorber amount has been performed using a constant mixing ratio of absorber and a pressure-temperature profile given by McClatchey et al. (1970) for a mid-latitude summer. Calculations have been made for a range of tangent heights in the lower stratosphere to simulate limb paths viewed from a satellite at a height of 1000 km and a balloon at 35 km. From calculations including refraction (with a refractive index given by equation D.3) and excluding refraction (i.e. $\mu = 1$), the changes in angles and absorber amounts caused by neglecting refraction are obtained. These are shown in figures D.2 and D.3. It can be seen that the effects of refraction decrease roughly exponentionally with tangent height and are approximately proportional to tangent height pressure.

The changes shown in these figures are calculated for constant tangent heights. However, for limb scanning experiments the usual known variable associated with each measurement is not tangent height but angle. The following relations can be used to transform changes at constant tangent height into changes at constant angle, so long as the changes are small:

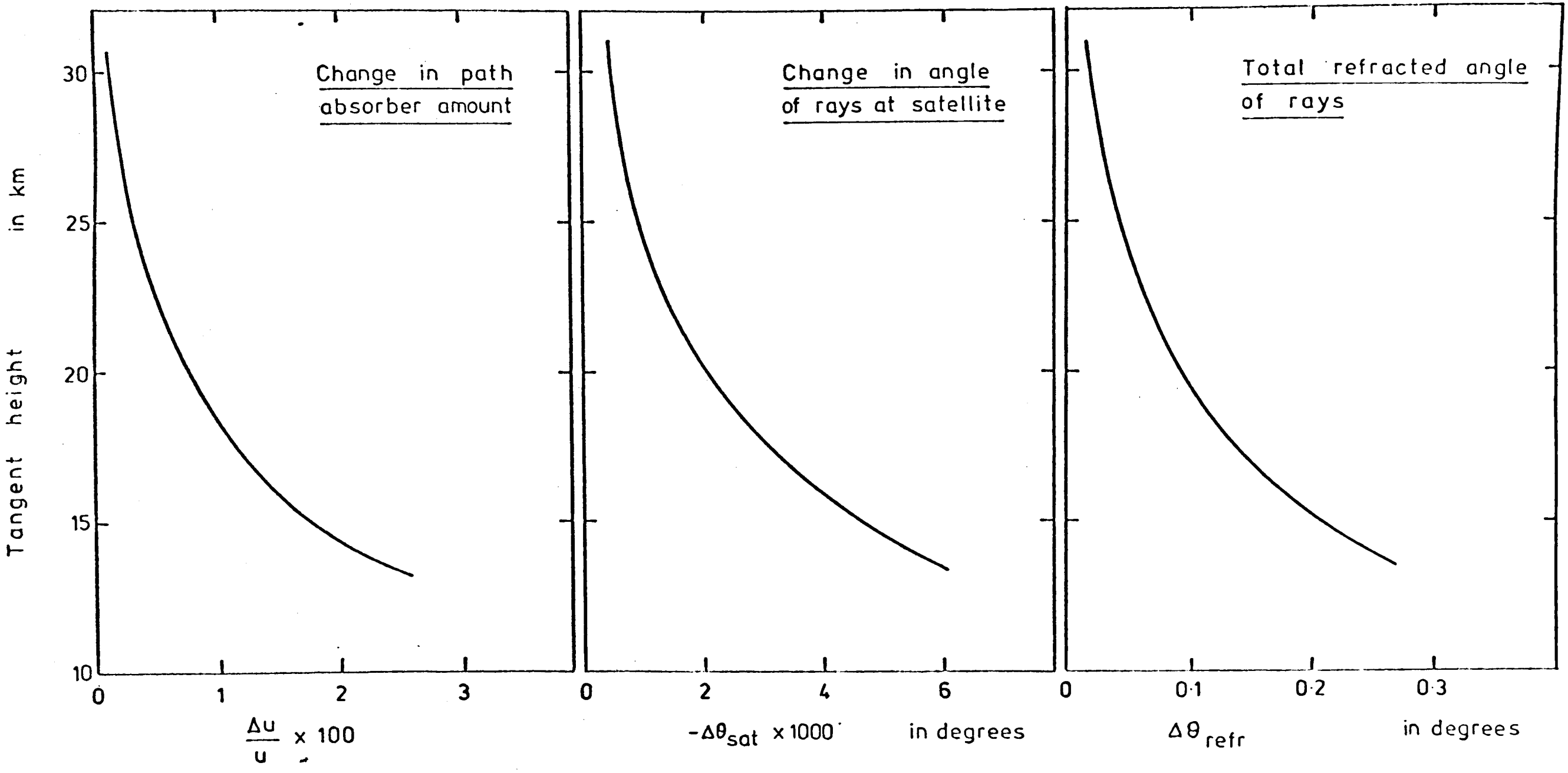

Figure D.2 Changes caused by refraction for constant tangent height: limb path viewed from satellite at 1000 km.

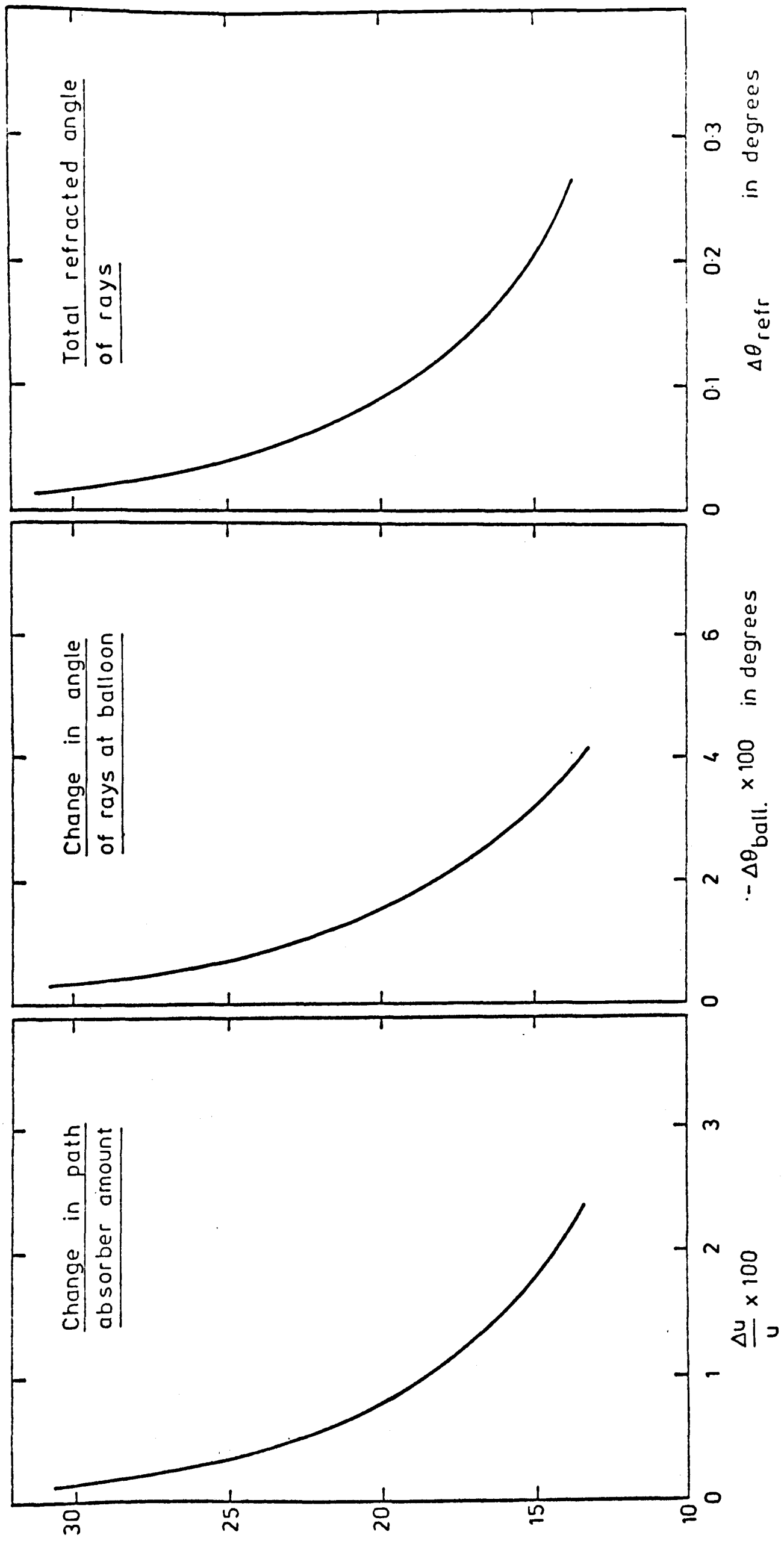

Figure D.3 Changes caused by refraction for constant tangent height: limb path viewed from balloon at 35 km.

$$\left(\frac{\partial z}{\partial \mu}\right)_{\theta} = \frac{-\left(\partial\theta/\partial\mu\right)_z}{\left(\partial\theta/\partial z\right)_{\mu}}, \qquad (D.4)$$

$$\text{and} \quad \frac{1}{u}\left(\frac{\partial u}{\partial \mu}\right)_{\theta} = \frac{1}{u}\left(\frac{\partial u}{\partial \mu}\right)_z + \frac{1}{u}\left(\frac{\partial u}{\partial z}\right)_{\mu}\left(\frac{\partial z}{\partial \mu}\right)_{\theta} = \frac{1}{u}\left(\frac{\partial u}{\partial \mu}\right)_z - \frac{1}{H}\left(\frac{\partial z}{\partial \mu}\right)_{\theta}, \qquad (D.5)$$

where z = tangent height,

θ = angle,

μ = refractive index,

u = absorber amount,

H = scale height.

The following results have been obtained for a typical stratospheric worst case — a limb path tangential at the tropopause (16 km and 110 mb) and a scale height of 6.4 km.

Let us first consider emission experiments for which the usual known angle, θ, is the zenith angle of the rays incident at the instrument (the angle of view). This angle has been calculated directly. For solar occultation experiments, however, the known angle, θ, is the solar zenith angle (obtained from the latitude and longitude of the instrument and the time of day). The change in this angle is the change in the sum of the angle of view and the total refracted angle of the ray — considerably larger than the angular change for the emission case.

The quantities obtained from the calculations illustrated in figures D.2 and D.3 are $(\partial\theta/\partial\mu)_z$, $(\partial\theta/\partial z)_{\mu}$ and $(1/u)(\partial u/\partial\mu)_z$, where $\partial\mu$ has been used to refer to the difference in refractive index produced by including refraction. Using these calculated values and equations D.4 and D.5, we obtain the changes in the required quantities

at constant angle caused by the inclusion of refraction as shown below:

		$\left(\frac{\partial\theta}{\partial\mu}\right)_z$ in degrees for relevant angle		$\left(\frac{\partial\theta}{\partial z}\right)_\mu$ in deg. km^{-1}	$\left(\frac{\partial z}{\partial\mu}\right)_\theta$ in km from eq. D.4	$\frac{1}{u}\left(\frac{\partial u}{\partial\mu}\right)_z$	$\frac{1}{u}\left(\frac{\partial u}{\partial\mu}\right)_\theta$ from equation D.5	
emission	balloon		-0.0279	-0.12	-0.23	0.014	$0.014 + \frac{0.23}{6.4}$	0.050
	satellite		-0.0039	-0.015	-0.26	0.015	$0.015 + \frac{0.25}{6.4}$	0.055
solar occultation	balloon	-0.0279 + 0.1702	+0.1423	-0.12	+1.2	0.014	$0.014 - \frac{1.2}{6.4}$	-0.17
	satellite	-0.0039 + 0.1716	+0.1677	-0.015	+11.2	0.015	$0.015 - \frac{11.2}{6.4}$	-1.74

The values given for a satellite instrument in solar occultation are not strictly valid since they do not represent small changes, but they serve to show the dominating effect of refraction on both the tangent height and absorber amount for this case. In general, the above table shows that the effects of refraction are more important in solar occultation than in emission. Also, since the example given represents the worst stratospheric case, the error in absorber amount caused by omitting refraction is never greater than ~5% for emission and may often be neglected.

Appendix E. Synchronous demodulation of signals.

The waveform of the energy received by the detector is shown in figure 6.1 and is produced by the following processes. The waveform created by fast chopping of the incident solar radiation is approximately square wave and can be expressed as a Fourier series:

$$E_1 = \tfrac{1}{2} x_w + \tfrac{1}{2} x_w \sum_{n=1}^{\infty} a_n \sin n\omega_w t \,, \qquad (E.1)$$

where the coefficients, a_n, depend on the exact shape of the waveform. This energy is modulated at PMC frequency by absorption of the gas in the cell to give the energy incident on the detector:

$$E_2 = \left(\tfrac{1}{2} x_w + \tfrac{1}{2} x_w \sum_{n=1}^{\infty} a_n \sin n\omega_w t\right)\left(1 + \tfrac{1}{2}\frac{x_s}{x_w} \sin \omega_s t + \frac{x_s}{x_w}\sum_{m=2}^{\infty} b_m \sin m\omega_s t\right). \qquad (E.2)$$

Only the fundamental component of the slow chopping is shown in figure 6.1, but harmonics are included here, as they are present although with smaller amplitudes than the fundamental component. Like a_n, the coefficients, b_m, depend on the exact shape of the waveform. The terms produced by emission from the optics and the PMC gas have been omitted from equations E.1 and E.2. This is shown to be a valid approximation for the HCl PMR in chapter 6.1.

The preamplifier and the first stage of the signal channel (a high-pass filter) produce a voltage at the input to the high frequency phase-sensitive detector (PSD) which

is proportional to the energy incident on the detector with the constant and low frequency terms filtered out:

$$V_3 = \tfrac{1}{2} x_w \left(\sum_{n=1}^{\infty} a_n \sin n\omega_w t \right) \left(1 + \tfrac{1}{2} \frac{x_s}{x_w} \sin \omega_s t + \frac{x_s}{x_w} \sum_{m=2}^{\infty} b_m \sin m\omega_s t \right). \qquad (E.3)$$

The filters also apply some h.f. rejection, which serves to alter the relative values of the coefficients, a_n. Here, as in the remainder of this discussion, the gains of the various stages of the electronics have been omitted, since we are primarily interested in the nature of the waveforms transmitted by the electronics.

The effect of the high frequency PSD is to multiply the input voltage, V_3, by a transfer function. Since the PSD switches from one state to another at the reference frequency (in this case the wideband frequency), the transfer function can be expressed as

$$T_1 = c_0 + \sum_{n'=1}^{\infty} c_{n'} \sin n'\omega_w t \, . \qquad (E.4)$$

For a perfect PSD, the input is multiplied by +1 and -1 alternately, and so the transfer function is a square wave of unit amplitude. In this case,

for even n', $c_{n'} = 0$,

and for odd n', $c_{n'} = 4/n'\pi$.

However, to maintain generality and to include the possibility of an imperfect PSD, equation E.4 will be used in its general form.

The output of the PSD is therefore given by

$$V_4 = V_3\, T_1$$

$$= \tfrac{1}{2}\, x_W \sum_{n=1}^{\infty} \tfrac{1}{2}\, c_n a_n \left(1 + \tfrac{1}{2}\,\frac{x_S}{x_W}\,\sin\omega_S t + \frac{x_S}{x_W}\sum_{m=2}^{\infty} b_m \sin m\omega_S t\right)$$

$$+ \text{(a.c. terms in } \omega_W \text{ and its harmonics)}. \qquad (E.5)$$

The wideband output voltage ramp (less integrator offset) is proportional to the d.c. component of V_4, as the integrator effectively filters out a.c. components:

$$\underline{V_5 = \tfrac{1}{4}\, x_W \sum_{n=1}^{\infty} c_n a_n}\ . \qquad (E.6)$$

V_4 is also the input to the sideband stage (see figure 5.7). The band-pass filter only transmits frequencies $\sim\omega_S$, and so the input voltage to the low frequency PSD has the form,

$$V_6 = \tfrac{1}{4}\, x_S\, (\tfrac{1}{2}\sin\omega_S t) \sum_{n=1}^{\infty} c_n a_n \qquad (E.7)$$

This PSD has a transfer function similar in form to that of the high frequency PSD, though in general the exact coefficients will vary:

$$T_2 = d_0 + \sum_{m'=1}^{\infty} d_{m'} \sin m'\omega_S t\ . \qquad (E.8)$$

The output of this PSD is therefore given by

$$V_7 = V_6\, T_2$$

$$= \tfrac{1}{8}\, x_S\, d_1 \sum_{n=1}^{\infty} c_n a_n + \text{a.c. terms}\ . \qquad (E.9)$$

The sideband output voltage ramp (less integrator offset)

is then proportional to the d.c. component of V_7:

$$V_8 = \tfrac{1}{16}\, x_S\, d_1 \sum_{n=1}^{\infty} c_n a_n \quad . \qquad (E.10)$$

From equations E.6 and E.10, the ratio of the sideband to wideband output voltage is obtained:

$$\frac{S_{SB}}{S_{WB}} = \frac{V_8}{V_5} = \frac{1}{4}\, d_1 \frac{x_S}{x_W} \qquad (E.11)$$

Thus the ratio of the output voltages is proportional to the ratio of the amplitudes of the energy modulations due to chopping by the PMC and the rotating chopper. For a perfect sideband PSD with references correctly phased with respect to the signal, $d_1 = 4/\pi$.

$$\frac{S_{SB}}{S_{WB}} = \frac{1}{\pi}\, \frac{x_S}{x_W} \qquad (E.12)$$

This derivation has omitted the gains of the various stages. If there is a gain, G, in the stages between the sideband input (fast PSD output) and the low frequency PSD input, equation E.12 becomes

$$\frac{S_{SB}}{S_{WB}} = \frac{1}{\pi}\, G\, \frac{x_S}{x_W} \qquad (E.13)$$

The discussion has also assumed that there are no cosine terms in T_1 and T_2. These arise if the references are incorrectly phased with respect to the signal or if

they are of imperfect shape. It can be shown, however, that these lead only to a.c.terms which are effectively filtered out by the integrators.

Appendix F. A fault in the signal channel.

F.1 The nature of the fault

The signal channel of the HCl PMR contained a fault which affected the data obtained by the instrument during the balloon flight. The fault was in the high frequency phase-sensitive detector (PSD). The circuit diagram of this PSD as designed is shown in figure F.1 and its position in the signal channel in figure 5.7.

When operating correctly, the wideband references provide current alternately to switch on the left-hand and then the right-hand transistor and thus cause the FETs to be switched on in turn. Equivalent circuits representing the two states of the PSD are shown in figures F.2 (a) and (b). States (a) and (b) have gains of +1 and -1 respectively, and in this way every other half-cycle of the input waveform is inverted. This has the same effect as multiplying the input waveform by a unit square wave at wideband frequency.

Two errors were made in the construction of the circuit. Firstly, resistor R_1 was 2K and not 10K as designed. Consequently the associated transistor was never switched on and so point C was never pulled negative to turn off the FET. Also, bad soldering caused a short between points C and D. The equivalent circuit for the non-inverting half-cycle is shown in figure F.2 (c). Analysis of this circuit shows that the gain is still +1 to a very good approximation, and so the non-inverting half-cycle is unaffected. However, the equivalent circuit

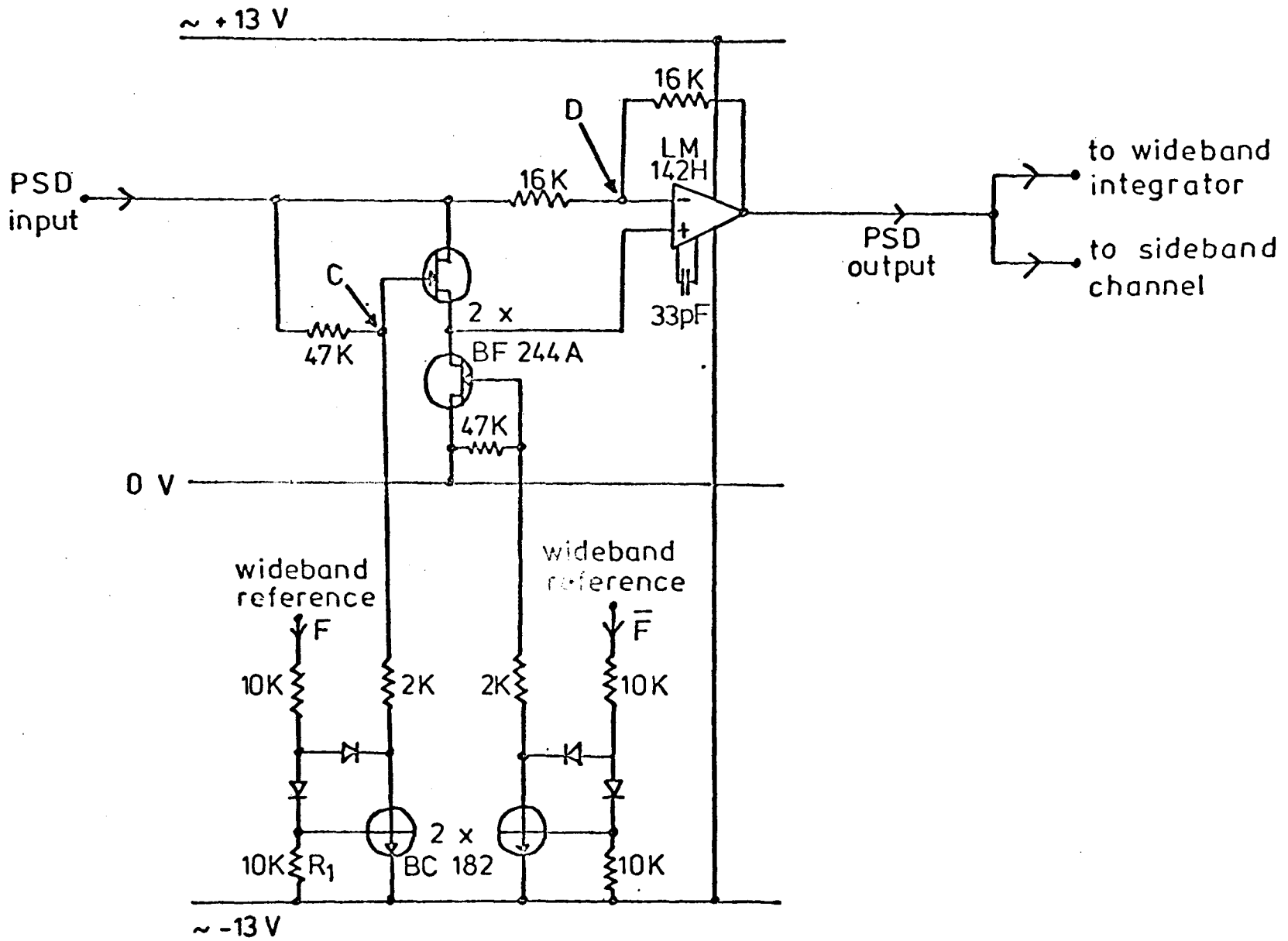

Figure F.1 Wideband phase-sensitive detector.

(a)

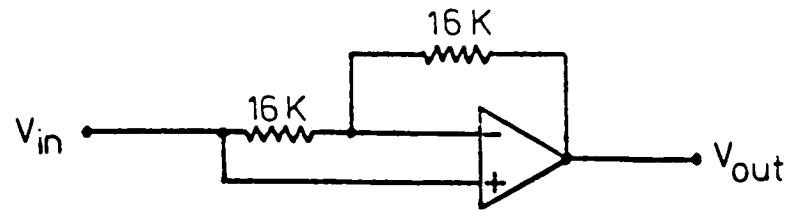

Gain = +1

(b)

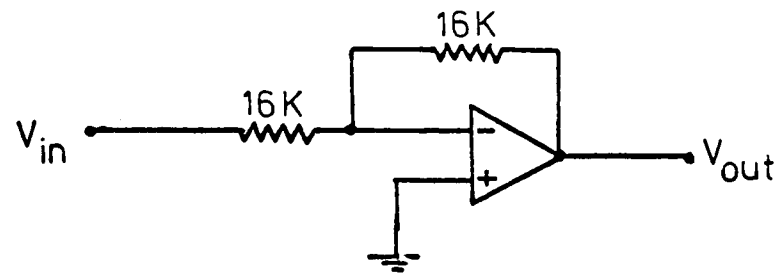

Gain = -1

(c)

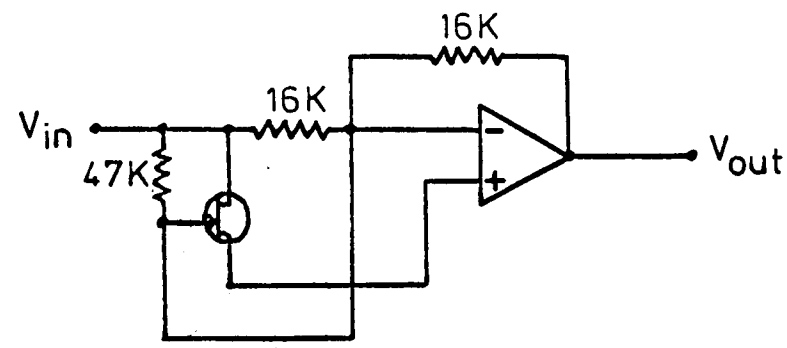

Gain = +1

(d)

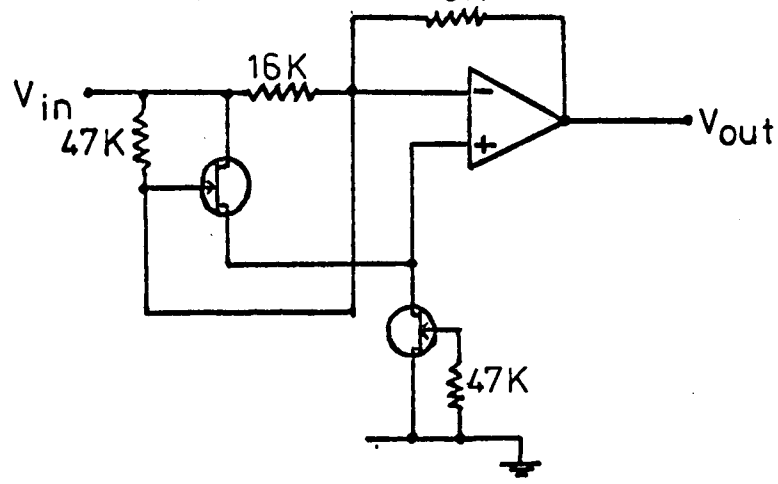

Gain = $f(V_{in})$

(e)

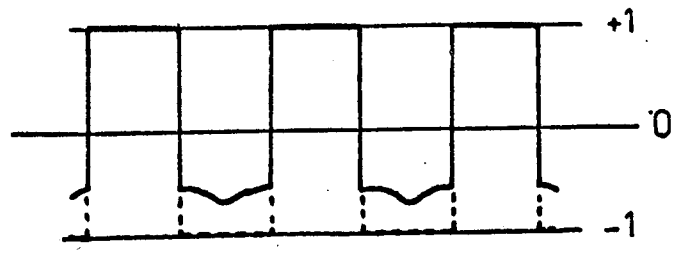

Transfer function of faulty PSD

Figure F.2 Illustrating faulty PSD.

for the inverting half-cycle (figure F.2 (d)) has a variable gain which is a function of the effective drain-source resistances of the FETs, which in turn are functions of the input voltage. The transfer function of the PSD is therefore typically of the shape given in figure F.2 (e), although the exact shape varies with the input signal waveform and amplitude. Examination of the PSD input and output waveforms on an oscilloscope confirmed this.

F.2 Effects of the fault

The linearity of the wideband PSD containing the fault was measured in the laboratory. The amplitude of the PSD input voltage was varied by feeding the signal channel with a constant signal and varying the gain resistor preceding the PSD. A plot of wideband integrator output (less offset) against amplifier gain resistor (which is proportional to PSD input) is shown in figure F.3. This verifies that the fault introduces a non-linearity in the relationship between wideband energy and wideband output voltage. The equivalent test was not performed for the sideband output voltage, since problems of signal-to-noise ratio and stability under laboratory conditions precluded adequately accurate results.

The non-linearity of at least one channel appears at first to threaten reliable interpretation of the data. However, it is shown in chapters 6 and 7 that for this instrument the signals from the seperate channels are never used independently — only the ratio of sideband to wideband

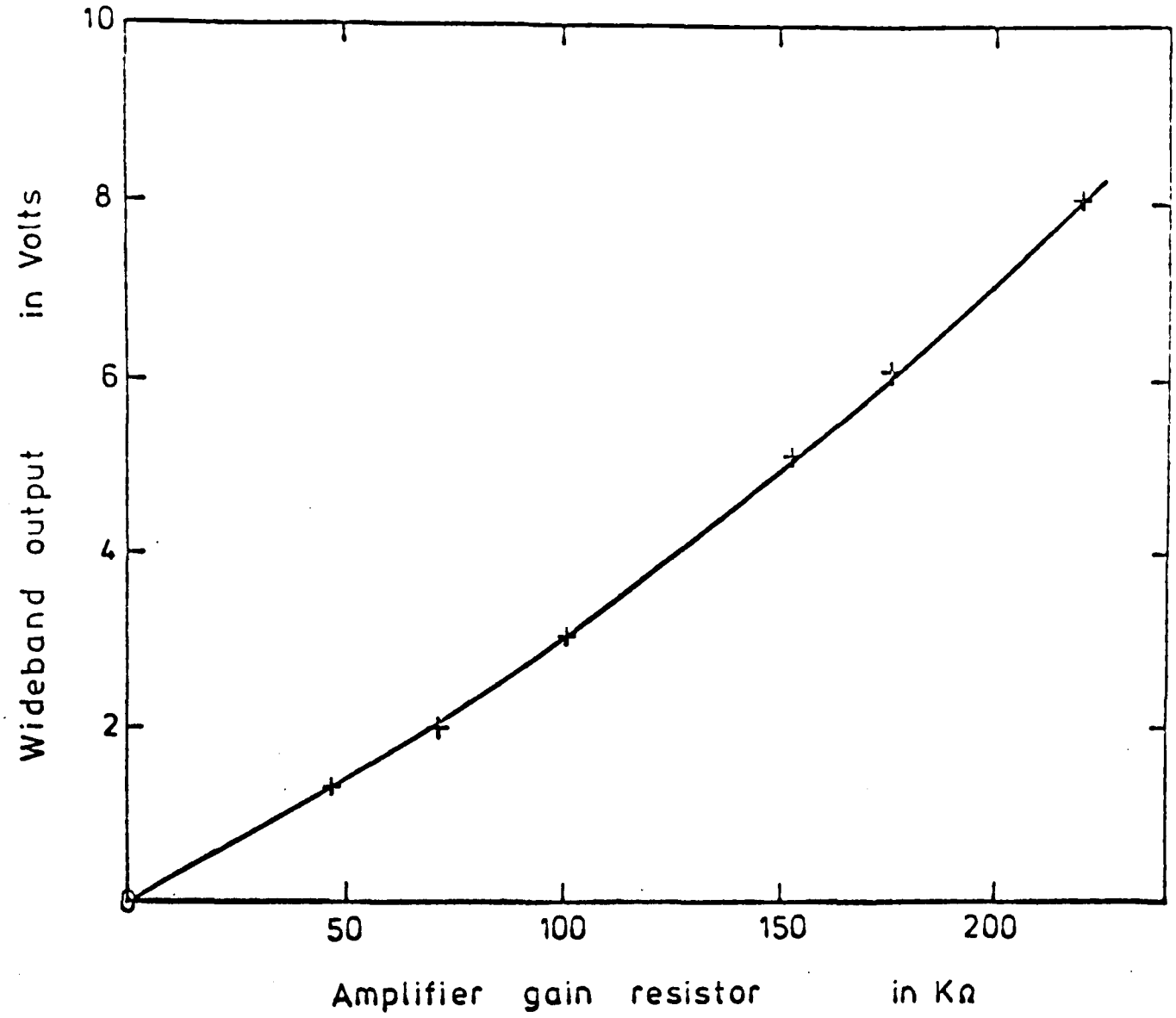

Figure F.3 Illustrating non-linearity of wideband channel.

is used. Now, in appendix E a general expression is derived for the ratio of the output voltages of the two channels (equation E.11). This derivation assumes nothing about the transfer function of the wideband PSD except that it is a Fourier series of the wideband frequency, ω_W. The transfer function shown in figure F.2 (e) for the faulty PSD meets this criterion and so the linearity of the ratio of signals will hold for this circuit.

The effect of the variable transfer function is on the coefficients, c_n, in equation E.4. These will be variables dependent on the input voltage, and so the absolute levels of the wideband and sideband outputs given by equations E.6 and E.10 will not be proportional to their respective incident energy amplitudes, x_W and x_S. However, since the variable, c_n, appears in the same form in both expressions, the ratio between the signals is independent of c_n and therefore linear.

These arguments will hold so long as the amplitude of modulation at PMC frequency, x_S, is very much less than that at chopper frequency, x_W. Under these conditions the amplitude of the input waveform, which affects the gain of the wideband PSD, is changed insignificantly when x_S varies for a constant value of x_W.

Appendix G. Correcting the measured PMR signals for the effects of other atmospheric constituents.

The PMR signals measured by viewing the sun through the atmosphere are attenuated not only by HCl but also by other atmospheric constituents. It is shown here that to a first approximation the two effects can be considered separately. The effects of other constituents can then be applied as a correction to the measured data to give values which can be compared with the results of a model which assumes that other absorbers are absent from the atmosphere.

A line-by-line PMR program which assumes non-overlapping lines and neglects other constituents performs the following calculation:

$$SB_c = \sum_i S_i f_i \quad , \tag{G.1}$$

where S_i is the sideband signal with no atmospheric absorber, produced at the detector by the PMC for the ith line and weighted by optics transmission, solar black body function, detector responsivity, etc.,

f_i is a transmission function which varies with the absorber amount of HCl in the atmospheric path,

and the summation is performed over all the HCl lines in the band.

Obviously, with no atmospheric HCl, $f_i = 1$, and so

$$SB_c = (SB_c)_o = \sum_i S_i \quad . \tag{G.2}$$

The principal quantity calculated by the program is the PMR transmission:

$$\bar{\tau}_c = \frac{SB_c}{(SB_c)_o} = \frac{\sum_i S_i f_i}{\sum_i S_i} \quad . \qquad (G.3)$$

The real sideband signal, however, corresponds to the following quantity:

$$SB_m = \sum_i S_i f_i (\tau_s)_i (\tau_a)_i \quad , \qquad (G.4)$$

where τ_s and τ_a represent the transmission of the atmosphere caused by processes other than HCl absorption. τ_s accounts for the processes which are independent of or slowly varying with wavenumber and τ_a for those which vary rapidly with wavenumber, namely molecular absorption by species other than HCl. With no atmospheric attenuation,

$$SB_m = (SB_m)_o = \sum_i S_i \quad . \qquad (G.5)$$

Consider now the measured wideband signal. It corresponds to the quantity,

$$WB_m = \sum_n \beta_n (\tau_s)_n (\tau_a)_n \delta\nu_n \quad , \qquad (G.6)$$

where β_n is the total energy received from the sun over the interval, $\delta\nu_n$, weighted by optics transmission, detector responsivity, etc.,

$(\tau_s)_n$ and $(\tau_a)_n$ are the mean values over the

interval, $\delta\nu_n$, of the transmissions caused by the processes discussed above,

and the summation is performed for all the intervals, $\delta\nu_n$, over the whole transmitting range of the wideband filter.

Wideband absorption due to HCl is neglible in comparison and so has been omitted. With no atmospheric attenuation,

$$WB_m = (WB_m)_o = \sum_n \beta_n \delta\nu_n \qquad (G.7)$$

From the data measured at sunset the quantity, (SB/WB), is calculated and is expressed as a fraction of its full scale value to give a measured PMR transmission:

$$\bar{\tau}_m = \frac{SB_m / WB_m}{(SB_m)_o / (WB_m)_o} = \frac{SB_m / (SB_m)_o}{WB_m / (WB_m)_o} \; . \qquad (G.8)$$

Substituting into equation G.8 from equations G.4, G.5, G.6 and G.7, we obtain

$$\bar{\tau}_m = \frac{\sum_i S_i f_i (\tau_s)_i (\tau_a)_i}{\sum_i S_i} \times \frac{\sum_n \beta_n \delta\nu_n}{\sum_n \beta_n (\tau_s)_n (\tau_a)_n \delta\nu_n} \; . \qquad (G.9)$$

Since τ_s varies slowly with wavenumber and the HCl band is roughly symmetrical, we may assume that it will affect sideband and wideband proportionally. Therefore,

$$\bar{\tau}_m \simeq \frac{\sum_i S_i f_i (\tau_a)_i}{\sum_i S_i} \times \frac{\sum_n \beta_n \delta\nu_n}{\sum_n \beta_n (\tau_a)_n \delta\nu_n} \; . \qquad (G.10)$$

$$\bar{\tau}_m \simeq \frac{\dfrac{\sum_i S_i f_i (\tau_a)_i}{\sum_i S_i (\tau_a)_i} \times \dfrac{\sum_i S_i (\tau_a)_i}{\sum_i S_i}}{\dfrac{\sum_n \beta_n (\tau_a)_n \delta\nu_n}{\sum_n \beta_n \delta\nu_n}} \qquad (G.11)$$

Assuming that the values of $(\tau_a)_i$ are sufficiently randomly distributed in magnitude amongst the values of S_i for them not to affect significantly the PMR transmissions caused by atmospheric HCl, then

$$\frac{\sum_i S_i f_i (\tau_a)_i}{\sum_i S_i (\tau_a)_i} \simeq \frac{\sum_i S_i f_i}{\sum_i S_i} , \qquad (G.12)$$

and so from equations G.11 and G.12,

$$\bar{\tau}_m \simeq \frac{\sum_i S_i f_i}{\sum_i S_i} \times \frac{\bar{\tau}_{SB}}{\bar{\tau}_{WB}} , \qquad (G.13)$$

where $\bar{\tau}_{SB} = \dfrac{\sum_i S_i (\tau_a)_i}{\sum_i S_i}$ and $\bar{\tau}_{WB} = \dfrac{\sum_n \beta_n (\tau_a)_n \delta\nu_n}{\sum_n \beta_n \delta\nu_n}$,

and they represent the mean transmissions of the sideband and wideband signals respectively caused by other atmospheric constituents.

From G.3 and G.13,

$$\bar{\tau}_c \simeq \bar{\tau}_m \times \frac{\bar{\tau}_{WB}}{\bar{\tau}_{SB}} \qquad (G.14)$$

Thus the measured PMR transmission, $\bar{\tau}_m$, can be corrected for the estimated effects of the other constituents through the calculated quantities, $\bar{\tau}_{SB}$ and $\bar{\tau}_{WB}$, to give $\bar{\tau}_c$, which

represents the PMR transmission which would be found in the absence of other absorbers. This value can then be compared with those calculated by the HCl PMR line-by-line program.

Several approximations are contained in the arguments presented above. However, if the correction to the measured data is small, then the error in the correction is only a second order effect. Moreover, despite the approximations, the corrected value will be an improvement on that uncorrected for other constituents.

Appendix H A reanalysis of some PMR measurements of stratospheric water vapour

H.1 Introduction

A balloon-borne PMR has been used to investigate the mixing ratio profile of stratospheric water vapour through measurement of the thermal emission from an atmospheric limb path. The instrument detected radiation from the pure rotation band of water vapour (~ 100 to 400 cm^{-1}). The measurements discussed here were obtained on a flight from Gap in the French Alps (44^{o} 35'N, 6^{o} 5'E) on 9th July, 1974. The instrument was raised by a hydrogen-filled balloon to a height of about 38 km and remained at its float altitude for about 5 hours. A complete account of the experiment is given by Chaloner (1976). He describes in detail the instrument, its laboratory testing and the procedures used to retrieve the mixing ratio profile of stratospheric water vapour from the data. This appendix is intended only as a reappraisal of the retrieval and reference should be made to Chaloner for all experimental details, much of the relevant data and a full account of the original retrieval technique.

The development of a general line-by-line computer model to perform theoretical calculations of the signals expected from a PMR is discussed in chapter 4.

At the expense of many hours of computer time, it has been possible using such a model to make calculations of expected H_2O PMR signals more accurately than the model used by Chaloner allows. He performed the initial retrieval using a strong pressure-broadened line model to represent the spectral characteristics of the atmospheric emission and its modulation by the PMR. Although such a model is a good approximation under the prevailing PMC and atmospheric conditions, a line-by-line approach enables the calculations to be performed more rigorously. In particular, whereas the original retrieval used a single homogeneous path approximation in representing each atmospheric limb path, a line-by-line model, by virtue of the fact that it essentially performs a series of monochromatic transmission calculations, allows the structured atmospheric path to be represented by several homogeneous sections in series and thus is able to compute more accurately the radiation emitted from the path. Calculations based on a single path approximation, in which the path is characterized by one mass-weighted temperature, tend to lead to errors, since the mass-weighted temperature is not necessarily representative of the temperature at the part of the path from which most of the emission incident on the instrument originates, particularly when the emissivity of the path is high. Also the temperature dependences of line strength and half-width can be treated more directly using a line-by-line approach.

H.2 The data

The operational sequence of the instrument was a scan taking about $5\frac{1}{2}$ minutes and involving:

a) 24 s of "space" view (with a direction of view 30^{o} above the horizontal),

b) 16 s of internal black body view,

c) 32 steps of atmospheric views, 0.308^{o} apart in elevation and each 8 s long, covering the whole range of possible limb paths and some views at angles just above the horizontal.

Chaloner chose to analyse the period from scan 50 to scan 65 when the gains and offsets were relatively stable. For this period he fitted smoothed curves to the "space" view signals and the internal black body view signals for both the wideband and PMR channels. The radiation from the black body reaching the detector is proportional to the difference between the "black body" and "space" signals. Therefore, using the measured temperature of the black body and the appropriate band model for each channel (see Chaloner 1976, chapter 4) he was able to calculate the gain of the instrument for each scan in $Wm^{-2}sr^{-1}(cm^{-1})^{-1}$ per count. Thus each atmospheric view signal was expressed as a radiance, and the mean radiance measured in each mirror position for the period, scan 50 to scan 65, was calculated (see Chaloner, table 10.1).

Since the line-by-line approach uses a different spectral model, Chaloner's conversion from counts to radiance was inappropriate for the re-analysis calculations. The signals were converted to be independent of his spectral model by expressing the radiance as a fraction of those from a black body at 300 K (using the expressions which he derives in chapter 4). In this way the data used in the reanalysis represented more closely what was actually measured - an atmospheric signal as a fraction of an internal black body signal. The fractional signals so calculated are plotted for the PMR and wideband channels in figures H.1 and H.2 respectively. They have been plotted against the zenith angle of the viewing direction using Chaloner's estimate of attitude - that mirror position 15 corresponded to 14.7 steps (each of 0.308^{o}) below the horizontal. This represents only an initial estimate of attitude; it is recalculated below. The tangent heights given in the diagrams have been calculated on the assumptions that Chaloner's estimate of attitude was correct and that the balloon float altitude was 38.4 km.

Figures H.1 and H.2 provide the basic data for the reanalysis; they represent the measured signals with which theoretical calculations for postulated H_2O mixing ratio profiles may be compared. The other data used in the retrieval are summarized in table H.1.

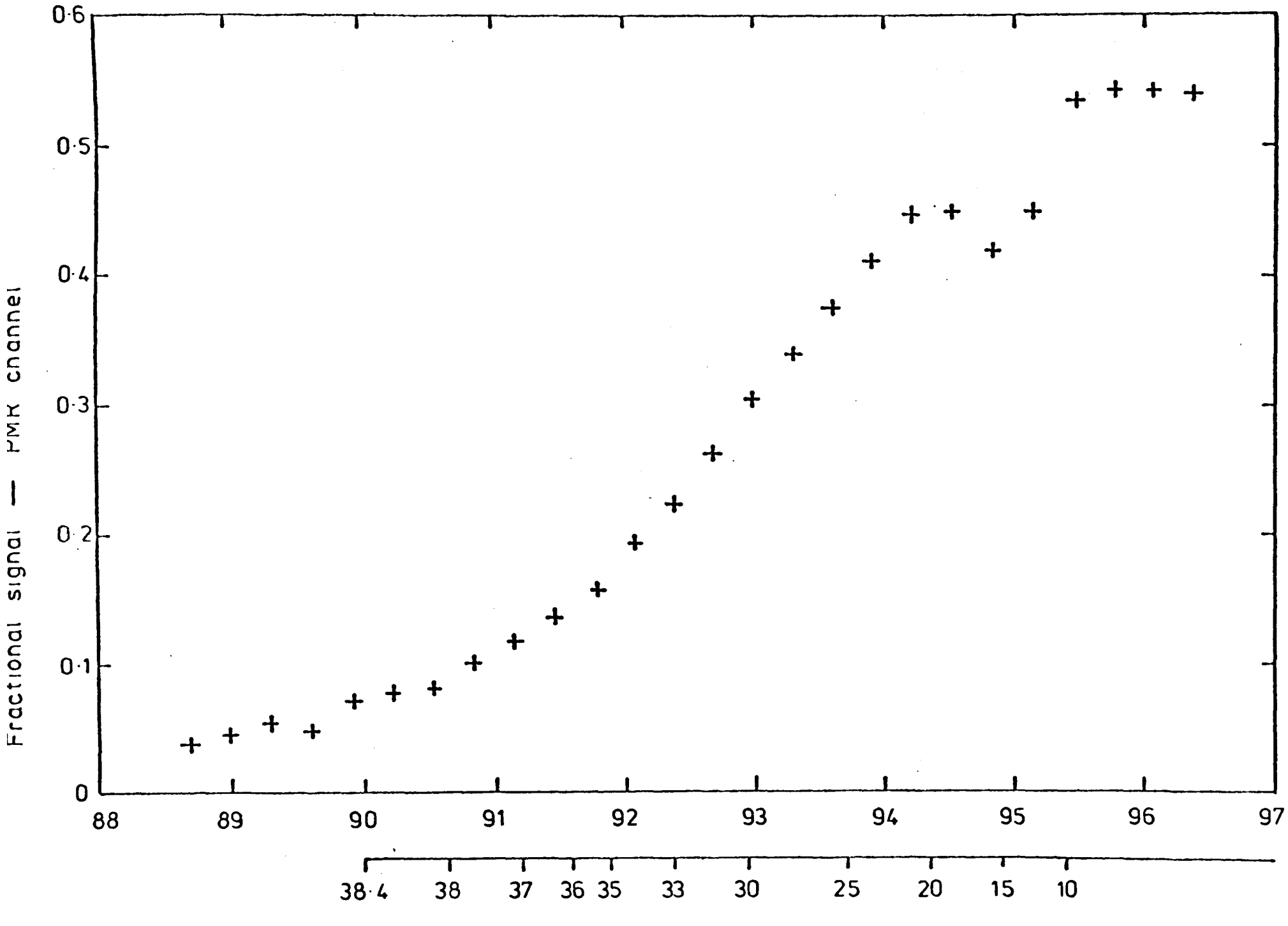

Signals expressed as a fraction of the signal from a black body at 300 K.

Angles of view and tangent heights calculated using preliminary estimate of attitude.

Figure H.1 Measured PMR signals.

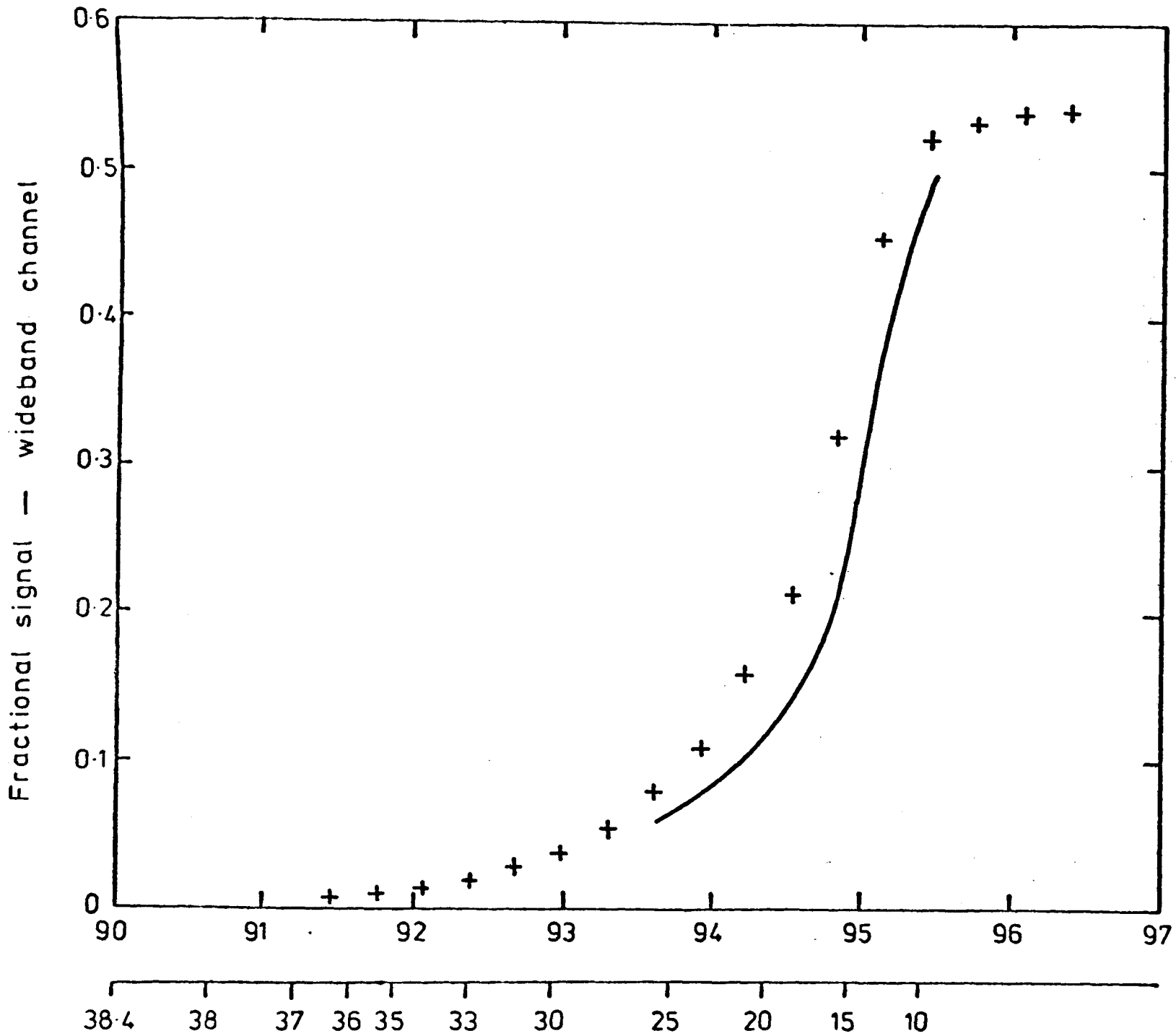

——— Expected signals from atmosphere with mixing ratio profile assumed for lower stratosphere and troposphere.

Signals expressed as a fraction of the signal from a black body at 300 K.

Angles of view and tangent heights calculated using preliminary estimate of attitude.

Zenith angle of view in degrees

Tangent height in km

Figure H.2 Measured wideband signals.

Table H.1 Data used in the retrieval of the water vapour mixing ratio profile.

PMC parameters : length = 6 cm

mean pressure = 14.42 torr = 0.01897 atm.

temperature = 305 K

compression ratio = 1.1

Spectral data : wavenumbers, strengths, nitrogen-broadened Lorentz half-widths and lower state energies from the tabulation of McClatchey et al. (1973)

self-broadening coefficient, $\beta = 7.2$

[definition : $(\alpha_L)_{SELF} = (1 + \beta)\ (\alpha_L)_{N_2}$]

temperature dependence of Lorentz half-widths assumed to be $\propto T^{-\frac{1}{2}}$

Atmospheric temperature-pressure profile : see Chaloner (1976), fig. 10.9

Optics transmission profile : see Chaloner (1976), figure 5.7

Instrument altitude : 38.4 km

Except where stated, the required information has been obtained from C.P. Chaloner via his D. Phil. thesis (1976) or through private communication.

H.3 The retrieval

Using the data given in table H.1 and the general line-by-line program, GENLIN, a series of calculations of expected PMR and wideband signals was made for a range of postulated H_2O mixing ratio profiles. All signals were computed as fractions of the signal from a black body at 300 K. GENLIN allows the limb path viewed from a balloon to be represented by up to 7 homogeneous sections in series. The absorber amount and absorber-weighted pressure and temperature for each section are calculated using a ray tracing routine and thus a better approximation to the emission from the path is achieved than with a single homogeneous path representation. The vertical extents of the sections of the path were carefully chosen in order to minimize the variation of atmospheric temperature and pressure over the sections, particularly for those containing most of the absorber amount in the path.

Assuming Chaloner's estimate of attitude to be correct, a stratospheric mixing ratio profile was postulated and the expected PMR signals calculated as a function of view angle. By making comparison between the calculated and measured signals, an improved profile was estimated, and this iterative procedure was followed until good agreement was obtained between measurement and calculation. The resulting mixing ratio profile is shown in figure H.3 along with that obtained by Chaloner using his less sophisticated retrieval

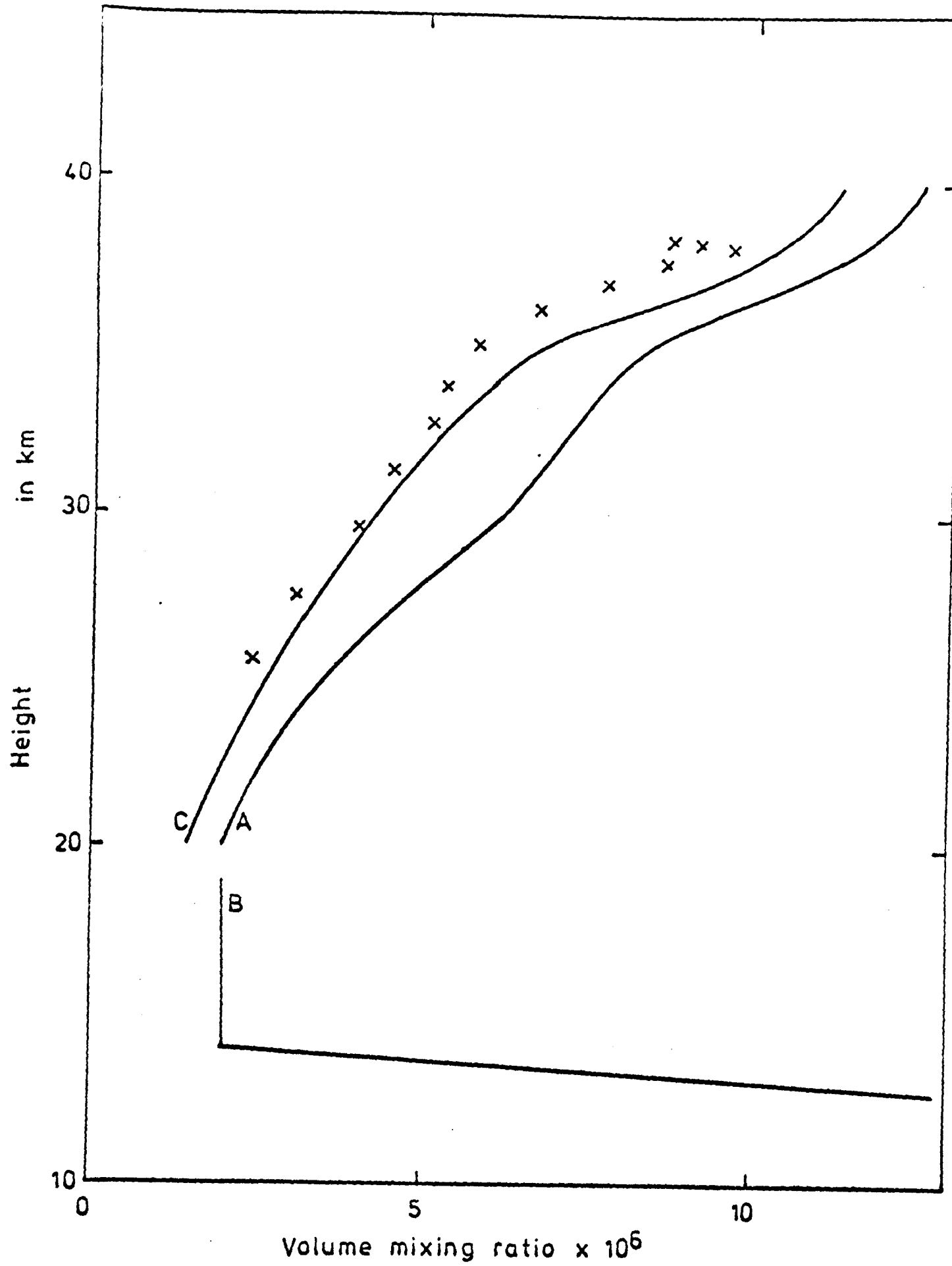

× Chaloner's retrieved profile.

A From PMR channel data using original attitude estimate.

B Assumed profile for calculation of attitude.

C Final profile from PMR channel data using new attitude estimate.

Figure H.3 Retrieved H_2O mixing ratio profiles.

technique. No attempt was made to retrieve mixing ratios below 20 km for two reasons. Firstly, large uncertainties in the retrieved value become inevitable as the emissivity of the path approaches unity. Secondly, there is an anomaly in the measured PMR signals - a pronounced dip centred at 94.8^{o} - which cannot be interpreted in terms of any reasonable mixing ratio profile. This feature has not been fully investigated but may have been caused by transient signals in the PMR channel associated with the large change in wideband energy as the instrument's direction of view stepped through the tropopause. This region of PMR channel data was therefore regarded as unreliable, and only those PMR signals for zenith angles less than 94^{o} (using the original estimate of attitude) were used in the retrieval.

Since Chaloner's estimate of attitude was based on the analysis of wideband signals, it was necessary to check it using GENLIN calculations of expected wideband signal. This was done by assuming a constant volume mixing ratio in the lower stratosphere consistent with the profile retrieved from the PMR channel (i.e. 2×10^{-6}), a tropospheric mixing ratio equivalent to a relative humidity of 70% and a humidity tropopause coincident with the temperature tropopause at 14 km. The assumed profile is shown in figure H.3. The wideband signals expected from this profile were calculated and smoothed to allow for the effects of the real field of view using the method

suggested by Chaloner (chapter 10.12). The smoothed values give a curve which is plotted in figure H.2 and from which it is concluded that the original estimate of attitude is in error. A calculation of the mean displacement of the calculated curve from the measured data gave an error in the original attitude estimate of 0.225 degrees. However, several factors lead to a large uncertainty in this value: the stratospheric mixing ratio below 20 km and the height of the humidity tropopause are not known precisely, and the smoothing technique used is not exactly appropriate for the real field of view. Consequently, the total uncertainty in attitude is estimated to be ~ 0.1 degrees.

Using the new estimate of attitude, the PMR channel calculations were repeated to find a mixing ratio profile which gave calculated signals consistent with the measured signals (those shown in figure H.1 shifted by 0.225 degrees). The resulting mixing ratio profile is shown in figure H.3 and represents the best estimate of mixing ratio above 20 km. The change in the lower stratospheric mixing ratio produced by the attitude correction is sufficiently small for it to have a negligible effect on the calculation of the attitude correction itself.

H.4 Errors

The errors from all sources were analysed

in a manner similar to that used by Chaloner, and they are summarized in table H.2. Many of them are essentially the same as those computed by Chaloner and comment is only made here on those sources of error over which we disagree by a large amount. The line-by-line model enabled the computations of error to be made by changing the mixing ratios by 20% and using the changes in the expected signals so produced to calculate the mixing ratio uncertainties from the following sources: errors in gain, radiative zero, attitude, self-broadening coefficient, atmospheric temperature and digitizer resolution and non-linearity. The use of this method accounts for the small discrepancies between these calculations and those of Chaloner, who used more approximate methods of error estimation.

The spectroscopic errors have been re-estimated at $\sim \pm 15\%$. This is mainly due to the uncertainty in the self-broadening coefficient, β. Chaloner calculated an appropriate β for the PMR channel to be 7.2 from laboratory transmission measurements. Line-by-line calculations have been performed to model the transmission measurements and it is concluded that 7.2 is an appropriate value, although there is an uncertainty of ± 1 caused by the scatter on the measured transmissions (see Chaloner, figure 8.9). This uncertainty alone leads to an error of 13% in mixing ratio, and so 15% from all spectroscopic sources is considered reasonable.

Tangent height in km	Percentage error caused by :							Total percentage error
	± 1% gain error	± 1% zero error	± 0.4 km altitude error	± 0.1 deg attitude error	spectroscopic errors	± 1 K atmospheric temperature error	± 1.5% digitizer error	
20	5	12	1	13	15	4	18	30
25	3	9	3	11	15	3	13	25
30	3	9	5	11	15	2	14	26
33	2	9	6	10	15	1	14	25
35	1	8	7	7	15	1	13	24
38	1	12	10	7	15	1	18	29

Table H.2 Retrieval of H_2O mixing ratio profile : error estimates.

The total error in radiance caused by digitizer resolution and digitizer non-linearity is estimated to be ~ ± 1.5% of the radiance from a black body at 300 K, and mixing ratio errors from this source have been calculated accordingly.

The combined error from all sources has been calculated by taking the root of the sums of the squares of the individual errors. The final retrieved profile with its total errors is shown in figure H.4.

H.5 Conclusions

Despite the disagreement over attitude and the differences in retrieval technique, the profile produced by this reassessment is very similar to that obtained by Chaloner in the original retrieval. However, in addition to the mixing ratios obtained from the PMR channel data, Chaloner attempted to retrieve mixing ratios in the lower stratosphere from the wideband channel and thus reported two profiles which were not consistent with one another.
This reanalysis has used a different approach. It has demanded consistency between the two channels, used the wideband data and a best estimate of the mixing ratio around the tropopause to retrieve attitude and then derived the mixing ratio profile from the PMR channel data only.

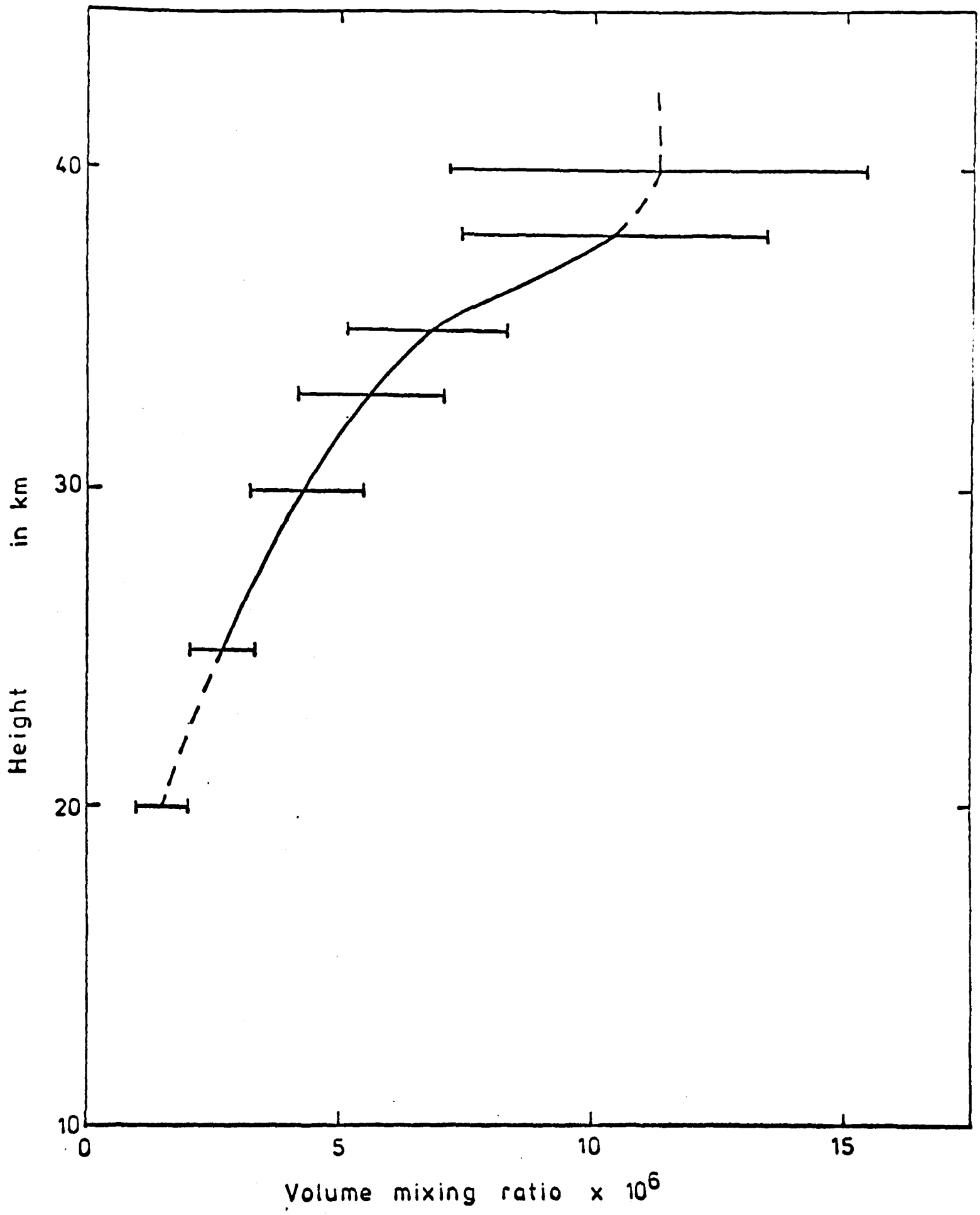

Figure H.4 Final H_2O mixing ratio profile.

REFERENCES

Ackerman M., Frimout D., Girard A., Gottignies M., Muller C.
Geophys. Res. Lett., 3, 81-83 (1976).
Stratospheric HCl from infra-red spectra.

Ackerman M., Frimout D., Muller C.
Nature, 269, 226-227 (1977).
Stratospheric CH_4, HCl and ClO and the chlorine-ozone cycle.

Anderson J.G., Margitan J.J., Stedman D.H.
Science, 193, 501-503 (1977).
Atomic chlorine and the chlorine monoxide radical in the stratosphere: three in situ observations.

Armstrong B.H., Nicholls R.W.
Pergamon Press (1972).
Emission,absorption and transfer of radiation in heated atmospheres.

Ballard J.
D. Phil. thesis, Oxford (to be published).

Barnett J.J.
Department of Atmospheric Physics, Oxford, internal memorandum.

Benedict W.S., Herman R., Moore G.E., Silverman S.
Can. J. Phys., 34, 850-875 (1956).
The strengths, shapes and widths of infra-red lines. The HCl fundamental.

Bennett H.E.
J. Opt. Soc. Am., 53, 1389-1394 (1963).
Specular reflectance of aluminized ground glass and the height distribution of surface irregularities.

Ben-Reuven A., Kimel S., Hirshfeld M.A., Jaffe J.H.
J. Chem. Phys., 35, 955-962 (1961).
Theory and measurement of pressure-induced shifts of HCl lines due to noble gases.

Chaloner C.P.
D. Phil. thesis, Oxford (1976).

Cicerone R.J., Stolarski R.S., Walters S.
Science, 185, 1165-1166 (1974).
Stratospheric ozone destruction by man-made chlorofluoromethanes.

Crutzen P.J.
Ambio, 3, 201-210 (1974).
Estimates of possible variations in total ozone due to natural causes and human activities.

Crutzen P.J.
Geophys. Res. Lett., 1, 205-208 (1974).
Estimates of possible future ozone reductions from continued use of fluoro-chloro-methanes (CF_2Cl_2, $CFCl_3$).

Crutzen P.J., Isaksen I.S.A.
Unpublished paper (1976).
The impact of the chlorocarbon industry on the ozone layer.

Curtis P.D., Houghton J.T., Peskett G.D., Rodgers C.D.
Proc. R. Soc. Lond. A., 337, 135-150 (1974).
Remote sounding of atmospheric temperature from satellites. V. The pressure modulator radiometer for Nimbus F.

Delderfield J.
D. Phil. thesis, Oxford (1977).

Drayson S.R.
J. Q. R. S. T., 16, 611-614 (1976).
Rapid computation of the Voigt profile.

Drummond J.R.
D. Phil. thesis, Oxford (1977).

Eggleton E.A.J., Cox R.A., Derwent R.G.
New Scientist, 70, 402-403 (1976).
Will chlorofluorocarbons really affect the ozone shield?

Ehhalt D., Heidt L.E., Lueb R.H., Roper N.
Proc. Third Conf. on CIAP, 153 (1974).
Vertical profiles of CH_4, H_2, N_2O and CO_2 in the stratosphere.

Farmer C.B., Raper O.F., Norton R.H.
Geophys. Res. Lett., 3, 13-16 (1976).
Spectroscopic detection and vertical distribution of HCl in the troposphere and stratosphere.

Farmer C.B., Raper O.F.
Geophys. Res. Lett., 4, 527-529 (1977).
The HF:HCl ratio in the 14-38 km region of the stratosphere.

Goldring H., Benesch W.
Can. J. Phys., 40, 1801-1813 (1962).
Widths of HCl overtone lines at various temperatures.

Goody R.M.
Oxford University Press (1964).
Atmospheric radiation I.

Gray L.D., Selvidge J.E.
J. Q. R. S. T., 5, 291-301 (1965).
Relative intensity calculations for carbon dioxide.

Harries J.E., Moss D.G., Swann N.R.
Nature, 250, 475-476 (1974).
H_2O, O_3, N_2O and HNO_3 in the arctic stratosphere.

Harries J.E. (1975).
see The Report of the Committee on Meteorological Effects of Stratospheric Aircraft (COMESA), 1972-5.

Harries J.E.
Reviews of Geophys. and Space Phys., 14, 565-575 (1976).
The distribution of water vapour in the stratosphere.

Heidt L.E., Lueb R., Pollock W., Ehhalt D.H.
Geophys. Res. Lett., 2, 445-447 (1975).
Stratospheric profiles of CCl_3F and CCl_2F_2.

Houdeau J.-P., Larvor M., Haeusler C.
C. R. Ac. Sci., C, 284, 307-310 (1977).
The widths and shifts at low temperature of lines of the fundamental vibration-rotation band of $H^{35}Cl$ when broadened with nitrogen.

Houghton J.T., Smith S.D.
Oxford University Press (1966).
Infra-red physics.

Houghton J.T., Peskett G.D., Ballard J., Drummond J.R., Doherty E., Wale M.J.
Proceedings of the symposium on radiation in the atmosphere, 309-311 (1976).
The stratospheric and mesospheric sounder for Nimbus G.

Houghton J.T.
Cambridge University Press (1977).
The physics of atmospheres.

Jarnot R.F.
D. Phil. thesis, Oxford (1976).

Kimel S., Hirshfeld M.A., Jaffe J.H.
J. Chem. Phys., 31, 81-84 (1959).
Pressure induced shifts of HCl absorption lines in the infra-red.

Krey P.W., Lagomarsino R.J., Toonkel L.E.
J. Geophys. Res., 82, 1753-1766 (1977).
Gaseous halogens in the atmosphere in 1975.

Krueger A.J., Minzner R.A.
NASA X-651-73-22 (1973).
A proposed mid-latitude ozone model for the U.S. standard atmosphere.

Kurzeja R.J.
J. Atm. Sci., 34, 1120-1129 (1977).
Effects of diurnal variations and scattering on ozone in the stratosphere for present-day and predicted future chlorine concentrations.

Lazrus A.L., Gandrud B.W., Woodard R.N., Sedlacek W.A.
Geophys. Res. Lett., 2, 439-441 (1975).
Stratospheric halogen measurements.

Lazrus A.L., Gandrud B.W., Woodard R.N., Sedlacek W.A.
J. Geophys. Res., 81, 1067-1070 (1976).
Direct measurements of stratospheric chlorine and bromine.

Lazrus A.L., Gandrud B.W., Greenberg J., Bonelli J., Mroz E., Sedlacek W.A.
Geophys. Res. Lett., 4, 587-589 (1977).
Mid-latitude seasonal measurements of stratospheric acidic chlorine vapour.

Lovelock J.E.
Nature, 230, 379 (1971).
Atmospheric fluorine compounds as indicators of air movements.

Lovelock J.E., Maggs R.J., Wade R.J.
Nature, 241, 194-196 (1973).
Halogenated hydrocarbons in and over the Atlantic.

Lovelock J.E.
Nature, 252, 292-294 (1974).
Atmospheric halocarbons and stratospheric ozone.

McClatchey R.A., Fenn R.W., Selby J.E.A., Garing J.S., Volz F.E.
AFCRL Rep. 70-0527, Environ. Res. Pap. 331 (1970).
Optical properties of the atmosphere.

McClatchey R.A., Benedict W.S., Clough S.A., Burch D.E., Calfee R.F., Fox K., Rothman L.S., Garing J.S.
AFCRL Rep. TR-73-0096, Environ. Res. Pap. 434 (1973).
AFCRL atmospheric absorption line parameters compilation.

Molina M.J., Rowland F.S.
Geophys. Res. Lett., 1, 309-312 (1974).
Predicted present stratospheric abundances of chlorine species from photodissociation of carbon tetrachloride.

Molina M.J., Rowland F.S.
Nature, 249, 810-812 (1974).
Stratospheric sink for chlorofluoromethanes: chlorine atom-catalysed destruction of ozone.

Mroz E.J., Lazrus A.L., Bonelli E.J.
Geophys. Res. Lett., 4, 149-150 (1977).
Direct measurement of stratospheric fluoride.

Murcray D.G., Murcray F.H., Williams W.J.
Appl. Opt., 6, 191-196 (1967).
A balloon-borne grating spectrometer.

NASA Assessment Report (September 1977).
Effects of chlorofluoromethanes on stratospheric ozone.

Penner S.S.
Pergamon Press (1959).
Quantitative molecular spectroscopy and gas emissivities.

Petrov S.B., Podkladenko M.V.
Optics and Spectroscopy, 38, 141-142 (1975).
Width of spectral lines of HCl when broadened by collisions with CO_2 and N_2.

Petrov S.B.
Optics and Spectroscopy, 39, 150-151 (1975).
Half-widths of lines in the fundamental band of HCl at different temperatures.

Pierluissi J.H., Vanderwood P.C., Gomez R.B.
J. Q. R. S. T., 18, 555-558 (1977).
Fast calculational algorithm for the Voigt profile.

Plyler E.K., Tidwell B.D.
Z. fur Elek., 64, 717-720 (1960).
The rotational constants of hydrogen chloride.

Prasad S.S.
Planet. Spac., 24, 1187-1193 (1976).
Some aspects of the stratospheric Cl-ClO-Cl cycle: possible roles of ClO^*, $ClNO_3$ and HOCl.

Proposal for the Nimbus G satellite.
Department of Atmospheric Physics, Oxford, memorandum (1973).

Rank D.H., Birtley W.B., Eastman D.P., Wiggins T.A.
J. Chem. Phys., 32, 296-297 (1960).
Pressure induced shifts of HCl lines due to foreign gases.

Raper O.F., Farmer C.B., Toth R.A., Robbins B.D.
Geophys. Res. Lett., 4, 531-534 (1977).
The vertical distribution of HCl in the stratosphere.

Rodgers C.D., Williams A.P.
J. Q. R. S. T., 14, 319-323 (1974).
Integrated absorption of a spectral line with a Voigt profile.

Rowland F.S.
New Scientist, 64, 717-720 (1974).
Aerosol sprays and the ozone shield.

Rowland F.S., Molina M.J.
Reviews of Geophys. and Space Phys., 13, 1-35 (1975).
Chlorofluoromethanes in the environment.

Rowland F.S., Spencer J.E., Molina M.J.
J. Phys. Chem., 80, 2711-2713 (1976 a).
Stratospheric formation and photolysis of chlorine nitrate.

Rowland F.S., Spencer J.E., Molina M.J.
J. Phys. Chem., 80, 2713-2715 (1976 b).
Estimated relative abundance of chlorine nitrate among stratospheric chlorine compounds.

Rundel R.D., Stolarski R.S.
J. Geophys. Res., 81, 5759-5764 (1976).
A re-examination of the photochemistry of the Cl_2-O_3 system.

Schmeltekopf A.L., Goldan P.D., Henderson W.R., Harrop W.J., Thompson T.L., Fehsenfeld F.C., Schiff H.I., Crutzen P.J., Isaksen S.A., Ferguson E.E.

Geophys. Res. Lett., 2, 393-396 (1975).

Measurements of stratospheric $CFCl_3$, CF_2Cl_2 and N_2O.

Schofield J.T.

D. Phil. thesis, Oxford (to be published).

Simonaitis R., Heicklen J.

Planet. Space Sci., 23, 1567-1569 (1975).

Perchloric acid: a possible sink for stratospheric chlorine.

Snider D.E.

J. Atm. Sci., 32, 2178-2184 (1975).

Refractive effects in remote sensing of the atmosphere with infra-red transmission spectroscopy.

Stedman D.H., Chameides W.L., Cicerone R.J.

Geophys. Res. Lett., 2, 333-336 (1975).

The vertical distribution of soluble gases in the troposphere.

Stolarski R.S., Rundel R.D.

Geophys. Res. Lett., 2, 443-444 (1975).

Fluorine photochemistry in the stratosphere.

Sundararaman N.

Prepared for the U.S. Dept. of Transportation, FAA-EQ-77-2 (1976).

Summary of upper atmospheric data.

Sze N.D.

Paper distributed at Manufacturing Chemists Association meeting (October 1977).

Some recent developments in atmospheric chemistry.

Thekaekara M.P.

Solar Energy, 14, 109-127 (1973).

Solar energy outside the earth's atmosphere.

Toth R.A., Hunt R.H., Plyler E.K.
J. Mol. Spec., 35, 110-126 (1970).
Line strengths, line widths and dipole moment function for HCl.

Toth R.A., Darnton L.A.
J. Mol. Spec., 49, 100-105 (1974).
Line widths of HCl broadened by CO_2 and N_2 and CO broadened by CO_2.

Toth R.A., Brown L.R., Hunt R.H.
J. Mol. Spec., 67, 1-33 (1977).
Line positions and strengths of methane in the 2862 to 3000 cm^{-1} region.

Volz A., Ehhalt D.H., Cosatto H.
Paper submitted to PAGEOPH (1977).
The vertical distribution of CFM and related species in the stratosphere.

Wale M.J.
D. Phil. thesis, Oxford (to be published).

Williams W.J., Kosters J.J., Goldman A., Murcray D.G.
Geophys. Res. Lett., 3, 379-382 (1976 a).
Measurements of stratospheric halocarbon distributions using infra-red techniques.

Williams W.J., Kosters J.J., Goldman A., Murcray D.G.
Geophys. Res. Lett., 3, 383-385 (1976 b).
Measurement of the stratospheric mixing ratio of HCl using infra-red absorption technique.

Wofsy S.C., McElroy M.B., Yung Y.L.
Geophys. Res. Lett., 2, 215-218 (1975).
The chemistry of atmospheric bromine.

Wofsy S.C., McElroy M.B., Sze N.D.
Science, 187, 535-536 (1975).
Freon consumption: implications for atmospheric ozone.

Zander R., Roland G., Delbouille L.
Geophys. Res. Lett., 4, 117-120 (1977).
Confirming the presence of hydrofluoric acid in the upper stratosphere.